Designing Particle-Based Functional Materials

Naomi Kumano

Designing Particle-Based Functional Materials

Naomi Kumano

A thesis submitted to Department of Molecular and Macromolecular Chemistry,
Graduate School of Engineering, Nagoya University
for the degree of Doctor of Philosophy

April 2021

Abstract

This thesis is concerned with particle-based functional materials for automotive applications. To produce next-generation automobiles, automotive manufacturing industries must overcome several key challenges, including improving productivity while reducing energy consumption and producing automobiles that are attractive and functional for customers. In addition, automotive manufacturing industries must develop strategies to reduce the environmental impact related to the manufacture, use, and disposal of automobiles. For these missions, materials development plays an important role. In particular, functional materials composed of particles and polymers are becoming increasingly important. Particle-based functional materials used in automobiles include interior/exterior coating films, electrodes for rechargeable batteries and fuel cells, exhaust-gas purification catalysts, and capacitors. Thus, the present study details research and development for three major issues related to such materials. The primary purpose of this thesis is to demonstrate new colored materials and functional materials for use in interior/exterior coatings of automobiles. To solve the problems of high performance and high-speed production of electrodes for fuel cell vehicles, a secondary purpose is to control the rheological behavior of electrode precursors (catalyst ink) and the cracking behavior of electrodes (catalyst layer) by controlling the aggregation of particles.

First, consumer desire for attractive colors necessitates the development of new alternatives to traditional pigments that contain heavy metals, which may be toxic, and to dyes that fade easily under extended exposure to UV light. Therefore, I here propose three types of new colored materials. Specifically, I demonstrate new colored materials that exhibit brilliant color changes, without dyes or pigments, covering the whole visible region in response to temperature changes. The response is achieved through changes in both the diffraction properties and the wavelength dispersion of the refractive index. The newly prepared colored materials can be formed into any shape and exhibit a stable color for an extended period. They therefore have potential applications as interior/exterior materials. In addition, a new colored material consisting of a particle gel network and a liquid crystal that can undergo changes in color covering the whole visible region and can exhibit an opaque milky color in response to temperature variation is also presented. This material has an angle independent color and can function as a multicolor polymer-dispersed liquid crystal. This system might be suitable for use in energy-saving multicolor displays for automotive interior decoration. In addition, the novel pigments synthesized in the present work represent environmentally friendly and nonfading pigments composed of black graphite nanosheets (GNSs) and TiO_2. The black GNSs enhance the interference color contrast and

the randomly oriented GNS pigment exhibits angle-independent color in the coating film by diffuse reflection. Thus, these novel pigments have potential applications as interference pigments for automobile paints.

Second, interior/exterior coatings need to be long-lasting and remain scratch-free. Scratch resistance has therefore become one of the most important properties of automotive coatings. Hence, I propose novel coatings with scratch-recovery characteristics that enable surface deformations to recover over time, eventually becoming invisible to the naked eye. I explore the remarkable improvement in scratch-recovery characteristics without sacrificing hardness by using a base resin with a siloxane main chain instead of a carbon–carbon main chain such as that of an acrylic polyol. The newly prepared coatings have potential applications in automobile coatings because they exhibit both sufficient hardness and scratch recovery characteristics superior to those of conventional coatings.

Third, because agglomerated structures of carbon-black-supported Pt (Pt/C) nanoparticles in catalyst inks affect their productivity and performance, identifying and controlling the structural parameters that control the dispersion state of Pt/C agglomerates is important. Thus, I propose solutions to quality control problems related to the high viscosity of the catalyst ink, which leads to difficulty in slot-die coating, where cracks formed in the catalyst layer during drying can adversely affect performance and durability. I show that the agglomerate structures can be controlled by the effects of adsorbed and nonadsorbed ionomers on the Pt/C surface, leading to changes in the rheological behavior of the catalyst ink and in the crack behavior of the catalyst layer. The research presented herein demonstrates that catalyst inks with the desired viscosity in the stable coating window can be obtained by increasing the affinity between the Pt/C and ionomers by changing the water content in the dispersion medium. Moreover, I suggest a useful index for understanding the cracking behavior of catalyst layers and possible measures for preventing catalyst-layer cracking, including increasing the affinity between the Pt/C and the ionomers.

Acknowledgements

I would like to express my sincere gratitude to my supervisor, Professor Takahiro Seki, Associate Professor Yukikazu Takeoka in Nagoya university, for their invaluable guidance, continuous advice and constructive criticism throughout my research. I would also like to thank Professor Atsushi Satsuma, Professor Ayae Sugawara-Narutaki, Junior Associate Professor Atsushi Noro in Nagoya university, for the discussion on my thesis.

My sincere thanks are also due to the members of Seki lab. in Nagoya university. Special mention should be made of Professor Shusaku Nagano, Professor Tomonari Umemura, Assistant Professor Mitsuo Hara, Mr. Hiromasa Suzuki, Mr. Masahiro Honda in Nagoya university. I am also thankful to Associate Professor Imran Abu Bin, Dr. Rashid Harun-Ur, Dr. Huda Muhammad Nurul, Ms. Megumi Yamamoto, Ms. Yoshie Goto, Mr. Masashi Okubo, Mr. Daiki Kondo, Mr. Hiroaki Goto.

I must also thank all my colleagues and ex-colleagues in the members of Organic materials and Coating lab. and Slurry special assigned lab. in TOYOTA Central R&D Labs., particularly Dr. Kanji Mori, Dr. Hiromitsu Tanaka. Their fruitful discussion and collaboration have benefited this study. The discussions and collaboration with Dr. Kenji Kudo, Dr. Ishii Masahiko, Dr. Hiroshi Nakamura, Mr. Akimoto Yusuke in TCRDL. have been also very helpful and are gratefully acknowledged. I would also express my thanks to Dr. Makoto Kato, Dr. Akihiko Suda in TCRDL and Mr. Ishii Masahiko in Toyota Motor Company. I am also thankful to Dr. Yoshifumi Maegawa and Dr. Yoshio Sageshima in TCRDL for their helpful advices.

Finally, I would like to thank my family and friends for their love, tolerance, patience and constant encouragement during this work.

Without valuable support from everyone, my PhD journey over 10 years would not have been possible.

Naomi Kumano

Table of Contents

Chapter 1

General Introduction

1.1 Background

To produce next-generation automobiles, the automotive manufacturing industry must overcome several key challenges, including improving productivity while reducing energy consumption and producing automobiles that are attractive to and functional for customers. In addition, the automotive manufacturing industry must develop strategies to reduce the environmental impact related to the manufacture, use, and disposal of automobiles. These strategies are summarized in Figure 1.

For these objectives, materials development plays an important role. In particular, functional materials composed of particles and polymers are becoming increasingly important. Particle-based functional materials used in automobiles include interior/exterior coating films, electrodes for rechargeable batteries and fuel cells, exhaust-gas purification catalysts, and capacitors (Figure 2). Examples of particle-based functional materials are discussed as follows.

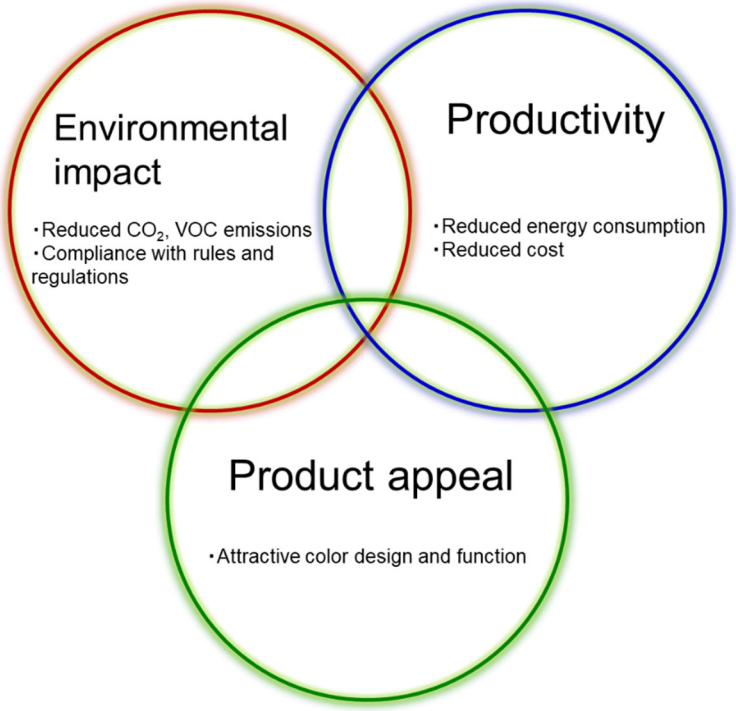

Figure 1. Key elements of automotive product development

(1) Interior/exterior coating films: The appearance of an automobile, which is related to the coating films on its surfaces, is an important factor influencing customers' purchase decisions. The coating film on the exterior of an automobile is a particle-based functional material composed of a polymer and particles such as pigments. The development of pigments and colored materials has led to new appearance options for automobiles. Since 2000, the development of next-generation automotive coating films has been strongly focused on environmental issues such as reducing CO_2 and volatile organic compound (VOC) emissions during the manufacture of films, avoiding the use of harmful substances, and responding to the diverse needs of customers. In recent years, adding value by using new colored materials and new functional materials has become a priority.

(2) Electrodes for rechargeable batteries and fuel cells: Since the beginning of the automotive industry ~100 years ago, automotive technology has focused on internal combustion engine vehicles (ICEVs). However, reductions in CO_2 emissions by improving existing techniques are approaching their limit; numerous countries have announced that they will ban ICEV sales before 2030. Therefore, the development of next-generation cars is urgently needed in the automotive industry[1]. Since the 2000s, fuel cell vehicles (FCVs), plug-in hybrid vehicles (PHEVs, PHVs), and battery electric vehicles (BEVs, EVs) have become commercially available. However, further advances in the performance of batteries and in high-speed techniques for mass production are required. Electrodes are particle-based functional materials prepared by dispersing particles and polymers in a solvent, coating them onto a substrate, and drying them. The evolution of these materials and production technologies has led to innovations in next-generation automobiles. Because the structure of electrodes changes not only with the material but also with the production method, which also affects the electrodes' electrochemical performance, the structure of electrodes and precursors should be controlled to enable the high-performance and high-efficiency production of next-generation automobiles.

(3) Exhaust-gas purification catalysts: With increasing traffic, air pollution caused by automotive exhaust gas has become increasingly problematic [2]. Exhaust-gas purification catalysts have been developed and introduced to reduce the emissions of harmful components of automotive

exhaust [3, 4]. A monolithic three-way catalyst is a particle-based functional material composed of a powdered catalyst and polymers coated onto a honeycomb-structured ceramic support. Changing the solvent composition, material, or slurry process can lead to particle aggregation and structural changes that adversely affect catalytic performance. Therefore, the dispersion/aggregation state of the particles in the slurry must be controlled.

(4) Capacitors: The number of electronic components in automobiles is increasing each year, and multilayer ceramic capacitors are used in electronic control modules [5, 6]. Approximately 1000 multilayer ceramic capacitors are used in each ICEV, but ~10,000 will be used in each EV. The ceramic layer in multilayer ceramic capacitors is composed of ceramic particles and a polymer that binds the particles together [5]. The dispersed state of ceramic particles in a slurry also affects their structure and performance after sintering. Better understanding and control of the dispersed state of the particles is needed.

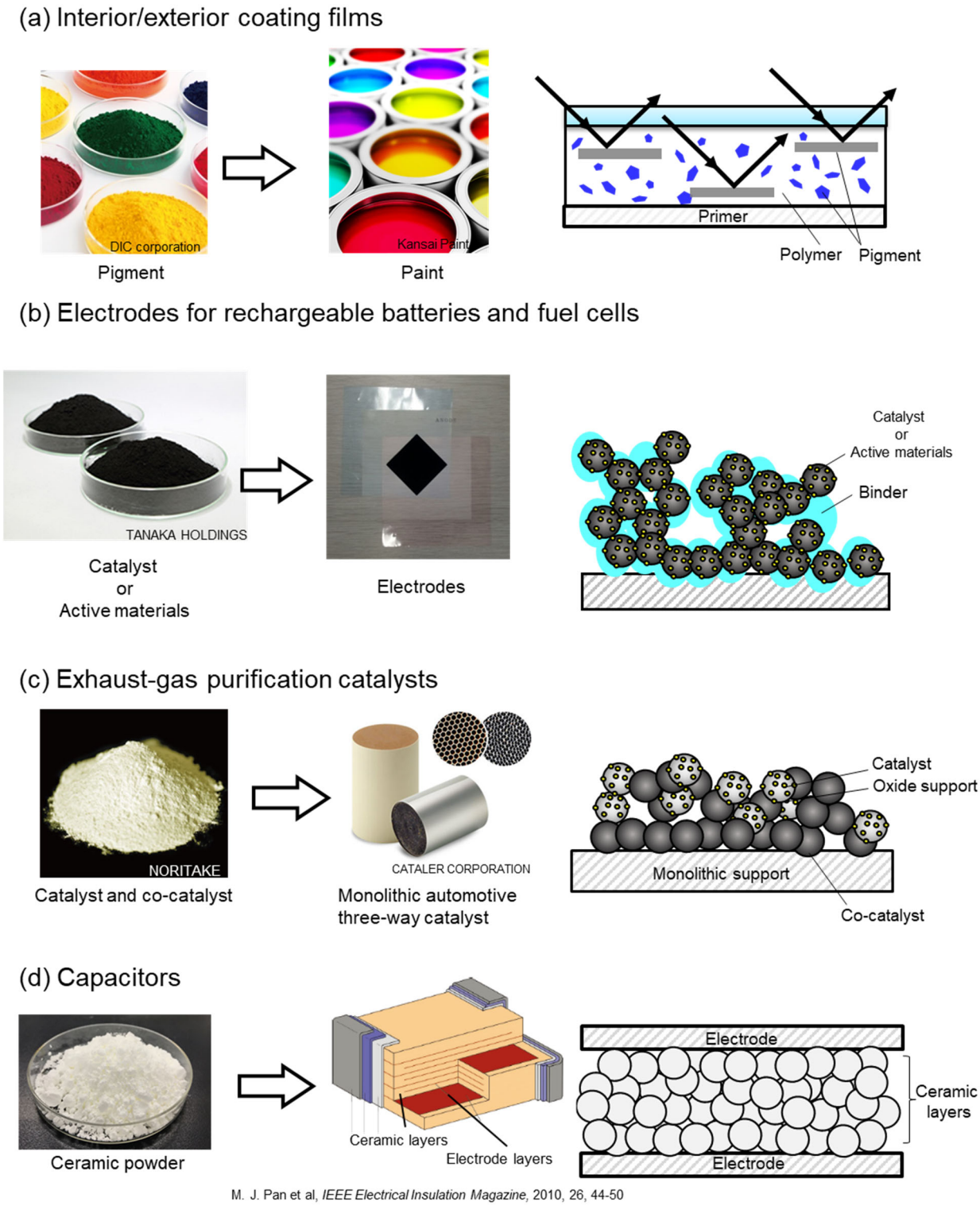

Figure 2. Particle-based functional materials for automotive applications

Particle-based functional materials are commonly used in automobiles. Given the changes in the environment surrounding automobiles, the importance of particle-based functional materials will continue to increase. Two objectives guide the future development of particle-based functional materials. The first objective is to develop the functions of materials to add value and improve performance. The development of new materials themselves is important, and functionalization can also be achieved by modifying the polymers, coarsely aggregating each particle, and arranging the particles, among other approaches. The second objective is to develop a production technology for obtaining a desired structure. The relationship between performance and processing methods is not fully understood because conventional development is based on trial-and-error approaches. As the importance of particle-based functional materials increases, each process needs to be understood and controlled. A production technology of particle-based functional materials is a key technology for achieving both high performance and high productivity of next-generation automobiles [7]. Furthermore, the use of harmful organic solvents should be reduced as much as possible and processes should be transitioned to water-based systems. The use of high-solid systems that involve minimal amounts of solvents will shorten drying times and reduce energy consumption, thereby reducing costs [8, 9]. Even if the methods and conditions are changed, a systematic understanding is required to enable stable production of particle-based functional materials with a desired structure.

Thus, the present study details research and development effects to address three major issues related to such functional materials. The background of each field, previous research, and unresolved problems are discussed in the following subsections.

1.2 Automotive coatings

1.2.1 Recent trends in interior/exterior coatings

The purpose of applying a coating to the exterior of an automobile is to provide an attractive appearance and protect the steel substrate from external factors. A typical coating system for an automotive exterior is composed of an electrodeposition (ED) layer, primer, and topcoat, whose compositions depend on the required function of each layer, as shown in Figure 3. The ED layer is corrosion resistant and prevents the steel substrate from rusting. This function was remarkably improved by the introduction of cationic electrodeposition coatings and the rotary bell atomizer in the 1980s. The primer layer has properties that render it resistant to stone chipping and conceal unevenness, leading to a smoother surface and preventing degradation of the ED layer by blocking UV light. The topcoats enhance the appearance (e.g., brilliance, gloss, color, and visual effect) of the coating. The topcoats are applied as a basecoat containing dispersed pigment and a polymer and a transparent clearcoat without pigment, followed by single curing in an oven. In the late 1980s, a new type of coating material with improved anticorrosion performance and durability was developed and introduced, thereby satisfying a basic level requirement for coatings. To satisfy diverse customer needs, new colored materials and functional materials that provide additional value for automobiles are required.

In addition, lightweight plastics have been widely used to improve fuel efficiency [10]. Plastics do not need to be painted and cured in an oven because they do not rust. One option to reduce the emission of VOCs and CO_2 during the manufacture of automobiles is to replace coating methods with a dry decoration method, which involves no or very small amounts of solvents. The dry decoration method is included decorative film method which decorative film are adhered or transferred onto the substrate and molded into color plastics method which used to precolour polymers with pigment in the plastic injection molding process [11] (Figure 4). Decorative films have already been used as interior materials, which have lower durability requirements than exterior materials. In recent years, the quality and durability of decorative films have improved, resulting in their use in exterior applications. The demand for the decorative method as an alternative to painting will continue to increase.

The use of lights and displays in automobile interiors (e.g., interior ambient lighting, central information displays, instrument clusters, and electric mirrors) is also increasing with the

development of autonomous driving technology. Promoting the "fun to drive" factor of automobiles will require the development of materials and displays whose colors and effects change in response to the location, music, and mood. Such materials enable the production of a passenger compartment that suits individual tastes and purposes.

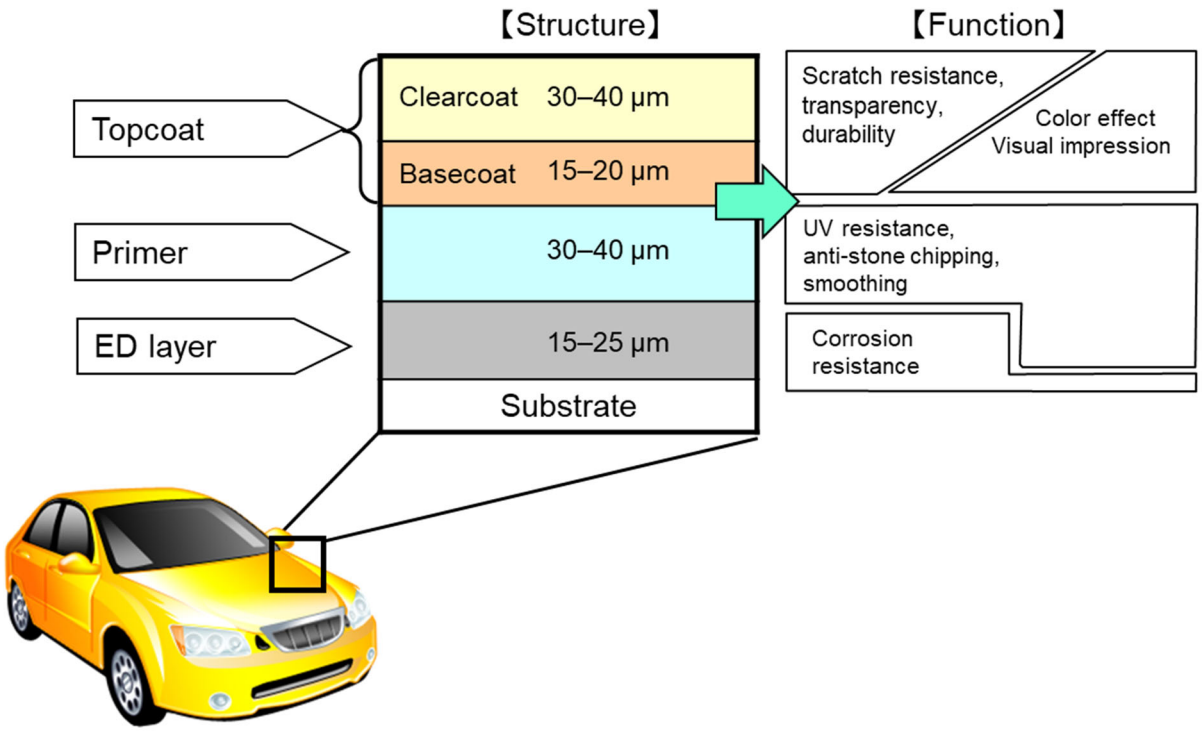

Figure 3. Structural composition of car paint

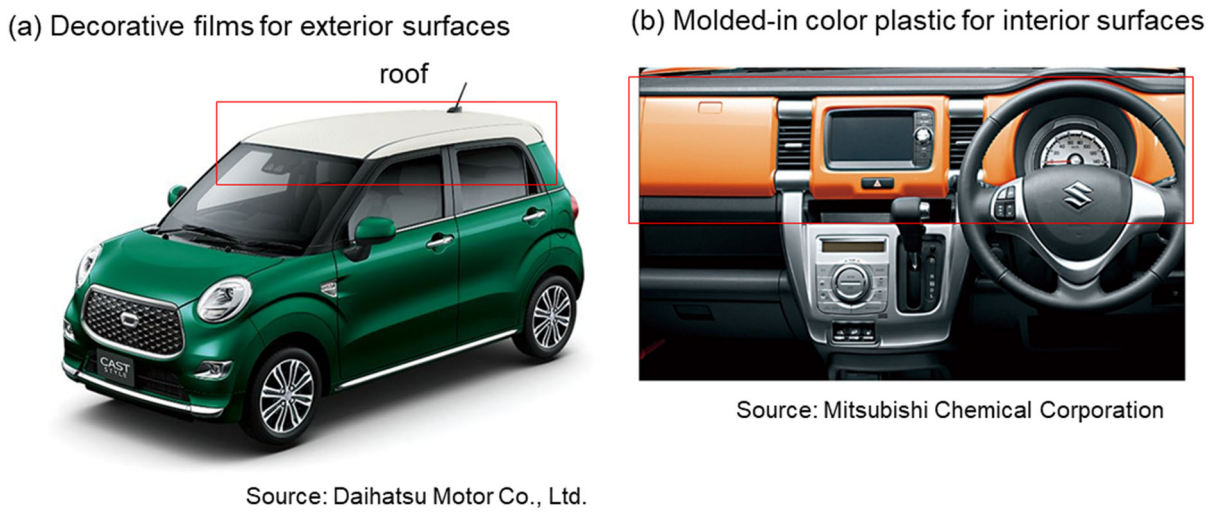

Figure 4. Decoration methods as alternatives to painting

1.2.2 Recent trends and present issues related to pigments and decorative materials

Figure 5 shows conventional pigments used in automotive coatings. Absorption pigments are used to impart color, and approximately 50 types of inorganic and organic pigments with excellent weather resistance have been developed [12, 13]. However, the development of new pigments is stucking because it needed to overcome high-level of color brightness and durability of the existing pigments. Conventional pigments for achieving a luster effect are classified into two types: pearl pigments and metallic-effect pigments. Pearl pigments are transparent flaky substrates coated with a film of metal oxide aligned parallel on the surface of a coating film, resulting in a natural pearl-like appearance because of interference color corresponding to the thickness of the metal oxide film [14-16]. Metallic-effect pigments are composed of aluminum flakes that are aligned parallel on the surface of a coating film, resulting in a shiny metallic luster effect because of the strong reflection of light.

In the 1980s, a substantial advancement in pigments was the improvement of the durability and orientation control technology of aluminum flake [17], and the improvement of the durability and brightness of highly saturated absorption pigments. In the 1980s, Toyota launched titanium dioxide-coated micas as pigments for automotive coatings. Since then, the development of new colors has been based on improvements in the aforementioned pigment types [18, 19].

Because automobiles are stored or used outdoors for long periods, pigments that do not fade are desired. In addition, among the pigments used thus far, many are being banned because they contain toxic heavy metals. Thus, brightly colored materials that are nonfading and nontoxic have potential applications as colored materials for automobiles. Structural colored materials are among the most promising candidates. The color of structurally colored materials originates from their microstructure, which has a length scale comparable to the desired optical wavelength, enabling them to exhibit color through optical effects such as the interference, refraction, or diffraction of light (Figure 6). Various pigments or films with structural color have been introduced and used as interior materials for automobiles (Figure 7). However, structural-colored materials face several unresolved problems. First, because microstructure should be made, the large-scale production of structural-colored materials is difficult, which makes them expensive. A colored material that can be easily prepared via a self-assembly method would be a candidate for use in automotive applications. Second, structural materials composed of transparent or white materials exhibit a milky-white appearance that may be difficult to distinguish by the naked eye. To address this issue, researchers have used black

materials that absorb transmitted light and reduce scattering light [20-28]. Third, pigments exhibit color that changes with the viewing angle, which may not be desirable depending on the color design and the application (e.g., optical devices, labels, and sensors) (Figure 8). Some solutions have been proposed to address these issues [29-34]. A colored material that solves these problems could potentially be used as an interior/exterior material.

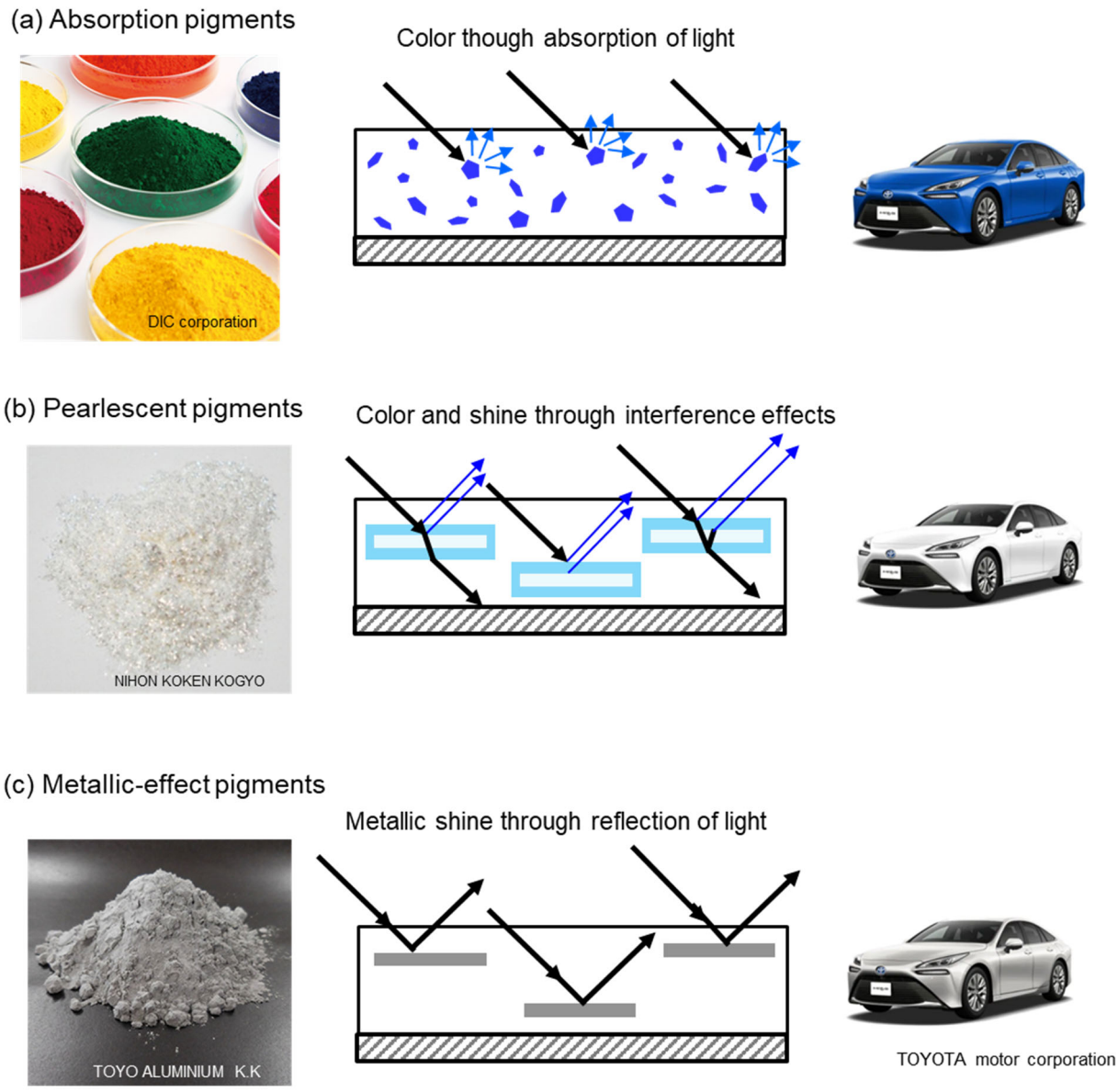

Figure 5. Optical properties of conventional pigments for automobiles

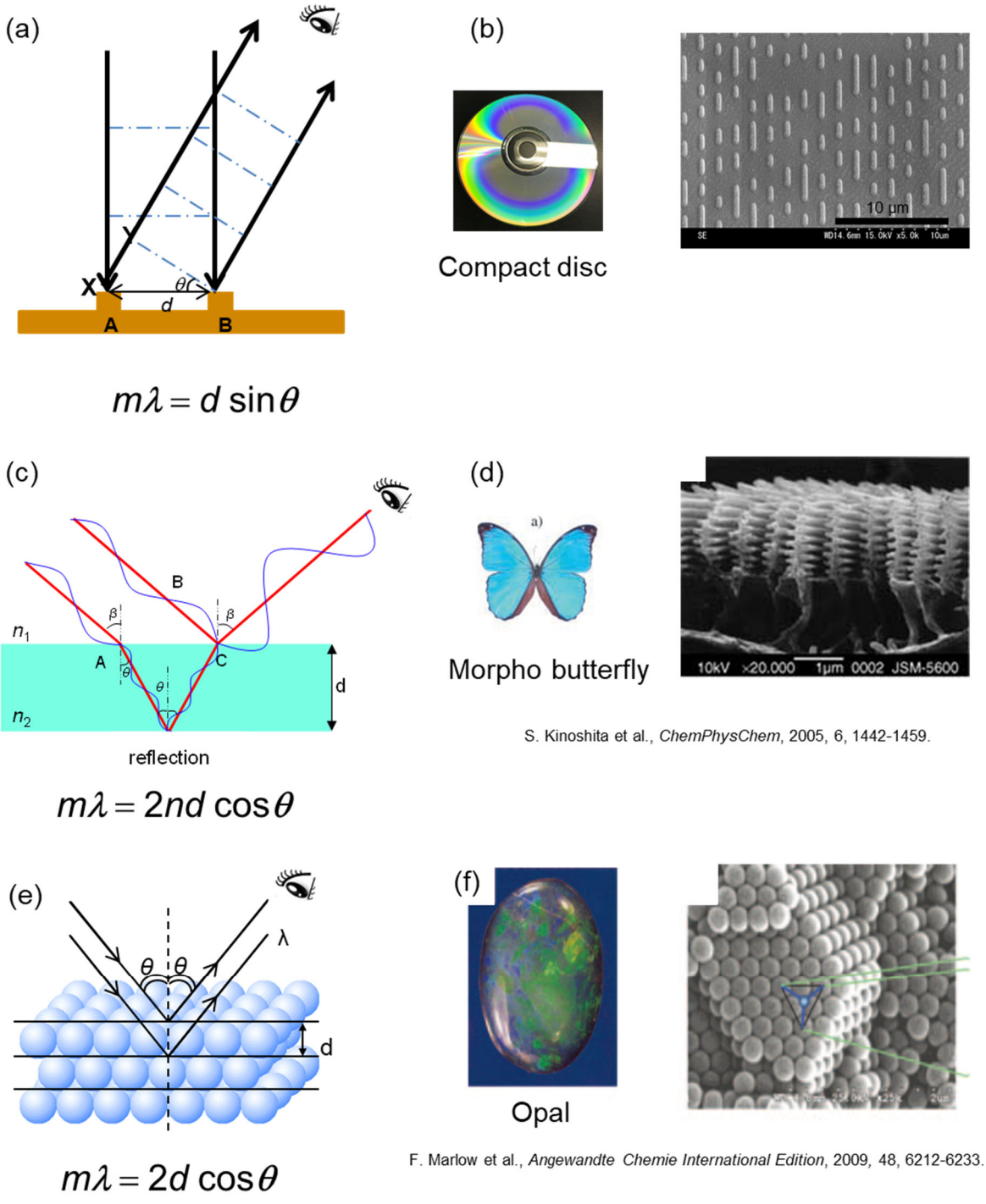

Figure 6. SEM images of structural coloration
(a), (b) Diffraction; (c), (d) interference; (e), (f) Bragg's law, where *m is* the order number, λ is the wavelength of light, d is the interplanar distance, and θ is the diffraction angle.
(a), (c), (e) Schematics; (b), (d), (f) photographs and SEM images.

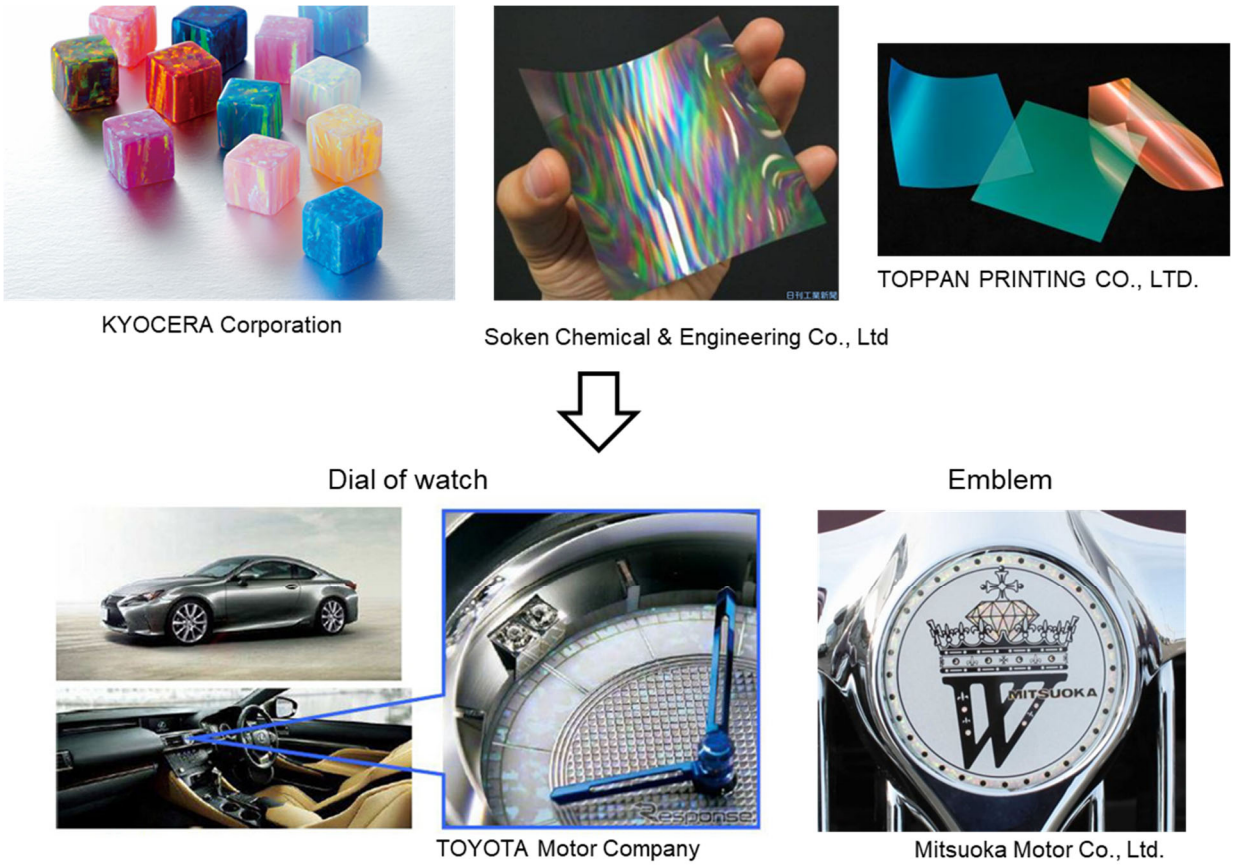

Figure 7. Structural color materials expected to be used in commercial applications.

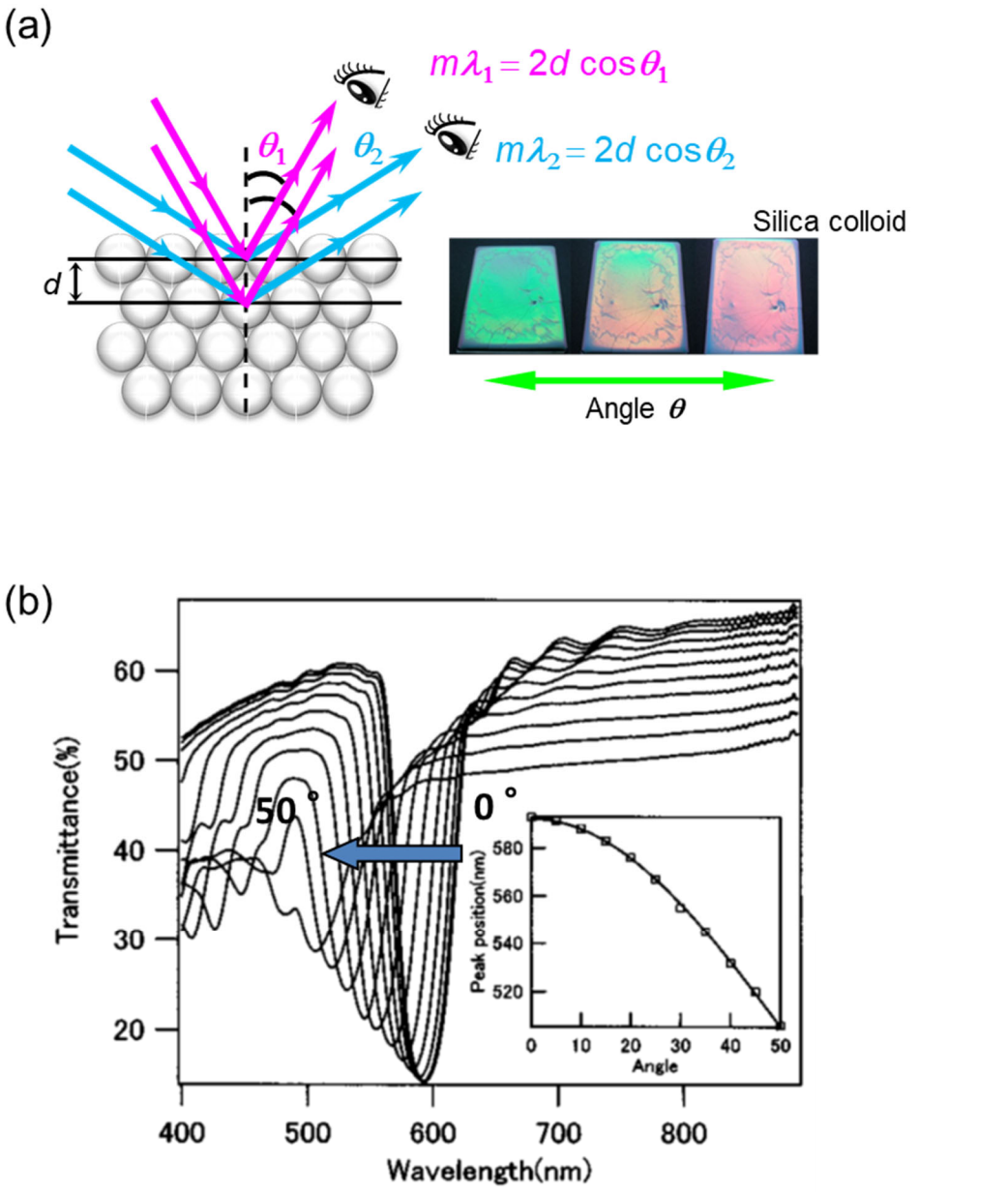

O. Sato et al. *Chem. Mater.* 2002, 14, 760-765.

Figure 8. Angle dependence of structural color: Variations in the pattern's spacing often give rise to an iridescent effect because the reflected color depends upon the viewing angle. (a) Picture of a silica colloid film. (b) Transmittance spectra of a colloid gel.

1.3 Recent trends and present problems with functional coatings

Future automotive coatings should have new functions to meet the increasingly diverse needs of customers. Thus far, various functional coating films have been developed (Table 1). For example, the method of controlling the wettability of the surface has been applied to functional coating films, and the resultant hydrophobic coating films have been used to prepare drip-proof surfaces, prevent snow accretion, and prevent fingerprint adhesion. Hydrophilic coating films have been used for cloud-proof coatings and self-cleaning coatings [35-39]. To prevent temperature increases in interior spaces in hot weather, solar or infrared reflective coatings that reflect infrared solar radiation have been developed.

Table 1. Functional coating technology

Category	Properties
Mechanical& Chemical	Scratch resistance, Self-healing, Anti-dirt, Super-hydrophobic or hydrophobic, Snow accretion prevention
Optical	Luminescent, Fluorescent, Structure color, Mat, Stimuli-responsive color, Bioinspired color
Electrical	Antistatic, Electromagnetic wave shielding
Heat	Solar or heat reflective, Infrared reflective

Consumer surveys have revealed that scratch resistance is one of the most important properties of automotive coatings (Figure 9) [40, 41]. Scratches in these coatings are classified into two types: fracture-type scratches and deformation-type scratches. For fracture-type scratches, self-repairing coatings containing oxetane, which re-forms a crosslinked network under exposure to ultraviolet light after the coating has been scratched, has been proposed [42]. Moreover, self-healing coatings containing a microencapsulated monomer and catalyst that re-form the crosslinked network underupon heating after the coating has been damaged have also been developed [43]. However, some unresolved problems related to durability and appearance impede the commercialization of

these coatings. For deformation-type scratches a few microns deep, such as scratches created by car washing or by blown sand and dust, a scratch-resistant coating has been developed and introduced onto the market (Figure 10) [44].

One of the most popular methods of obtaining coatings with high scratch resistance is to use a polymer with a high crosslink density or low glass-transition temperature (T_g)[45]. Increasing the crosslink density increases the toughness of a coating, thereby improving its scratch resistance. However, decreasing the T_g increases the flexibility of coatings, reducing the stress concentration and making the coating more difficult to rupture. Moreover, a lower T_g increases the speed of scratch recovery [46-48]. Low-T_g coatings such as rubber exhibit fast recovery characteristics but lack sufficient hardness. The high molecular mobility at room temperature leads to practical problems of poor chemical resistance and permanent soiling of soft surfaces. Therefore, these approaches are not satisfactory solutions for increasing scratch resistance. Moreover, they do not address large, easily visible deformation-type scratches caused by keys, fingernails, tree branches, or shopping carts [40]. Self-recovery coatings that exhibit fast recovery characteristics for large deformation-type scratches and that satisfy all of the requirements for high-level scratch-resistance performance are needed for next-generation coatings.

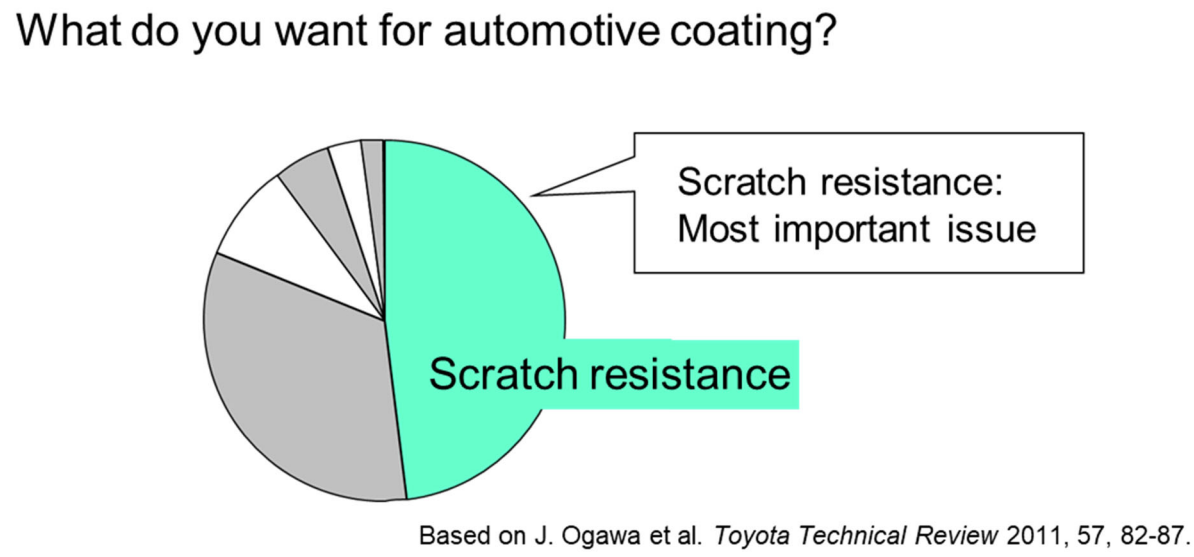

Figure 9. Customer needs survey for Japan, USA, Germany, France, and England.

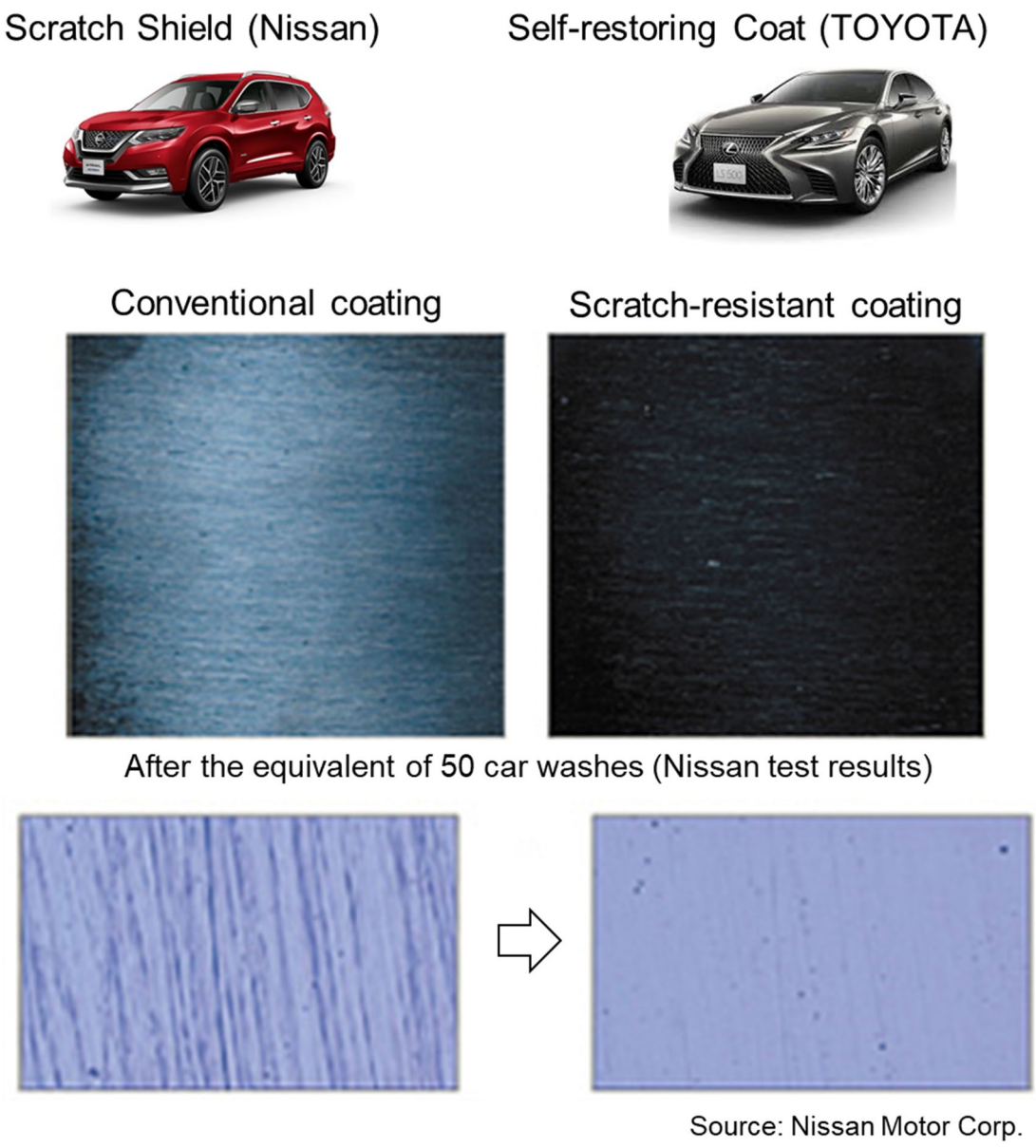

Figure 10. Commercialized scratch-resistant coating

1.4 Fuel cell vehicles

1.4.1 Advantages of fuel-cell vehicles

FCVs use a fuel-cell stack, which produces electricity via a chemical reaction between hydrogen and oxygen, as the power source for their electric traction motor. FCVs are promising next-generation vehicles because, during operation, they do not emit CO_2, which is a major cause of global warming, or SO_2 and NOx, which are atmospheric pollutants; their only byproduct is water. Table 2 shows a comparison of EVs and FCVs [49]. The apparent advantages of FCVs over EVs include greater energy efficiency, rapid startup at subfreezing temperatures (cold start-up) [50], a long driving range of more than 600 km, and a short recharge time ~3 minutes to refuel a tank of hydrogen, which is similar to the refueling time of an ICEV [51, 52].

Table 2. Comparison between EV and FCV

	FCV	EV
Well-wheel energy efficiency from natural gas	36%	24%
Driving range	600 km	200 km
Recharge time	3 min	8 h
Cold start	−30° C	0° C
Infrastructure	☹	☺

Y. Morimoto et al. presented at ACEPS2017, 2017/8/22, GYEONGJU, KOREA.

Figure 11 shows the difference between cruising range and cost [49]. EVs have a lower cost when the cruising range is short because they require only a small number of batteries; however, when the cruising range is long, additional batteries are required, which increases the cost and weight, resulting in lower fuel consumption rate in EV. FCVs require a stack and hydrogen tank irrespective of their cruising range; thus, their cost is high at low cruising range but their cruising range can be easily extended by increasing the tank capacity. Thus, FCVs are better positioned for use as long-distance, large vehicles, whereas EVs are better positioned for use as short-distance, urban vehicles (Figure 12). The threshold will change depending on the future performance and cost of both EVs and FCVs;

however, the threshold is expected to approach 200 km, and this trend will not change. An FCV named MIRAI was launched in the mass market by Toyota in 2014. Hydrogen stations have been developed, and they are currently in the stage of dissemination and practical application. However, several challenges need to be overcome, such as reducing the production cost of fuel cell stacks and hydrogen tanks and increasing vehicle performance, durability, and reliability [53, 54]. New facilities for hydrogen storage or filling stations for hydrogen must also be constructed [55].

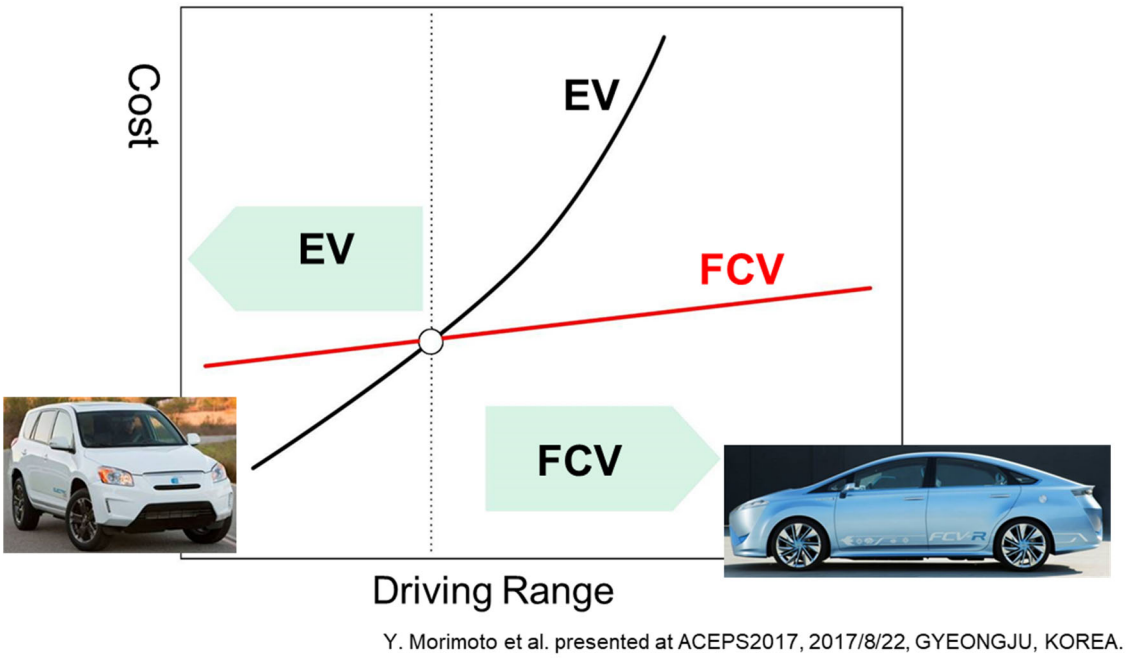

Figure 11. Comparison between an electric vehicle (EV) and a fuel-cell vehicle (FCV)

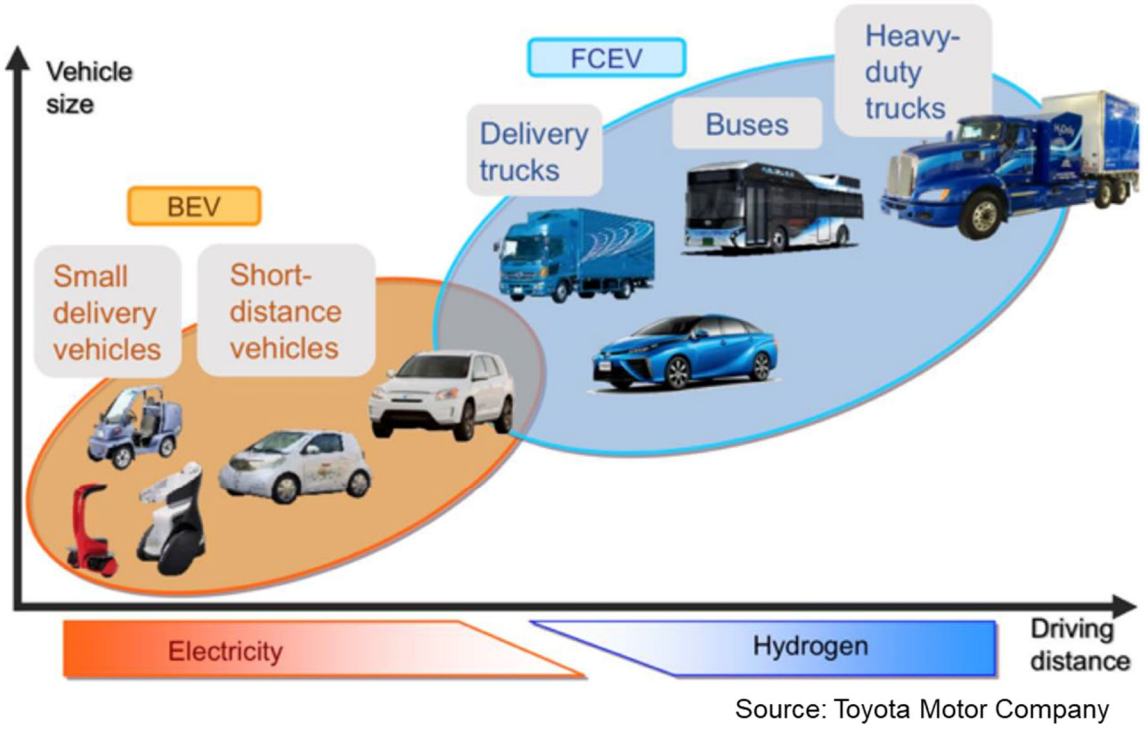

Figure 12. Strategy of next-generation vehicle development

(BEV = battery electric vehicle, FCEV = fuel-cell electric vehicle)

1.4.2 Components of a polymer electrolyte fuel cell

The polymer electrolyte fuel cell (PEFC) is a promising power source because it operates at a relatively low temperature and has become sufficiently mature and robust to be used in automotive applications [56]. Figure 13 shows the principle of electric power generation by a typical PEFC. PEFCs comprise an anode and a cathode separated by a polymer electrolyte membrane. When hydrogen is supplied through the anode, the catalyst dissociates the hydrogen into protons (H^+) and electrons (e^-). Because only H^+ can flow through the polymer electrolyte membrane, the electrons can be drawn as a source of electricity flowing through a load circuit to the cathode, where water is formed by the reaction between protons and oxygen at the catalyst surface. The gas diffusion layer (GDL) and a microporous layer (MPL), which is a porous material, are located between the catalyst layer and the flow channel. These layers prevent water from condensation, thereby promoting water evacuation and facilitating gas transport to the catalyst layer.

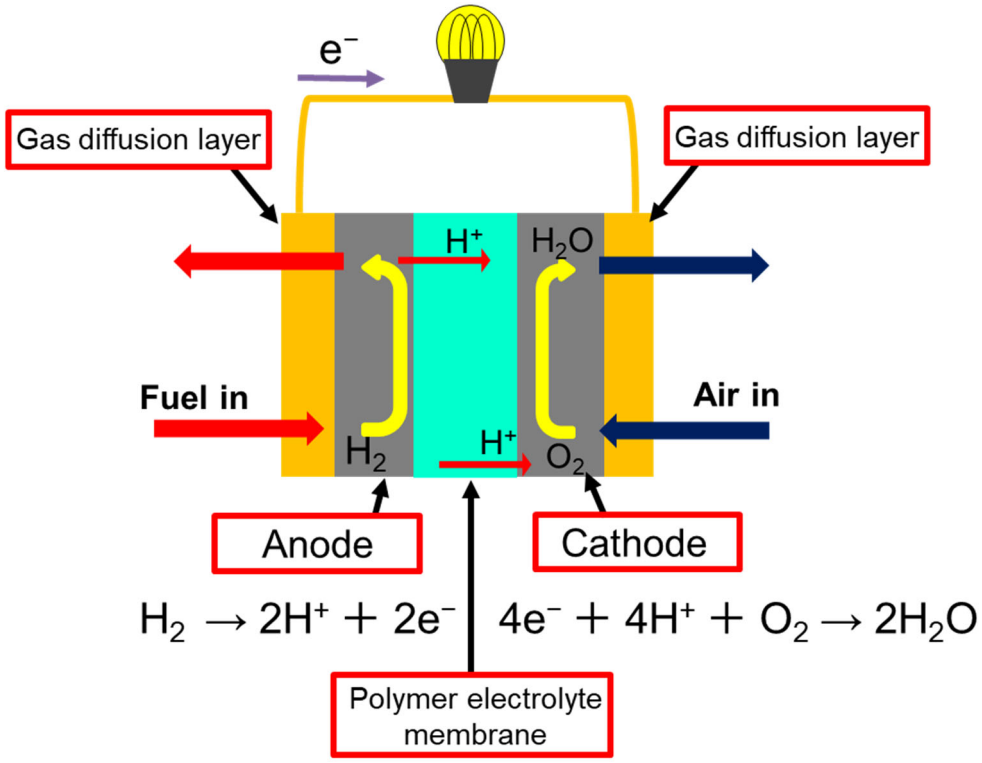

Figure 13. Schematic of a polymer electrolyte fuel cell

1.4.3 Current problems in controlling catalyst ink formation and the catalyst layer structure

Catalyst layers are formed from catalyst inks consisting of carbon-black-supported platinum (Pt) nanoparticles (Pt/C), perfluorinated sulfonic acid ionomers, and a dispersion medium (Figure 14). Two coating processing methods have been developed for catalyst layers: direct coating onto the membrane or GDL, and decal transfer to the membrane. The catalyst layer needs to appropriately distribute the Pt/C and ionomer while also controlling the pore structure because the electrochemical reaction occurs in the reaction field (three-phase boundary) of the catalyst, ionomer, and gas phase. Increasing the area of the three-phase boundary with a well distributed catalyst leads to improved electrode performance. The formation of pathways in the Pt/C and ionomer is critical for electrochemical reactions because pathways enable the smooth flow of protons and electrons [57, 58]. The porosity and pore diameter should be optimized to improve the gas and water transportation efficiency (Figure 15). As previously described, controlling the electrode structure requires accurate control of the characteristics of the catalyst ink, which is a precursor for an electrode, although the catalyst ink changes with time. Moreover, because this catalyst ink is black and opaque, its direct observation or characterization using optical measurements is difficult. To address this problem, researchers have examined ink formation using dynamic light scattering (DLS) [59], ultra-small-angle neutron scattering [60, 61], ultra-small-angle X-ray scattering [62], and transmission electron microscopy [63, 64] (Figure 16). These techniques require the sample to be sufficiently diluted (typically <1 wt%) [65, 66] to allow light or a beam to pass through the sample without substantial scattering. However, the agglomerated structures of Pt/C in catalyst inks are not yet fully understood because of a lack of evaluation methods that do not involve dilution, especially for high-concentration catalyst inks used in manufacturing processes.

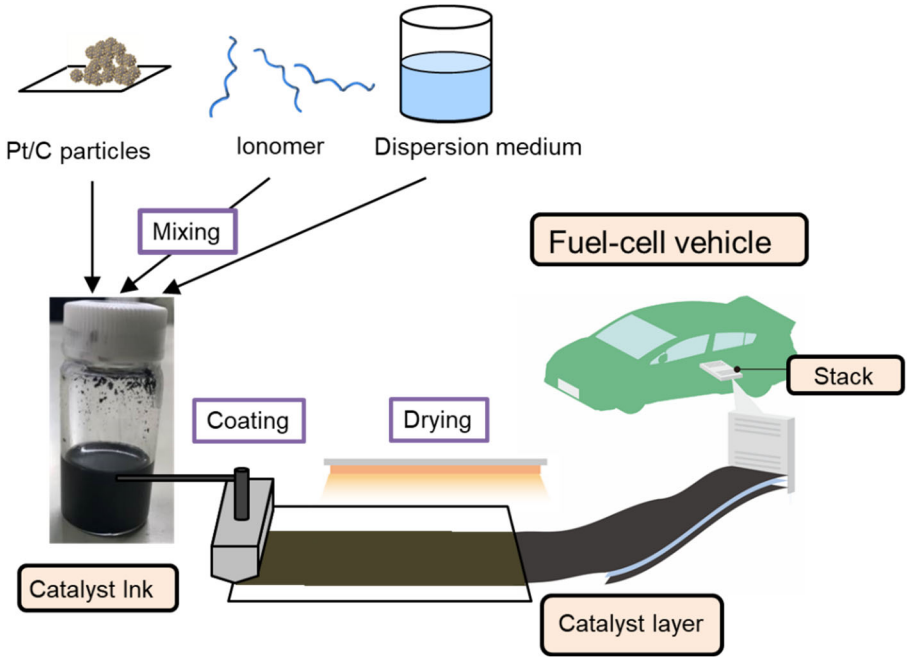

Figure 14. A typical catalyst-layer manufacturing process

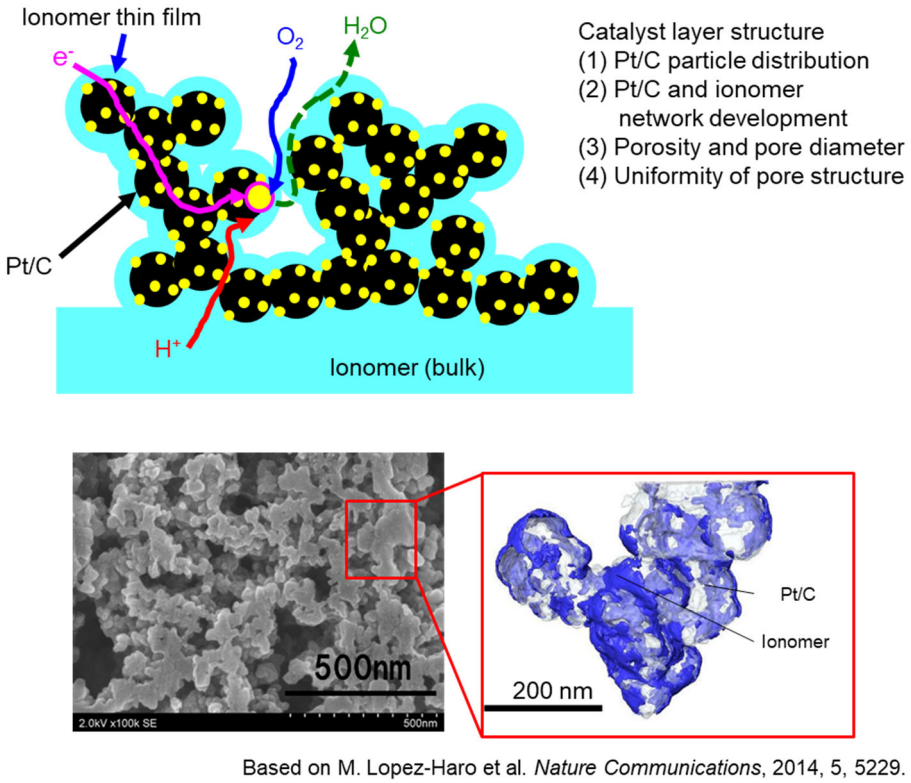

Based on M. Lopez-Haro et al. *Nature Communications*, 2014, 5, 5229.

Figure 15. Schematics and SEM micrograph of the porous fuel-cell catalyst layer structure

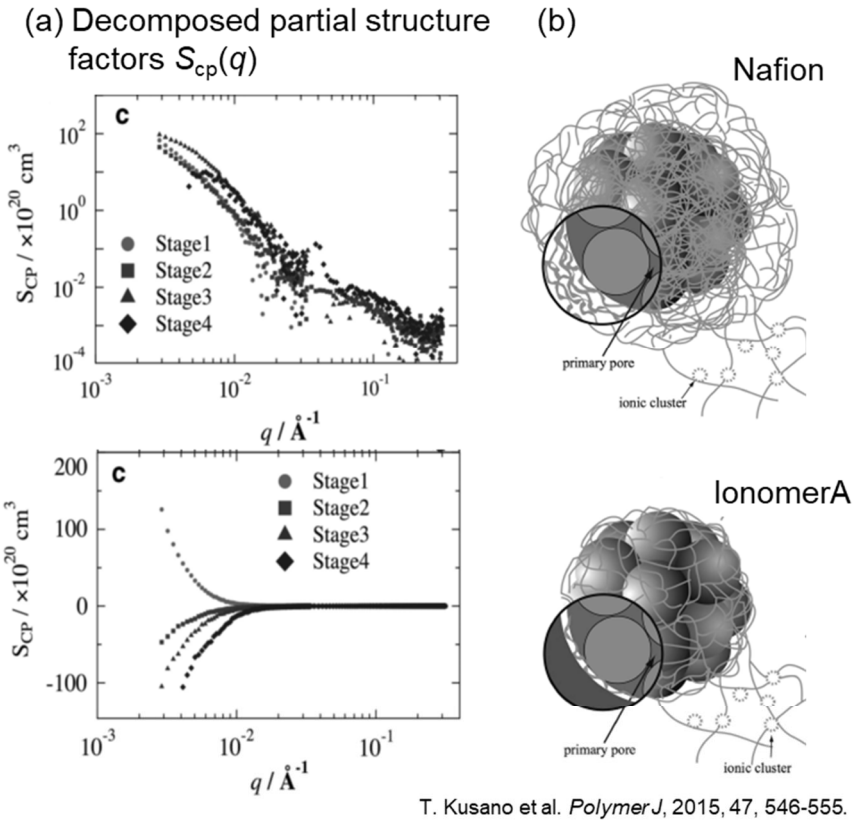

T. Kusano et al. *Polymer J*, 2015, 47, 546-555.

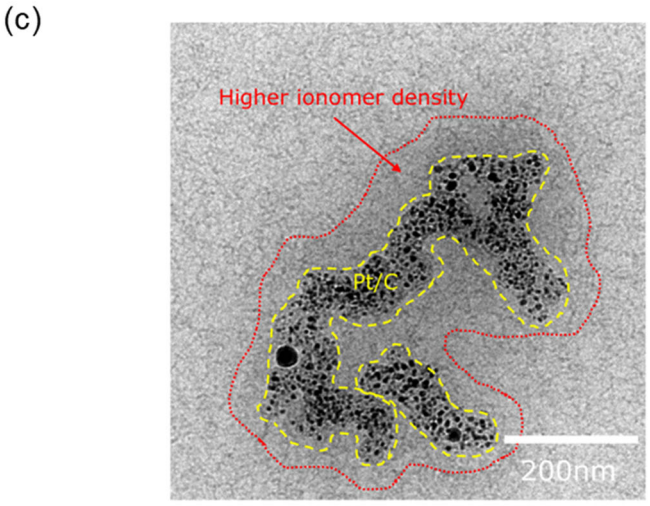

S. Takahashi et al., *Electrochimica Acta*, 2017, 224, 178-185.

Figure 16. Schematics of catalyst ink formation:
(a) contrast-variation small-angle neutron scattering (CV-SANS) profiles for a catalyst ink with carbon and different ionomers;
(b) schematic of the structure of carbon and different ionomers, as revealed by CV-SANS;
(c) cryogenic electron transmission microscopy (cryo-TEM) image of a catalyst ink

In addition, a catalyst layer should exhibit high porosity to ensure high fuel cell performance because a highly porous catalyst layer allows gas and water to easily flow; however, highly porous catalyst layers are brittle. The drying of a thin catalyst ink film on a substrate often results in the formation of cracks. Several studies have reported changes in crack patterns depending on the type of catalyst ink solvent [67], the catalyst ink mixing time [68], and differences in the microporous layer used as a substrate [66]. In another study, the structural evolution of a catalyst ink during the drying process was investigated using the contrast-variation small-angle neutron scattering (CV-SANS) method. The results suggested that a catalyst layer formed by a catalyst ink with low interaction between the ionomers and Pt/C contained numerous cracks (Figure 17)[69]. The factors affecting crack behavior in catalyst layers are a topic of debate, and the mechanism is poorly understood. Cracks in catalyst layers are microstructures and have diverse effects on performance and durability. Thus, the mechanism leading to cracks in catalyst layers should be clarified and cracking should be controlled and restricted.

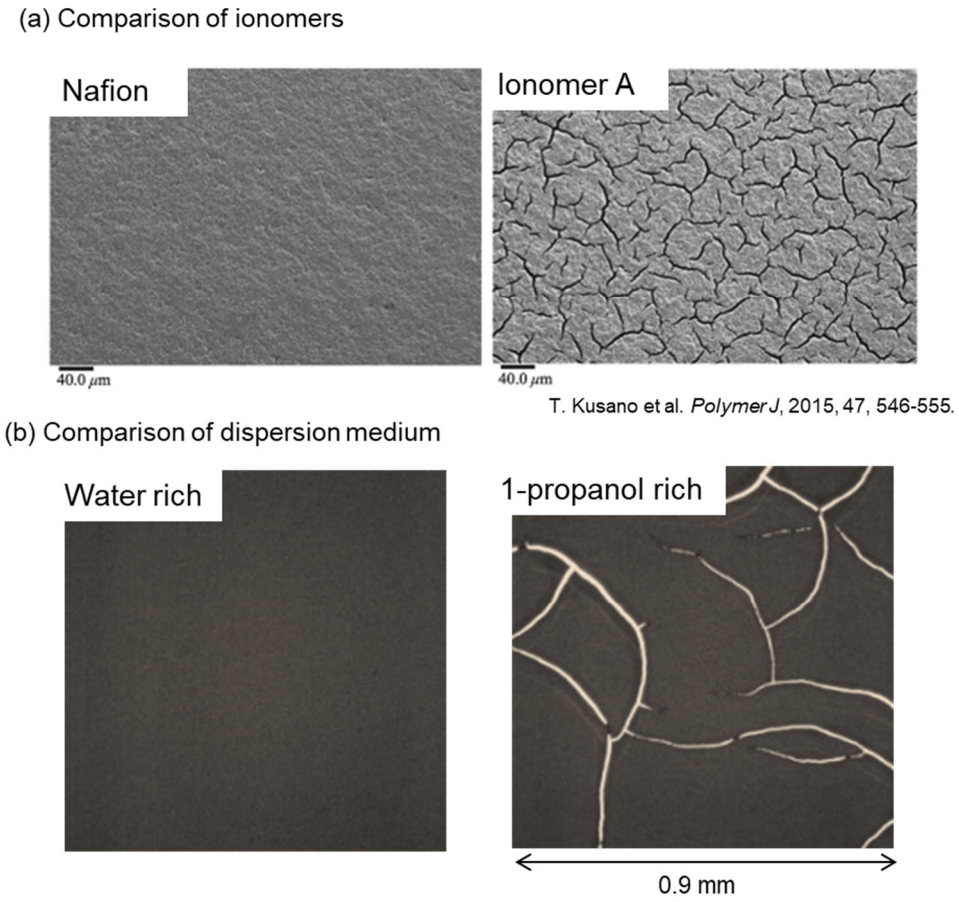

Figure 17. SEM images of a catalyst layer with cracks

1.4.4 Present problems in the mass production of catalyst layers

Currently, FCVs occupy only a small share of the vehicle market. However, some automobile manufacturers have announced shifts from limited FCV production to mass FCV production. Their cost could be dramatically reduced as larger production runs lower unit costs. One of the solutions for mass production is speeding up the roll-to-roll process. FCVs require approximately 400 fuel cells (800 catalyst layers) in a stack to achieve sufficient power output. The intermittent coating method is used to prepare catalyst layers in continuous high-speed processes because it does not apply the catalyst ink to unnecessary parts, thereby reducing catalyst waste [70]. In the intermittent coating method, patterned coating/noncoating is repeated intermittently (Figure 18). However, even with the same material, slight variations in the solvents and processes can cause a change in viscosity. During coating of an unstable catalyst ink, a high viscosity can cause problems in the coating and liquid-transfer processes, adversely affecting the quality of the coating films and the ability to control the thickness [71]. Solving these problems requires a comprehensive understanding of catalyst ink formation and the factors affecting the inks' rheological behavior.

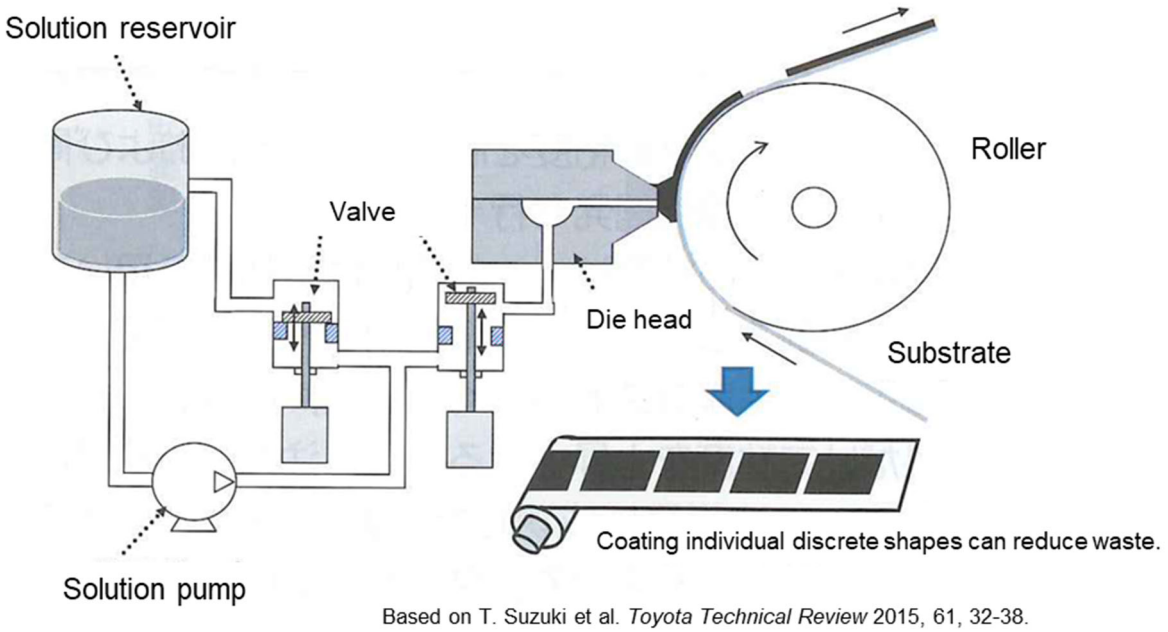

Figure 18. Intermittent slot-die coating

1.5 Study objectives

The aforementioned research and products suggest that several issues need to be overcome to improve the applicability of particle-based functional materials for next-generation automobiles. Therefore, investigations that address three major issues related to coatings and fuel cell electrodes by using particle-based functional materials are performed in this work:

(1) Demonstration of new color materials without dyes or absorption pigments

Structural color materials that are nonfading and nontoxic have potential applications in automotive coatings. However, the fabrication of structural color materials from mesoscale structures is time-consuming, requires great effort, and, in some cases, is expensive when existing top-down or bottom-up approaches are used. Thus, a facile self-assembly approach is needed to prepare new color materials for practical use. The first objective of this work is to prepare, via a facile one-pot preparation method, new color materials that do not contain dyes or pigments.

In addition, chromic materials have rarely been used in conventional coatings because of their poor durability. If chromic materials with high durability can be prepared, they can be used for interior decoration. The second objective of this work is to develop new chromic materials with a simple process that do not contain dyes or pigments.

In addition, structural materials composed of transparent or white materials exhibit weak structural colors because of light scattering, which results in a milky-white appearance that may be difficult to distinguish by the naked eye. The third objective of this work is to demonstrate novel pigments that exhibit enhanced colors caused by thin-film interference through absorption of scattered light by black materials.

(2) Demonstration of new scratch-recovery coatings.

Consumers generally desire longer-lasting scratch-free coatings. Understanding how scratch characteristics change over time is therefore important. However, the degradation and physical aging processes of scratch-resistant coatings under usage conditions are not yet fully understood. I first investigate the relationship between scratch resistance and chemical changes in conventional coatings in an outdoor weathering test. I then demonstrate new scratch-recovery polyorganosilsesquioxane coatings with superior weather resistance.

(3) Control of rheological behavior of catalyst ink and cracking behavior of catalyst layer

Because agglomerated structures of Pt/C nanoparticles in catalyst inks affect their productivity and performance, identifying and controlling the structural parameters that govern the dispersion state of Pt/C agglomerates are important. To solve the problems of poor performance and inadequate high-speed production of electrodes for fuel cell vehicles, modulations are made for the rheological behavior of a catalyst ink and the cracking behavior of a catalyst layer by controlling the aggregation of particles by changing their dispersion medium.

1.6 Outline of the thesis

The thesis is organized as follows:

Chapters 2 to 4 describe the use of particle-based functional materials to develop a new colored system that exhibits attractive color without dyes or harmful pigments.

In Chapter 2, a thermosensitive colored system composed of porous gels and a solvent is developed using particle-based functional materials and the system is shown to display bright and angle-independent coloration.

In Chapter 3, multicolored polymer-dispersed liquid crystals are developed on the basis of the information acquired about the mechanism in Chapter 2 to control the coloration and an opaque milky color in response to temperature variation.

Chapter 4 describes the development of new pigments that contain no heavy metals, are nonfading, and exhibit enhanced colors as a result of thin-film interference through the absorption of scattered light by black materials.

Chapters 5 and 6 describe functional coatings by particle-based functional materials with scratch recovery characteristics.

Chapter 5 describes an investigation of the relationship between chemical changes and scratch resistance to understand how scratch recovery characteristics change under automotive use conditions.

In Chapter 6, crosslinked polyorganosilsesquioxane coatings with weather resistance are demonstrated to exhibit scratch recovery characteristics superior to those of conventional coatings.

Chapters 7 to 8 describe the preparation of catalyst inks to control the rheological behavior and the formation of catalyst layers, thereby controlling cracking behavior and enabling the stable production of catalyst layers.

Chapter 7 first describes the effect of ionomer adsorption onto Pt/C, where the rheological behavior and dispersion state of Pt/C agglomerates in catalyst inks are controlled.

Chapter 8 describes the mechanism leading to the formation of cracks on catalyst layers during drying and proposes methods to control cracks, focusing on the aggregate structure of the catalyst inks and the microstructure of the catalyst layers.

Chapter 9 summarizes the main findings of the thesis and presents suggestions for future work.

References

[1] S. G. Chalk and J. F. Miller, *Journal of Power Sources,* **2006**, 159, 73-80.

[2] M. V. Twigg, *Catalysis Today*, **2011**, 163, 33-41.

[3] J. Kašpar, P. Fornasiero, and N. Hickey, *Catalysis Today*, **2003**, 77, 419-449.

[4] T. Kreuzer, E. S. Lox, D. Lindner, and J. Leyrer, *Catalysis Today*, **1996**, 29, 17-27.

[5] M. J. Pan and C. A. Randall, *Ieee Electrical Insulation Magazine,* **2010**, 26, 44-50.

[6] H. Kishi, Y. Mizuno, and H. Chazono, *Japanese Journal of Applied Physics Part 1-Regular Papers Short Notes & Review Papers*, **2003**, 42, 1-15.

[7] W. B. Hawley and J. Li, *Journal of Energy Storage*, **2019**, 25, 100862.

[8] T. A. Misev and R. van der Linde, *Progress in Organic Coatings*, **1998**, 34, 160-168.

[9] D. J. Kirsch, S. D. Lacey, Y. Kuang, G. Pastel, H. Xie, J. W. Connell*, et al.*, *ACS Applied Energy Materials*, **2019**, 2, 2990-2997.

[10] K. Mase, *NIPPON GOMU KYOKAISHI*, **2008**, 81, 383-387.

[11] T. Fukuta, M. Nozue, A. Kobayashi, and A. Suzuki, *Seikei-Kakou*, **2015**, 27, 445-447.

[12] "Polycyclic Pigments," in *Industrial Organic Pigments*, ed, **2004**, 421-566.

[13] "Azo Pigments," in *Industrial Organic Pigments*, ed, **2004**, 183-419.

[14] G. Pfaff, *High Performance Pigments PartII, Chapter7*: VCH Verlag GmbH & Co. KGaA, **2001**.

[15] G. Pfaff and P. Reynders, *Chemical Reviews*, **1999**, 99, 1963-1981.

[16] F. J. Maile, G. Pfaff, and P. Reynders, *Progress in Organic Coatings*, **2005**, 54, 150-163.

[17] A. Kiehl and K. Greiwe, *Progress in Organic Coatings*, **1999**, 37, 179-183.

[18] F. Hirano and T. Yamane, *Journal of the Japan Society of Colour Material*, **2019**, 92, 349-354.

[19] T. Tsukimori, Y. Takagi, A. Yokoyama, S. Ichii, M. Omura, and M. Ito, *Transactions of Society of Automotive Engineers of Japan*, **2019**, 50, 581-584.

[20] M. Kohri, Y. Nannichi, T. Taniguchi, and K. Kishikawa, *Journal of Materials Chemistry C*, **2015**, 3, 720-724.

[21] Y. Takeoka, S. Yoshioka, A. Takano, S. Arai, K. Nueangnoraj, H. Nishihara*, et al.*, *Angewandte Chemie International Edition*, **2013**, 52, 7261-7265.

[22] Y. Takeoka, S. Yoshioka, M. Teshima, A. Takano, M. Harun-Ur-Rashid, and T. Seki, *Scientific Reports*, **2013**, 3.

[23] X. X. Yao, Y. C. Bai, Y. J. Lee, Z. M. Qi, X. H. Liu, and Y. D. Yin, *Journal of Materials Chemistry*

C, **2019**, 7, 14080-14087.

[24] Y. Xue, F. Wang, H. J. Luo, and J. F. Zhu, *ACS Applied Materials & Interfaces*, **2019**, 11, 34355-34363.

[25] A. Kawamura, M. Kohri, G. Morimoto, Y. Nannichi, T. Taniguchi, and K. Kishikawa, *Scientific Reports*, **2016**, 6.

[26] S. Cho, T. S. Shim, J. H. Kim, D. H. Kim, and S. H. Kim, *Advanced Materials*, **2017**, 29, 1700256.

[27] B. Yi and H. F. Shen, *Chemical Communications*, **2017**, 53, 9234-9237.

[28] M. Xiao, Y. W. Li, M. C. Allen, D. D. Deheyn, X. J. Yue, J. Z. Zhao*, et al.*, *ACS Nano*, **2015**, 9, 5454-5460.

[29] Y. Takeoka, M. Honda, T. Seki, M. Ishii, and H. Nakamura, *ACS Applied Materials & Interfaces*, **2009**, 1, 982-986.

[30] J. D. Forster, H. Noh, S. F. Liew, V. Saranathan, C. F. Schreck, L. Yang*, et al.*, *Advanced Materials*, **2010**, 22, 2939-2944.

[31] I. Lee, D. Kim, J. Kal, H. Baek, D. Kwak, D. Go*, et al.*, *Advanced Materials*, **2010**, 22, 4973-4977.

[32] S. Y. Lee, H. Kim, S.-H. Kim, and H. A. Stone, *Physical Review Applied,* **2018**, 10, 054003.

[33] Y. Takeoka, S. Yoshioka, A. Takano, S. Arai, K. Nueangnoraj, H. Nishihara*, et al.*, *Angewandte Chemie International Edition*, **2013**, 52, 7261-7265.

[34] M. Kohri, Y. Tamai, A. Kawamura, K. Jido, M. Yamamoto, T. Taniguchi*, et al.*, *Langmuir*, **2019**, 35, 5574-5580.

[35] A. Solga, Z. Cerman, B. F. Striffler, M. Spaeth, and W. Barthlott, *Bioinspiration & Biomimetics*, **2007**, 2, S126-S134.

[36] R. N. Wenzel, *Industrial & Engineering Chemistry*, **1936**, 28, 988-994.

[37] R. Wang, N. Sakai, A. Fujishima, T. Watanabe, and K. Hashimoto, *The Journal of Physical Chemistry B*, **1999**, 103, 2188-2194.

[38] M. Suzuki, M. Yoshikawa, K. Iimura, H. Satone, and K. Ishii, *Journal of the Society of Powder Technology, Japan*, **2013**, 50, 405-409.

[39] R. Wang, K. Hashimoto, A. Fujishima, M. Chikuni, E. Kojima, A. Kitamura*, et al.*, *Nature*, **1997**, 388, 431-432.

[40] L. Feng, B. Benhamida, C.-Y. Lu, L. P. Sung, P. Morel, A. T. Detwiler*, et al.*, *Progress in Organic*

Coatings, **2018**, 125, 339-347.

[41] K. K. Junya Ogawa, Takayuki Kawano, *Toyota Technical Review*, **2011**, 57, 82-87.

[42] B. Ghosh and M. W. Urban, *Science*, **2009**, 323, 1458-1460.

[43] S. H. Cho, S. R. White, and P. V. Braun, *Advanced Materials*, **2009**, 21, 645-649.

[44] H. Nakasuji, *Journal of The Surface Finishing Society of Japan*, **2014**, 65, 480-483.

[45] R. A. Ryntz, B. D. Abell, G. M. Pollano, L. H. Nguyen, and W. C. Shen, *Journal of Coatings Technology*, **2000**, 72, 47-53.

[46] C. Seubert, M. Nichols, K. Henderson, M. Mechtel, T. Klimmasch, and T. Pohl, *Journal of Coatings Technology and Research*, **2010**, 7, 159-166.

[47] P. Bertrand-Lambotte, J. L. Loubet, C. Verpy, and S. Pavan, *Thin Solid Films*, **2002**, 420-421, 281-286.

[48] N. Aleksy, G. Kermouche, A. Vautrin, and J. M. Bergheau, *International Journal of Mechanical Sciences*, **2010**, 52, 455-463.

[49] Y. Morimoto, "Present status and challenges of Automotive Fuel Cells," presented at the The 9th Asian Conference on Electrochemical Power Sources 2017, GYEONGJU, KOREA, **2017**.

[50] Z. Wan, H. Chang, S. Shu, Y. Wang, and H. Tang, *Energies*, **2014**, 7, 3179-3203.

[51] A. M. Philip Pindo Mok, "Automotive fuel cells clean power for tomorrow's vehicles " presented at the 1999 Society of Automotive Engineers, **1999**.

[52] E. D. Matthew Brekken, "An Analysis of the True Efficiency of Alternative Vehicle Powerplants and Alternative Fuels," presented at the 1998 Society of Automotive Engineers, **1998**.

[53] R. Borup, J. Meyers, B. Pivovar, Y. S. Kim, R. Mukundan, N. Garland*, et al.*, *Chemical Reviews*, **2007**, 107, 3904-3951.

[54] B. D. J. C.E. Thomas, Franklin D. Lomax, Jr.and Ira F.Kuhn, Jr., "Societal Impacts of Fuel Options for Fuel Cell Vehicles," presented at the 1998 Society of Automotive Engineers, **1998**.

[55] V. Rman, "The Hydrogen Fuel Option for Fuel Cell Vehicle Fleets," presented at the 1999 Society of Automotive Engineers, **1999**.

[56] B. B. Woong-chul Yang, Nicholas Fletcher, Ric Pow, "Control Challenges and Methodologies in Fuel Cell Vehicle Development," in *Proceedings of the 1998 International Congress on Transportation Electronic*, **1998**, 363-370.

[57] M. Lopez-Haro, L. Guétaz, T. Printemps, A. Morin, S. Escribano, P. H. Jouneau*, et al.*, *Nature*

Communications, **2014**, 5, 5229.

[58] E. Passalacqua, F. Lufrano, G. Squadrito, A. Patti, and L. Giorgi, *Electrochimica Acta*, **2001**, 46, 799-805.

[59] S. A. Berlinger, B. D. McCloskey, and A. Z. Weber, *The Journal of Physical Chemistry B*, **2018**, 122, 7790-7796.

[60] M. Shibayama, T. Matsunaga, T. Kusano, K. Amemiya, N. Kobayashi, and T. Yoshida, *Journal of Applied Polymer Science*, **2014**, 131.

[61] R. Balu, N. R. Choudhury, J. P. Mata, L. de Campo, C. Rehm, A. J. Hill*, et al.*, *ACS Applied Materials & Interfaces*, **2019**, 11, 9934-9946.

[62] S. Khandavalli, J. H. Park, N. N. Kariuki, D. J. Myers, J. J. Stickel, K. Hurst*, et al.*, *ACS Applied Materials & Interfaces*, **2018**, 10, 43610-43622.

[63] F. Yang, L. Xin, A. Uzunoglu, Y. Qiu, L. Stanciu, J. Ilavsky*, et al.*, *ACS Applied Materials & Interfaces*, **2017**, 9, 6530-6538.

[64] S. Takahashi, J. Shimanuki, T. Mashio, A. Ohma, H. Tohma, A. Ishihara*, et al.*, *Electrochimica Acta*, **2017**, 224, 178-185.

[65] S. Shukla, S. Bhattacharjee, A. Z. Weber, and M. Secanell, *Journal of The Electrochemical Society*, **2017**, 164, F600-F609.

[66] M. B. Dixit, B. A. Harkey, F. Shen, and K. B. Hatzell, *Journal of The Electrochemical Society*, **2018**, 165, F264-F271.

[67] A. Therdthianwong, P. Ekdharmasuit, and S. Therdthianwong, *Energy & Fuels*, **2010**, 24, 1191-1196.

[68] Y. Komoda, K. Okabayashi, H. Nishimura, M. Hiromitsu, T. Oboshi, and H. Usui, *Journal of Power Sources*, **2009**, 193, 488-494.

[69] T. Kusano, T. Hiroi, K. Amemiya, M. Ando, T. Takahashi, and M. Shibayama, *Polymer Journal*, **2015**, 47, 546-555.

[70] T. K. Suzuki Toshiyuki, Mikio Wada, Masafumi Koizumi, Atsushi Nogi, Tooru Oda, *Toyota Technical Review*, **2015**, 61, 32-38.

[71] A. N. Takeshi Nagasawa, Teppei Ikeda, Shimpei Yano, Shinya Takeshita, Takuya Itakura, *Toyota Technical Review*, **2021**, 66, 34-39.

Chapter 2

Tunable Angle-Independent Color from a Phase-Separated Porous Gel

2.1 Introduction

In the natural world, there exist many sources of inspiration for the creation of new high-performance materials. Structural color observed in various creatures, plants, and minerals has received a great amount of attention in recent years because of its eye-catching, non-photobleachable, and energy-saving properties, which are important for developing unprecedented coloring materials. One of the most popular methods to obtain artificial structurally colored materials is the elaboration of periodic dielectric structures on a length scale that is comparable to the wavelength of light in materials and thus causes multiple Bragg reflections. However, the fabrication of such mesoscale structures requires a great amount of time, effort, and, in some cases, cost when using existing top-down or bottom-up approaches. Herein, I demonstrate a facile self-assembly approach to obtain a porous gel exhibiting angle-independent color using a principle different from that of traditional dielectric periodically structured materials. The channel-like porous structure in the gel might be self-assembled from the phase-separated polymers that result from spinodal decomposition and it might be locked in by kinetic arrest, likely through entanglement or cross-linking. The porous swollen gel changes color reversibly with solvent, covering the whole visible region in response to solvent composition and temperature by means of changes in the wavelength dispersions of the refractive indices of the gel portion and the solvent portion in the pore.

Structural color is generally defined as coloration caused by complicated and diverse interactions between light and materials, such as interference effects, diffraction grating, light scattering, and dispersion of refractive index, and it essentially does not lose the energy of the light [1–3]. For the reason, structural color has been the subject of extensive studies for applications in energy saving mobile devices with a reflective full-color paperlike display. Though structural coloration can be caused by not only periodic dielectric structures but also randomly dispersed particles and a simple prism, recent studies of artificial structurally colored materials have focused mainly on the fabrication of periodical microstructures, such as multilayer films[4–6] and photonic crystals [7–9]. This trend is in part due to the relative ease to understand the structures, and the simple principle of Bragg diffraction, which generates structural color from periodic dielectric structures. However, to design a reflective full color paperlike display with a wide viewing angle, the angle dependence of the structural color based on Bragg diffraction becomes a major issue.

Recently, I demonstrated for the first time that amorphous arrays with a short-range order prepared from submicrometer spherical colloidal gel particles[10] or silica colloidal particles[11] are capable of displaying angle-independent structural color and can be applied to nonfading color materials and full-color paperlike displays. Theoretical interpretations for the existence of a photonic band gap causing structural color in amorphous array systems were also provided by some groups [12, 13]. Counterintuitively, however, the practical fabrication of amorphous arrays from colloidal particle suspensions is a more complicated task than expected and is one of the most important challenges for large-scale production.

On this issue, living matter may give us a hint. Analogous structures and the principle of structural coloration are also found in some living matter [14, 15]. For example, the amorphous packing of submicrometer spheres or tortuous channels composed of β-keratin and air nanostructures found in the feather barbs of birds produce vivid structural color without angular dependence. The structural color of the feather barbs may be produced by wavelength-selective scattering of light from the nanostructures with a short-range order, which must rely on the same principle as the above-described artificial systems. According to Dufresne, Prum, and co-workers [14], the nanostructures in feather barbs are self-assembled by the phase separation of β-keratin from a cellular cytoplasm; the polymerization of β-keratin drives the phase separation within a cell, and arrest of the phase separation is facilitated by the entanglement or cross-linking of β-keratin filaments. As the molecular weight of β-keratin filaments increases, the entropic incentive for mixing drops, and the phase boundary shifts to higher temperatures, resulting in phase separation. If nucleation and growth occur, the system forms a submicrometer sphere-type nanostructure. When the phase separation is preceded by spinodal decomposition, a tortuous channel type nanostructure can evolve spontaneously.

This assumption stimulated our interest in fabricating such phase-separated structures by self-assembly approaches for artificial colored materials. Therefore, our initial target was a biomimetic, facile preparation of self-assembled nanostructured and structurally colored materials with short-range order on a length scale that is comparable to the wavelength of visible light. However, the self-assembled fabricated channel-type porous gel revealed unexpected tunable color in response to solvent composition and temperature even though the average domain size in the porous gel was much larger than the wavelength of visible light. Herein, I explain our new

discovery about the facile preparation of the angle independent colored material and its reversible tuning coloration depending on the solvent composition and the environmental temperature.

2.2 Materials and methods

2.2.1 Sample preparation

Figure 1 shows chemical structures of compounds used for preparation of poly(MEO2). First, a 30 mL stoppered pear-shaped flask was loaded with 4,4'-dinonyl-2,2'-dipyridyl (26.2 mg) and 2-(2-methoxyethoxy) ethyl methacrylate (9.03 g). The solution was sealed with a three-way stopcock and cycled three times between nitrogen gas and vacuum to remove oxygen. Methyl 2-bromopropionate (6.69 mg) was added to the solution using a microsyringe. Next, this solution was moved using a cannula to another stoppered test tube containing CuBr (4.59 mg) and filled with nitrogen gas. The uniformly dissolved solution was divided into 1.25 mL test tubes in a globe box filled with nitrogen gas. The sealed test tubes were placed into constant-temperature baths at several temperatures, and the polymerizations proceeded for 19 h. Table 1 summarized synthesis of poly(MEO2) under various reaction conditions. The newly formed polymer gels were washed with acetone and obtained as clear and colorless gels or opaque gels. The preparation of linear poly(MEO2) was the same as that of the gels but the temperature and reaction time were 60°C and 2 h, respectively. The linear polymer was purified by dialysis. The number average molecular weight of the polymer was determined by gel permeation chromatography.

2.2.2 Measurements

The microstructure of the gels was investigated by scanning electron microscopy (SEM, JEOL JSM 5600). The samples were coated with a 15 nm gold layer, and the microscope was operated at 10 kV. Optical photographs of the samples were taken on a digital microscope (KEYENCE VHX-500). Transmittance spectra of the samples were measured using an Ocean Optics USB 2000 fiber optic spectrometer by altering the angle of incidence from 0° to 40° within a cell whose temperature was controlled by a circulating water bath. The dispersion of the samples was measured by a multiple wavelength refractometer (ATAGO DR-M2) connected to a circulating water bath. An electronic thermometer (As One TM-300) with a precision of 0.1°C was used to continuously monitor the temperature of the prism of the refractometer.

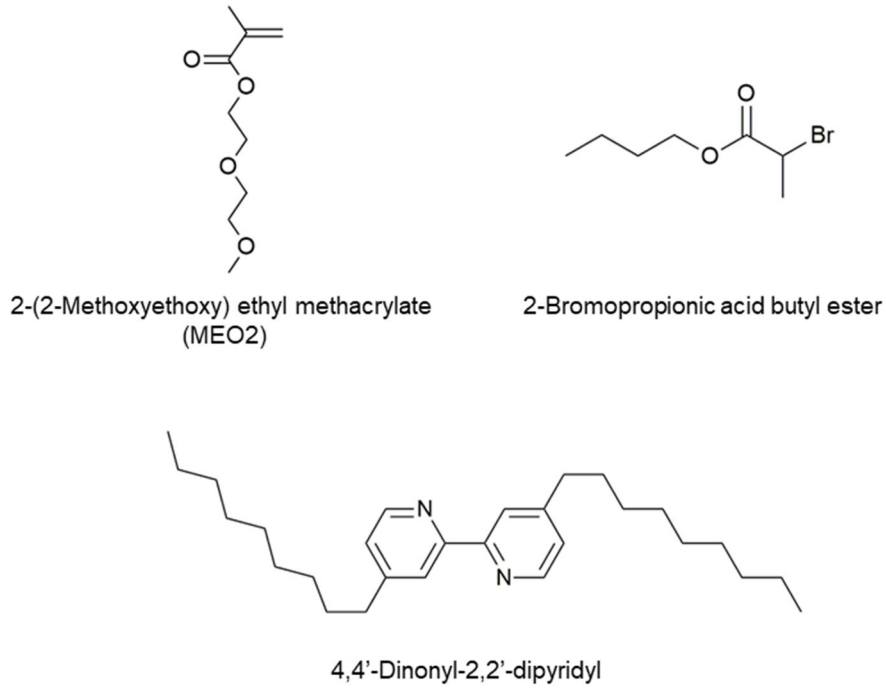

Figure 1. Chemical structures of compounds used for preparation of poly(MEO2).

Table 1. Synthesis of poly(MEO2) under various reaction conditions.

Run	[M] : [I] : [CuI] : [L]	Reaction time / h	Temp. / ℃
Run 1-1	1500 : 1 : 1 : 2	19	-13
Run 1-2		19	4
Run 1-3		19	15
Run 1-4		19	20
Run 1-5		19	26
Run 1-6		19	30
Run 1-7		3	50
Run 1-8		3	60

[M], [I], [CuI], and [L] are the concentrations of the monomer, the initiator, CuBr, and ligand, respectivery.

2.3 Results and Discussion

The microstructure in the porous gel was self-assembled by phase separation of poly{2-(2-methoxyethoxy)ethyl methacrylate} [poly(MEO2)] along with reversible deactivation radical polymerization, the so-called atom transfer radical polymerization (ATRP)[16, 17] that is an example of a living radical polymerization, of MEO2 using 2-bromopropionic acid butyl ester as an initiator and the CuBr/4,4'-dinonyl-2,2'-dipyridyl catalytic system without solvent below 20°C (Figure 2, Figure 3). Above a reaction temperature of 50°C, the gels obtained were transparent and homogeneous (Figure 4). The resulting gels at a reaction temperature between 20°C and 50°C were mixtures of the phase-separated portion and the homogeneous portion. These results indicate that the polymerization-induced phase-separation mechanism is an upper critical solution temperature behavior [18].

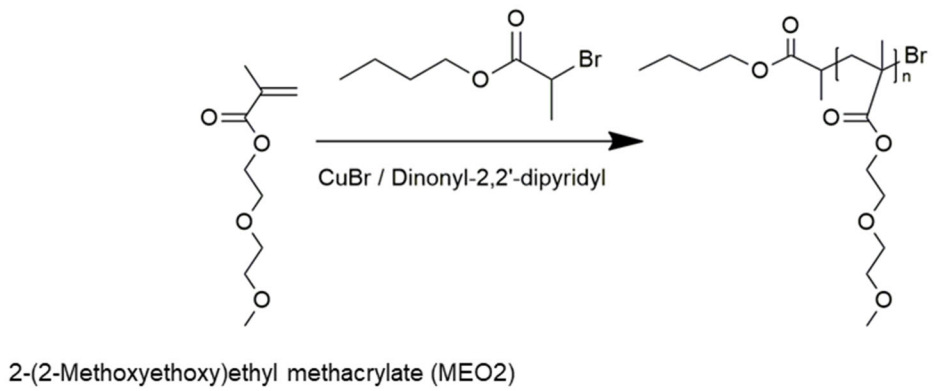

Figure 2. Reaction scheme of poly(MEO2).

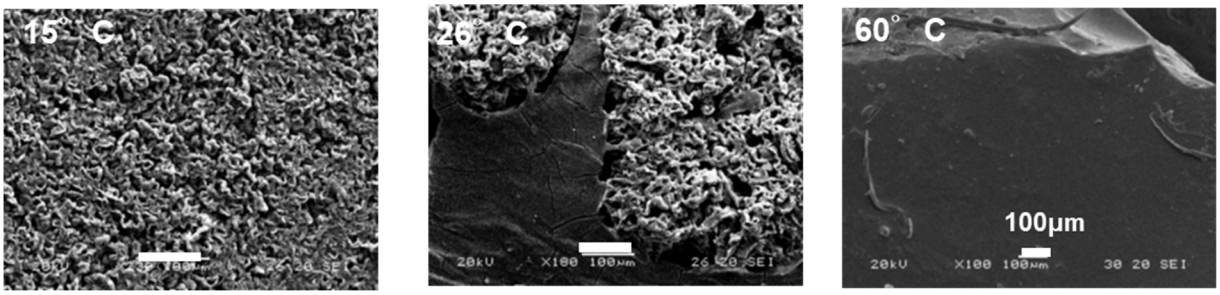

Figure 3. SEM image of gels prepared at various temperatures. Scale bars: 100 μm

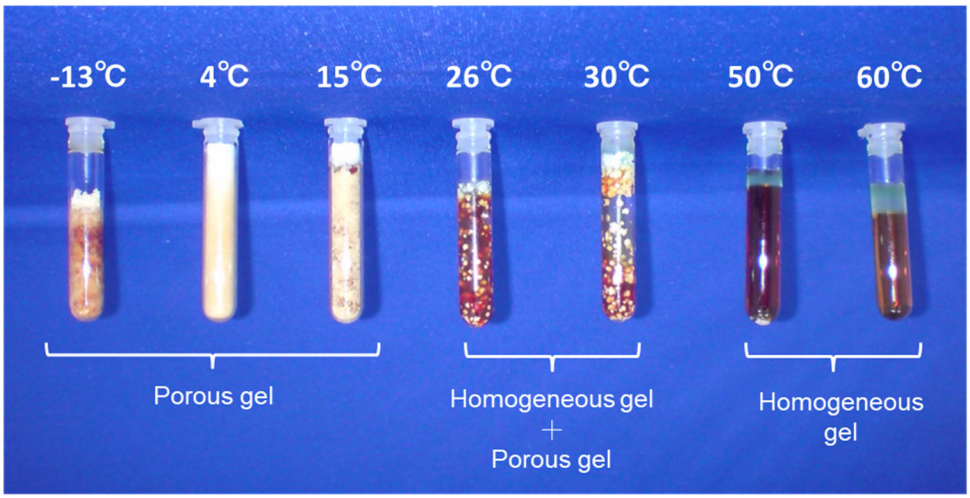

Figure 4. Optical photograph image of poly(MEO2) gels prepared at different temperatures.

As the molecular weight of poly(MEO2) increases as a result of ATRP, the position of the phase boundary shifts to higher temperature over time, and the phase separation by spinodal decomposition or nucleation and growth can proceed. Judging from the channel-type morphology of the phase-separated microstructure observed in the gel, the phase separation might be induced by spinodal decomposition. The resultant gel swells slightly in toluene, which is a good solvent for poly(MEO2) (Figure 5a), but the microstructure is almost maintained, despite the lack of a cross-linker. The unstable phase-separated microstructure is probably locked in by kinetic arrest, likely through the entanglement or crosslinking of poly(MEO2). As a result, the microstructure consists of isotropic, tortuous, and twisting channels with a characteristic length of about 10 μm, which is considerably larger than the wavelength of visible light. The size of a scattering substance is parameterized by the ratio of its characteristic length r and the wavelength of light λ as $\alpha=2\pi r/\lambda$[19]. If the value of α becomes sufficiently larger than 1, the geometrical optic approximation can be applied to evaluate the interaction between the light and the scattering substance. Consequently, we must be able to treat this porous gel as a diffuse reflective material.

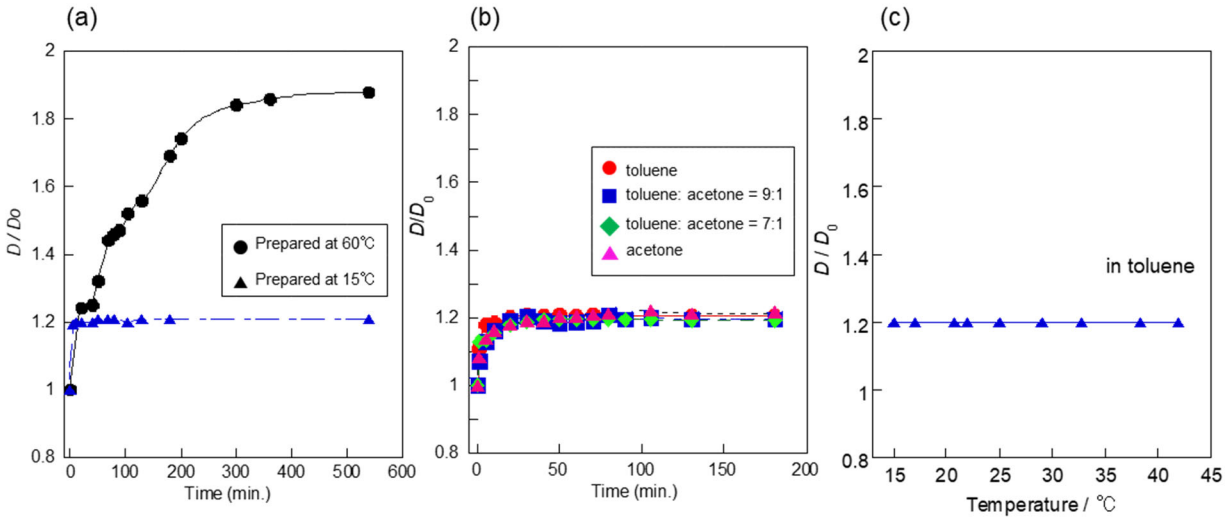

Figure 5. The swelling ratios D/D_0 of cylindrical gels, where D_0 is the diameter of the cylindrical gel at the preparative state and D is the diameter of a cylindrical gel under specific conditions, were measured at several conditions.
(a) Swelling kinetics of cylindrical gels after immersion in pure toluene at 25°C. These gels were prepared at different temperatures.
(b) Swelling kinetics of cylindrical gels, prepared at 15°C, after immersion in different compositions of solvents at 26°C.
(c) Temperature-dependent equilibrium swelling ratio of the porous gel prepared at 15°C in pure toluene.

Figure 6a shows the transmission spectra of the porous gel in toluene/acetone mixed solvents at 20°C. A quite broad peak at around 766 nm is observed from the porous gel in pure toluene. However, the color of the porous gel is brilliant blue in pure toluene (Figure 6b). From the transmission spectra, it can be assumed that the blue color must be mainly caused by the diffuse reflection of short-wavelength visible light. The position of the peak, λ_{max}, moves to a shorter wavelength, and the peak sharpens with increasing acetone in the mixed solvent. The color of the porous gel also changes depending on the composition of the mixed solvent; the color must be generated by the diffuse reflection of visible light with wavelengths that are both shorter and longer than the peak wavelength. It is noteworthy that light of a certain wavelength range where the sharp peak can be seen in the transmission spectra can pass through this porous gel depending on the solvent composition. This optical property is obviously different from the optical properties of the amorphous arrays prepared from submicrometer spherical particles and the nanostructures in feather barbs. A downward peak, which can be attributed to a partial photonic band gap, can be observed in the transmission spectra of the amorphous arrays. The transmission spectra measured at different angles for the porous gel in different solvent compositions are shown in Figure 6c,d. The peaks occurred at certain wavelengths depending on the solvent composition and did not depend on the angle from 0° to 40° (Figure 6e). In Figure 6f, the peak position of the spectra and the refractive indices of the mixed solvents are plotted as a function of the solvent composition. A similar tendency was observed for both changes with increasing toluene composition; the variation in the peak position is likely to be associated with the change in the refractive indices of the mixed solvents.

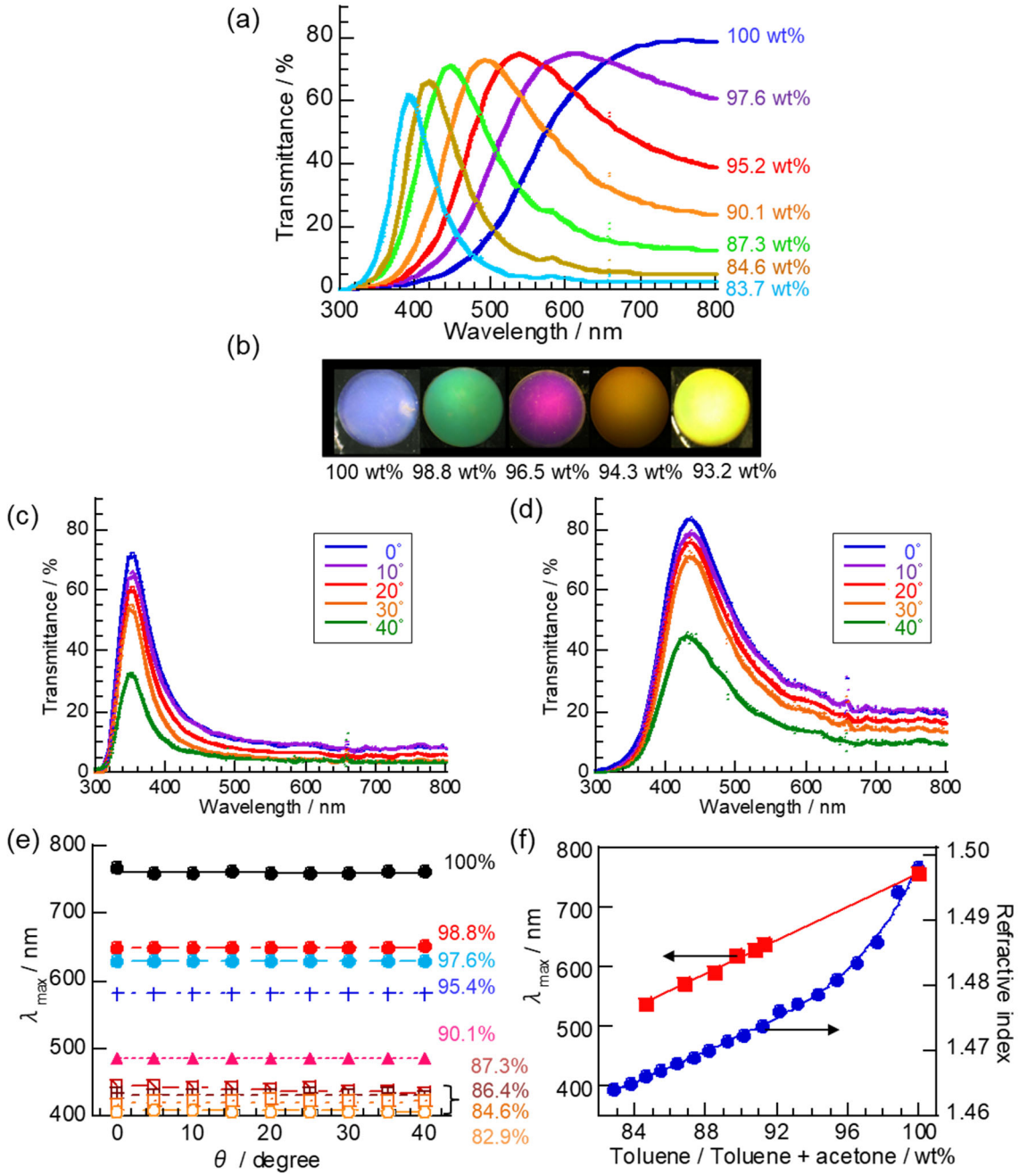

Figure 6. (a) Solvent composition dependence of transmission spectra and (b) optical photographs of a porous gel at 20°C. The porous gel was prepared at 15°C. The scale bar in (b) is 1mm. (c), (d) Transmission spectra of the porous gels in different solvent compositions measured at various angles at 20°C. The mass percentages in these figures represent the concentration of toluene in the mixed solutions. (c) 75 wt% toluene, (d) 85 wt% toluene. (e) Plots showing λ_{max} of the transmission spectra for the porous gels in various solvent compositions versus angle at 20°C. (f) Plots showing the refractive index n of the solvents at 589 nm and λ_{max} of the transmission spectra versus the toluene compositions in the mixed solvents.

Temperature-dependent transmission spectra of the porous gel in pure toluene were also observed because the refractive index of the solvent is also subjected to temperature change. As shown in Figure 7a, the peak position of the spectra shifted to the shorter wavelength, and the peak becomes sharper with a rise in temperature. The refractive index of toluene and the peak position also decrease with increasing temperature (Figure 7b). Meanwhile, the swelling degrees of the porous gels remain unchanged with variations in solvent composition and temperature (Figure 5b,c), which indicates that variation in the size of the microstructure does not contribute to the change in the color.

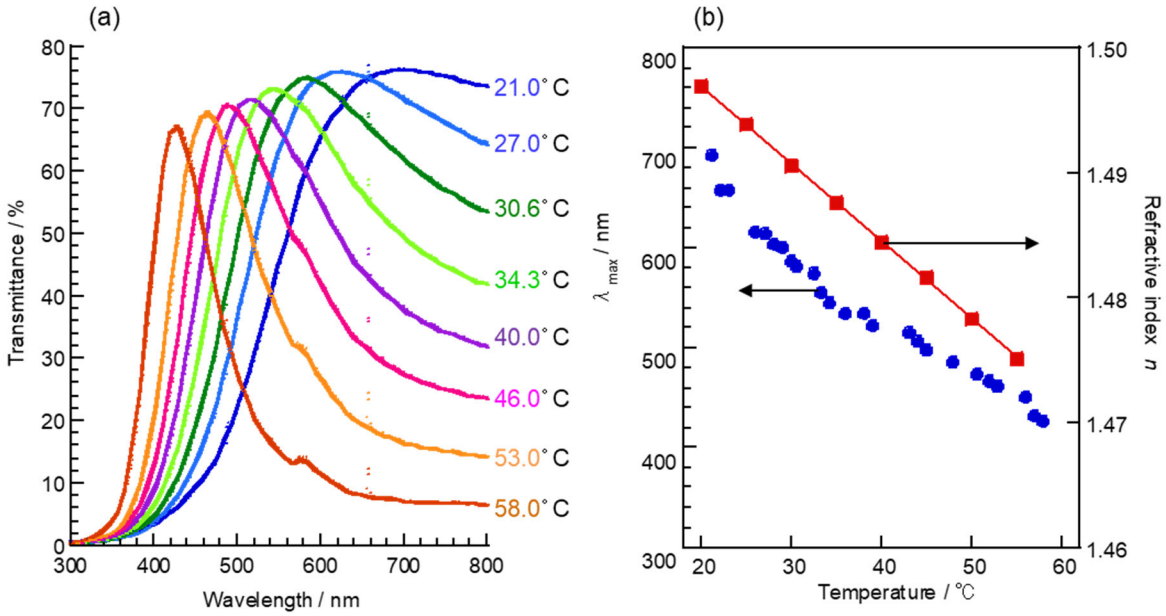

Figure 7. (a) Temperature dependence of transmittance spectra of the porous gels in pure toluene. The porous gel was prepared at 15°C. (b) Plots showing λ_{max} of the transmission spectra of the gel in pure toluene and the refractive index *n* of toluene at 589 nm versus temperature.

To evaluate the contribution from the change in the refractive indices of the solvents and gel portions to the color change, the dispersion, which is a wavelength-dependent refractive index, was measured for each portion. I used poly(MEO2) [M_n (number average molecular weight) =1.02×10^5] toluene solutions with several concentrations of the polymer in substitution for the gel portion because of the difficulties in obtaining the refractive indices of the actual gel portion. The diffuse reflection from a macroporous gel filled with a solvent requires a difference in the refractive indices

between the gel portion and the solvent portion. For example, in the case that these refractive indices are different at all visible wavelengths, the porous gel diffusely reflects white light and becomes opaque. In the experimentally observed dispersion curves for most polymer solutions, except for the 10 wt% solution, the refractive indices are smaller than those in pure toluene over all visible wavelengths at 20°C (Figure 8a). However, the dispersion curve of the 10 wt% poly(MEO2) solution intersects with that of toluene at around 650 nm and 20°C. If the refractive indices of the gel portion and the solvent are equal, a certain wavelength of light around the intersection can pass through the porous gel, while the other wavelengths of light are diffusely reflected. As a result, I see the upturned peaks in the transmission spectra of the porous gel. To test this hypothesis, the dispersion curves of the 10 wt% poly(MEO2) solution and toluene at different temperatures were estimated, followed by identification of the position of the intersection between the two curves with the temperature change. Cauchy's approximate equation [20] was used to estimate the appropriate dispersion curves for each condition, based on the experimentally measured five plots of refractive indices (Figure 8b). The determined intersections between the two curves of the 10 wt% poly(MEO2) solution and toluene depending on the temperature were compared to the peak wavelength of the spectra (Figure 8c) with a change in temperature. The intersections reasonably reflected the trend of the peak position of the transmission spectra with increasing temperature, which supports our hypothesis that the tunable coloration of the swollen porous gel is caused by the coincidence at one wavelength of the dispersion curves of the gel portion and the solvent portion, depending on solvent composition and temperature. Judging from Figure 8b, the sharpness of the peak must be attributed to the intersection of two dispersion curves with large angle. As a result, the porous gel exhibits brilliant colors. I demonstrated that the newly prepared colored materials can be formed into any shape and exhibit angle-independent color for an extended period (Figure 9).

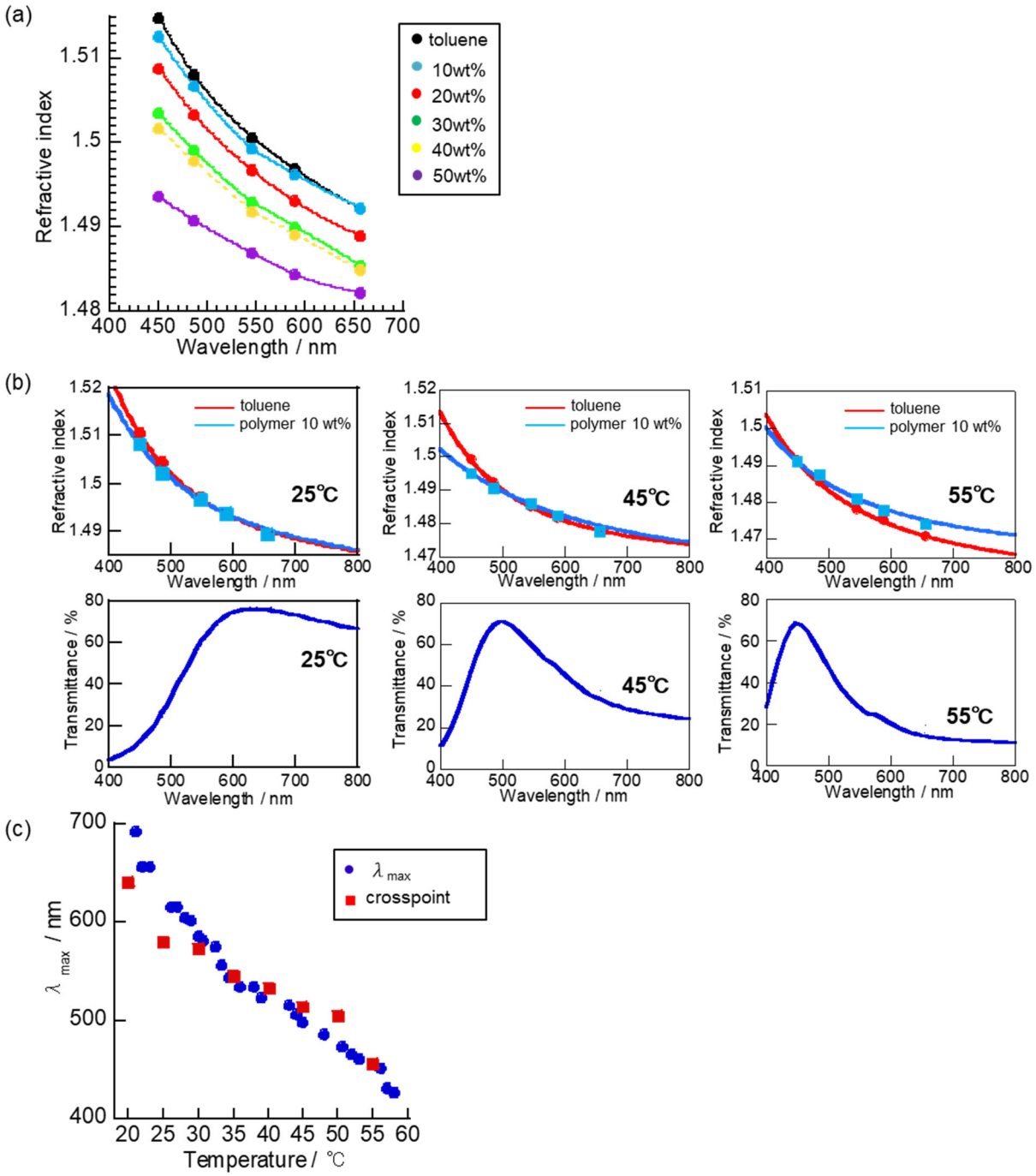

Figure 8. (a) Plots showing the refractive index n of the poly(MEO2) toluene solutions with various concentrations and pure toluene depending on the wavelength at 20°C. (b) Dispersion curves of pure toluene and the 10 wt% poly(MEO2) toluene solution compared at various temperatures. The intersection of these curves changed depending on temperature. The transmission spectra were obtained from the porous gel in toluene at different temperatures. (c) λ_{max} of the transmission spectra of the 10 wt% poly(MEO2) toluene solution at various temperatures compared with the temperature-dependent intersections obtained by Cauchy's approximate equation.

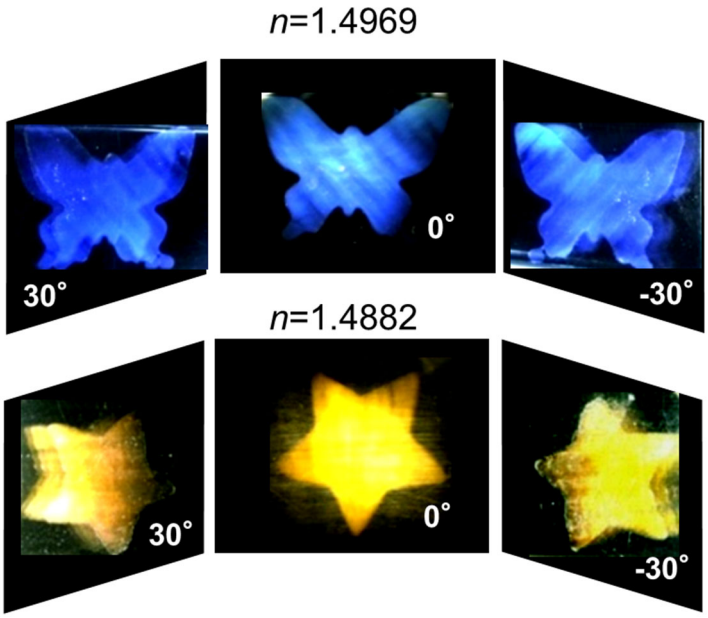

Figure 9. Photo images of the porous gels at various angles of incidence in different solutions. Here, *n* is the refractive index of each solvent.

2.4 Conclusion

So far, a few systems have been reported that use various dispersions of two different media for making optical filters [21–29]. Because, however, most systems are composed of crushed insoluble inorganic powders immersed in organic solvents or colloidal suspensions, it has been difficult to obtain colored materials with large-scale production useful for making paperlike displays. Only Watanabe's group recently found that homogeneously prepared hydroxypropyl cellulose film exhibits colors using the similar effect when the film is swollen with solvent [30], but the colors are subtle. In contrast, our structurally colored material generated using the phase-separation method can be obtained without difficulty, and exhibits brilliant colors: this colored material represents a promising new material for the manufacture of reflective full-color displays with a wide viewing angle, energy saving, and nonfading color materials. Moreover, as it has an interconnected porous structure, and also can be prepared in other stimuli-sensitive polymer systems, the newly prepared structurally colored materials should have potential as sensors and monolith systems for reactors and separation.

Reference

[1] P. Vukusic, J. R. Sambles, C. R. Lawrence, *Nature* **2000**, 404, 457 – 457.

[2] A. R. Parker, V. L. Welch, D. Driver, N. Martini, *Nature* **2003**, 426, 786 – 787.

[3] S. Kinoshita, *Structural Colors in the Realm of Nature*, World Scientific Publishing, Shingapore, **2008**.

[4] K. Busch, S. L lkes, R. B.Wehrspohn, *Photonic Crystals* (Ed.:H. F ll), Wiley-VCH, Weinheim, **2004**.

[5] J. J. Walish, Y. Kang, R. A. Mickiewicz, E. L. Thomas, *Adv. Mater.* **2009**, 21, 3078 – 3081.

[6] M. A. Haque, G. Kamita, T. Kurokawa, K. Tsujii, J. P. Gong, *Adv. Mater.* **2010**, 22, 5110 – 5114.

[7] A. C. Arsenault, D. P. Puzzo, I. Manners, G. A. Ozin, *Nat. Photonics* **2007**, 1, 468 – 472.

[8] M. Harun-Ur-Rashid, T. Seki, Y. Takeoka, *Chem. Rec.* **2009**, 9, 87 – 105.

[9] K. Matsubara, M. Watanabe, Y. Takeoka, *Angew. Chem.* **2007**, 119, 1718 – 1722; *Angew. Chem. Int. Ed.* **2007**, 46, 1688 – 1692.

[10] Y. Takeoka, M. Honda, T. Seki, M. Ishii, H. Nakamura, *ACS Appl. Mater. Interfaces* **2009**, 1, 982 – 986.

[11] M. Harun-Ur-Rashid, A. Bin Imran, T. Seki, M. Ishi, H. Nakamura, Y. Takeoka, *ChemPhysChem* **2010**, 11, 579 – 583.

[12] C. J. Jin, X. D. Meng, B. Y. Cheng, Z. L. Li, D. Z. Zhang, *Phys. Rev. B* **2001**, 63, 195107.

[13] K. Edagawa, S. Kanoko, M. Notomi, *Phys. Rev. Lett.* **2008**, 100, 013901.

[14] E. R. Dufresne, H. Noh, V. Saranathan, S. G. J. Mochrie, H. Cao, R. O. Prum, *Soft Matter* **2009**, 5, 1792 – 1795.

[15] R. O. Prum, R. H. Torres, *Integr. Comp. Biol.* **2003**, 43, 591 – 602.

[16] K. Matyjaszewski, J. H. Xia, *Chem. Rev.* **2001**, 101, 2921 – 2990.

[17] M. Kato, M. Kamigaito, M. Sawamoto, T. Higashimura, *Macromolecules* **1995**, 28, 1721 – 1723.

[18] S. Yamago, *Chem. Rev.* **2009**, 109, 5051 – 5068.

[19] J. C. Stover, *Optical Scattering: Measurement and Analysis,* SPIE Optical Engineering Press, **1995**.

[20] M. Cauchy, Philos. *Mag. Ser.* 3 **1941**, 8, 459 – 469.

[21] C. Christiansen, *Ann. Phys. Chem.* **1884**, 23, 298 – 301.

[22] G. C. Crossmon, *Anal. Chem.* **1948**, 20, 976 – 977.

[23] W. C. Price, K. S. Tetlow, *J. Chem. Phys*. **1948**, 16, 1157 – 1162.

[24] M. Cloupeau, S. Klarsfel, *Appl. Opt.* **1973**, 12, 198 – 204.

[25] D. D. Saperstein, *J. Phys. Chem.* **1987**, 91, 6659 – 6663.

[26] K. Balasubramanian, M. R. Jacobson, H. A. Macleod, *Appl. Opt.* **1992**, 31, 1574 – 1587.

[27] N. J. Goddard, A. E. Maturell, *Appl. Opt.* **1995**, 34, 7318 – 7320.

[28] M. Franz, B. M. Fischer, M. Walther, *Appl. Phys. Lett.* **2008**, 92– 94, 021107-1–3.

[29] T. D. Ibragimov, *J. Appl. Spectrosc.* **2009**, 76, 752 – 755.

[30] S. Edo, K. Okoshi, S. Kang, M. Tokita, T. Kaneko, J. Watanabe, *Langmuir* **2010**, 26, 1743 – 1746.

Chapter 3
Multicolor Polymer-Dispersed Liquid Crystals

3.1 Introduction

The widespread utilization of personal-use multimedia has triggered a vigorous expansion in the manufacturing of cheap, simple and power-saving displays. Because the most widely used liquid crystal (LC) displays are composed of many different sets of optical elements – such as color filters, polarizing plates, and alignment films – the simplification of such designs will potentially lead to decreases in the cost of manufacturing and better power-saving capabilities. A display with a polymer-dispersed liquid crystal (PDLC) film is one of the simplest models possible because it has no polarizing plate or alignment film [1–6]. Although this display is structurally simplified and very bright, there is still room for improvement due to the use of a color filter. Displays consisting of stimuli-sensitive multichromic materials are among the leading candidates for such ideal simple systems [7, 8].

Herein, I report the preparation of a new material that changes its color – covering the whole visible region – in response to temperature by means of changes in both the diffraction properties and the wavelength dispersions of its refractive indices. Our material is a composite of a particle gel network and an LC; it is structurally identical to a traditional PDLC system. Thus, the LC is randomly arranged in the particle gel network at lower temperatures, resulting in a scattering of applied white light. This results in a translucent or milky white appearance. However, when the LC reaches an isotropic state at higher temperatures, a particular wavelength of light – at which the two different wavelength-dependent dispersion curves for the particle gel network and the LC intersect – can predominantly transmit through the composite material. As a result, the composite material exhibits bright coloration and also reveals a change in color in response to temperature because the cross-point of the two wavelength-dependent dispersion curves varies with temperature.

In recent years, structurally colored materials have been the subject of extensive study due to their possible application in paints, textiles, cosmetics, sensors and displays [9, 10]. Structurally colored materials that do not suffer from photobleaching or lose light energy are encouraging candidates for power-saving display systems. One of the most widely anticipated structurally colored materials for such applications is a photonic crystal with a periodic optical nanostructure comprised of submicron particles [11, 12] and large-molecule block copolymers [13, 14]. However, angle-dependent structural color based on Bragg diffraction from a photonic crystal is unfavorable for use in display technology.

To obtain structurally colored materials exhibiting angle-independent color, I prepared two types of nanostructured materials. One is an amorphous array system composed of submicron particles that have a pseudo-photonic band gap [15, 16]. Thus far, I have used soft gel particles and hard silica particles to prepare amorphous arrays, and both types of arrays reveal structural color without angle dependence due to the short-range order of the particles. The other nanostructured material is a self-assembled particle gel network filled with an appropriate solvent, the dispersion curve of which intersects with that of the polymer in the visible region [17]. Here, the dispersion is a variation of the refractive index with wavelength. This system also exhibits angle-independent color using a principle different to that of the above-mentioned photonic crystals and also to that of amorphous arrays. I believe that these angle-independent structurally colored systems can be front-runners for the manufacture of energy-saving display systems.

In this study, I attempted to expand the latter, recently developed, system's potential for application in a functional multicolor PDLC display. PDLC devices do not require a polarizing plate or an alignment film for modulating light because the LC droplets, confined in a particle gel in which the particle size is comparable to visible wavelengths, scatter light due to the refractive index mismatch between the LC droplets and the particle gel [1–6]. Consequently, the PDLC devices work as optical shutters or smart windows that can change these aspects between clear states and opaque states. If I can add more functions to PDLC devices, such as the ability to display different colors, these devices may find application in power-saving multicolor displays. To implement this concept, I turn to our recently exploited structurally colored material [17].

3.2 Materials and methods

3.2.1 Sample preparation

Figure 1 shows chemical structures of compounds used for preparation of the multi-colour PDLC. In a typical experiment, a 3 mL test tube was loaded with MMAA (400 mg, 4.04 mmol), BIS (100 mg, 0.649 mmol), methanol (200 mg, 6.25 mmol) and an appropriate amount of hexane (50–300 mg). Nitrogen gas was bubbled into the solution for 30 min to remove dissolved oxygen. After adding azobisisobutyronitrile (10.2 mg, 9.03×10^{-5} mol) as an initiator to the solution, the sonicated solution was placed in a thermal bath at 60 °C for 24 h to obtain a particle gel network. For the preparation of homogeneous clear polymer networks for dispersion curves, hexane (which is a poor

solvent for the particle gel network) was not added to the solution. The obtained particle gel network was washed with methanol and dried under vacuum. Each particle gel network was cut into a disc shape approximately 1 mm thick. The disc-shaped particle gel network was sandwiched between two slide glasses with a 1 mm-thick teflon spacer, and the pieces were clipped together. Various compositions of LCs composed of 5CB and/or 5PCH were impregnated into the particle gel network in the cell at 70 °C. Binary mixtures of the LC of given compositions were heated at 80 °C for 1 h and were thoroughly mixed. After impregnation of the LCs, the cell was sealed with UV-cured adhesive.

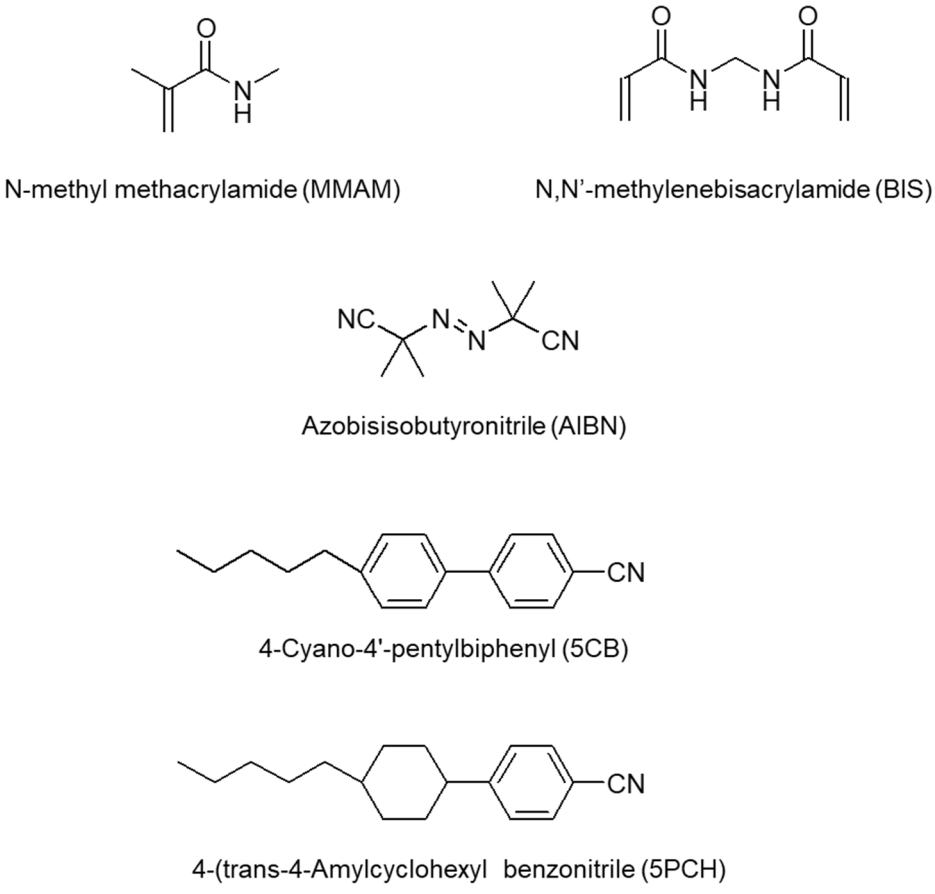

Figure 1. Chemical structures of compounds used for preparation of the multi-colour PDLC.

3.2.2 Measurements

The microstructures of the MMAA–BIS particle gel networks were observed using SEM (Jeol JSM 5600 instrument). The samples were coated with a 15 nm gold layer, and operating voltage at 10 kV. Small LC samples were taken for differential scanning calorimetry (DSC) analysis (Seiko Instruments DSC3200) to estimate T_{NI} and T_m. The heating and cooling rates were 2 °C min^{-1} in all cases. The phase behavior of the LCs was also examined by POM. A polarizing optical microscope (Olympus BH-2) with a hot stage (Mettler FP90) and a CCD camera (Olympus DP12–2) was used for visual observation. The dispersion of the LCs was measured by a multiple-wavelength refractometer (ATAGO DR-M2) connected to a circulating water bath (LAUDA RE-104). An electronic thermometer (AS ONE TM-300) with a precision of ± 0.1 °C was used to continuously monitor the temperature of the refractometer prism. The dispersion of the MMAA–BIS particle gel network was measured by a multiple-wavelength refractometer (Carl Zeiss PR-2) connected to a circulating water bath (HAAKE circulator N6-C41). Transmittance spectra of the samples were measured using an Ocean Optics USB 2000 fiber-optic spectrometer by changing the temperature on a hot stage (Mettler FP90). Optical photographs of the samples were taken on a digital microscope (KEYENCE VHX-500).

3.3 Results and discussion

I adopted a simple procedure to make particle gel networks with well-controlled particle size distributions in the same manner used for making porous polymer monoliths, with production by a phase separation process. Porous polymer monoliths are macroporous materials prepared by polymerising vinyl monomers and cross-linkers in the presence of an appropriate porogenic solvent [18–21]. The size of the pore can be readily controlled by the amount of porogenic solvent used.

In this work, particle gel networks composed of *N*-methyl methacrylamide (MMAA) and *N*, *N*'-methylene-bisacrylamide (BIS) as the monomer and cross-linker, respectively, were prepared using hexane as a porogenic solvent. Figure 2 shows scanning electron microscopy (SEM) images of the MMAA–BIS particle gel networks with varying amounts of hexane. With 50 mg hexane, the dried MMAA–BIS particle gel network is faint blue to the eye (Figure 3a) and is composed of microparticles with diameters of less than 100 nm. The particle size in the MMAA–BIS particle gel network increases with an increase in the amount of hexane present: dried MMAA–BIS particle gel

networks composed of particles larger than 500 nm become opaque (Figure 3b and c). Judging from the morphologies of the phase-separated structures of the MMAA–BIS polymer network particles, the formation of the structures must be caused by nuclear formation, while growth occurs via polymerization [22, 23].

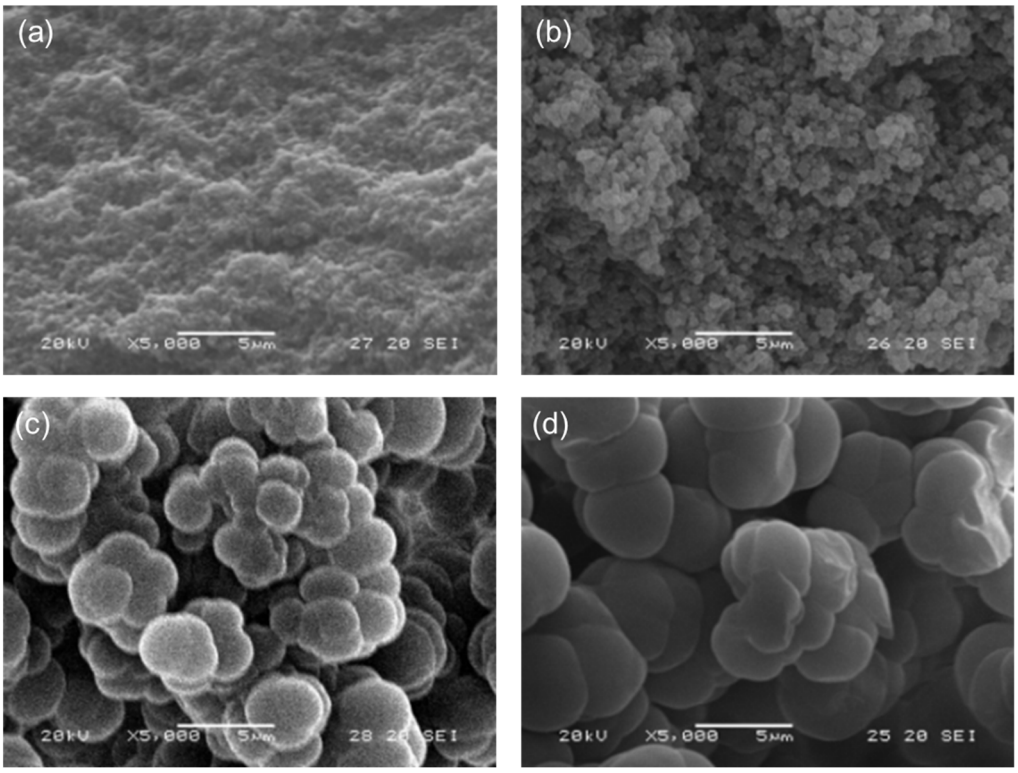

Figure 2. SEM images of MMAA-BIS particle gel networks upon the addition of various amounts of hexane as a porogenic solvent: (a) 50, (b) 100, (c) 200, (d) 300 mg of hexane.

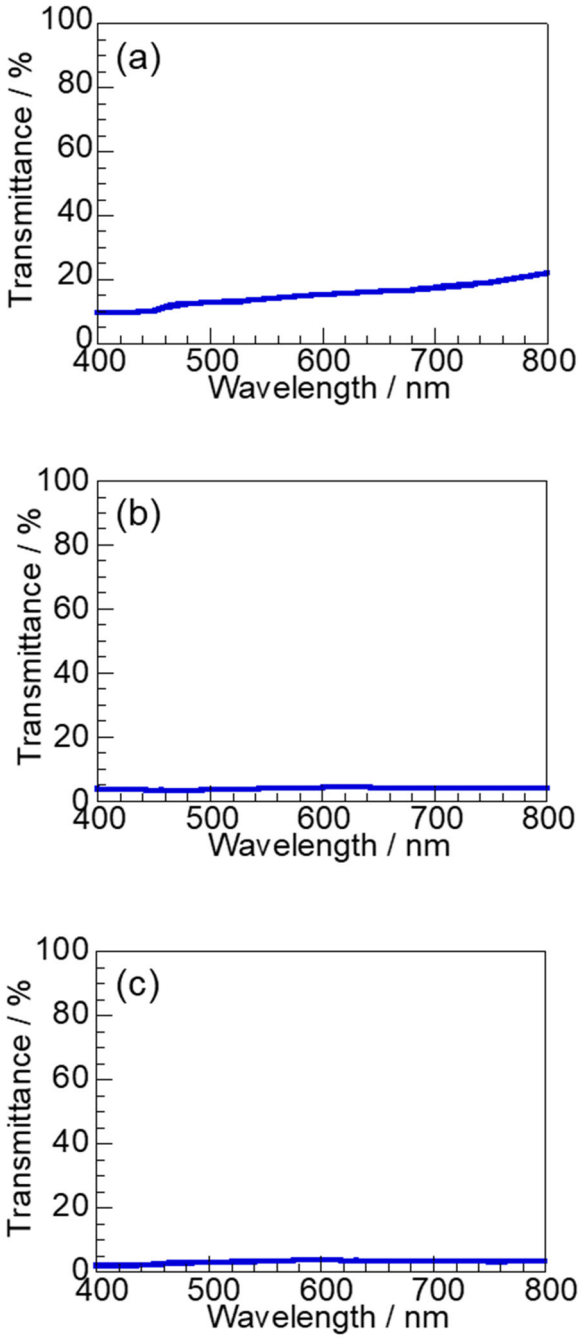

Figure 3. Transmittance spectra for MMAA-BIS particle gel networks:
(a) Sample in Fig. 2(a), (b) Sample in Fig. 2(b), and (c) Sample in Fig. 2(d).

To construct a multicolor PDLC system, I used an MMAA–BIS particle gel network comprised of about 5 μm particles (Figure 2d). As the size of a scattering substance is parameterised by the ratio of its characteristic length r and the wavelength of light λ ($\alpha = 2\pi r/\lambda$) [24] and because a geometrical optics approximation can be applied to evaluate the interaction between light and a scattering substance when the value of α is sufficiently larger than 1, I can treat this MMAA–BIS particle gel network as a simple diffuse reflective material. I previously reported that the coloration of a particle gel network immersed in an appropriate solvent can be caused by means of the coincidence at one wavelength of the dispersion curves of the particle gel portion and the solvent portion [17]. Naturally, a colored material can be obtained by the impregnation of a particle gel network with an appropriate isotropic LC based on the same principle. For an appropriate isotropic LC, the dispersion of the isotropic LC must intersect with the dispersion of a particle gel network at a certain wavelength in the visible region. Because of this requirement, prior to selecting a LC for the construction of a multicolor PDLC system, I must know the dispersion of the MMAA–BIS particle gel network. Figure 4 shows the dispersion curves of the MMAA–BIS particle gel network at 25 and 50 °C, compared with those of two types of popular LCs at different temperatures (see below). The refractive index of the MMAA–BIS particle gel network at 25 °C changes from 1.531 at 404.7 nm to 1.509 at 706.5 nm: the Abbe number (ν_D), which is a measure of the material's dispersion in relation to the refractive index, of this MMAA–BIS particle gel network is 50. The refractive indices of MMAA–BIS particle gel network at 50°C in the visible region are slightly smaller than those at 25°C. However, the change is vanishingly small compared with those of the liquid crystals used. To reveal the coloration of the MMAA–BIS particle gel network filled with a LC, the dispersion curve of the LC above its isotropic point must intersect with that of the MMAA–BIS particle gel network in the visible region [25–27]. If I have an appropriate pure LC meeting this requirement, a multicolor PDLC can be obtained without difficulty. However, even LC mixtures can meet this condition, and the use of a LC mixture can be advantageous for the goal of obtaining a multicolor PDLC that is useful over a wide range of temperatures.

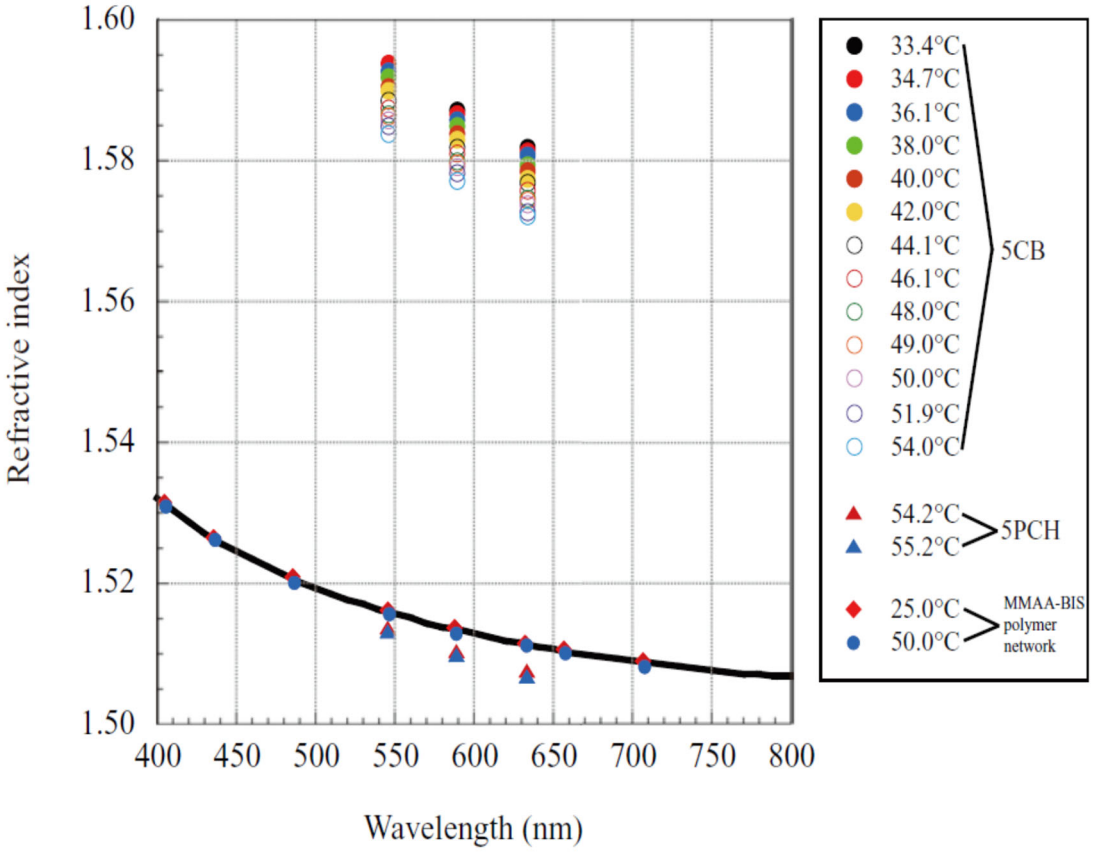

Figure 4. Dispersion curves of the MMAA-BIS particle gel network and of 5CB and 5PCH at several temperatures. The solid line was obtained by a least squares method: $n=(2.1658+5.2095\times10^{-2}\lambda^{2}+6.2057\times10^{-2}\lambda^{-2}-1.2961\times10^{-2}\lambda^{-4}+1.7484\times10^{-3}\lambda^{-6}-8.8452\times10^{-5}\lambda^{-8})^{1/2}$. The numeric data of 5CB and 5PCH are quoted from Ref. [29].

Here, I show a procedure for assembling a multicolor PDLC using a MMAA–BIS particle gel network and a thermotropic LC mixture. I used 4-cyano-4'-pentylbiphenyl (5CB) and 4-(trans-4-pentyl-cyclohexyl) benzonitrile (5PCH) as LCs. Both are thermotropic LCs, exhibiting phase transitions from the isotropic phase into the nematic LC phase as the temperature decreases [28]. The liquid-crystal transition temperatures between the nematic phase and the isotropic phase, T_{NI}, of 5CB and 5PCH are 33.4 and 53.6 °C, respectively (Figure 5).

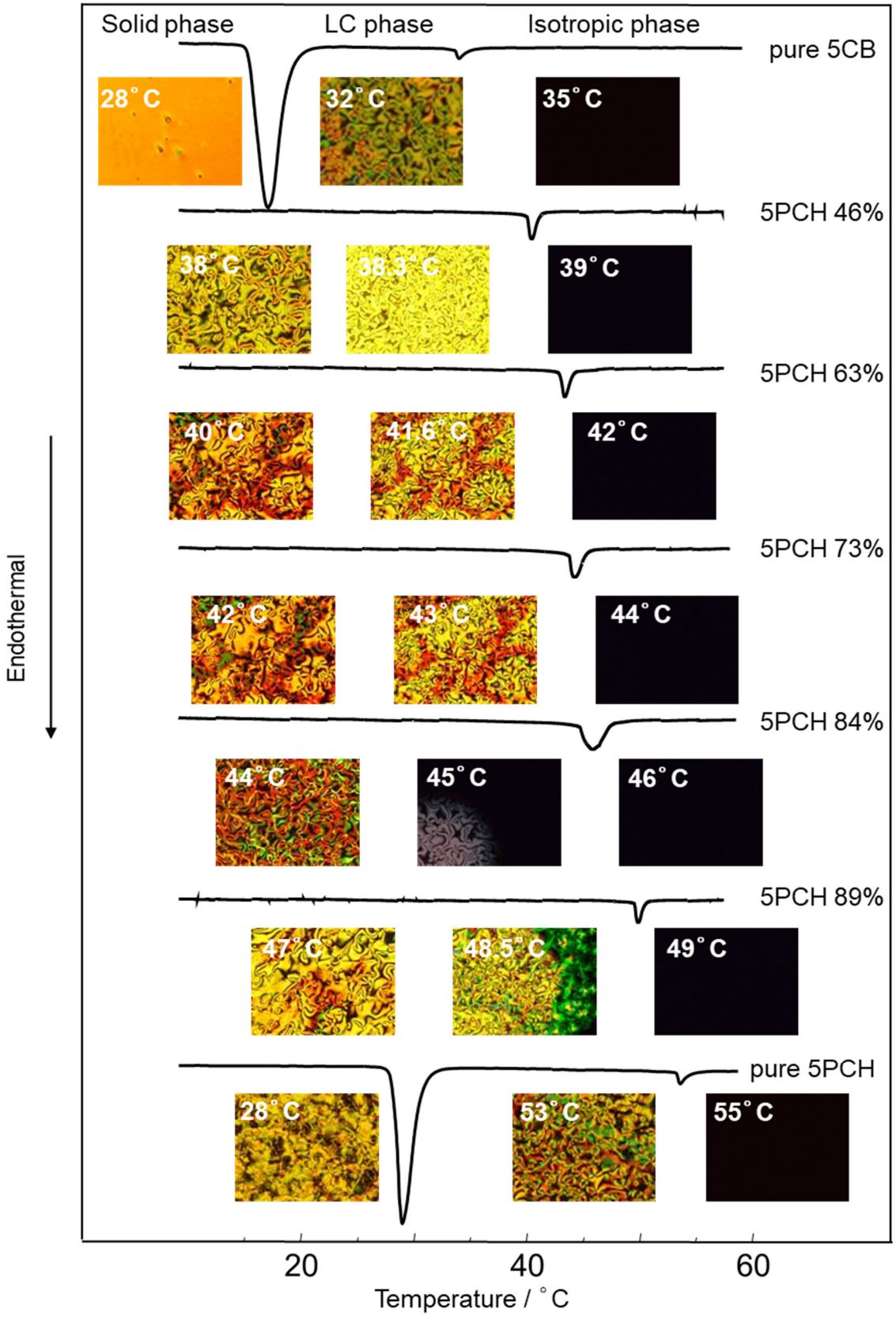

Figure 5. DSC thermograms and POMs for LCs.

The thermotropic LC phase transition can be observed in not only these pure compounds but also these mixtures. A plot of T_{NI} measured by DSC versus the composition is shown in Figure 6. These molecules can be a eutectic mixture, and the T_{NI} of the mixed LCs continuously changes from 33.4 to 53.6 °C, depending on the composition. For each pure LC, there exist two endothermic peaks in the measurement range (0–100°C) of DSC: the lower one and the upper one exhibit the melting point (T_m) and T_{NI}, respectively. The melting points of 5CB and 5PCH are 17.8 and 29.8 °C, respectively, but those of the mixtures are lower than both of these values due to their eutectic properties; the melting points of the mixtures cannot be observed above 0 °C. As a result, the liquid-crystal ranges of the mixtures become wider than the ranges of the pure compounds. This situation provides a wide effective temperature range for the PDLC. If the LC mixture is filled in the particle gel network without alignment, this composite scatter light strongly due to fluctuations in the LC and mismatches in the refractive indices between the particle gel network and the LC below T_{NI}, thereby producing an opaque result. Meanwhile, above T_{NI}, the mixture is in the isotropic phase and exhibits a normal dispersion curve (Figure 7). The refractive indices of 5CB and 5PCH vary from 1.594 at 546 nm to 1.582 at 633 nm and from 1.514 at 546 nm to 1.508 at 633 nm, respectively, at each T_{NI} [29, 30]. Because these dispersion curves do not intersect with the dispersion curve of the MMAA–BIS particle gel network even at different temperatures (Figure 4), the MMAA–BIS particle gel network filled with only 5CB or 5PCH scatters light strongly even above T_{NI}. However, the dispersion curves for the mixtures of given compositions can intersect at certain wavelengths with the dispersion curve of the MMAA–BIS particle gel network in the visible region. In these cases, a certain wavelength of light near the intersection can pass through a composite film comprising the MMAA–BIS particle gel network filled with the LC mixtures, while the other wavelengths of light are diffusely reflected (Figure 8). As a result, I see upturned peaks in the transmission spectra of the composite films: the composites reveal vivid color. Judging from the coloration mechanism of this system, the morphology of a particle gel has an insignificant effect on the color, as long as the particle gel diffusely reflects light.

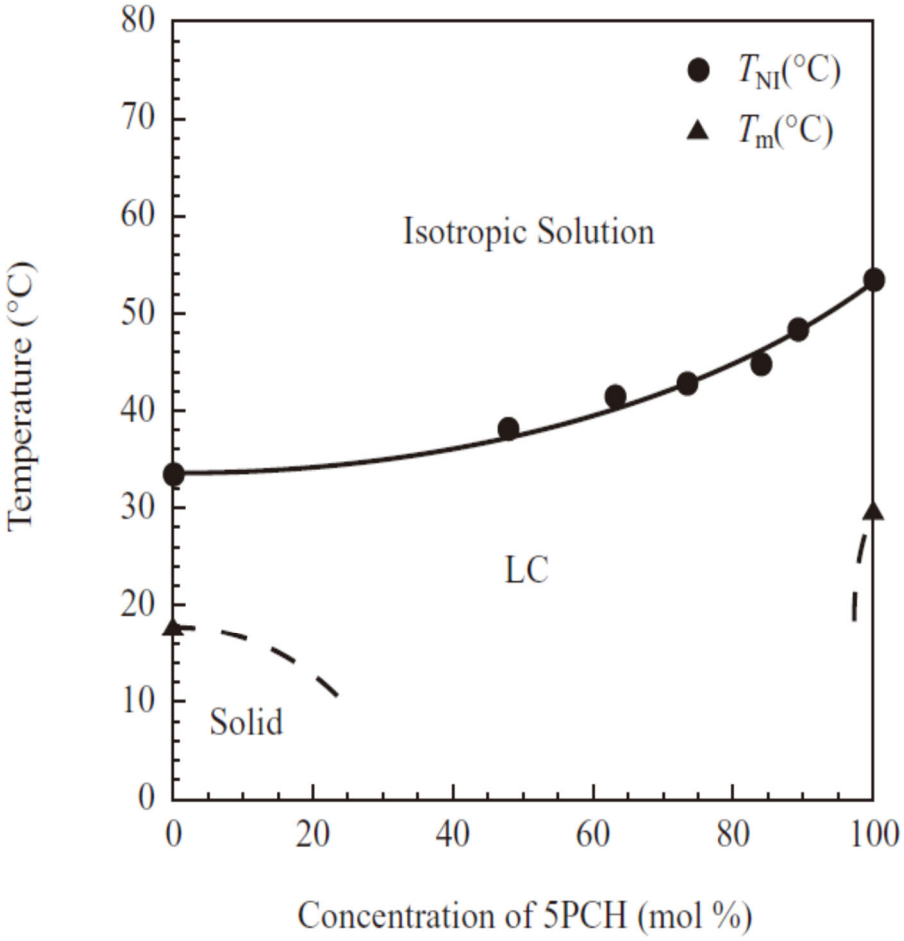

Figure 6. Phase diagram of the 5CB and 5PCH mixture.

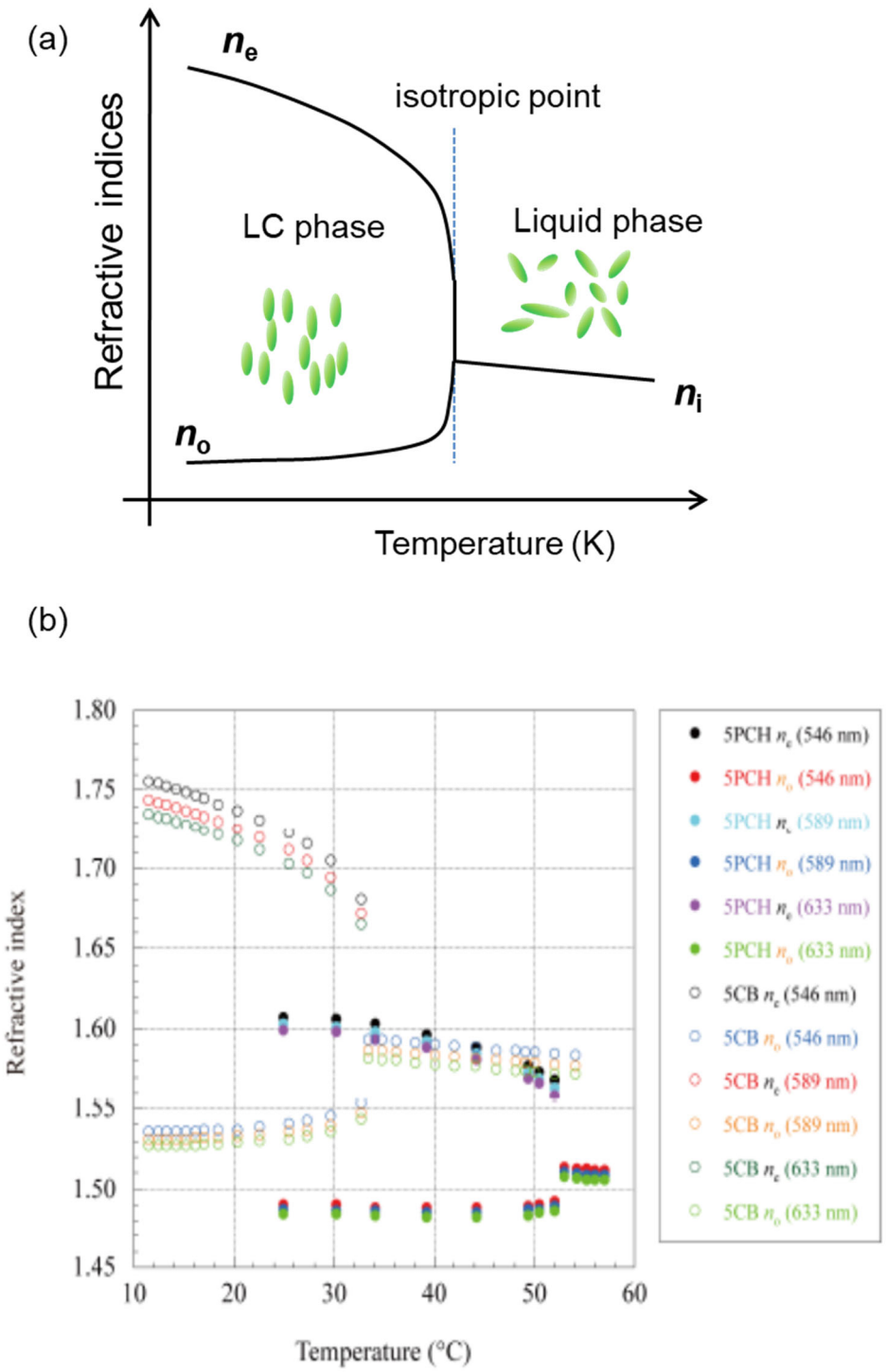

Figure 7. (a) Conceptual scheme of the thermotropic LC. (b) Temperature dependence of refractive indices of 5CB and 5PCH measured at different wavelengths. The numeric data are quoted from Reference 29. In the right box, n_e and n_o are refractive indices for the extraordinary ray and the ordinary ray, respectively.

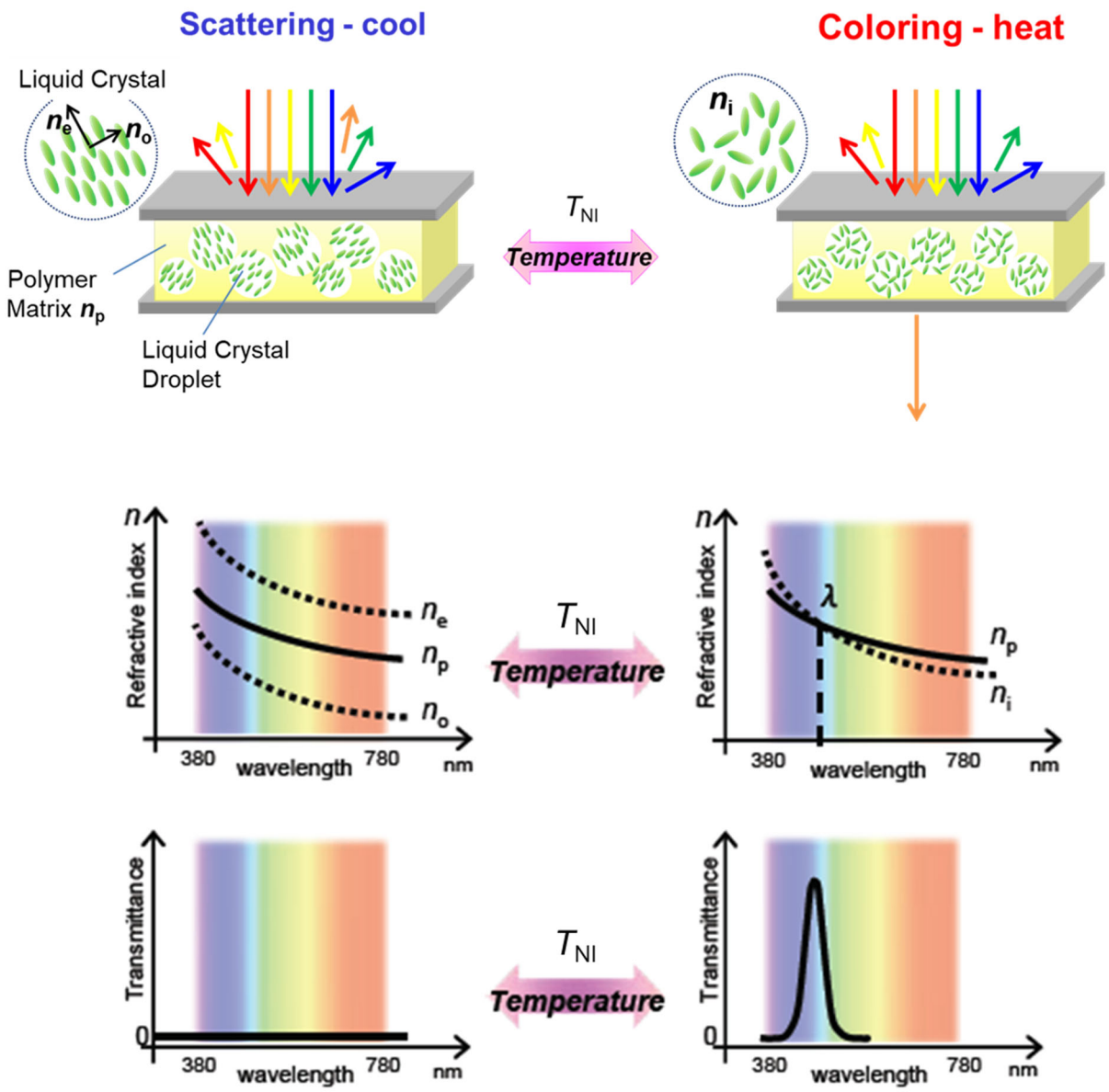

Figure 8. Conceptual scheme of the multi-colour PDLC. n_e and n_o are refractive indices for the extraordinary ray and the ordinary ray for the LC, respectively. n_i and n_p are the refractive indices for the isotropic states of the LC and polymer matrix, respectively.

Figure 9a shows transmission spectrum of the MMAA–BIS particle gel network filled with the LC mixture (73% of 5PCH) at different temperatures. The T_{NI} of this LC mixture is 42 °C. At 27 and 33 °C, where the LC mixture is in a nematic state, the composite film blocks the transmission of visible light. Thus, the composite film is opaque. In contrast, above T_{NI}, a certain peak is observed in each transmission spectrum at different temperatures. In addition, the peak position is shifted to a shorter wavelength with increasing temperature, caused by the change in the intersection point of the dispersion curves. Accordingly, the composite film reveals a reversible variation in the coloration with temperature (Figure 9b). If the composition of the LC mixture is changed, the temperature variation of the color is also changed (Figure 9c–f). Thus, I can build a tailored tunable multicolor PDLC using this procedure (Figure 9g). In addition, the coloration of this system may be controllable by an electric field due to the sensitivity of the LC to electric fields. I am currently studying an electrically tunable multicolor display using the same system.

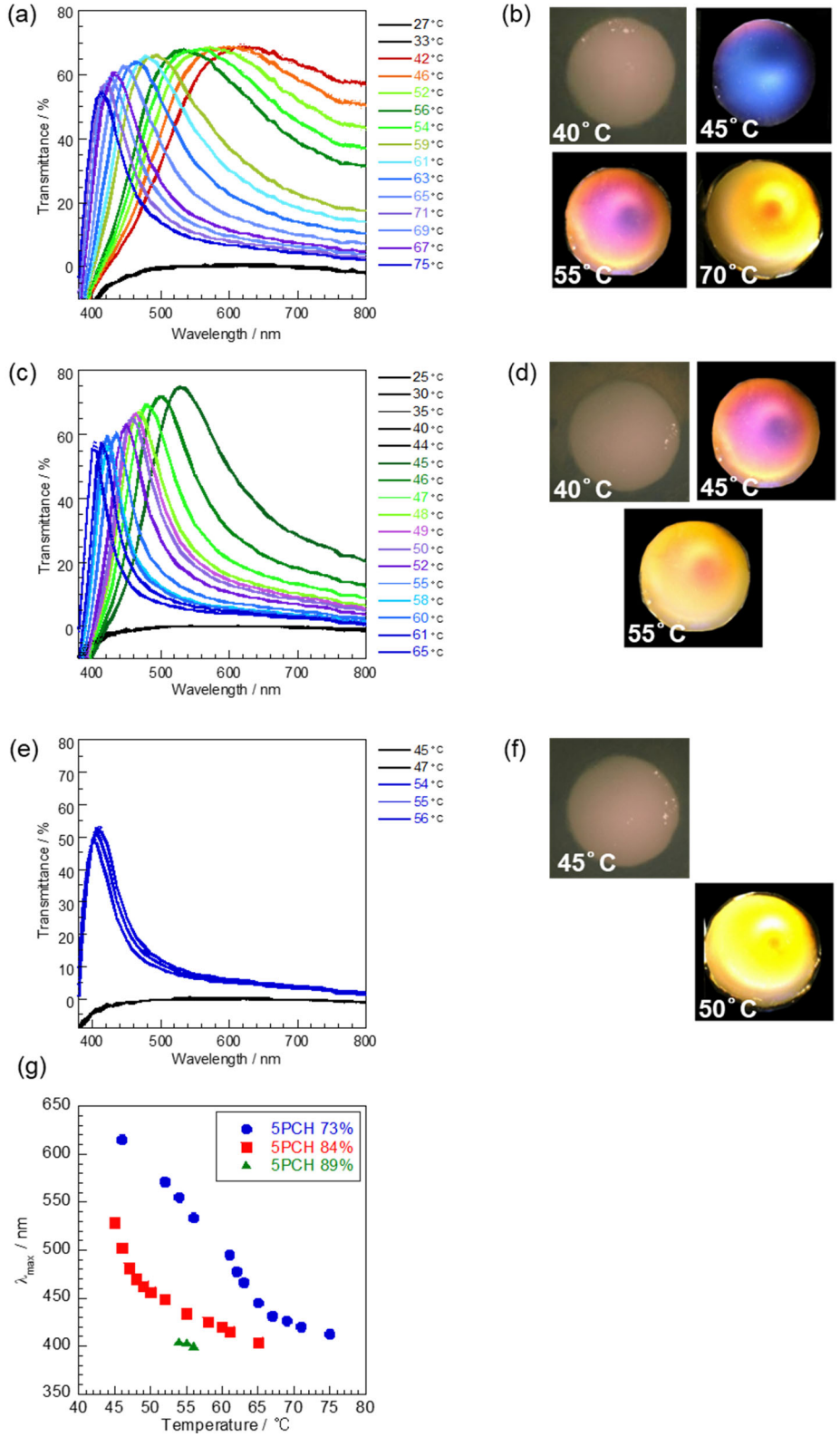

Figure 9. Temperature dependence of the transmission spectra of the MMAA-BIS particle gel network filled with LC mixtures and optical photographs:
(a),(b): 73% 5PCH; (c),(d): 84% 5PCH; and, (e),(f):89% 5PCH. (g) Temperature dependence of λ_{max} of the transmission spectra in (a), (c), and (e).

3.4 Conclusion

Our findings demonstrate that a MMAA–BIS particle gel network filled with mixed LCs of 5CB and 5PCH can exhibit changes in color covering the whole visible region and an opaque milky color upon temperature variation. In contrast to previously studied photonic band gap materials, this system is easy to prepare as a large-sized display due to its facile one-pot preparation method and its mechanism of coloration. Because this composite film displays low angle-dependent color and can act as a multicolor PDLC, I believe that this system may be available for energy saving multicolor displays.

References

[1] J. W. Doane, N. A. Vaz, B. G. Wu, S. Zumer, *Appl. Phys. Lett.* **1986**, 48, 269.

[2] J. W. Doane, A. Golemme, J. L. West, J. B. Whitehead, B. G. Wu, *Mol. Cryst. Liq. Cryst.* **1988**, 165, 511.

[3] D. Dutta, H. Fruitwala, A. Kohli, R. A. Weiss, *Polym. Eng. Sci.* **1990**, 30, 1005.

[4] T. Kato, N. Mizoshita, K. Kishimoto, *Angew. Chem. Int. Ed.* **2006**, 45, 38.

[5] R. L. Sutherland, V. P. Tondiglia, L. V. Natarajan, T. J. Bunning, W. W. Adams, *Appl. Phys. Lett.* **1994**, 64, 1074.

[6] V. Vorflusev, S. Kumar, *Science* **1999**, 283, 1903.

[7] C. Adachi, T. Tsutsui, S. Saito, *Appl. Phys. Lett.* **1989**, 55, 1489.

[8] J. Kido, M. Kimura, K. Nagai, *Science* **1995**, 267, 1332.

[9] S. Kinoshita, S. Yoshioka, *ChemPhysChem* **2005**, 6, 1442.

[10] O. Sato, S. Kubo, Z. Z. Gu, *Acc. Chem. Res.* **2009**, 42, 1.

[11] K. Ueno, K. Matsubara, M. Watanabe, Y. Takeoka, *Adv. Mater.* **2007**, 19, 2807.

[12] A. C. Arsenault, D. P. Puzzo, I. Manners, G. A. Ozin, *Nat. Photonics* **2007**, 1, 468.

[13] Y. J. Lu, H. W. Xia, G. Z. Zhang, C. Wu, *J. Mater. Chem.* **2009**, 19, 5952.

[14] J. J. Walish, Y. Kang, R. A. Mickiewicz, E. L. Thomas, *Adv. Mater.* **2009**, 21, 3078.

[15] Y. Takeoka, M. Honda, T. Seki, M. Ishii, H. Nakamura, *ACS Appl. Mater. Interfaces* **2009**, 1, 982.

[16] M. Harun-Ur-Rashid, A. Bin Imran, T. Seki, M. Ishii, H. Nakamura, Y. Takeoka, *ChemPhysChem* **2010**, 11, 579.

[17] N. Kumano, T. Seki, M. Ishii, H. Nakamura, Y. Takeoka, *Angew. Chem. Int. Ed.* **2011**, 50, 4012 –4015.

[18] Q. C. Wang, F. Svec, J. M. J. Frechet, *Anal. Chem.* **1993**, 65, 2243.

[19] Q. C. Wang, F. Svec, J. M. J. Frechet, *J Chromatogr. A* **1994**, 669, 230.

[20] F. Svec, J. M. J. Frechet, *Science* **1996**, 273, 205.

[21] Y. Ueki, T. Umemura, J. X. Li, T. Odake, K. Tsunoda, *Anal. Chem.* **2004**, 76, 7007.

[22] S. Yamago, *Chem. Rev.* **2009**, 109, 5051.

[23] E. R. Dufresne, H. Noh, V. Saranathan, S. G. J. Mochrie, H. Cao, R. O. Prum, *Soft Matter* **2009**, 5, 1792.

[24] J. C. Stover, *Optical Scattering: Measurement and Analysis,* SPIE Optical Engineering Press **1995**.

[25] G. C. Crossmon, *Anal. Chem.* **1948**, 20, 976.

[26] S. Edo, K. Okoshi, S. Kang, M. Tokita, T. Kaneko, J. Watanabe, *Langmuir* **2010**, 26, 1743.

[27] N. J. Goddard, A. E. Maturell, *Appl. Opt.* **1995**, 34, 7318.

[28] L.-C. Khoo, S.-T. Wu, *Optics and Nonlinear Optics of Liquid Crystals*, World Scientific Publishing Co. Pte. Ltd. **1993**.

[29] J. Li, C. H. Wen, S. Gauza, R. B. Lu, S. T. Wu, *J. Display Technol.* **2005**, 1, 51.

[30] J. Li, S. Gauza, S. T. Wu, *J. Appl. Phys.* **2004**, 96, 19.

Chapter 4

Preparation of Interference Pigment Using Black Graphite Nanosheet

4.1 Introduction

Several companies are investigating new alternatives to traditional pigments that contain heavy metals, which may be toxic, and to dyes that fade easily under extended exposure to UV light. Structurally colored materials that are nonfading and nontoxic have the potential for widespread adoption in applications such as paints, inks, textiles, cosmetics, sensors, and displays. The color of structurally colored materials originates from their microstructure, which has a length scale comparable to the desired optical wavelength, resulting in optical effects such as interference, refraction, or diffraction of light. Artificial structurally colored materials have been developed, including colloidal crystals, amorphous colloidal arrays, and pearl pigments. Colloidal crystals and amorphous colloidal arrays with a periodicity on the scale of one-half the wavelength of visible light exhibit structural color by reflecting only light of a specific wavelength on a film [1]. Pearl pigments are transparent flaky substrates coated with a film of metal oxide. Pearl pigments aligned parallel on the surface of a coating film demonstrate a natural pearl-like design by exhibiting an interference color corresponding to the thickness of the metal oxide film [2, 3]. However, these structural materials composed of transparent or white materials exhibit weak structural colors because of light scattering, which results in a milky-white appearance that may be difficult to distinguish by the naked eye under certain lighting conditions [4].

Animals with vivid colors may provide a hint toward a possible solution to the aforementioned issue. For example, the brilliant structural colors of peacocks and Morpho butterflies originate from black melanin granules that contribute to the absorption of transmitted light and to the reduction of background light, resulting in enhanced colors [5, 6]. This effect can be mimicked by various structurally colored materials. Structurally colored materials with enhanced colors have been developed, including colloidal crystals, amorphous colloidal arrays containing carbon materials [7, 8], black materials prepared by calcination [9, 10], polydopamine [4, 11-13], and synthetic melanin nanoparticles [14]. Similarly, an interference pigment with a black material used as a substrate or interference layer is known to block light of other wavelengths by diffuse reflectance, resulting in high-saturation pigments with greater interference color than conventional pearl pigments (Figure 1). Other authors have reported interference pigments with black materials such as black iron oxide-coated mica [15], titanium oxide/reduced titanium oxide-coated mica [16, 17], titanium oxide/ilmenite-coated mica [18], and titanium oxide-coated mica containing carbon black [19].

These pigments exhibit color that changes with the viewing angle because the optical path difference depends on the angle of incidence of the light. For automotive and other consumer markets, pigments that produce a color that depends on the viewing angle are widely used because the color change accentuates the shading of a 3D shape. However, this effect may not be desirable for optical devices, labels, inks, and sensors because of the different colors observed at different viewing angles.

To overcome the aforementioned issue, our objective was to achieve enhanced colored materials with angle independence using black interference pigments. I demonstrate a new pigment prepared using graphite nanosheets (GNSs), which are a novel black flaky material, as a substrate for enhanced interference coloration. GNSs are obtained by wet pulverization of graphite into flakes [20]. GNSs have a particle length of several micrometers and a sheet thickness of several tens of nanometers, making them a thinner and smaller substrate than conventional black pigments, which have a particle size on the order of several tens of micrometers and a thickness of several hundred nanometers. The pigments with small particle sizes tend to have a more random orientation than the pigments with large particle sizes [21]. As previously mentioned, angle-dependent color changes of an interference pigment can be achieved when the interference pigment orientates parallel to the surface in a coating film because the light path length differences for the light interference change depending upon the viewing angle. However, the resultant color from a coating film with a random orientation of interference pigment would be almost angle-independent because of the additive sum of colors resulting from the random orientation of pigment particles with different sides oriented toward the observer [3]. Thus, GNSs are expected to result in pigments that are independent of viewing angle because the small pigment particles are randomly oriented.

Herein, I demonstrate for the first time that GNSs with good dispersibility in water can be prepared using a mild oxidation agent and a polymer dispersant. The mild oxidation agent intercalates between carbon layers and induces cleavage while oxidizing the surfaces of the layers, with little destruction of the graphite structure in the c-axis direction. Simultaneously, the polymer dispersant intercalates between the cleaved carbon layers to stabilize the cleavage surfaces, thus promoting interlayer exfoliation. To the best of our knowledge, our preparation method for GNSs is easier than previously published methods. I also demonstrate that a pigment that exhibits interference color can be prepared by sol–gel synthesis of a TiO_2 layer on GNSs and that a

multicolor pigment can be prepared by controlling the thickness of the interference layer.

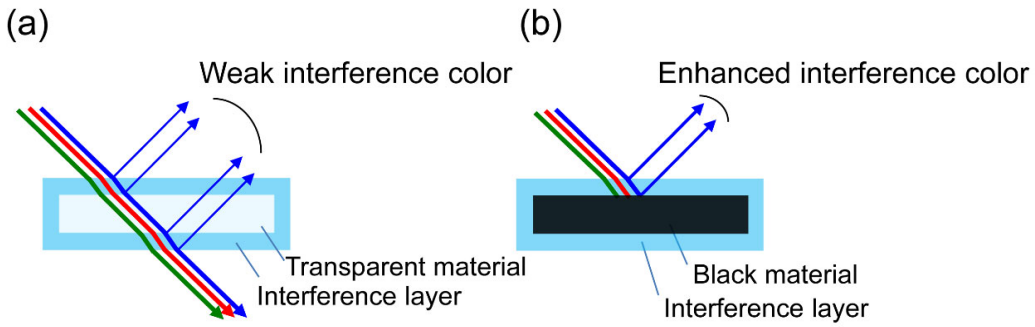

Figure 1. Difference in interference colors depending on substrate color: (a) transparent substrate (e.g., mica) and (b) black substrate (e.g., graphite).

4.2 Materials and Methods

A schematic of the procedure for the synthesis of the GNS pigment is shown in Figure 2. Instead of using fuming nitric acid or the detonation technique conventionally used to exfoliate GNSs [22-24], I used a hydrogen peroxide–urea complex as a milder oxidizing agent to refine the graphite while maintaining its sheet structure. Hydrophobic GNSs capable of being well-dispersed in hydrophobic solvents were prepared using poly(styrene-co-2-vinylpyridine) (poly(ST-2VP)) as a dispersant. Hydrophilic GNSs were prepared by adding an anionic polymer dispersant that interacted with the pyridine groups of poly(ST-2VP) to increase the surface charge. The GNS pigment was obtained via a sol–gel process.

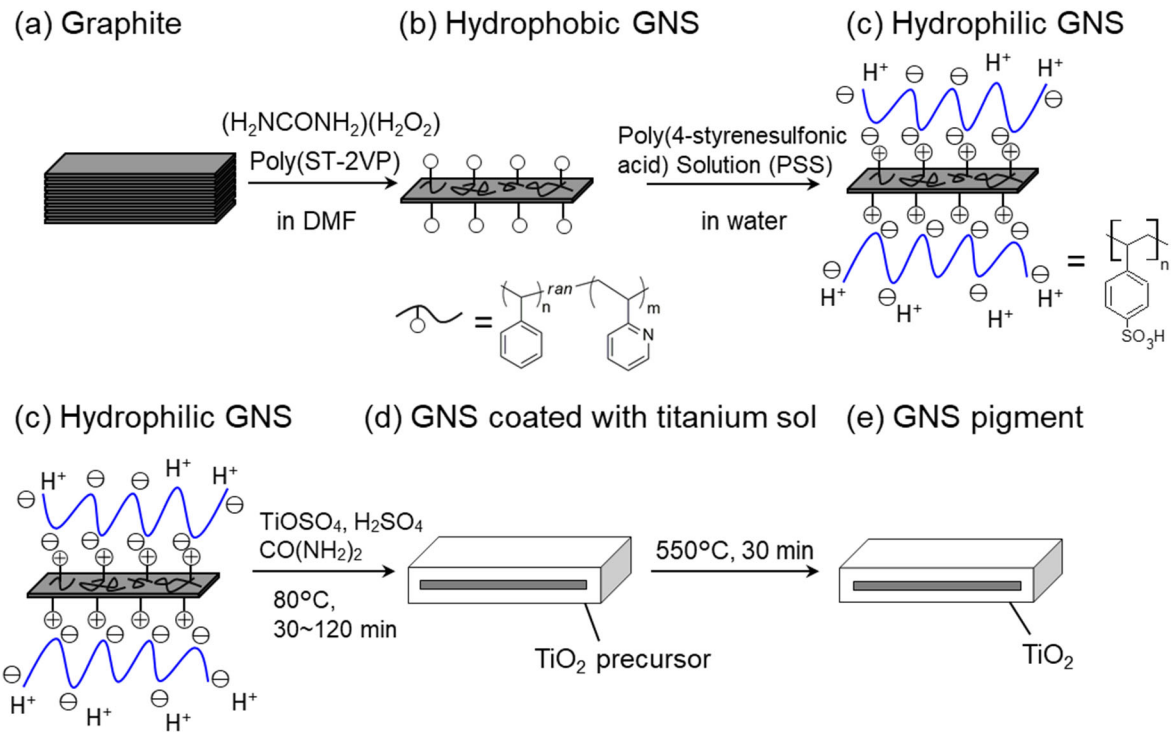

Figure 2. Synthesis scheme of the GNS pigment.

4.2.1 Preparation

4.2.1.1 Preparation of the hydrophobic polymer dispersant (poly(ST-2VP))

Poly(ST-2VP) was synthesized by free-radical polymerization in 100 mL of toluene under a N_2 atmosphere using 50 mg of 2,2'-azodiisobutyronitrile as an initiator, and 18 g of styrene (ST) and 2 g of 2-vinylpyridine (2VP) as monomers. The reaction was conducted for 6 h at 85°C. The obtained poly(ST-2VP) was purified by reprecipitation from chloroform as a good solvent and hexane as a poor solvent, and then vacuum-dried overnight. The polymer dispersant poly(ST-2VP) (Scheme 1)

was analyzed as follows. The composition of poly(ST-2VP) was estimated by ^{1}H-NMR spectroscopy (JEOL, JNM-ECX400P, 400 MHz) at room temperature. $CDCl_3$ was used as a solvent. The number-average molecular weight (M_n) of poly(ST-2VP) was estimated by gel-permeation chromatography (GPC) equipped with a multiangle light-scattering detector (GPC-MALLS/Shodex GPC-101; column: K-805L; detector: differential refractometer) and converted using calibration curves for standard polystyrene samples. $CHCl_3$ was used as an eluent to adjust the concentration to 0.1 mg/mL.

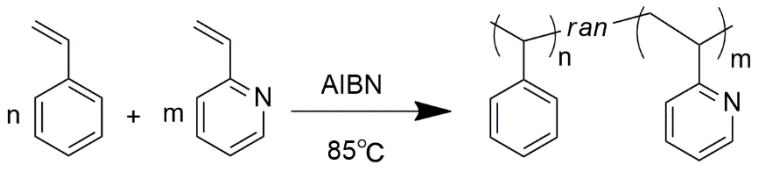

Scheme 1. Synthesis of poly(ST-2VP) via free-radical polymerization

4.2.1.2 Preparation of hydrophobic GNSs

Graphite (12.5 g; Nippon Graphite Ind., EXP-P), 12.5 g of hydrogen peroxide–urea complex (Sigma-Aldrich), 1.25 g of poly(ST-2VP), and 500 mL of dimethylformamide (DMF) were mixed and then processed with a wet pulverizing and dispersing device (Sugino, Star Burst, oblique-type collision chamber) at a pressure of 200 MPa for 10 passes. The resultant dispersion was filtered, washed with DMF, and then vacuum-dried to obtain hydrophobic GNSs.

4.2.1.3 Preparation of hydrophilic GNSs

Hydrophobic GNS particles (10 g) and 500 mL of water were mixed, and the pH was adjusted to 1 or less with 4.3 g of poly(4-styrenesulfonic acid) (PSS) solution (Wako Pure Chemical) as the mixture was subjected to ultrasonic dispersion for 1 h. The dispersion was then filtered, washed with water, and filtered again to obtain a hydrophilic GNS whose surface was modified with a hydrophilic polymer dispersant.

4.2.2 Characterization of GNSs

The elemental content of the GNS surface was examined by X-ray photoelectron spectroscopy (XPS; ULVAC PHI, Quantera SXM) with Al Kα radiation using an analyzer at a pass energy of 26

eV with 0.1 eV energy resolution. The energy shift due to charging was corrected by setting the C 1s binding energy to 284.5 eV. To quantify defects, Raman spectra were recorded at 532 nm excitation wavelength using a Raman spectrophotometer (JASCO, NRS-3300).

4.2.3 Preparation of titanium(IV) oxide-coated GNS pigment

The GNS pigment was prepared by suspending hydrophilic GNSs in a $TiOSO_4$ aqueous solution containing urea and hydrolyzing them with heat, resulting in the formation of a TiO_2 precursor on the GNSs. This method has been suggested to suppress rapid precipitation during the coating process [25]. In the hydrolysis of $TiOSO_4$, sulfuric acid is generated in the reaction (Equation 1). In a $TiOSO_4$ aqueous solution with urea, the urea is decomposed at elevated temperatures, generating NH_4^+ (Equation 2), thereby neutralizing sulfuric acid generated in the reaction and avoiding rapid precipitation. In the present study, I examined whether the interference layer could be formed on the substrate by hydrolysis of $TiOSO_4$ via a reaction controlled using urea:

$$TiOSO_4 + 2H_2O \longrightarrow TiO(OH)_2 + H_2SO_4 \quad (1)$$

$$OC(NH_2)_2 + H^+ + 2H_2O \longrightarrow HCO_3^- + 2NH_4^+ \quad (2)$$

GNSs (0.5 g) were dispersed in 25 mL of deionized water. H_2SO_4 (FUJIFILM Wako Pure Chemical, precision analysis grade), urea (FUJIFILM Wako Pure Chemical, reagent special grade), and $TiOSO_4$ aqueous solution were added to the dispersion. The resultant suspension was heated at 80°C with stirring. The $TiOSO_4$ aqueous solution was obtained by diluting titanium(IV) oxysulfate–sulfuric acid hydrate (Sigma-Aldrich) with water and leaving it for 2 h to completely dissolve the solid. Table 1 shows the concentrations of the H_2SO_4, urea, and $TiOSO_4$ aqueous dispersion. The GNSs were collected in small amounts (~0.1 g of dry weight) every 10–15 min starting from the initiation of the process; the samples were suction-filtrated and washed with deionized water and 1 mol/L NaOH aqueous solution. The obtained GNS pigment was dried for 15 h at 80°C. The GNS pigment was fired at 550°C in air for 30 min using a tubular furnace (Asahi Rika, ARF-50 K 700 W) to obtain TiO_2-coated GNSs.

Table 1. Experimental conditions for a hydrous titanium oxide coating in hydrolysis of $TiOSO_4$

No.	$TiOSO_4$ (mol/L)	H_2SO_4 (mol/L)	$CO(NH_2)_2$ (mol/L)	Temperature (°C)	Time (min)
1	0.44	0.05	0.1	80	30
2	0.44	0.05	0.1	80	45
3	0.44	0.05	0.1	80	50
4	0.44	0.05	0.1	80	60
5	0.44	0.05	0.1	80	120

4.2.4 Characterization of GNS pigment

The obtained GNS pigment was observed by scanning electron microscopy (SEM). SEM observations were performed using a Hitachi SU3500 operated at an acceleration voltage of 15.0 kV. The crystal phase of TiO_2 was identified by X-ray diffraction (XRD, RINT2000, Rigaku) using Cu-Kα (λ = 1.542 Å) radiation. The 2θ measurement range was 10° to 90°, and the tube voltage and current were 40 V and 30 mA, respectively.

4.2.5 Characterization of coating film containing GNS pigment

Acrylic polyol was synthesized by free-radical polymerization in 104 g of methyl isobutyl ketone under a N_2 atmosphere, using 33 g of tert-butyl peroxy-2-ethylhexanoate (Nippon Oil & Fats Co., Ltd., PERCURE® O) as an initiator and acrylic monomers (Table 2). The reaction was conducted for 6 h at 110°C. Acrylic polyol with a hydroxyl content of 178 mg KOH/g was obtained. The acrylic polyol exhibited M_n = 6400 and M_w/M_n = 1.9, as determined by GPC. To obtain acrylic urethane paint, 26 g of acrylic polyol and 10 g of 1,6-hexamethylene diisocyanate (Asahi Kasei Chemicals Corp., Duranate™ TPA-100, NCO content of 23%) as a curing agent were mixed just prior to application. Toluene was added to reduce the viscosity. The isocyanate curing agent was reacted with the acrylic polyol in a ratio of 1.0 isocyanate groups per hydroxyl group.

The GNS pigment was blended with acrylic urethane paint. The GNS pigment represented 5 wt% of the solid content of the entire paint. Coating films were prepared by pouring acrylic urethane paint in the chamber slide as a mold and subsequently left at room temperature for 24 h, and then cured at 140°C for 30 min. The dry thickness was adjusted to be 100-150 μm. Visual observation

and recording of the reflection spectrum were carried out from the glass side. UV–vis spectra were acquired with a UV–vis spectrophotometer (Shimadzu, UV-3600 with an integrating sphere attachment) to measure the diffuse-reflection component without specular reflection. Barium sulfate was used as the reference plate.

Cross-sectional specimens of coating films were prepared using a focused ion beam (FIB, Hitachi High-Technologies Corp., NB500) system. The fabrication process consisted of two stages: rough milling with a Ga^{+}-ion beam generated at an accelerating voltage of 40 kV and with a beam-limiting aperture size of 300 μm for 2 h, followed by fine-finish milling using a beam-limiting aperture size of 150 μm for 30 min. Cross-sections were observed by field-emission scanning electron microscopy (FE-SEM, Hitachi High-Technologies Corp., Regulus 8230). The size of the hydrophilic GNS and the thickness of TiO_2 were measured using the open-source image processing program ImageJ [26]

Table 2. Sample specifications of acrylic polyol

Monomer	g
Methyl methacrylate	37.6
2-Hydroxyethyl methacrylate	53.1
Caprolactone modified methacrylate*	41.3
Styrene	33.0

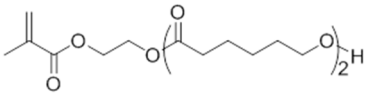

caprolactone modified methacrylate*

4.3 Results and Discussion

4.3.1 Characterization of hydrophobic polymer dispersants

The yield of poly(ST-2VP), which was obtained as a white solid, was 16.5%. Figure 3 shows the ^{1}H-NMR spectrum. The ST:2VP ratio was calculated as 6.7:1 from the number of protons of the side chain, as determined from the 1H-NMR spectrum. The M_n of poly(ST-2VP) was 89,000, as determined by GPC. From these results, the degree of polymerization of ST and 2VP was found to be 737 and 110, respectively.

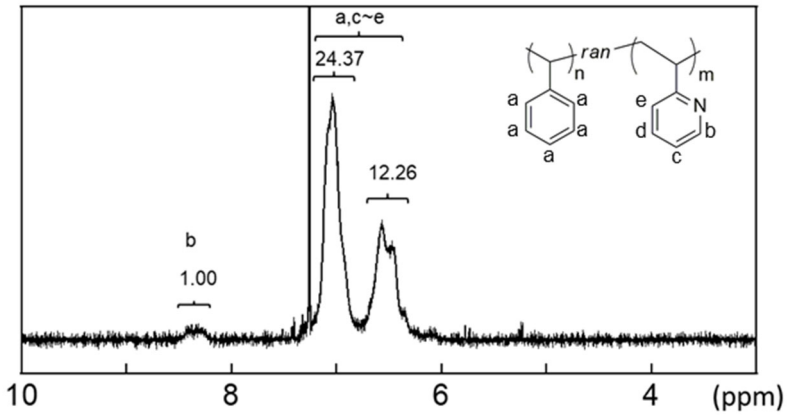

Figure 3. ^{1}H-NMR spectrum of poly(ST-2VP).

4.3.2 Characterization of hydrophobic GNS and hydrophilic GNS

Raman spectra were recorded to evaluate the amount of defects introduced into the graphite particles in the dispersion prepared by the hydrogen peroxide–urea method. Figure 4 shows the Raman spectrum of raw-material graphite particles, hydrophobic GNSs, and hydrophilic GNSs. A small D-band (in the region 1270–1450 cm^{-1}), sharp G-band (~1579 cm^{-1}), and a 2D-band comprising two components, 2D1 and 2D2 (~2700 cm^{-1}), were observed in the spectra of all of the samples. The sharp G-band peak is the stretching vibration of sp2 carbon. The intensity ratio (I_D/I_G) of the hydrophobic and hydrophilic GNSs (I_D/I_G = 0.08) is only slightly greater than that of graphite (I_D/I_G = 0.03), indicating that few defects were induced by damage during exfoliation. Moreover, neither the shape of the 2D band, the G-band peak position, nor the intensity ratio (I_D/I_G), which can be used to determine the number of graphene layers in GNSs [27, 28], substantially changed after exfoliation. This result suggests that the number of graphene layers in the GNSs might be greater than 20 [28].

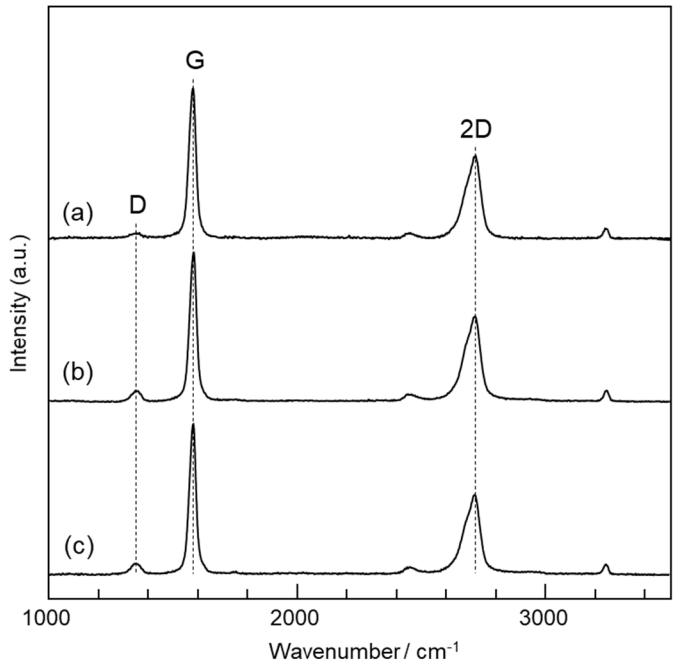

Figure 4. Raman spectra: (a) graphite, (b) hydrophobic GNSs, and (c) hydrophilic GNSs.

The concentrations of C, O, and S elements of the graphite and GNS surfaces were measured by XPS. Figure 5 shows raw data sets of high-resolution XPS spectra. Table 3 summarizes the fractions of carbon, oxygen, and sulfur derived from the evaluation of the C 1s, O 1s, and S 1s peaks. When the raw-material graphite particles were treated only with a hydrogen peroxide–urea complex in the absence of poly(ST-2VP), the amount of oxygen increased from 1.9 to 3.0 at. %, which indicates that the surface was oxidized by the acid treatment. However, when the raw-material graphite particles were treated with the hydrogen peroxide–urea complex in the presence of poly(ST-2VP), the O content decreased from 1.9 to 1.6 at. %, which indicates that poly(ST-2VP) was adsorbed onto the surface, thereby covering O atoms in the surface of hydrophobic GNS with poly(ST-2VP). A possible mechanism is explained as follows. The hydrophobic surface of pristine graphite interacts with the PS part via a hydrophobic–hydrophobic mechanism. A hydrophilic surface containing OH and COOH groups as a result of exposure to an oxidation agent during the dispersion process exhibits good affinity with the pyridine moiety. Thus, poly(ST-2VP) was adsorbed onto the GNS surface. In hydrophilic GNSs, the amount of O increased from 1.6 to 1.8 at. %, and S atoms were also observed, which indicates that PSS was

adsorbed onto the hydrophilic GNS. This thesis deals with synthesis of highly-designed functional periodic mesoporous organosilicas (PMOs) and their applications.

Table 3. Carbon and oxygen content of GNS surface analyzed by XPS (at. %)

at. %	C	O	S
Graphite	98.0	1.9	—
Graphite with hydrogen peroxide–urea complex without poly(ST-2VP)	97.0	3.0	—
Hydrophobic GNSs	98.4	1.6	—
Hydrophilic GNSs	98.1	1.8	0.1

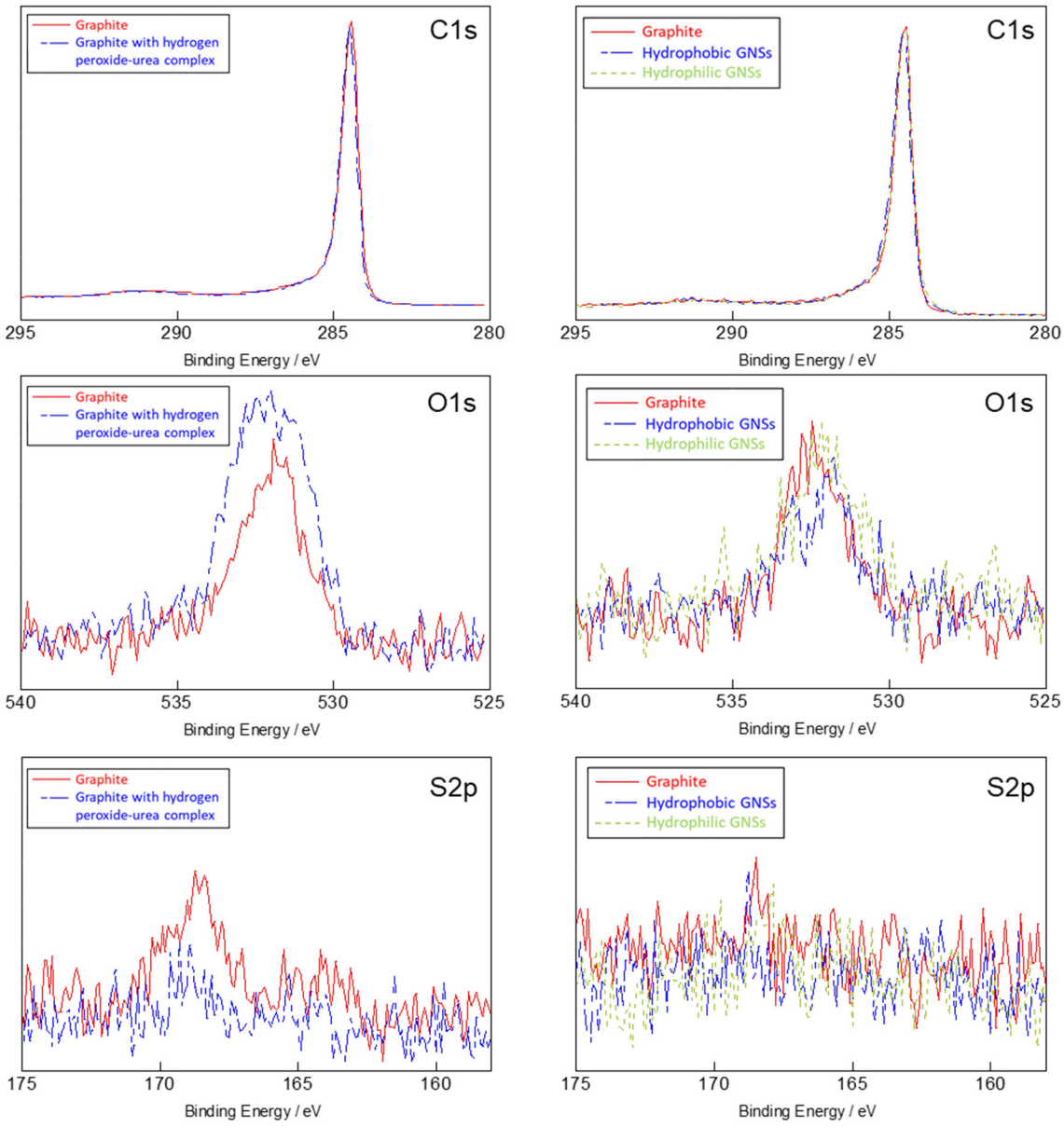

Figure 5. High-resolution XPS spectra from which the data in Table 2 were extracted.

Figure 6 shows the corresponding SEM images. As shown in Figure 6(a), raw-material graphite particles were sphere-like, with a diameter greater than 100 μm. The hydrophobic GNSs and hydrophilic GNSs were plate-like, with lengths of 1 to 7 μm and smooth surfaces (Figure 6(b) and 6(c)). No difference in size was observed between the hydrophobic and hydrophilic GNSs. Hydrophobic and hydrophilic GNSs dispersed in various solvents are shown in Figure 7, which demonstrates the dispersibility of the GNSs. The hydrophobic GNSs were dispersed in a solvent such as acetone, hexane, ethanol, or toluene but could not be dispersed in water. These results indicate that hydrophobic GNS particles agglomerate when water is added because of the hydrophobic poly(ST-2VP) adsorbed onto the surface of the hydrophobic GNSs. By contrast, the hydrophilic GNSs could be dispersed in water. These results indicate that the PSS was adsorbed onto the GNS surface via ionic bonding using the pyridine rings of the poly(ST-2VP) as active sites to increase the surface charge. Good dispersion of the hydrophobic GNSs in water produces special optical effects. Alignment of the GNSs with their front facing the water results in the highest reflectance and a change from bright to dark as the viewing angle changes. This dependency on the angular strength of the reflected light is known as the flip-flop effect in paint, which is commonly observed with flake-shaped pigments [29, 30]. The flip-flop effect was observed in the aqueous dispersion of hydrophilic GNSs. This effect indicates that the hydrophilic GNSs were well-dispersed, with a two-dimensional (2D) structure in water.

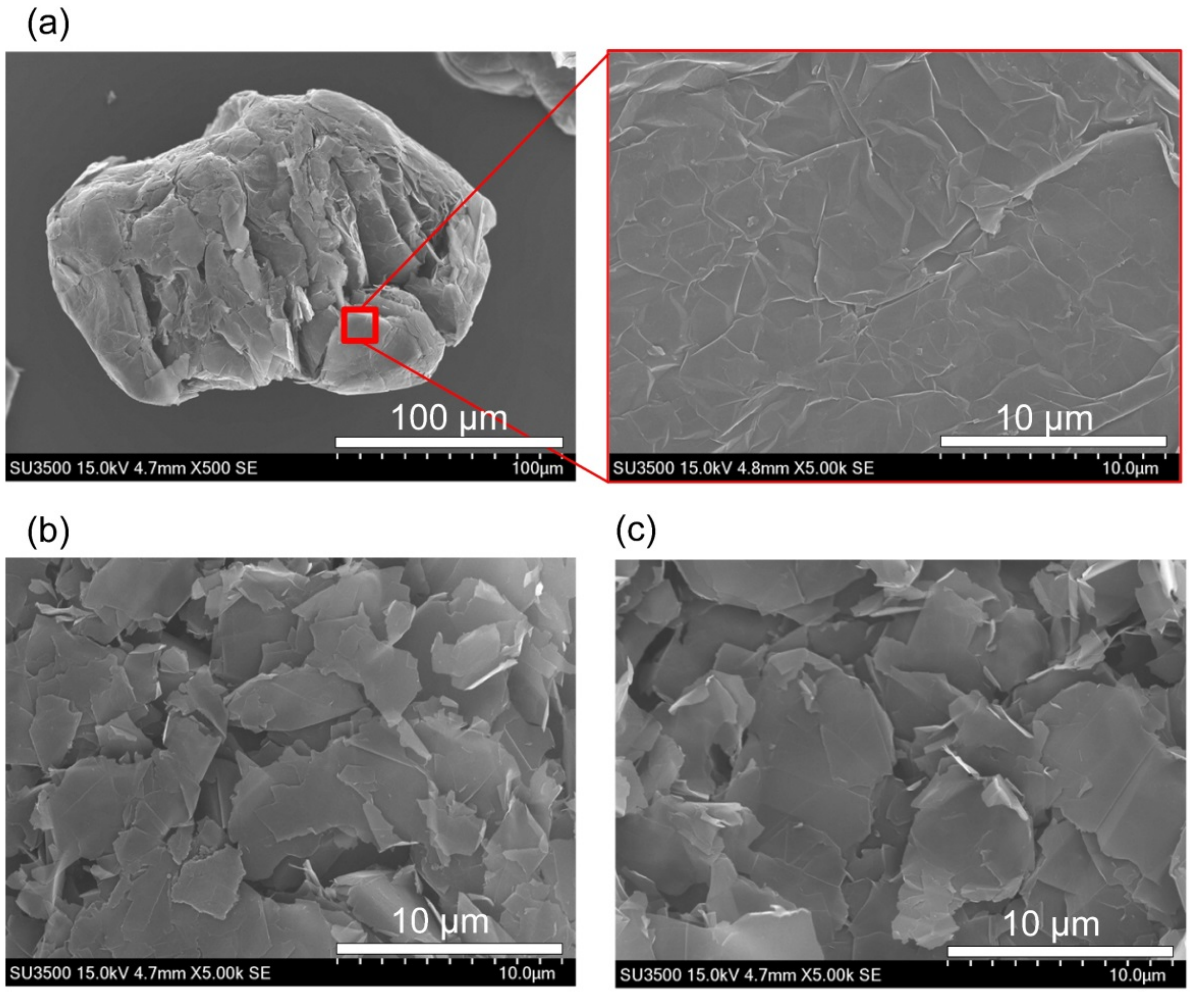

Figure 6. SEM images of GNS: (a) graphite, (b) hydrophobic GNS, and (c) hydrophilic GNS.

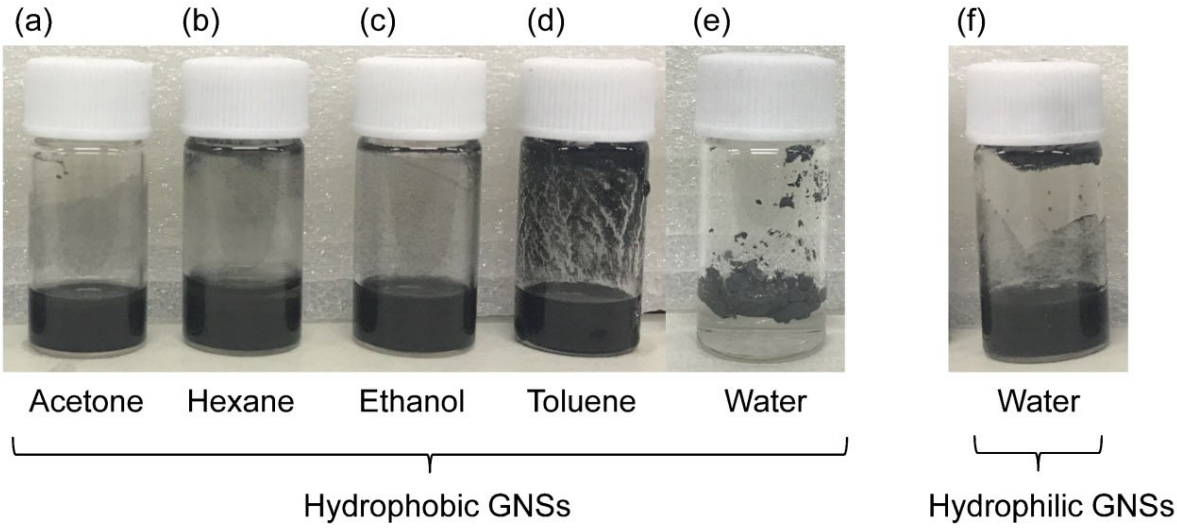

Figure 7. GNSs dispersed in various solvents: (a)–(e) hydrophobic GNSs and (f) hydrophilic GNSs.

4.3.3 Characterization of GNS pigments

The hue of the GNS pigment prepared by hydrolysis of $TiOSO_4$ changed, depending on the reaction time, to yellow, red, purple, blue, or green interference color (Figure 8(a)–(e)). This result indicates that the film thickness increased in accordance with the reaction time, causing a change in the color of the particles as a result of a change of the interference wavelength. Figure 8(f) shows SEM images of the GNS pigments. The surface of the hydrophilic GNSs was coated with a film of TiO_2; however, the film had cracks. By examining in which step the cracks formed, I found that cracks had already formed when the GNSs coated with a layer of TiO_2 precursor were dried at 80°C. This behavior is attributed to the GNSs having been modified with polymer dispersant on their surface; the polymer dispersant led to weak adhesion between the GNSs and TiO_2 precursor, which resulted in the film also shrinking in the lateral direction on the pigment surface during drying of the TiO_2 precursor.

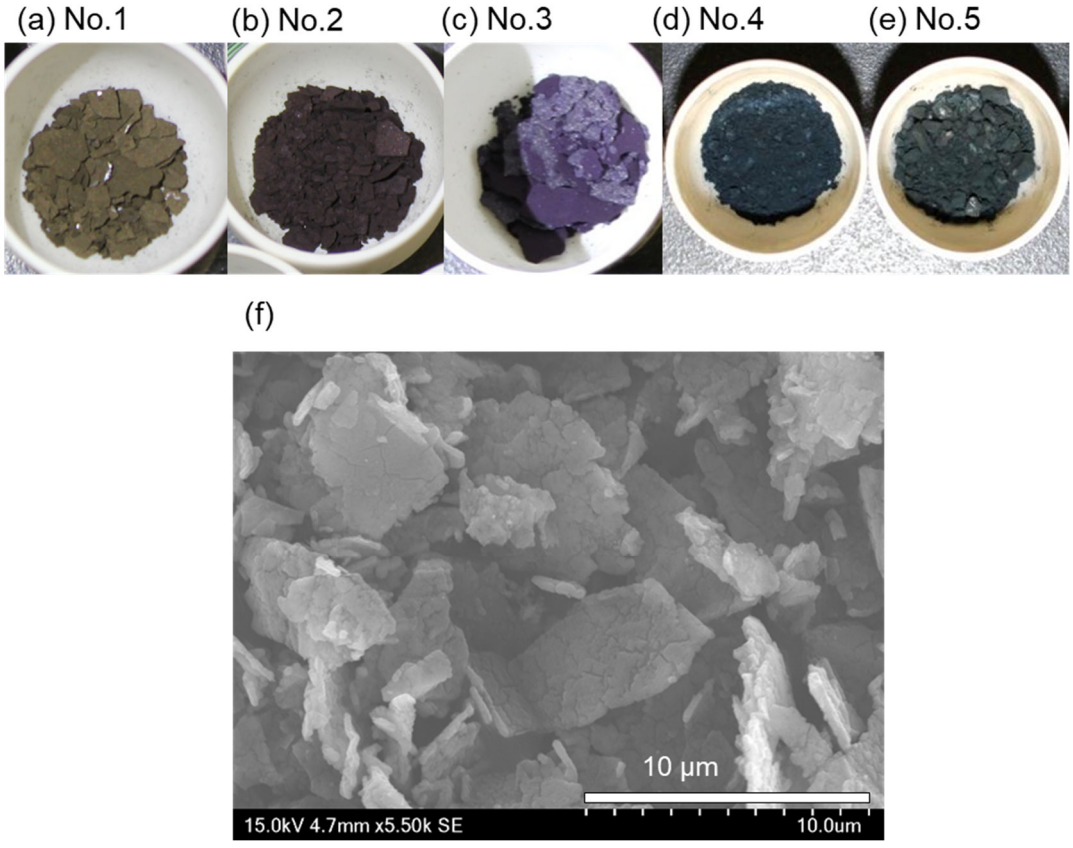

Figure 8. (a)–(e) Photographs of GNS pigments prepared using various reaction times (reaction times: (a) 30 min, (b) 45 min, (c) 50 min, (d) 60 min, and (e) 120 min). (f) SEM image of GNS pigment No. 4.

Figure 9(a, b) shows the results of the XRD analysis of hydrophilic GNSs. The 2θ peaks at 26.0°, 54.2°, and 86.8° correspond to the graphite basal planes along the c-axis: (002), (004), and (006), respectively (■ in Figure 9). 2θ peaks corresponding to other planes—(100), (101), (110), (112)—were also observed. Figure 9(c, d) shows the results of the XRD analysis of the crystal phase of TiO2 in the GNS pigments. In addition to the hydrophilic GNS peak, the 2θ peaks at 25.2°, 37.5°, 47.2°, 62.3°, and 74.7° correspond to the (101), (004), (200), (204), and (215) planes of anatase-type TiO_2, respectively (▼ in Figure 9). These peaks are attributed either to GNSs or to anatase-type TiO_2, with no other peaks observed. Therefore, the TiO_2 on the pigment was anatase-type TiO_2.

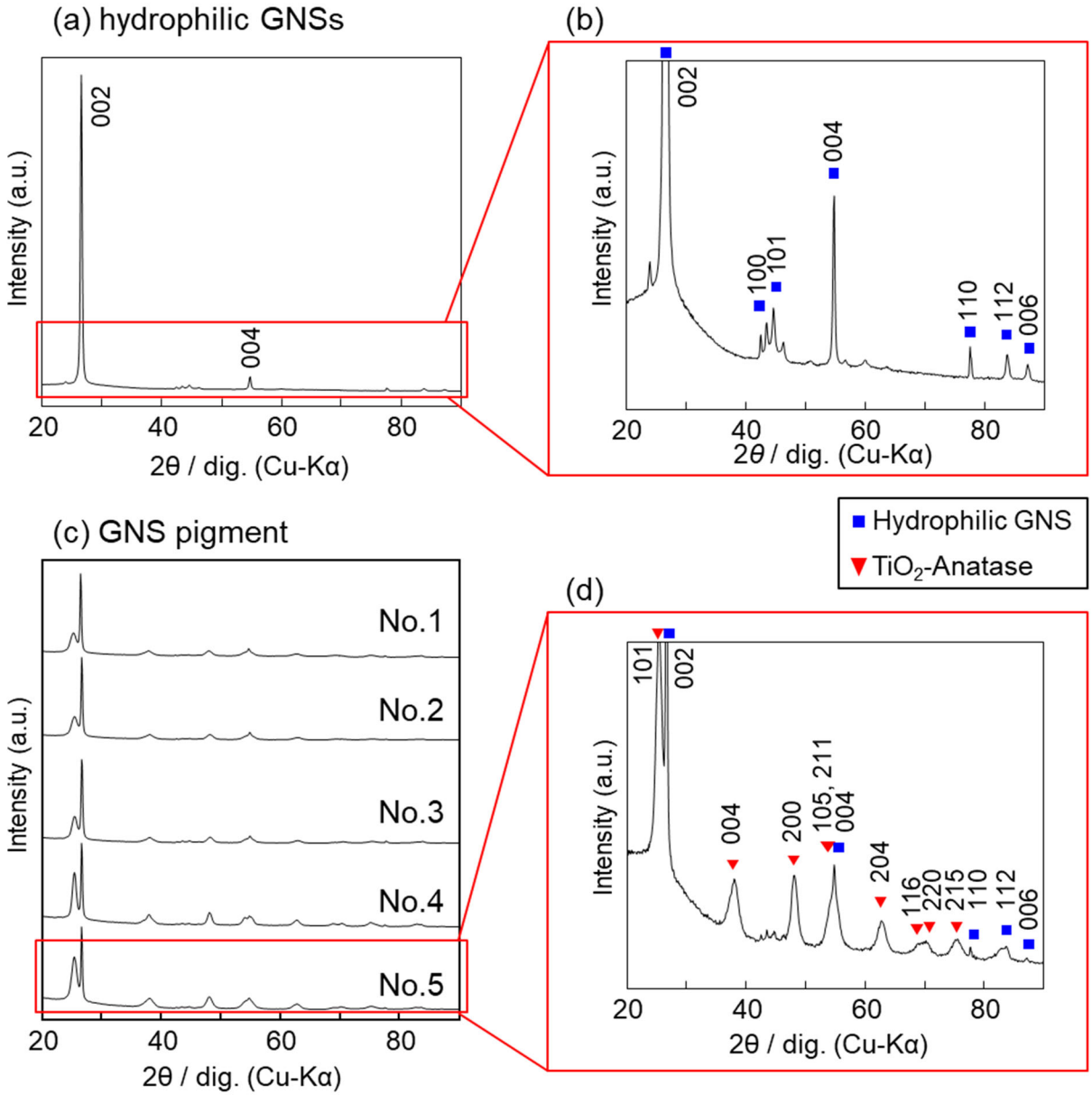

Figure 9. (a) X-ray diffraction (XRD) pattern of hydrophilic GNSs; (b) magnified image of (a). (c) XRD pattern of GNS pigments (No. 1–5); (d) magnified image of pattern No. 5.

4.3.4 Characterization of coating films containing GNS pigments

Figure 10 shows photographs and reflection spectra of coating films containing GNS pigments. The films exhibit a series of interference colors from yellow to red, purple, blue, and green. Figure 9(a)–(c) shows cross-sectional SEM images of coating film No. 2 with a red interference color, No. 4 with a blue interference color, and No. 5 with a green interference color. The hydrophilic GNSs used as a substrate for the pigment exhibit a thickness of 50 to 180 nm. The film thickness of TiO_2 increased from 60.0 ± 9.7 nm to 85.6 ± 14.6 nm and 126.3 ± 17.4 nm with increasing reaction time. These results indicate that the TiO_2 film thickness can be controlled by the reaction time of $TiOSO_4$.

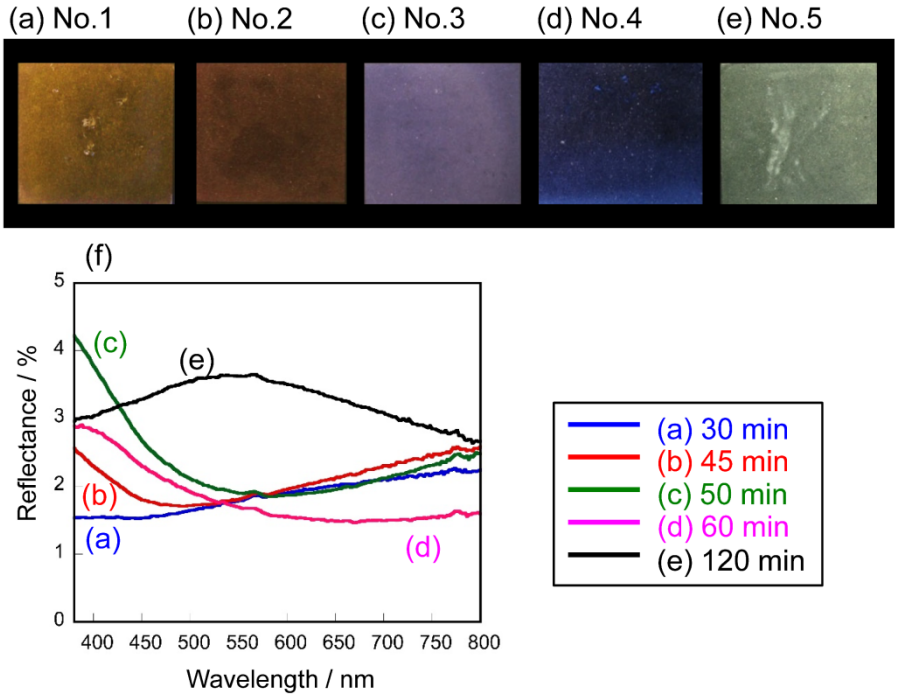

Figure 10. Optical characterization of coating films. (a)–(e) Optical images of coating films and (f) the recorded reflectance spectrum of each coating film.

To test the aforementioned hypothesis, I used a standard thin-film interference model and calculated the reflectance of one layer of anatase TiO_2 on the GNS substrate of a coating film. The thin-film interference model that I used is shown in Figure 11, where d_1 is the film thickness,

ϕ_0 is the angle of incidence in medium 0, ϕ_1 and ϕ_2 are the angles of refraction in media 1 and 2, respectively, and $n_0, n_1,$ and n_2 are the refractive indexes in media 0, 1, and 2, respectively. ϕ_1, ϕ_2 can be calculated by Snell's law (1):

$$n_0 \sin\phi_0 = n_1 \sin\phi_1 = n_2 \sin\phi_2 \qquad (1)$$

The basis on the interference theory is the Fresnel equations, which give the Fresnel reflection (r_{01}, r_{12}) coefficients as follows. The Fresnel reflection coefficients for the parallel and perpendicular polarized light at the planar interface between two linear isotropic media are represented by r_p and r_s, respectively:

$$r_{01s} = \frac{n_0 \cos\phi_0 - n_1 \cos\phi_1}{n_0 \cos\phi_0 + n_1 \cos\phi_1}$$

$$r_{01p} = \frac{n_1 \cos\phi_0 - n_0 \cos\phi_1}{n_1 \cos\phi_0 + n_0 \cos\phi_1}$$

$$r_{12s} = \frac{n_1 \cos\phi_1 - n_2 \cos\phi_2}{n_1 \cos\phi_1 + n_2 \cos\phi_2}$$

$$r_{12p} = \frac{n_2 \cos\phi_1 - n_1 \cos\phi_2}{n_2 \cos\phi_1 + n_1 \cos\phi_2}$$

λ is wavelength. β is the phase difference of multiply reflected wave inside medium 1 as it transverses once from one boundary to the other. The phase difference β is given by

$$\beta = \frac{2\pi n_1 d_1 \cos\phi_1}{\lambda}$$

The total reflected amplitude *r* is given by

$$r = \frac{r_{01} + r_{12} e^{-i2\beta}}{1 + r_{01} r_{12} e^{-i2\beta}}$$

The reflectance R is the squared magnitude of r:

$$R = |r|^2$$

The model reflection spectrum can be obtained by plotting R as a function of λ contained in β.

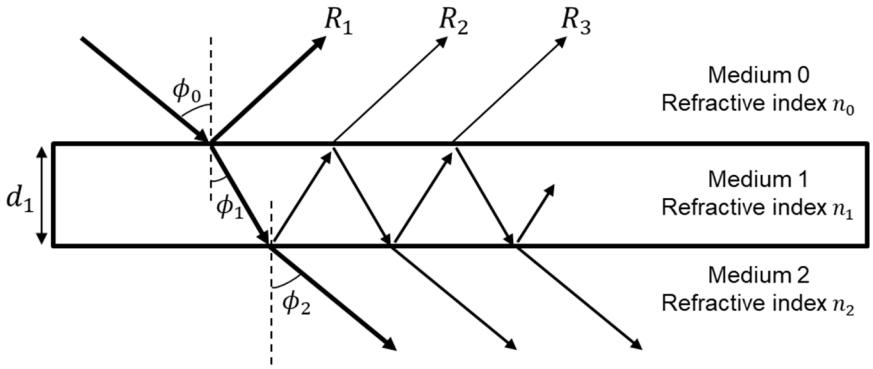

Figure 11. Schematic of thin-film interference

The theoretical reflectance spectrum was estimated from a model thin-film interference equation [3][31] under the assumption that the angle of incidence was 0° and that the refractive index of the coating films, anatase TiO_2, and GNSs was 1.5, 2.3 [32], and 2.6 [33], respectively. The TiO_2 film thickness d was measured from cross-sectional SEM images. Figure 12(d)–(f) shows the measured and model spectra of films No. 2, No. 4, and No. 5. A broad valley at ~493 nm is experimentally observed for film No. 2, and a broad valley at ~552 nm is observed in the model spectrum. Broad peaks at ~383 and ~540 nm are experimentally observed in the spectra of films No. 4 and No. 5, respectively, and broad valleys at ~394 and ~581 nm are observed in the model spectra. The model thin-film interference equation corresponds reasonably well with the measured reflectance spectrum, which supports our hypothesis that the tunable coloration of GNS pigments is caused by the thin-film inter-reflections of TiO_2, depending on the film thickness. However, the reflectance values in the measured reflectance spectra are 0.41 to 0.73 times higher than the reflectance values in the model reflectance spectra. These results indicate a poor orientation of the pigment. This effect is attributed to the GNS pigment particle size being smaller than that of conventional pearl pigments (10–200 μm), which makes alignment of the GNS pigment particles parallel to the substrate surface

difficult, favoring their random orientation in the coating films (Figure 13). Figure 14 shows images at different viewing angles of the coating films containing GNS pigments. These colors do not depend on the viewing angle. This result also suggests that GNS pigments were randomly oriented in the coating films.

This research demonstrated that randomly oriented GNS pigments exhibited angle-independent color in coating films. As future work, I will explore the orientation of the pigments to provide a clear understanding of the relationship between the size and orientation of pigments and the coloration and control method for obtaining brightly colored materials. As such, I expect to also demonstrate black pearl-like coatings through controlled orientation of densely arrayed pigments in films.

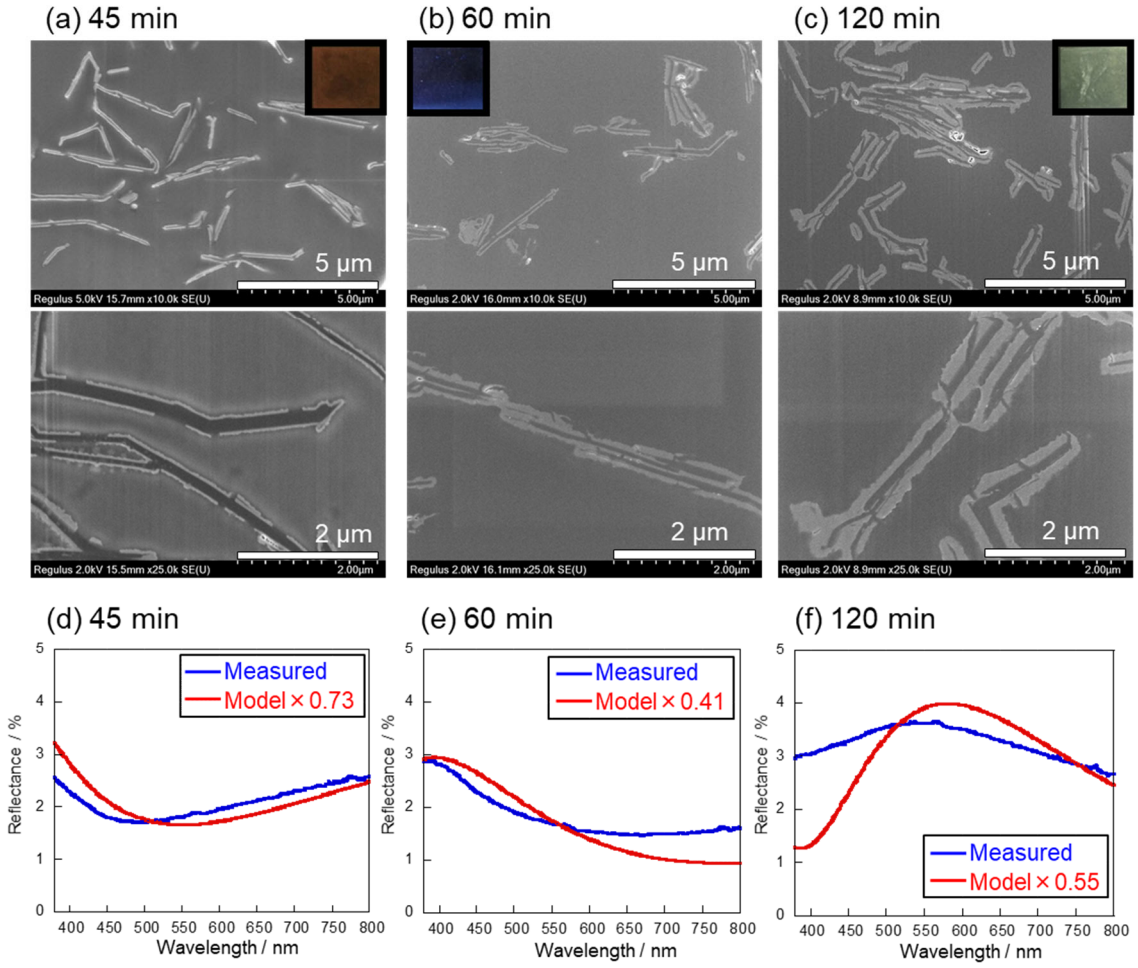

Figure 12. (a)–(c) SEM images of cross sections through the GNS pigments in coating films; (d)–(f) measured and modeled reflectance spectra of each coating film. Blue and red curves represent experimental and modeled reflectance spectra, respectively.

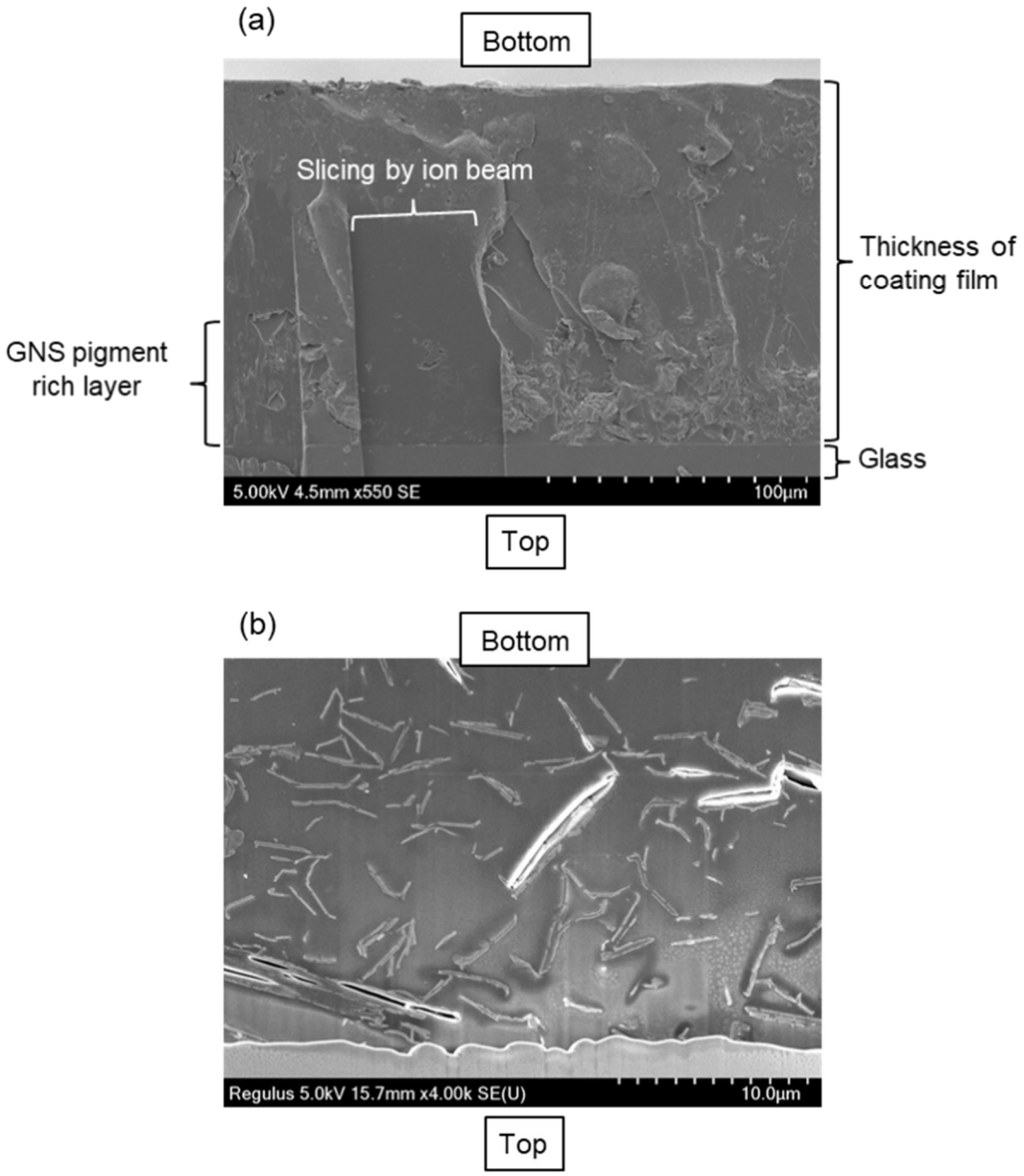

Figure 13. Cross-section SEM images of a coated film with a GNS pigment-rich layer: (a) the coating film and (b) the GNS pigment-rich layer

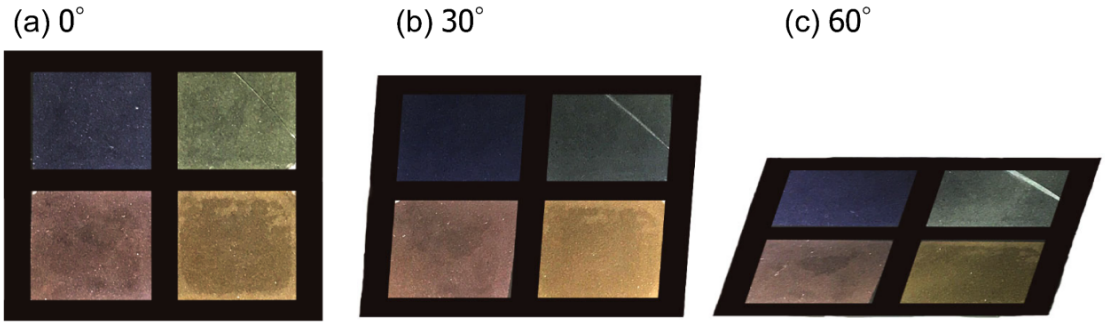

Figure 14. Photographs at different viewing

4.4 Conclusion

To obtain an interference color pigment with enhanced interference color, I prepared an interference layer of TiO_2 on a GNS substrate, which was a novel black sheet structure prepared by wet dispersion. The results are summarized as follows.

1. Using a hydrogen peroxide–urea complex as an oxidizing agent and poly(ST-2VP) as a dispersant in DMF, I prepared sheet-like (length and width of 1 to 7 μm, thickness of 50 to 180 nm) hydrophobic GNSs with a low defect concentration. Hydrophobic GNSs exhibited good dispersibility in hydrophobic solvents.

2. To disperse the hydrophobic GNSs in water, hydrophilic GNSs were prepared by adding an anionic polymer dispersant that interacted with the pyridine groups of poly(ST-2VP) to increase the surface charge.

3. The hydrophilic GNSs were coated with a TiO_2 precursor deposited onto the GNS surface via hydrolysis of $TiOSO_4$. A GNS pigment coated with anatase TiO_2 was obtained after thermal treatment.

4. GNSs with a sheet structure covered with a thin film of TiO_2 exhibited different reflectance colors depending on the thickness of the TiO_2 film.

The GNS pigments synthesized in the present work represent an environmentally friendly and nonfading pigment composed of conventional graphite and TiO_2. Our study showed that GNSs enhanced the color contrast and that the randomly oriented GNS pigment exhibited angle-independent color in the coating film by diffuse reflection. Ongoing studies will explore

modifications to the assembly procedures to control the orientation of the pigments and the coloration.

References

[1] Y. Takeoka, *Journal of Materials Chemistry*, **2012**, 22, 23299-23309.

[2] F. J. Maile, G. Pfaff, and P. Reynders, *Progress in Organic Coatings*, **2005**, 54, 150-163.

[3] G. Pfaff and P. Reynders, *Chemical Reviews*, **1999**, 99, 1963-1981.

[4] M. Kohri, Y. Nannichi, T. Taniguchi, and K. Kishikawa, *Journal of Materials Chemistry C*, **2015**, 3, 720-724.

[5] S. Yoshioka, S. Kinoshita, *Forma*, **2002**, 17, 169-181.

[6] S. Kinoshita, S. Yoshioka, Y. Fujii, N. Okamoto, *Forma*, **2002**, 17, 103-121.

[7] Y. Takeoka, S. Yoshioka, A. Takano, S. Arai, K. Nueangnoraj, H. Nishihara, et al., *Angewandte Chemie-International Edition*, **2013**, 52, 7261-7265.

[8] Y. Takeoka, S. Yoshioka, M. Teshima, A. Takano, M. Harun-Ur-Rashid, and T. Seki, *Scientific Reports*, **2013**, 3, 2371.

[9] X. X. Yao, Y. C. Bai, Y. J. Lee, Z. M. Qi, X. H. Liu, and Y. D. Yin, *Journal of Materials Chemistry C*, **2019**, 7, 14080-14087.

[10] Y. Xue, F. Wang, H. J. Luo, and J. F. Zhu, *ACS Applied Materials & Interfaces*, **2019**, 11, 34355-34363.

[11] A. Kawamura, M. Kohri, G. Morimoto, Y. Nannichi, T. Taniguchi, and K. Kishikawa, *Scientific Reports*, **2016**, 6, 33984.

[12] S. Cho, T. S. Shim, J. H. Kim, D. H. Kim, and S. H. Kim, *Advanced Materials*, **2017**, 29, (22), 1700256.

[13] B. Yi and H. F. Shen, *Chemical Communications*, **2017**, 53, 9234-9237.

[14] M. Xiao, Y. W. Li, M. C. Allen, D. D. Deheyn, X. J. Yue, J. Z. Zhao, et al., *ACS Nano*, **2015**, 9, 5454-5460.

[15] T. Noguchi, *Journal of Society of Cosmetic Chemists of Japan*, **1993**, 27, 304-313.

[16] F. Suzuki, Journal of the Japan Society of Colour Material, **1987**, 60, 481-487.

[17] A. Kimura, F. Suzuki, European patent EP0327739B, **1989**.

[18] Franz Klaus D, Ambrosius Kalus, Kanpp August, Brucker Hans D, United States Patent 4867793, **1987**.

[19] H. Bernhard, R. Esselborn, United States Patent 4076551A, **1976**.

[20] H. Tanaka, M. Kato, O. Watanabe, United States Patent 9096736B2, **2011**.

[21] Eric Kirchner, Jacqueline Houweling, *Progress in Organic Coatings*, **2009**, 64, 2–3, 287-293.

[22] G. H. Chen, W. G. Weng, D. J. Wu, C. L. Wu, J. R. Lu, P. P. Wang, et al., *Carbon*, **2004**, 42, 753-759.

[23] G. Sun, X. Li, Y. Qu, X. Wang, H. Yan, and Y. Zhang, *Materials Letters*, **2008**, 62, 703-706.

[24] G. Chen, D. Wu, W. Weng, and C. Wu, *Carbon*, **2003**, 41, 619-621.

[25] S. Yamabi and H. Imai, *Thin Solid Films*, **2003**, 434, 86-93.

[26] C. A. Schneider, W. S. Rasband, and K. W. Eliceiri, *Nature Methods*, **2012**, 9, 671-675.

[27] A. C. Ferrari, *Solid State Communications*, **2007**, 143, 47-57.

[28] Gupta, G. Chen, P. Joshi, S., *Nano Letters*, **2006**, 6, 2667-2673.

[29] C.S. McCamy, *Color Res. Appl.* **1996**, 21, 292–304.

[30] H.J. Streitberger, K.F. Dössel, Automotive Paints and Coatings, second ed., Wiley-VCH Verlag GmbH & Co. KGaA, Weinheim, **2008**. 182.

[31] R. M. A. Azzam, N. M. Bashara, "Ellipsometry and polarized light," North-Holland Pub. Co., New York, **1977**.

[32] D. J. Kim, S. H. Hahn, S. H. Oh, and E. J. Kim, *Materials Letters*, **2002**, 57, 355-360.

[33] H. S. Skulason, P. E. Gaskell, and T. Szkopek, *Nanotechnology*, **2010**, 21, 295709.

Chapter 5

Degradation of Scratch Resistance of Clear Coatings by Outdoor Weathering

5.1 Introduction

Car owners want their cars to have a long-lasting scratch-free appearance. Scratch resistance is thus one of the most important properties of automotive coatings [1-4]. Even superficial scratches or marring can deteriorate the high-gloss appearance of automotive coatings. Since the scratch resistance of automotive coatings is important for maintaining appearance, it is necessary to understand the changes in scratch resistance over time [4].

To evaluate coating service life, degradation evaluation methods have been combined with chemical and physical characterization techniques [5-8]. Typical degradation evaluation methods for coatings are outdoor weathering and accelerated weathering tests. Accelerated weathering tests are designed to simulate degradation under usage conditions in a short time. Commonly used scratch resistance tests include simulated car wash tests, scratch tests, rubbing tests, and micro-hardness tests [9]. Scratch tests are the preferred quantitative mechanical measurement method because they can sensitively detect the degradation of a coating surface [6, 10, 11].

Several studies have reported that the scratch resistance of coatings degrades after exposure to accelerated weathering [5, 6]. Possible mechanisms of this degradation include crosslink scission, which is caused by chemical reactions such as hydrolysis and leads to poor strength, and crosslink formation, which is caused by the recombination of free radicals from photo-oxidation and leads to a hard and brittle coating. Another possibility is that some residual crosslinking occurs during the early stage of exposure, making the coating hard and brittle.

Fourier transform infrared spectroscopy (FT-IR) is the most powerful tool for understanding changes in the chemical properties of coating surfaces [12, 13]. Other forms of spectroscopy and sample preparation techniques have been reviewed [14, 15]. Changes in the chemical and physical properties of polyester-urethane coatings exposed to accelerated weathering have been reported [8]. It was found that crosslink density diminished during exposure, making the coatings brittle. However, the tensile modulus of the coatings increased with exposure. These results suggested that in addition to diminished crosslink density, polymer physical aging during accelerated weathering contributes to the changes in mechanical properties. The degradation and physical aging processes are not yet fully understood, and thus further studies are required.

Accelerated weathering is commonly used to simulate normal usage conditions. In contrast, the outdoor weathering test is rarely used. However the effects of accelerated weathering may be

different from those caused by usage conditions [16]. Gerlock et al. [17] and Bauer et al. [18] reported the weathering chemistry of polyester urethane clear coats subjected to outdoor weathering tests in Florida or Arizona and various accelerated weathering tests. They found that none of the accelerated weathering tests was acceptable for their samples because isophthalate degradation, which does not occur in outdoor weathering tests, was observed using photoacoustic infrared spectroscopy [17]. However most clear coats today are based on acrylic resin backbones because of their good balance of cost, durability, and scratch performance [19]. Clear coat materials based on acrylic resin today need suitable verification to be applied accelerated weathering tests. Moreover, the effects of exposure conditions on scratch properties are not yet fully understood.

The present study investigates the relationship between scratch resistance and the chemical changes in acrylic clear coats in an outdoor weathering test. Differences in degradation between outdoor exposure and accelerated exposure are also discussed.

5.2 Materials and Methods

Three types of coating were exposed to outdoor weathering and investigated using a scratch test and FT-IR. The results were compared with those for coatings exposed to accelerated weathering tests.

5.2.1 Sample preparation

Three types of coating with two types of crosslinking commonly used in automotive coatings were examined in this study. The two isocyanate coatings based on acrylic resins (2K polyurethane coatings) are denoted Coating A (T_g = 70.0°C, as determined by tan δ curve from a dynamic mechanical analysis (DVA-220 dynamic mechanical analyzer, ITK Co., Ltd.) performed at a frequency of 1 Hz and a strain of 1%) and Coating B (T_g = 79.2°C), respectively. A 1K epoxy acid coating based on acrylic resins is denoted Coating C (T_g = 72.7°C). To simulate a typical automotive coating, the samples were prepared by successively applying an electrodeposited coating, a primer surfacer, a black finishing coat, and clear coat over a steel substrate. Coating films were prepared by spraying on the samples with a dry thickness of 30-40 μm and subsequently curing them at 140°C for 30 min.

5.2.2 Outdoor weathering test

Outdoor exposure was performed for 1, 3, 6, and 12 months in Okinawa, Japan. After the outdoor weathering test, the samples were stored at room temperature and humidity in the dark place. Table 1 shows the weather conditions for the outdoor exposure test sites in Naha, Okinawa, from August 2008 to July 2009. These data were provided by the Japan Meteorological Agency. One month in this study means a unit of time equal to 365/12 days.

Table 1. Weather conditions of outdoor exposure

Exposure	Sum of precipitation	Temperature	Relative humidity	Sum of sunshine duration	Daily global solar radiant exposure
month	mm	°C	%	h	MJ/m^2
1	139.5	29.0	73	243.3	21.3
2	267.5	28.2	74	150.5	16.1
3	214.5	26.4	72	208.1	15.9
4	119.0	22.5	72	114.5	10.3
5	19.5	18.7	64	130.5	9.8
6	32.5	16.7	64	103.9	9.7
7	37.0	19.9	73	134.9	13.2
8	165.5	19.6	75	87.5	12.4
9	132.5	20.5	70	133.0	16.1
10	185.0	23.7	73	219.4	21.6
11	402.0	26.4	81	159.9	18.5
12	62.0	29.2	77	253.8	22.8

5.2.3 Accelerated weathering tests

Three types of accelerated weathering test were performed on the coatings.

・Xenon weathering test. Accelerated weathering of the samples was carried out in an accelerated weathering chamber (ATRAS Ci4000) according to ISO11341:2004 for 240 h. The xenon weathering test protocol provides continuous exposure to xenon arc ultraviolet (UV) radiation (60 W/m^2 @ 300-400 nm irradiance), and 18 min of deionized water spray every 2 h with a black panel temperature of 63°C and a chamber temperature of 40±1°C. Borosilicate glass inner and outer filters were used with the xenon arc lump to simulate the spectral distribution under usage conditions.

・Xenon weathering test without water spraying. The xenon test without water was carried out on samples covered by borosilicate glass container, which had a rectangular envelope shape and was open at the bottom. This experiment was conducted under the same temperature and humidity as those in the xenon test but there was neither water droplet contacts nor dew on the coating surface. Samples used in the accelerated weathering chamber are shown in Figure 1.

・Water immersion test. A water immersion test was conducted on Coating A and Coating B. The samples were immersed in deionized water at 40°C for 240 h. A constant-temperature water bath was used (Yamato Scientific Co., Ltd., BA500)

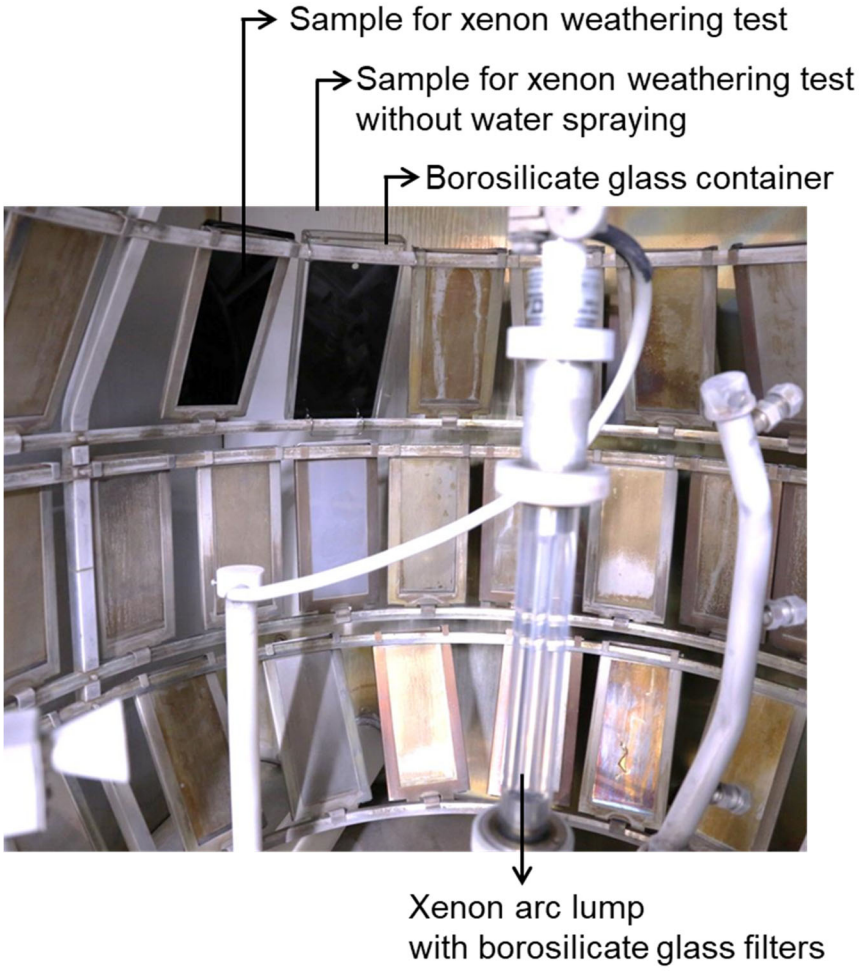

Figure 1. Photograph of xenon weathering test and xenon weathering test without water spraying in the accelerated weathering chamber

5.2.4. Scratch test

Scratch tests were carried out on a micro-scratch tester (CSM Instruments, MST) using a diamond stylus with a 0.1 mm tip radius at 25°C and 50-52% relative humidity. In the scratch tests, the load was progressively increased from 0.05 to 0.98 N at a scratch speed of 300 mm/min and a scratch length of 50 mm. When no cracks were observed in the scratch trail, the initial load was increased by 0.98 N and another scratch test was conducted. This process was repeated until cracks appeared. Scratch deformation and fracture were observed using confocal microscopy (Lasertec, OPTELICS H1200). As the normal force was increased from 0.05 to 4.98 N at a constant rate, the critical fracture force, defined as the force at which 10 cracks with a length of more than 50 μm were observed in the microscope view area (900 μm × 900 μm), was determined (Figure 2(a)). Although the critical fracture force can be used to quantify scratch resistance, the load at which the first crack forms is experimentally unstable. I thus chose the load at which a contiguous crack is initiated as a quantitative measure. The criterion I adopted (10 cracks with a length of more than 50 microns in a 900 μm × 900 μm field of view ensures high reproducibility and stability. The depth of the scratch deformation was measured from the coating surface plane (Figure 2(b)).

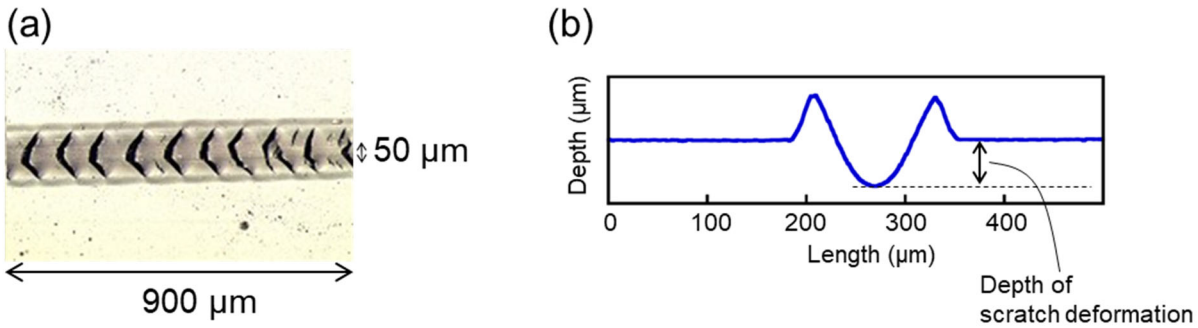

Figure 2. Definitions of scratch resistance parameters. (a) Optical micrograph of scratch fracture. Critical fracture force is defined as the force at which 10 cracks with a length of more than 50 μm are observed in a microscope view area (900 μm× 900 μm). (b) Cross-sectional profile. The depth of scratch deformation was measured from the coating surface plane.

5.2.5 FT-IR

The FT-IR spectra were obtained using an FT-IR spectrometer (Thermo Scientific, Nicolet iS50) equipped with a mercury-cadmium-telluride (MCT) detector with the attenuated total reflectance

(ATR) technique. The samples were washed with a sponge and mild detergent and wiped with alcohol before being analyzed. I selected a germanium prism with a contact area 100 μm in diameter as the internal reflection element, which permitted the infrared beam to a depth of between 0.3 μm (4000 cm^{-1}) and 1.2 μm (1000 cm^{-1}), to detect only the degradation of the topmost surface of the coatings. The spectra were recorded from 4000 to 400 cm^{-1} at a resolution of 8 cm^{-1}. A total of 64 scans were accumulated. The contact load was controlled to be a constant value to ensure high quantitative accuracy [20]. The difference spectra were obtained by subtracting the spectrum of the unexposed coating from that of the exposed coating without normalizing the spectra. The accuracy of difference spectra was checked by comparing spectra taken at two different locations in a same sample. The reproducibility of the difference spectra was estimated to be 2% in absorbance by comparing the results obtained at different locations.

5.3 Results and Discussion

5.3.1. Scratch properties of coatings subjected to various weathering tests

Figure 3 shows a typical micrograph of Coating A after the scratch test. Scratch deformation was observed on the coating surface, and fracture occurred with cracks at forces above the critical fracture force. This crack morphology was observed for all samples. Figure 4 shows the critical fracture force for coatings subjected to various weathering tests.

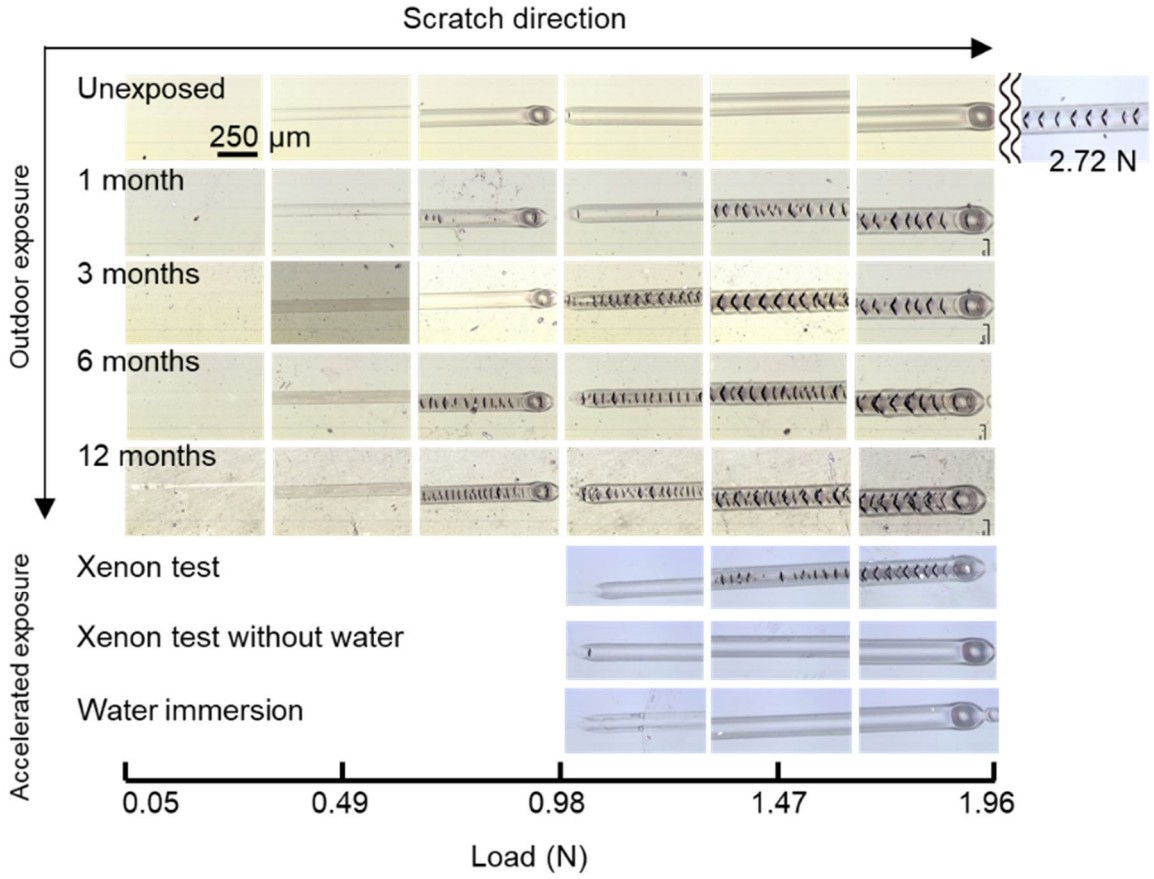

Figure 3. Optical micrographs of Coating A after scratch test. Each micrograph shows the typical position. Dents indicate scratch ends.

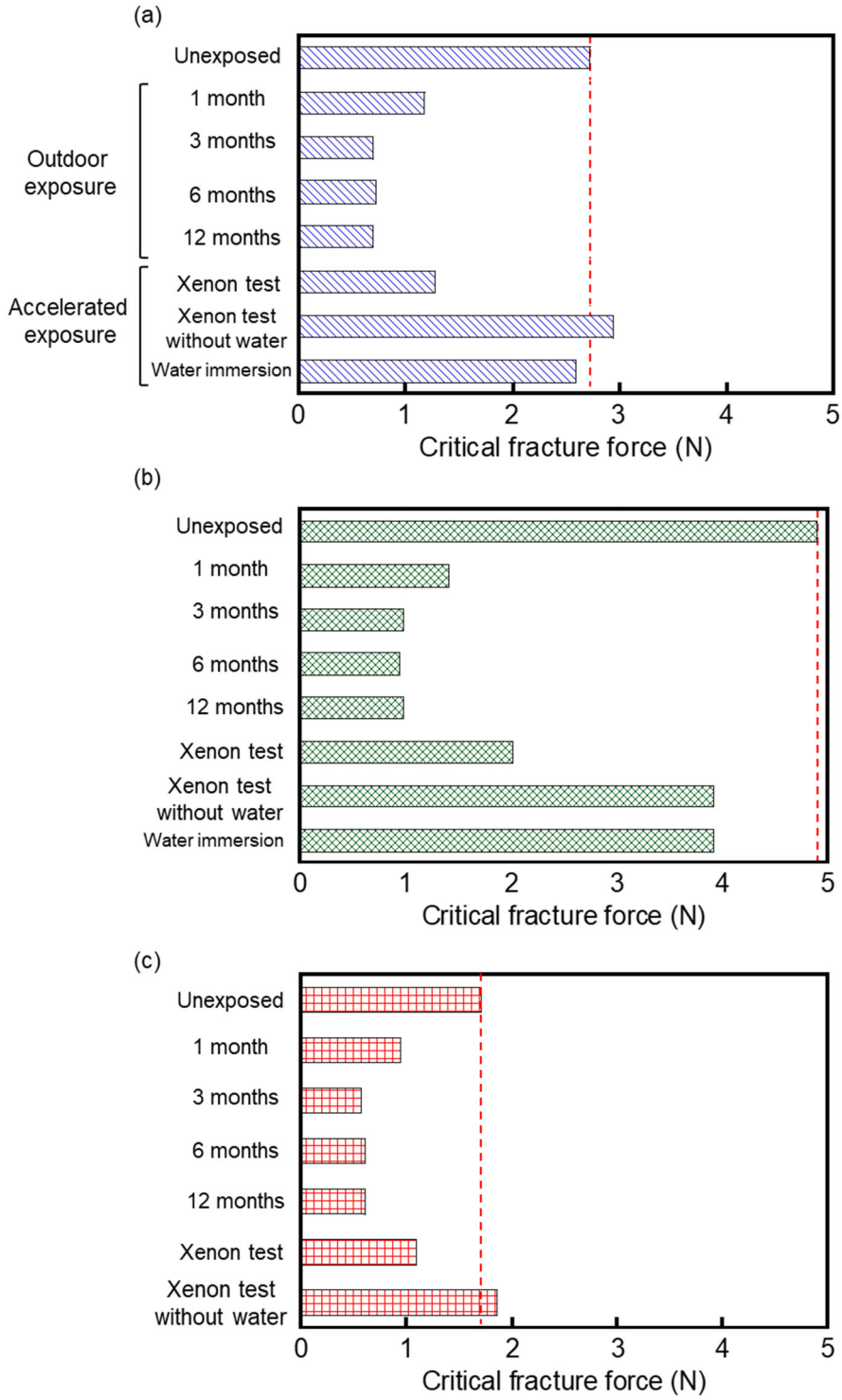

Figure 4. Critical fracture force plotted against outdoor exposure and accelerated exposure for (a) Coating A, (b) Coating B, and (c) Coating C.

The critical fracture force for unexposed coatings was found to be greater than that for coatings exposed to outdoor weathering for all sample types. No cracks were observed at 4.9 N in unexposed samples for Coating B. The critical fracture force of coatings exposed to outdoor weathering declined abruptly within 3 months, and then changed slightly from 3 to 12 months. It was found that the coatings become brittle after a short exposure (1 month) to outdoor weathering.

Figure 5 shows the relation between the load and depth of scratch deformation of the coatings in the scratch test. The progress curves of scratch deformation have a linear relationship with the normal load. There were no significant differences in the depth of scratch deformation between unexposed coatings and coatings exposed to outdoor weathering after 1 month for all sample types. As scratch deformation is related to viscoelastic properties, the results suggest that the viscoelastic properties of the coatings remained unchanged after 1 month of outdoor weathering. Thus, it is assumed that coatings exposed to outdoor weathering for 1 month had lower fracture resistance than that of unexposed coatings even though their viscoelastic properties were unchanged.

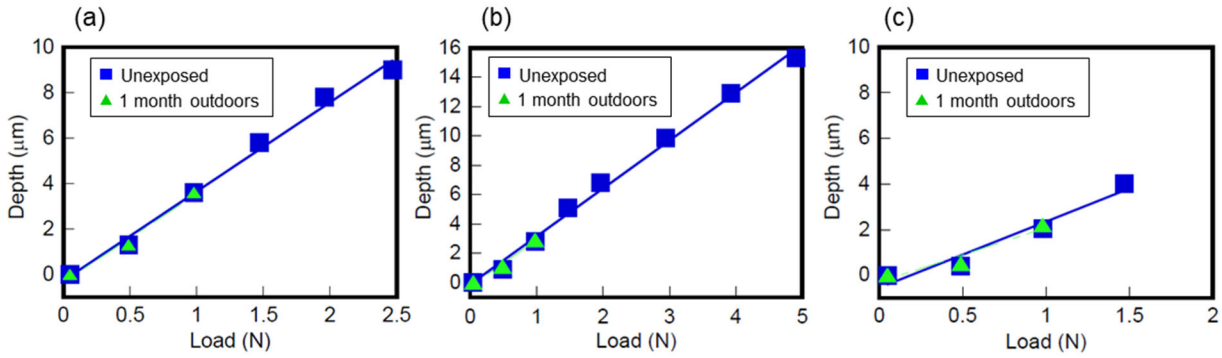

Figure 5. Relation between load and depth of scratch deformation in scratch test for (a) Coating A, (b) Coating B, and (c) Coating C.

The critical fracture force of coatings exposed to the xenon test without water or water immersion was almost the same as that of unexposed coatings. Coatings exposed to the xenon test exhibited cracks in the scratch trail, and their critical fracture force was as low as that of coatings exposed to outdoor weathering for 1 month. Scratch resistance degradation after 1 month of outdoor exposure could thus be reproduced by 240 h of the xenon test. Moreover, it was found that both water and ultraviolet light are necessary to reproduce the degradation.

5.3.2 Chemical changes of coating surfaces subjected to various types of exposure

Figures 6-8 show FT-IR difference spectra for various exposed and unexposed samples. Peaks rising and falling from the baseline indicate increases and decreases in the absorption of functional groups, respectively.

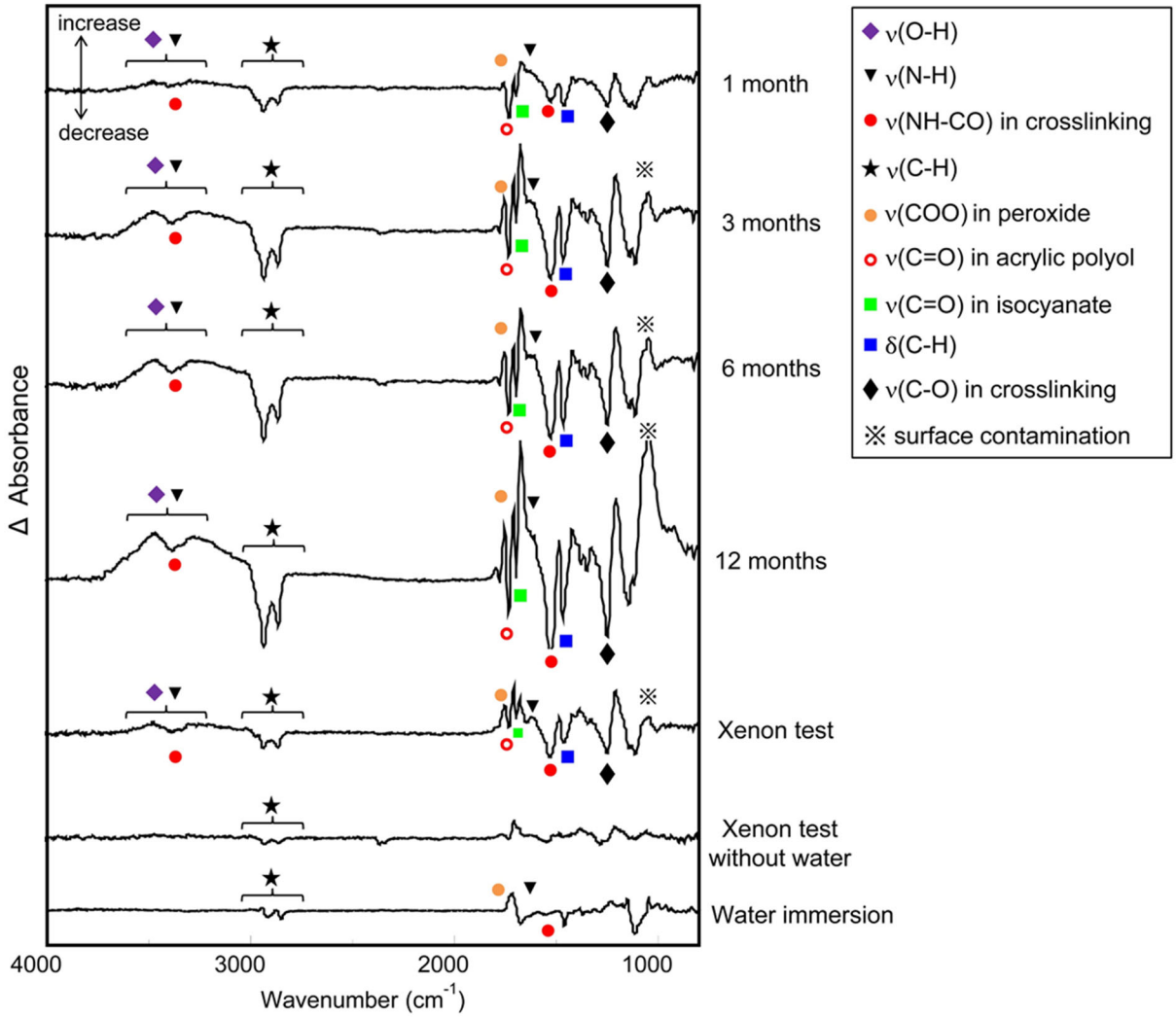

Figure 6. FT-IR difference spectra before and after tests for Coating A.

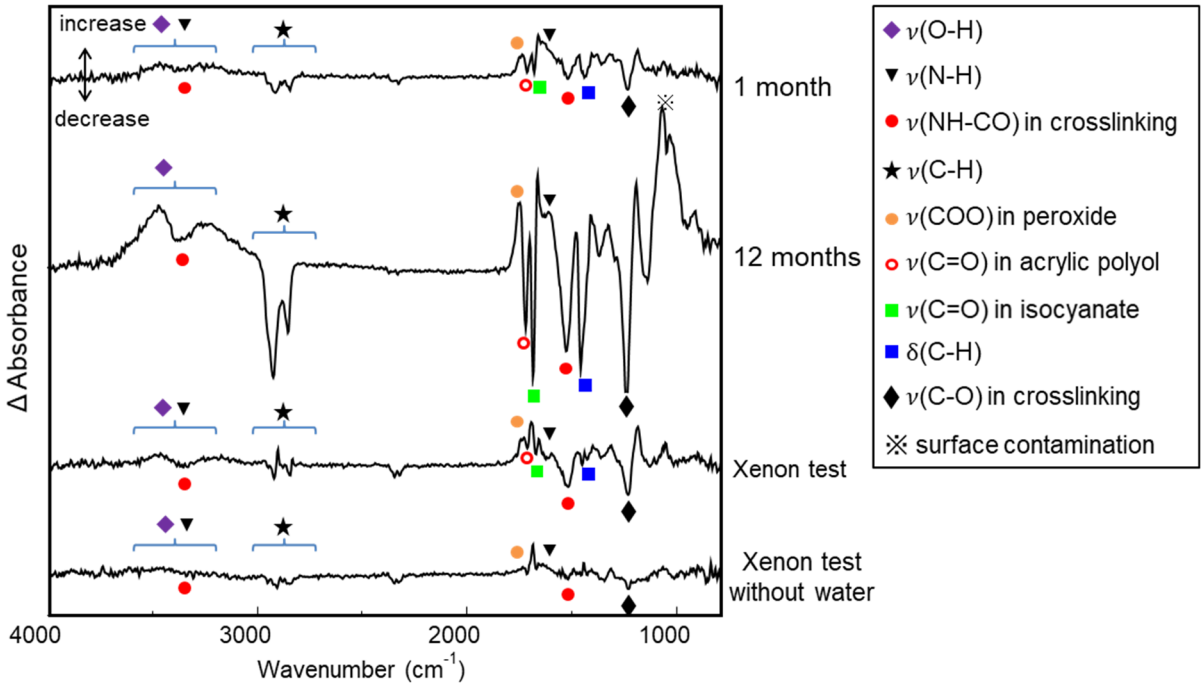

Figure 7. FT-IR difference spectra before and after tests for Coating B.

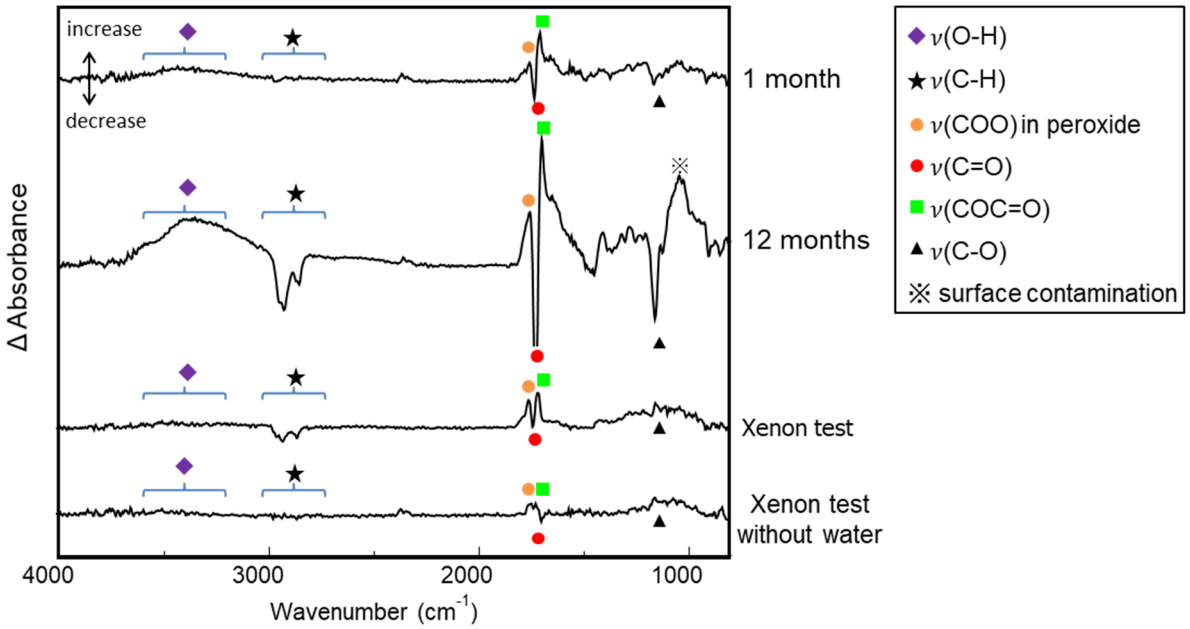

Figure 8. FT-IR difference spectra before and after tests for Coating C.

For the 2K polyurethane coatings, there were decreases with outdoor exposure time in CO-NH (amide II) bending absorption (peak area centered at 1510 cm^{-1}), C=O stretching (1741 and 1691 cm^{-1}), C-O stretching (1240 cm^{-1}), C-H stretching (2931 cm^{-1}), and C-H bending (1480 cm^{-1}), and increases in O-H stretching (3462 cm^{-1}) and N-H stretching (3280 cm^{-1}). This indicates that main chain scission occurs as a function of outdoor exposure time due to hydrolysis reactions (Scheme 1). The absorption peak at 1755 cm^{-1} indicates that peroxides were generated. These results indicate that the peroxides and radicals formed in the photo-oxidation reaction are responsible for the observed degradation. The photo-oxidation reaction leads to the scission of the polymer network or chain, resulting in decomposition at the coating surface.

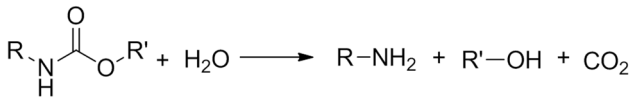

Scheme 1. Degradation reaction for 2K polyurethane coatings.

For the epoxy acid coatings, there were decreases with outdoor exposure time in the C=O stretching absorption (1727 cm^{-1}), C-H stretching (2927 cm^{-1}) and C-O stretching (1161 cm^{-1}), and increases in O-H stretching (3462 cm^{-1}) and CO-OH stretching (1700 cm^{-1}). Epoxy acid coatings consist of ester bonds formed in acrylic resin and in crosslinking; therefore, either one of the polymer network or chain scission occurs as a function of outdoor exposure time due to hydrolysis or photo-oxidation reactions (Scheme 2). An absorption peak at 1755 cm^{-1} appeared. Therefore, the polymer network or chain is assumed to be diminished by the photo-oxidation reaction for epoxy acid coatings.

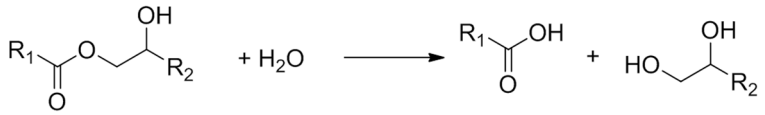

Scheme 2. Degradation reaction for epoxy acid coatings.

It was found that degradation on the surface is consistent with main chain scission for all samples. Possible mechanisms for this degradation on the surface, even after a short exposure time, are as follows. The attenuation of UV light that passes through the clear coat depends on pass length due to the effect of the UV light absorber additive. However, the UV light absorber cannot effectively shield the topmost surface of coatings due to the Lambert-Beer law. Therefore, UV light leads to the chemical degradation of the coating surface even after a short exposure. The UV light absorber is effective for deeper regions of the coatings, which thus retain their bulk properties.

5.3.3 Relationship between chemical degradation and scratch properties

The relationship between the critical fracture force and FT-IR absorption associated with main chain scission, degradation products, and desorption products was examined (Figure 9 and 10). After outdoor exposure for 3 months, the critical fracture force decreased and absorbance changed, indicating degradation of the coatings. This implies that there is a good correlation between the critical fracture force and the degradation reaction. This interpretation can also be applied to the epoxy acid coatings (Figure 11). However, the critical fracture force became almost constant from 3 to 12 months, even though degradation is assumed to have continued after 3 months. The critical fracture force is only weakly related to the degree of degradation after 3 months for all sample types. Therefore, scratch resistance degrades as a function of main chain scission in the early exposure period.

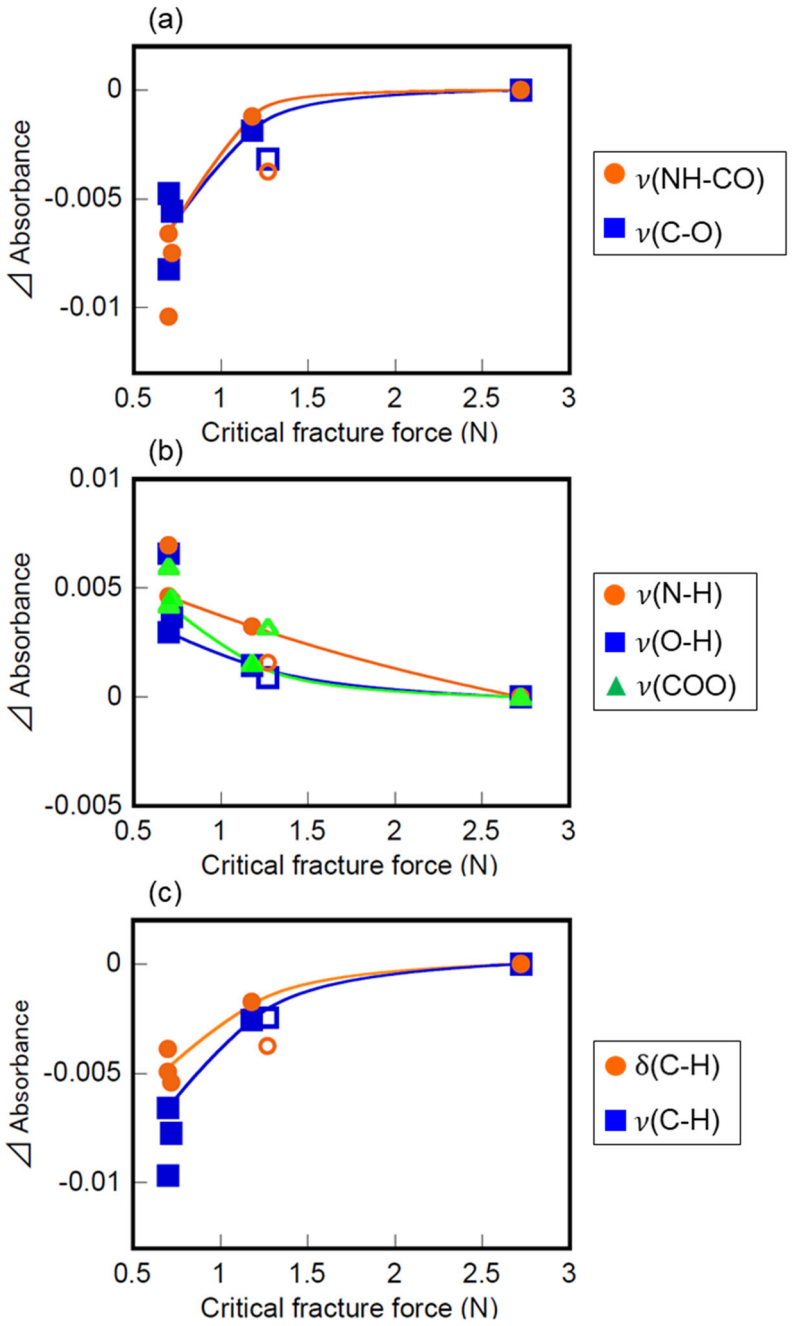

Figure 9. Relation between critical fracture force and absorbance for each group in Coating A. (a) Chain scission, (b) Degradation products, and (c) Desorption products. ●■▲: Outdoor weathering test, ○□△: 240-h xenon test.

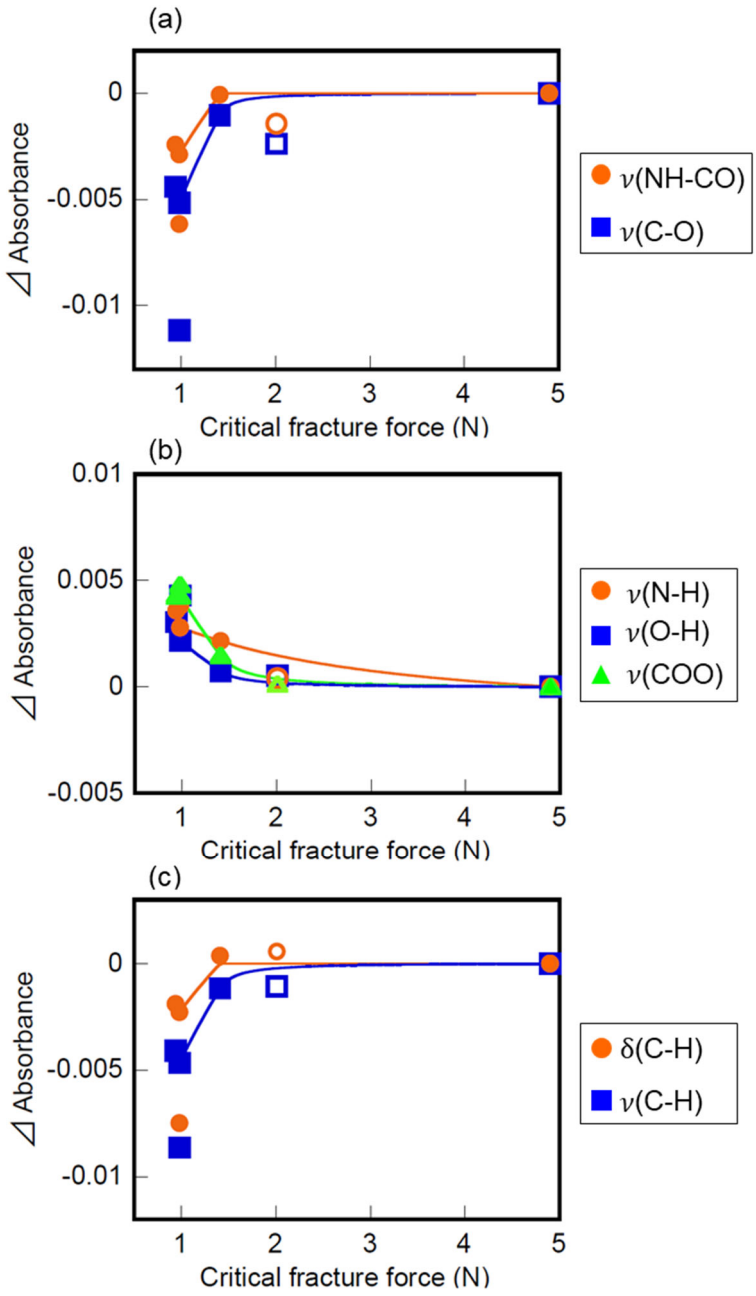

Figure 10. Relation between critical fracture force and absorbance for each group in Coating B. (a) Chain scission, (b) Degradation products, and (c) Desorption products. ●■▲: Outdoor weathering test, ○□△: 240-h xenon test.

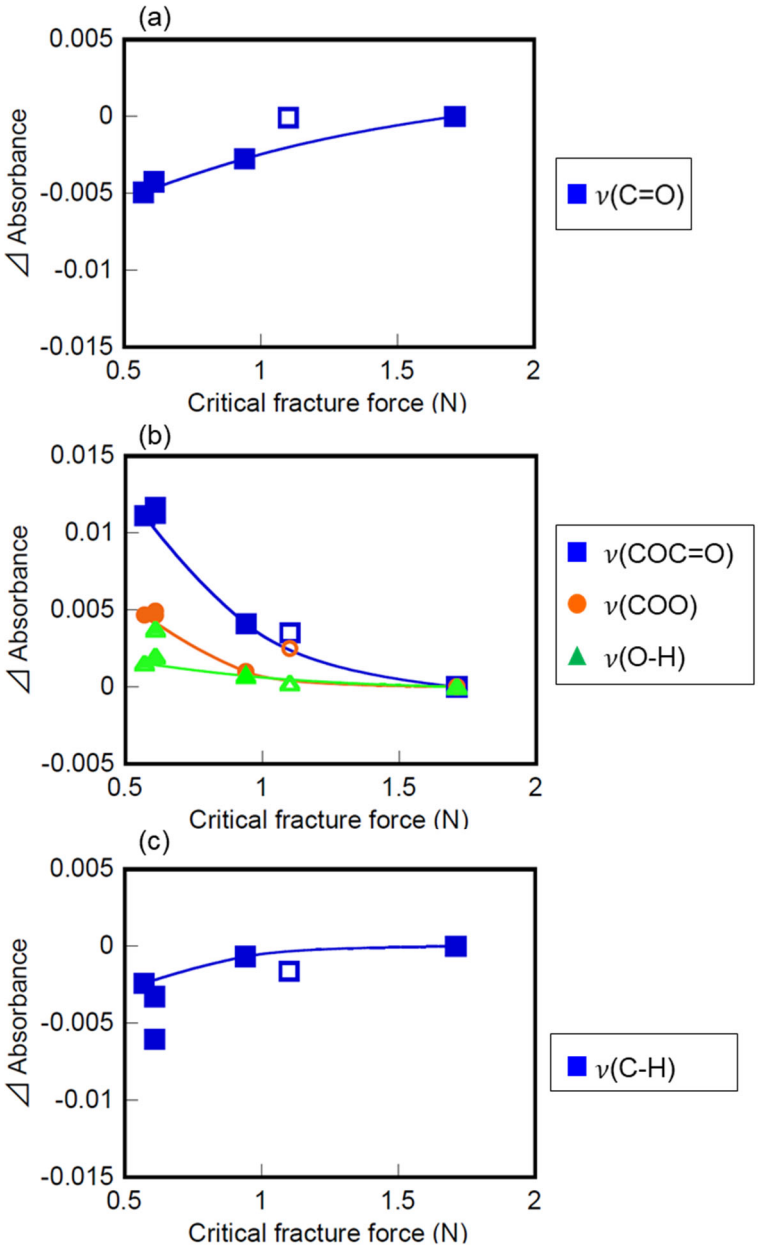

Figure 11. Relation between critical fracture force and absorbance for each group in Coating C. (a) Chain scission, (b) Degradation products, and (c) Desorption products. ●■▲: Outdoor weathering test, ○□△: 240-h xenon test.

5.3.4 Comparison of degree of degradation with outdoor exposure and accelerated exposure

To investigate the difference in the effects of outdoor exposure and accelerated exposure on these coatings, the degree of degradation determined from the FT-IR spectrum of each functional group was compared. Figure 12 shows the method used to estimate the equivalent exposure time for the alkyl bond. The difference in absorbance by the alkyl bond between outdoor exposure and accelerated exposure was 0.0024, indicating that the degree of degradation after 240 h of the xenon test corresponds to that after 0.94 months of outdoor exposure for Coating A. Tables 2-4 show outdoor exposure time that corresponds to accelerated exposure time for each functional group for Coating A, Coating B, and Coating C, respectively.

The degree of degradation after 240 h of the xenon test corresponds to that after 0.49-2.3 months of outdoor exposure for Coating A (Table 2). The amount of peroxide equivalent to 2.3 months was generated by photo-oxidation, and those of OH bonds and NH bonds equivalent to 0.49 and 0.62 months, respectively, were generated by the hydrolysis of crosslinks in the xenon test. The ratio of each reaction in the xenon test was different from that in the outdoor weathering test. The degree of degradation after 240 h of the xenon test without water corresponds to that after 0-0.84 months of outdoor exposure for Coating A. Therefore, the degradation reactions in the xenon test were more promoted than those in the xenon test without water. The degree of degradation after 240 h of the xenon test without water corresponds to that after 0-4.4 months of water immersion for Coating A. The amount of peroxide equivalent to 3.5 months was generated by photo-oxidation, and those of OH bonds and NH bonds equivalent to 0 and 0.63 months, respectively, were generated by the hydrolysis of crosslinks in water immersion. The ratio of each reaction in the water immersion test was different from that in the outdoor weathering test. The degradation reactions in various accelerated weathering tests were different from that in the outdoor weathering test for Coating B (Table 3) and Coating C (Table 4).

The degradation reactions with accelerated exposure were the same kinds as that with outdoor exposure, but the balance between the extents of reactions was not reproduced. The photo-oxidation reaction in the xenon test was more promoted than that in the outdoor weathering test. This may be due to the difference in exposure conditions between the outdoor weathering test and the accelerated weathering test in terms of UV radiation, temperature, and moisture, and the changes of these parameters or other substances derived from the environment.

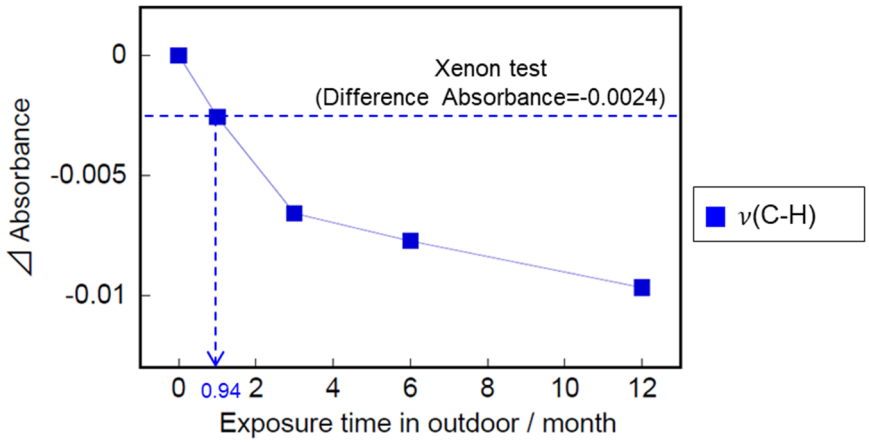

Figure 12. Estimation of outdoor exposure time that corresponds to the accelerated exposure from FT-IR absorption. (The difference in the absorbance of the alkyl bond was 0.0024, indicating that the degree of degradation in the xenon test after 240 h corresponds to that after 0.94 months of outdoor exposure for Coating A. The estimation line is the linear interpolant between experimental points.)

Table 2. Estimation of outdoor exposure time (months) that corresponds to 240h of accelerated exposure for Coating A

	ν(C-H)	ν(N-H)	ν(O-H)	ν(COO)	δ(C-H)	ν(C-O)	ν(NH-CO)
Xenon test	0.94	0.49	0.62	2.3	1.2	1.9	1.8
Xenon test without water	0.1	0.3	0.71	0.84	0.68	0.19	0.0
Water immersion	0.59	0.0	0.63	3.5	4.4	2.8	0.13

Table 3. Estimation of outdoor exposure time (months) that corresponds to 240h of accelerated exposure for Coating B

	ν(C-H)	ν(N-H)	ν(O-H)	ν(COO)	ν(C-O)	ν(NH-CO)
Xenon test	0.7	0.3	0.6	1.2	2.3	1.6
Xenon test without water	0.7	0.2	0.4	0.2	1.4	0.3

Table 4. Estimation of outdoor exposure time (months) that corresponds to 240h of accelerated exposure for Coating C

	ν(C-H)	ν(COC=O)	ν(COO)	ν(O-H)	ν(C=O)
Xenon test	2	0.95	1.7	0.35	0.0
Xenon test without water	1.3	0.0	0.17	0.0	0.0

5.4 Conclusions

This study revealed that the physical and chemical changes of coatings exposed to outdoor weathering are related to scratch resistance. These changes were compared to those in accelerated weathering tests.

After only 1 month of outdoor exposure, the scratch resistance of both isocyanate and epoxy acid coatings remarkably decreased even though there was almost no change in the bulk properties. This decrease in scratch resistance is likely due to crosslink scission in the coating surface layer by oxidation and hydrolysis during exposure.

Although the xenon test also lowered the scratch resistance and caused the same kinds of chemical changes as those found with outdoor weathering, the proportions of each reaction were different between the two types of weathering. Neither the xenon test without water spraying nor the water immersion test could reproduce the scratch resistance degradation found with outdoor weathering. These results indicate that the reproduction of the scratch degradation observed with outdoor weathering needs both light and water, and that the standard xenon test is unsuitable from the viewpoint of chemical reactions.

References

[1] Courter, J. L., *Journal of Coatings Technology*., **1997**, 69, 866, 57–63.

[2] Seubert, C. M. and Nichols, M. E., *Journal of Coatings Technology and Research*., **2007**, 4, 1, 21-30.

[3] Jardret, V., Lucas, B. N., Oliver, W. and Ramamurthy, A. C., *Journal of Coatings Technology*., **2000**, 72, 907, 79-88.

[4] Adamsons, K., *Journal of Coatings Technology and Research*, **2012**, 9, 6, 745-756.

[5] Adamsons, K., Blackman, G., Gregorovich, B., Lin, L. and Matheson, R., *Progress in Organic Coatings*, **1998**, 34, 1-4, 64-74.

[6] Gregorovich, B. V., Adamsons, K. and Lin, L., *Progress in Organic Coatings*, **2001**, 43, 1-3, 175-187.

[7] Seubert, C., Nichols, M., Henderson, K., Mechtel, M., Klimmasch, T. and Pohl, T., *Journal of Coatings Technology and Research*., **2009**, 7, 2, 159-166.

[8] Skaja, A., Fernando, D. and Croll, S., *Journal of Coatings Technology and Research.*, **2006**, 3, 1, 41-51.

[9] Seubert, C., Nietering, K., Nichols, M., Wykoff, R. and Bollin, S., *Coatings*, **2012**, 2, 4, 221-234.

[10] Kutschera, M., Sander, R., Herrmann, P., Weckenmann, U. and Poppe, A., *Journal of Coatings Technology and Research*, **2006**, 3, 2, 91-97.

[11] Jardret, V. and Morel, P., *Progress in Organic Coatings*, **2003**, 48, 2-4, 322-331.

[12] Adamsons, K., *Progress in Polymer Science*, **2000**, 25, 9, 1363-1409.

[13] Bauer, D. R., Gerlock, J. I., Mielewski, D. F., Peck, M. C. P. and Carter, R. O., *Industrial & Engineering Chemistry Research*, **1991**, 30, 11, 2482-2487.

[14] J. L. Gerlock, C. A. Smith, V. A. Cooper1, S. A. Kaberline, T. J. Prater, R. O. Carter III, A. V. Kucherov2, T. Misovski, and M. E. Nichols, *ACS Symposium Series*, **2002**, 805, 212-249.

[15] Makki, H., Adema, K. N. S., Peters, E., Laven, J., van der Ven, L. G. J., van Benthem, R. and de With, G. *Polymer Degradation and Stability*, **2015**, 121, 280-291.

[16] David R. Bauer, *Progress in Organic Coatings*, **1993**, 23, 105-114.

[17] Gerlock, J. L., Peters, C. A., Kucherov, A. V., Misovski, T., Seubert, C. M., Carter, R. O. and Nichols, M. E., *Journal of Coatings Technology*, **2003**, 75, 936, 34-45.

[18] Bauer, D. R., Peck, M. C. P. and Carter, R. O., *Journal of Coatings Technology*, **1987**, 59, 755, 103-109.

[19] Automotive Paints and Coatings, Second Edition, Wiley‐VCH Verlag GmbH & Co. KGaA, Dr. Karl‐Friedrich Dössel, **2008**, CHAPTER 6, 175-210.

[20] Esaki Yasuo, *J. Jpn. Soc. Colour Mater.*, **2005**, 78, 10, 473-479.

Chapter 6

Recovery of Scratch Deformation Formed on Crosslinked Polyorganosiloxane Films

6.1 Introduction

In recent years, the scratch resistance of automotive coatings has become an important issue with improving appearance and reducing the risk of failures such as cracking and peeling. Even very light scratches or marring can deteriorate the high-gloss appearance of an automotive coating. As consumers desire a longer lasting scratch-free appearance, scratch resistance has become one of the most important properties of automotive coatings [1, 2]. Scratches in these coatings have been classified into two types: fracture-type and plastic deformation type [1-8]. Fracture-type scratches represent permanent damage. On the other hand, surface deformations can recover over time, eventually even becoming invisible to the naked eye [4]. This phenomenon arises from purely elastic or elastic-plastic behavior and is called "self-recovery". As scratch recovery increases scratch resistance, its improvement is an important avenue of investigation, and the recovery of deformation-type scratches is the main focus of this paper.

The development of scratch-resistant coatings has primarily been based on 2K urethane systems [5]. 2K coatings consist of an acrylic polyol base resin and an isocyanate curing agent. 2K coatings are well known to exhibit superior scratch recovery compared to traditional automotive coatings such as 1K melamine coatings. Acrylic polyols have a higher mechanical strength and durability than other options, and have considerable flexibility in their molecular design. One of the most popular methods of obtaining coatings with high scratch resistance is the utilization of a high crosslink density or low glass transition temperature (T_g) [6]. Increasing the crosslink density increases the toughness of a coating, thereby improving the scratch resistance. On the other hand, decreasing T_g increases the flexibility of coatings, reducing stress concentration and making the coating more difficult to rupture. Moreover, a lower T_g increases the speed of scratch recovery [7-9].

Scratch recovery speed is related to T_g because the recovery of deformation is based on rheological phenomenon involving elastic or elastic-plastic behavior, which depends on the mobility of the main chain of the coating [10]. A previous study examined the relationship between the recovery speed of scratch deformation and temperature for coatings. As the difference between temperature and T_g decreased, the scratch deformation recovery speed increased [8]. This implies that when the temperature is very close to or above T_g, the viscoelastic relaxation may be fast, allowing higher molecular mobility. In contrast, minimal recovery was observed at room

temperature because of the low molecular mobility in the glass state below T_g. No other method for remarkably increasing scratch recovery properties was found, other than lowering T_g in conventional coatings. Low-T_g coatings have fast recovery characteristics like rubber but cannot obtain sufficient hardness. The high molecular mobility at room temperature induces practical problems of chemical resistance and permanent soiling of soft surfaces. Therefore, base resins with a carbon-carbon main chain such as an acrylic polyol are close to limits of improved scratch recovery characteristics and chemical resistance, as both properties arise from the same causes as molecular mobility [11, 12].

Thus, coatings containing siloxane materials are attracting increased attention in efforts to impart further scratch resistance to coatings [12, 13, 14]. Noh et al. investigated the scratch characteristics of automotive clearcoats based on an acrylic polyol resin with a silane-modified blocked isocyanate (SMBI) crosslinker. SMBI has two different functional groups per molecule: three alkoxysilane and two blocked isocyanate groups, which participate in the formation of crosslinking networks. Clearcoats with higher amounts of SMBI had a higher crosslinking density than conventional clearcoats without SMBI, and demonstrated superior scratch resistance in nano-scratch, Amtec–Kistler car-wash, and Crockmeter tests [12]. However, even in these clearcoats, deformation was not recovered at room temperature, but self-recovery did occur during heating at above T_g for 2 h [14]. The reason for this is likely that even with coatings containing a siloxane bond, viscoelastic properties based on main chain mobility were the same as those of conventional coatings.

Herein, I explore the remarkable improvement of scratch recovery characteristics using a base resin with a siloxane main chain, as opposed to a carbon-carbon main chain such as an acrylic polyol. Yoshii et al. compared siloxane polymers and PMMA, and reported that siloxane chains are flexible, and that their flexibility decreases as the crosslinking density increases. Moreover, the flexibility of the siloxane main chain in crosslinked polysiloxane is higher than that of PMMA with a main chain of carbon-carbon bonds at room temperature [15, 16]. Therefore, crosslinked polysiloxane with an appropriate crosslinking density was expected to exhibit superior mechanical properties and scratch recovery characteristics. However, few studies have reported the scratch recovery characteristics of polyorganosilsesquioxane-containing coatings.

Herein, I examine crosslinked polyorganosilsesquioxane coatings to investigate the possibility of their application as automotive clearcoats. A polyorganosilsesquioxane precursor was prepared by

hydrolysis reaction and a condensation reaction of trialkoxysilane with an amino group followed by isocyanate curing to form a coating. The scratch recovery characteristics of coating films crosslinked with polyorganosilsesquioxane were measured by micro scratch test and compared with those of conventional coatings.

6.2 Materials and Methods

Two different coatings were used in this study: one was a crosslinked polyorganosilsesquioxane coating (Si-film) and the other was a conventional 2K urethane coating (C-film). To obtain the Si-film, a precursor with an amino group (SiPP-AP) was synthesized by a sol-gel process, which involves the hydrolysis and dehydration-condensation reaction of trialkoxysilane with the amino group. Finally, the Si-film was obtained by crosslinking the amino group of SIPP-AP with isocyanate.

6.2.1 Sample preparation

6.2.1.1 Sample preparation of SiPP-AP

First, a 30 mL stoppered pear-shaped flask was loaded with methanol (3.5 ml) and phenyltrimethoxysilane (PTMS) (6.3 g, 0.032 mol) and 3-aminopropyltrimethoxysilane (APTMS) (5.7 g, 0.032 mol). The mixture was stirred for 30 minutes at room temperature. Then, while being stirred, 2.8 ml of an aqueous solution of 0.04 mol/L sodium hydroxide and toluene (6 ml) was added, and the stirring was continued for another 10 minutes. After that, the obtained solution was stirred for 6.5 h at 70°C (Scheme 1). The obtained SiPP-AP was washed with THF and Hexane and dried under vacuum. All chemicals employed were purchased from Tokyo Chemical Industry Co., Ltd., and all solvents were purchased from FUJIFILM Wako Pure Chemical Corporation and used without further purification.

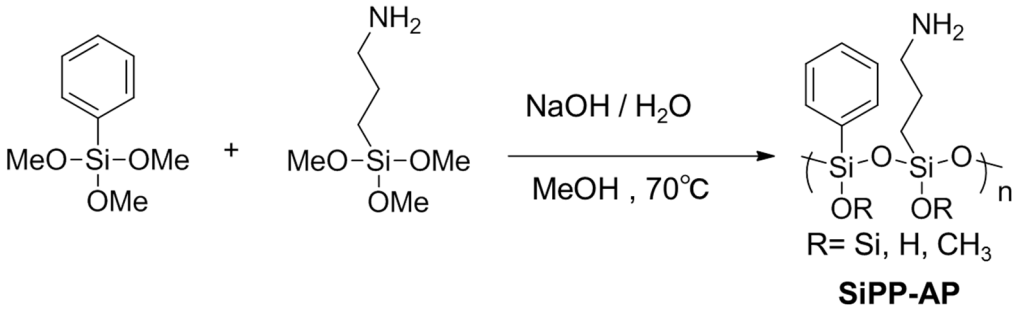

Scheme 1. Reaction scheme of SiPP-AP

6.2.1.2 Sample preparation: Si-film

SiPP-AP (1.00 g) and blocked isocyanate (0.76 g) were dissolved in methyl isobutyl ketone (1.00 g). Blocked isocyanate was synthesized by protecting the hexamethylene diisocyanate uretdione (ASAHI KASEI) with 3, 5-dimethylpyrazole (Tokyo Chemical Industry Co., Ltd.) in acetone. The blocked isocyanate was reacted with SiPP-AP in a ratio of 1.0 isocyanate groups per amino group of SiPP-AP. Blocked isocyanate groups can regenerate reactive isocyanate groups at curing temperatures by detaching the blocking agent that can react with the amino functional groups of SiPP-AP to form a urethane linkage. To simulate a typical automotive topcoat, the coating was prepared by successively applying an electrodeposition coating, an intermediate coating, and a base coating over a steel substrate to coat a 50-μm-thick film after curing. The Si-film was cured at 140°C for 30 min (Scheme 2). Samples for dynamic mechanical analysis were prepared by coating on a PP plate, followed by baking in a hot air oven at 140°C for 30 min and then peeling. The average thickness of the free-standing coating films (5 mm×30 mm) was 50 μm.

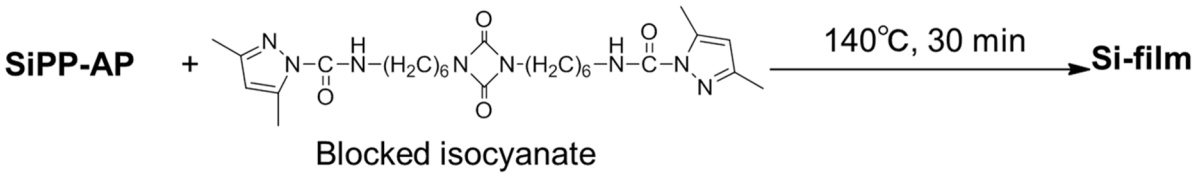

Scheme 2. Reaction scheme of Si-film

6.2.1.3 Sample preparation: C-film

A 1000 ml separable flask was loaded with methyl methacrylate (22.8 wt%), 2-hydroxyethyl methacrylate (32.2 wt%), caprolactone-modified methacrylate (25 wt%), Styrene (20 wt%), and methyl isobutyl ketone. Nitrogen gas was bubbled into the solution for 30 min to remove dissolved oxygen. After adding tert-butyl peroxy-2-ethylhexanoate (Nippon Oil & Fats Co., Ltd. PERCURE® O) (10 PHR) as an initiator to the solution, the solution was placed in a thermal bath at 110°C for 6 h to obtain an acrylic polyol with a hydroxyl content of 178 mg KOH/g. An isocyanate curing agent and toluene were added to the mixture to obtain a liquid coating. The isocyanate curing agent was a trimer of 1,6-hexamethylene diisocyanate (Asahi Kasei Chemicals Corporation, Duranate™ TPA-100, NCO content of 23%). The isocyanate curing agent was reacted with the acrylic polyol in a ratio of 1.0 isocyanate groups per hydroxyl group. The coated plate used for the scratch test and the free film for measuring the dynamic viscoelasticity were obtained by the same method used for the Si-film.

6.2.2 Characterization of SiPP-AP

・Thermogravimetric analysis

The relative composition by weight of organic groups in SiPP-AP was estimated by thermogravimetric analysis (EXSTAR 6000 TG/DTA 6300, Seiko Instruments Inc.) For each measurement, 17 mg of dried powdered sample was placed in a platinum sample pan and analyzed in the range from 25 to 900°C at a heating rate of 5°C/min with 0.5 L/min of air flow.

・Fourier transform infrared spectroscopy (FT-IR) measurement

FT-IR spectra were measured using a FT-IR AVATAR360 (Thermo Nicolet) in attenuated total reflection mode. Each spectrum was the average of 32 scans using a spectral resolution of 2 cm^{-1}, and a diamond prism was used.

・^{29}Si-NMR spectroscopy

Conversions for the polymerizations were estimated by ^{29}Si HD MAS NMR spectroscopy (AVANCE 400, manufactured by Bruker BioSpin).

6.2.3 Characterization of Si-film, C-film

6.2.3.1 Scratch behavior

Scratch tests were carried out on a CSM micro scratch tester using a diamond stylus with a 0.1 mm tip radius at 25°C and 50-52% RH. The scratch behavior of coatings can be evaluated in terms of the load at penetration depth (Pd) during scratching and the residual depth (Rd) after scratching. The typical scratch procedure is described below.

(a) A pre-scan with a very small constant load (0.05 N) was carried out to measure the surface profile and initial surface profile.

(b) Progressively increasing the load from 0.05 N to 1.96 N at scratch speed of 300 mm/min for a scratch length of 100 mm.

(c) A post-scan with a very small constant load (0.05 N) was carried out to measure the residual scratch depth in damaged coatings after scratching.

The penetration depth can be calculated as the difference between the displacement of the stylus in step b) and the depth measured in the initial surface profile ((b)–(a)). The residual depth can be calculated as the difference between the depth of the scratch deformation measured in the post-scan and the depth measured in the initial surface profile ((c)–(a)). The elastic recovery index was determined from Pd and Rd using equation (1).

$$Elastic\ recovery\ index = \frac{Pd-Rd}{Pd} \times 100 \quad (1)$$

The time dependence of scratch deformations caused by the macro-scratch tester at 1.96 N of force was measured from 15 min to 24 days after the scratch test by confocal microscopy (Lasertec OPTELICS H1200).

6.2.3.2 Dynamic mechanical analysis

DMA measurements were performed using an ITK Co., Ltd. DVA-220 dynamic mechanical analyzer. The DMA test was performed at a frequency of 1 Hz and a strain of 1%, with temperatures ranging from -50 to 160°C and a heating rate of 5 K/min.

6.3 Results and Discussion

6.3.1 Characterization of SiPP-AP

SiPP-AP obtained by the hydrolysis/dehydration condensation reaction of PTMS and APTMS was a transparent viscous liquid, soluble in general purpose solvents such as THF, acetone, ethyl acetate, and *N*, *N*-dimethylformamide. This indicates that SiPP-AP has the possibility of being a suitable base resin for the coatings. The thermal properties of the coatings were characterized by TGA in air to confirm that they corresponded with the mass ratio of the raw materials (Figure 1). For SiPP-AP samples, a 52% weight loss was observed from 200 to 700°C. After the weight loss of the SiPP-AP above 700°C, the weight loss of the sample approached 48%. This suggests that the amount of inorganic moieties in the resin remain in a platinum sample pan. The measured weight loss corresponded closely to the theoretically calculated fraction of inorganic moieties in the raw materials, which was 50%. The TGA characterization results indicated that the obtained SiPP-AP had the same composition ratio of PTMS and APTMS used in its preparation.

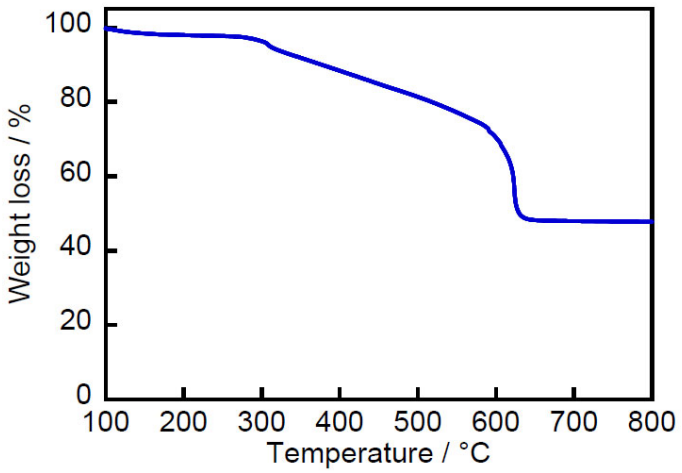

Figure 1. Weight loss of SiPP-AP on heating

6.3.1.1 Characterization of Si-film

A clear and crack-free Si-film was successfully prepared by reaction between SiPP-AP and blocked isocyanate (Figure 2). This suggests that the Si-film may be suitable for clearcoats.

Figure 3 shows FT-IR spectra of a prepared Si-film and SiPP-AP that are useful for evaluating the crosslinking reaction. Characteristic absorption peaks at 3440 cm^{-1} (ν_{Si-OH}), 3335 cm^{-1} (ν_{N-H}), 2930 cm^{-1} (ν_{C-H}), 1640 cm^{-1} (ν_{N-H}), 1510 cm^{-1} (ν_{N-H}), 1430 cm^{-1} (ν_{phenyl}), 1097 cm^{-1} ($\nu_{as,Si-O-Si}$), and 1024 cm^{-1} ($\nu_{as,Si-O-Si}$) were observed in SiPP-AP. Therefore SiPP-AP exhibited both a 1430 cm^{-1} phenyl group peak and 1640 cm^{-1} and 1510 cm^{-1} amino group peaks, indicating that the structure of PTMS and APTMS was maintained in the SiPP-AP. However, some changes in peak patterns were observed after curing, which increased the absorption peaks at 3335 cm^{-1}, 1640 cm^{-1}, and 1510 cm^{-1}. Therefore, amino groups of SiPP-AP had reacted with isocyanate groups through the formation of stable urea bonds. As expected, the Si-film was crosslinked SiPP-AP.

^{29}Si NMR spectra of SiPP-AP and Si-films (shown in Figure 4) were used to evaluate the condensation reaction. In the solid-state ^{29}Si NMR spectra, chemical shifts of -45 to -90 ppm were observed in four signals with different degrees of condensation. Four kinds of signals were observed at -57 ppm (C-Si=$(OSi)_2(OR)$, T^2), -65 ppm (Phenyl-Si$(OSi)_2(OR)$, $T^{2'}$), -72 ppm (C-Si≡$(OSi)_3$, T^3) and -80 ppm (Phenyl-Si≡$(OSi)_3$, $T^{3'}$), reflecting a highly condensed material in the SiPP-AP sample. The peak areas of T^2 and $T^{2'}$ decreased from SiPP-AP to Si-film, which indicates that the heating step used in curing may account for the increasing silanol condensation rate.

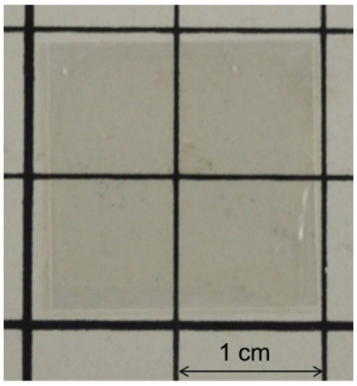

Figure 2. Photograph of Si-film

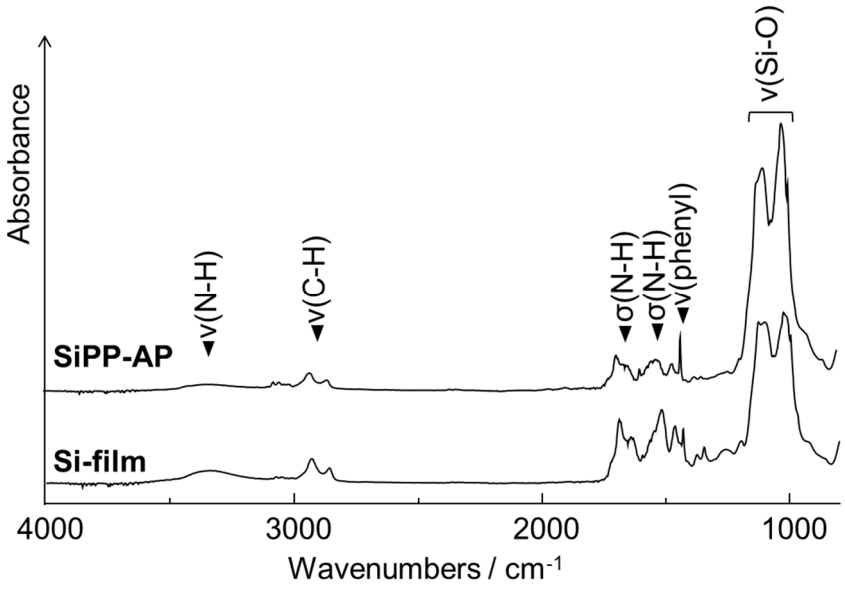

Figure 3. FT-IR spectrum of SiPP-AP and Si-film

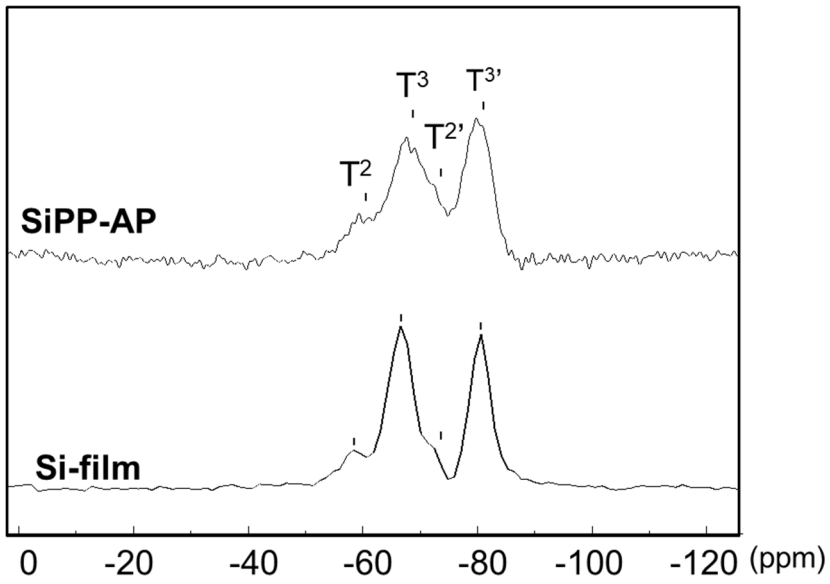

Figure 4. ^{29}Si-NMR spectrum of SiPP-AP and Si-film

6.3.1.2 Viscoelastic properties of films

The scratch recovery characteristics are related to viscoelastic properties. To compare the viscoelastic behavior of the films made of different main chain structure, Figure 5 shows storage modulus (*E'*) and tan δ against temperature obtained by DMA.

*E'*of the Si-film at room temperature was 1.1 GPa, compared to 1.8 GPa for the C-film, which was almost the same order of storage modulus. This indicates that the hardness of Si-film is similar to those of C-film at room temperature. *E'*of C-film drops about two orders or more around 70°C, which is so called glass transition, while that of Si-film gradually decreased about one order in wider temperature range. Glass transition makes large change in viscoelastic properties in C-film, so that the scratch recovery ability also largely changes. In the other hand, Si-film, which indicates no sharp transition in viscoelastic properties, holds the same scratch recovery ability through temperatures mentioned here. Though it is not clear that what parameter controlled the scratch recovery rate, Si-film has definitive advantage by low dependency of viscoelastic properties on temperature.

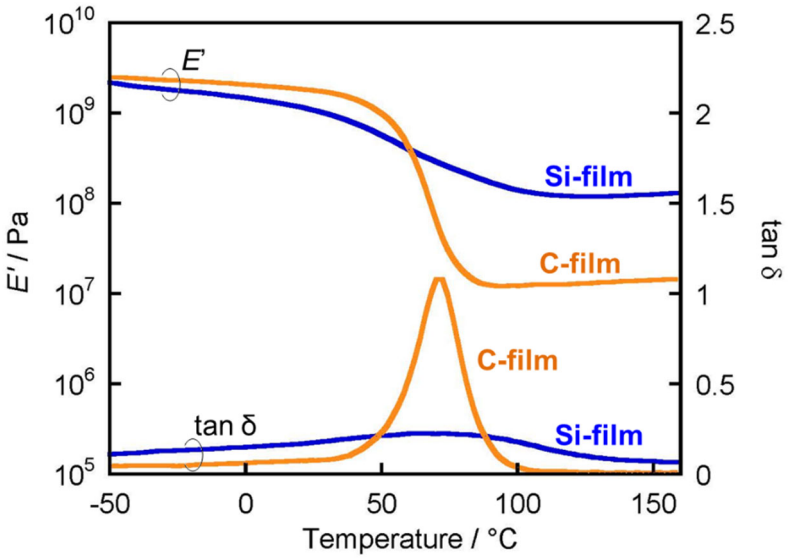

Figure 5. Dynamic storage modulus and tanδ

6.3.2 Scratch and recovery characteristics

6.3.2.1 Elastic recovery of scratch deformation

Figure 6 shows scratched surface images and scratch profiles during the aforementioned scratch test, indicating the progress of Pd and Rd on Si-films and C-films. The progress curves of Pd and Rd each exhibited a linear relationship with the vertical load. No fracture was observed on both coatings. The scratch depths at 1.96 N on Si-film recovered from 18.6 µm to 2.4 µm, whereas C-film recovered from 17.3 µm to 4.9 µm. While the Pd values of Si-film and C-film were similar, immediately after the scratch test the Rd value at 1.96 N of Si-film was less than that of C-film. The elastic recovery index after the scratch test was superior for the Si-film, which recovered 87%. The C-film only recovered 72% (Table 1).

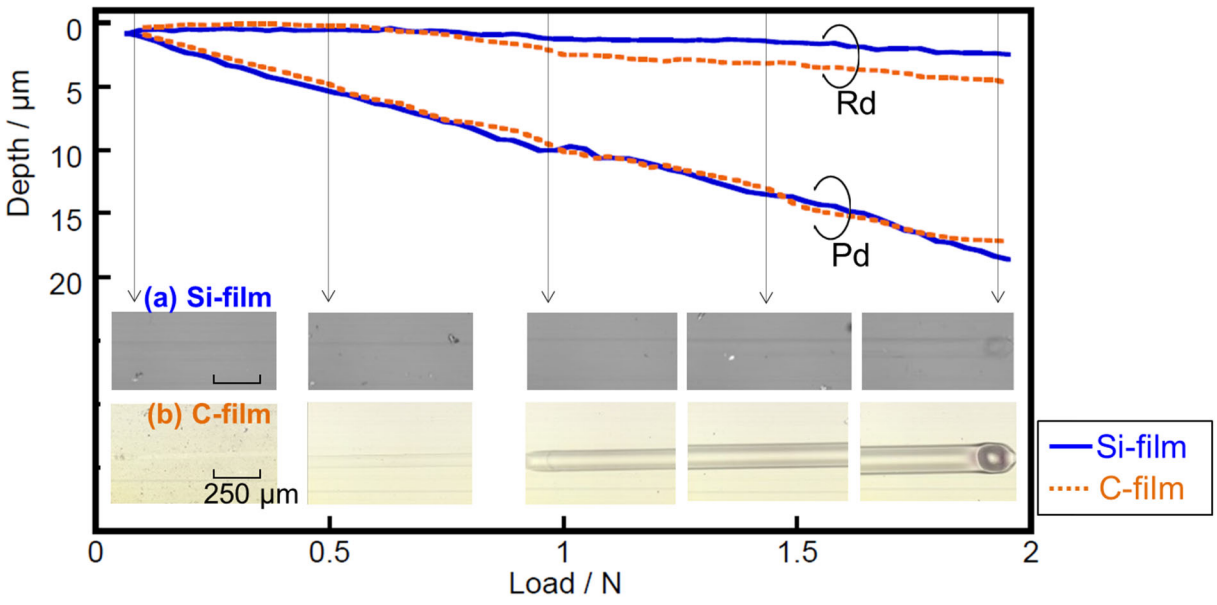

Figure 6. (Top) Progressive load scratch testing curve of Si-film(blue solid line) and C-film(red dotted line), (Bottom) Scratched surface (a) Si-film, (b) C-film

Table 1. Elastic recovery index at 1.96 N.

	Elastic recovery / %
Si-film	87
C-film	72

6.3.2.2 Residual deformation for 15 min after scratch test

Figure 7 shows images and cross-sectional profiles of scratch deformations 15 min after scratch testing at 1.96 N. A shallow groove and small shoulders were observed in the Si-film, while a deep groove over 4 μm deep and shoulders over 3 μm high were observed in the C-film. On the Si-film, the micro scratches were significantly flatter, and it was difficult to detect any residual deformation with the naked eye after 15 min.

In the Si-film tested at 1.96 N, the scratch depth recovered from 2.4 μm to 0.9 μm 15 min after scratch, whereas the C-film recovered from 4.9 μm to 4.1 μm. The Si-film recovered about twice as fast as the C-film. Thus, the Si-film demonstrated superior scratch recovery characteristics.

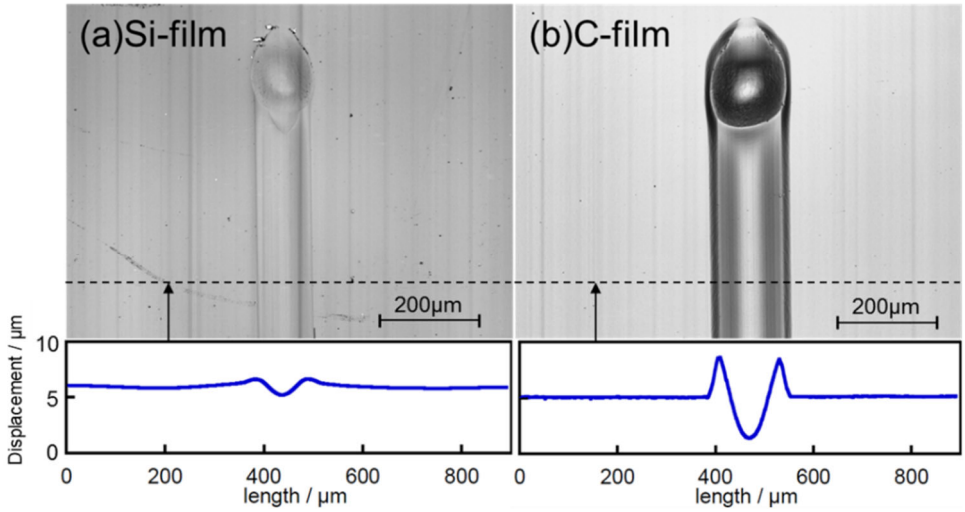

Figure 7. Scratch deformation remained after 15 min of test by micro-scratch tester equipped with 1 mm radius diamond tip.
(Top) Scratched surfaces observed by confocal microscope. Dents indicate scratch ends.
(Bottom) Cross-sectional profiles at load 1.96N.

6.3.2.3 Time dependence of scratch recovery behavior: scratch depth

Figure 8 shows the time dependence of Rd at 1.96 N for Si-film and C-film as measured using an optical confocal microscope at room temperature and covers a time period of 24 days. Rd on the Si-film changed from 0.9 μm to 0.7 μm, indicating that no significant recovery occurred. Rd of the C-film changed from 4.3 μm to 3.7 μm, decreasing linearly with the logarithm of time from 15 min to 24 days. Rd of the C-film recovered over time, which is too slow change more than 24 days, so scratch deformation of the C-film might remain as permanent damage. In contrast, Rd of the Si-film changed slightly because the strain was relaxed by 15 min after the scratch test, so a scratch deformation of 1 μm or less would remain but would be invisible to the naked eye.

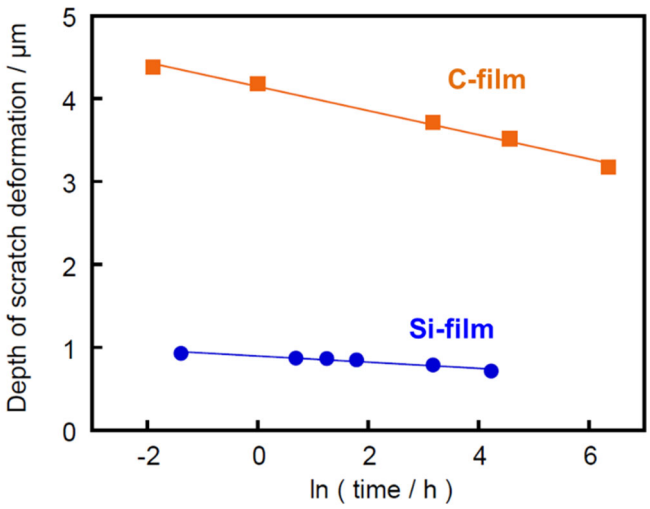

Figure 8. Scratch depth change in Si-film and C-film

6.4 Conclusion

The aim of this study was to investigate and demonstrate the superior scratch recovery capability of automotive coatings compared to conventional coatings. Si-films crosslinked with polyorganosilsesquioxane was prepared, and its recovery behavior was compared with that of a conventional coating (C-film). The Si-film was transparent and free of cracks, indicating its potential use as a clearcoat. The Si-film had a 20% higher elastic recovery index than the C-film, despite the same indentation depth. Over time, the Si-film recovered about twice as fast as the C-film, demonstrating the superior scratch recovery behavior of the Si-film. Scratch deformations on the Si-film almost disappeared after 15 minutes, even at room temperature.

Consequently, I have demonstrated that Si-film achieves both a hardness suitable for automobile coatings and superior scratch recovery behavior beyond that of conventional coatings. Automotive coatings based on a siloxane main chain may offer dramatically improved self-recovery.

Reference

[1] Courter, J. L., *J. Coat. Technol.*, **1997**, 69, 57–63.

[2] Seubert, C. M. and Nichols, M. E., *J. Coat. Technol.*, **2007**, 4, 1, 21-30.,

[3] Hara, Y., Mori, T. and Fujitani, T., *Progress in Organic Coatings*, **2000**, 40, 1-4, 39-47.

[4] Lin, L., Blackman, G. S. and Matheson, R. R., *Progress in Organic Coatings*, **2000**, 40, 1-4, 85-91.

[5] Seubert, C., Nietering, K., Nichols, M., Wykoff, R. and Bollin, S., *Coatings*, **2012**, 2, 4, 221-234.

[6] Ryntz, R. A., Abell, B. D., Pollano, G. M., Nguyen, L. H. and Shen, W. C., *J. Coat. Technol*., **2000**, 72, 904, 47-53.

[7] Seubert, C., Nichols, M., Henderson, K., Mechtel, M., Klimmasch, T. and Pohl, T., *J. Coat. Technol.*, **2010**, 7, 2, 159-166.

[8] Bertrand-Lambotte, P., Loubet, J. L., Verpy, C. and Pavan, S., *Thin Solid Films*, **2002**, 420, 281-286.

[9] Aleksy, N., Kermouche, G., Vautrin, A. and Bergheau, J. M., *International Journal of Mechanical Sciences*, **2010**, 52, 3, 455-463.

[10] Seubert, C., Nichols, M., Henderson, K., Mechtel, M., Klimmasch, T. and Pohl, T., *J. Coat.*

Technol., **2009**, 7, 2, 159-166.

[11] Kutschera, M., *J. Coat. Technol*., **2006**, 3, 2, 91–97.

[12] Matthijs Groenewolt, *Progress in Organic Coatings*, **2008**, 61, 106–109.

[13] Noh, S. M., Lee, J. W., Nam, J. H., Park, J. M. and Jung, H. W., *Progress in Organic Coatings*, **2012**, 74, 1, 192-203.

[14] Noh, S. M., Nam, J. H., Oh, J. K. and Jung, H. W., *J. Coat. Technol*., **2015**, 12, 1, 85-95.

[15] Yoshii, K., Yamashita, T., Machida, S., Horie, K., Itoh, M., Nishida, F. and Morino, S., *Journal of Non-Crystalline Solids*, **1999**, 246, 1-2, 90-103.

[16] Yoshii, K., Machida, S., Horie, K. and Itoh, M., *Polymer Journal*, **2000**, 32, 1, 37-42.

Chapter 7

Influence of Ionomer Adsorption on Agglomerate Structures in High-Solid Catalyst Inks

7.1 Introduction

Polymer electrolyte fuel cells (PEFCs) are among the most promising high-efficiency, zero-emission automotive power sources. However, several key challenges must be overcome to enable the widespread use of PEFCs; these challenges include reducing their cost as well as improving their productivity, performance, and durability. To resolve these issues, improving the material characteristics and structure of the catalyst layers is critical. These catalyst layers are formed from catalyst inks consisting of carbon-black-supported platinum (Pt) nanoparticles (Pt/C), perfluorinated sulfonic acid ionomers, and a dispersion medium. Because ink formation also affects the catalyst layer microstructure, the ink strongly influences performance [1-4]. To obtain a catalyst layer with the desired microstructure, the underlying principles of the entire process must be understood. In particular, the effects of adsorbed and nonadsorbed ionomers on the Pt/C surface and subsequent changes in the structure of Pt/C should be investigated in detail because these factors are affected by both the type of Pt/C [5, 6] and the composition of the dispersion medium [7-9].

Previous studies have examined ink formation using dynamic light scattering (DLS) [10], ultra-small-angle neutron scattering (USANS) [11, 12], ultra-small-angle X-ray scattering (USAXS) [5], and transmission electron microscopy (TEM) [13, 14]. These techniques require the sample to be sufficiently diluted to allow light or a beam to pass through the sample without substantial scattering. When the stability and interaction of particles is investigated using the Derjaguin–Landau–Verwey–Overbeek (DLVO) theory to characterize the competition between repulsive electrostatic forces and the van der Waals attraction force, diluted catalyst ink (<1 wt%) is commonly used [15, 16]. However, the agglomerated structures of Pt/C in catalyst inks are not yet fully understood because of a lack of evaluation methods that do not involve dilution, especially for high-concentration catalyst inks. On the basis of rheology and electrical conductivity measurements, I propose that Pt/C should be treated as an agglomerate with a fractal structure and a network in the case of high-solid (HS) catalyst inks. Therefore, this paper mainly discusses the agglomeration of Pt/C by focusing on ionomer adsorption onto the surface of Pt/C in a HS catalyst ink.

Carbon black (e.g., Vulcan® and Ketjenblack®) is commonly used as a carbon support in Pt/C. Carbon black has a hierarchical structure composed of primary particles with sizes ranging from 10 to 100 nm, which are strongly bonded together to form structures called aggregates, which are then formed by van der Waals attraction force into agglomerates (Figure 1). The size of agglomerates is

difficult to measure because their structure breaks up under shear flow. However, combinations of rheological and other measurements can be used to characterize the microstructure without dilution. For example, the network structures in carbon black suspensions for lithium-ion batteries [17] and redox flow batteries and capacitors [18-21] have been evaluated using a rheometer and AC impedance measurements.

In addition, when a carbon black slurry exhibits elastic properties, it can be considered a colloidal gel with a network consisting of agglomerates. One of the most useful evaluation methods to quantify the structure of these agglomerates is fractal analysis. Several experimental techniques are available to analyze the fractal dimensions in agglomerates using rheology, microscopy, and scattering [22]. From the standpoint of rheological measurements, a strongly agglomerated slurry displays a plateau modulus G'_0 with a power-law dependence on the particle volume fraction ($G'_0 \propto \phi^A$). The fractal dimension (df) is determined by the scaling exponent A, and models have been compared based on scaling theory. Various scaling-theory models have been proposed [23]. When df = 1.8, fractal-like structures become much more open because of diffusion-limited cluster aggregation (DLCA) [22]. DLCA is a fast process of cluster aggregation via van der Waals attraction force. The clusters move by Brownian motion and adhere to each other upon contact, which occurs when a high salt concentration is added to the suspension. Greater values of df indicate denser agglomerates. When df = 2.1, agglomerate structures are formed using more compact clusters via reaction-limited cluster aggregation (RLCA). RLCA is a slow process of cluster aggregation under a repulsive barrier, such as an electrostatic repulsive barrier due to the surface charge of the particles or a steric repulsive barrier due to adsorbed dispersants. Compact clusters form because, as a consequence of the repulsive barrier, clusters collide many times before actually sticking together. This process leads to some degree of interpenetration. These two regimes have been confirmed by simulations and experiments using various colloidal particles [24]. This analysis has been applied to manufacturing processes to, for example, predict the rheological properties of slurries used for lithium-ion batteries [25] and to analyze slurries for high-performance redox flow batteries and capacitors [21]. Although fractal analysis has not been previously applied to HS catalyst inks, I demonstrate in the present study that it is an applicable and useful index value for agglomerate structures. In addition, rheological analysis provides useful information about the microstructure, aiding identification of the coating performance and storage

stability of HS catalyst inks in manufacturing processes.

Hence, in this research, I investigated the relationship between the Pt/C agglomeration structure in HS catalyst inks and the extent of ionomer adsorption by Pt/C by examining the rheological behavior, electrical conductivity, and sedimentation of the inks. The adsorption was controlled by the water content of the dispersion medium. The fractal dimensions were evaluated from rheological data when the volume fraction of Pt/C ($\phi_{\mathrm{Pt/C}}$) changed. Furthermore, the effects of changing the type of Pt/C on the surface characteristics of Pt/C in the same dispersion medium are discussed.

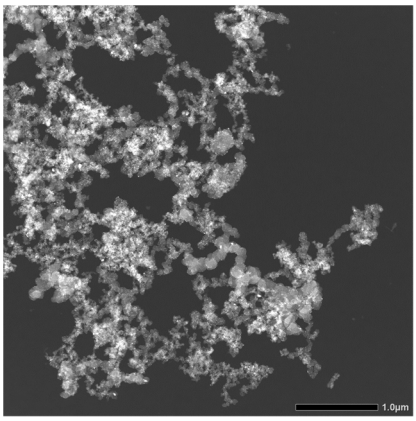

Figure 1. Typical TEM image of Pt/C agglomerate dried on a grid.

7.2 Materials and Methods

7.2.1 Catalyst ink preparation

The performance of PEFCs depends on the water/1-propanol ratio in the catalyst inks [26, 27]. Thus, four catalyst ink series containing different ratios of the water/1-propanol dispersion medium were examined. In addition, HS catalyst inks with a high alcohol content increase the risk of the Pt catalyzing combustion of the alcohol. I therefore chose water-rich catalyst inks with 48–89% water content. Furthermore, the type of Pt/C affects the microstructure of the catalyst inks and their rheological behavior [5]. Thus, three catalyst ink series with different types of Pt/C and the same dispersion medium ratio (water/1-propanol = 67/33) were examined. Table 1 summarizes the compositions of the catalyst inks. Pt/Vulcan (TEC10V30E, carbon black: Vulcan XC72R®, primary particle size 10–40 nm [28]) and Pt/Ketjen (TEC10E40E, carbon black: Ketjenblack®, primary particle size ~30 nm [29]) were purchased from Tanaka Kikinzoku Kogyo. Pt/Ketjen has a greater surface area and larger internal pore volume than Pt/Vulcan [5]. Vulcan (Vulcan XC72R®) with no Pt was purchased from Cabot Corp. All of the Pt/C types and solvents were used without further purification.

Ultrasonication enhances the dispersion of Pt/C because of the power input; however, achieving a completely uniform catalyst ink is difficult. A mixer enhances the uniformity of the whole catalyst ink. Moreover, insufficient degassing of the catalyst inks can adversely affect their rheological behavior. Therefore, ultrasonication, mixing, and degassing were used in the present work to prepare the catalyst inks [30].

In a typical experiment, a 20 mL sample tube was loaded with $0.005 \leq \phi_{Pt/C} \leq 0.067$ of Pt/C or carbon black and 5.5 wt% Nafion® (D2020 manufactured by The Chemours Co.). This sample was added to a dispersion consisting of water and 1-propanol in a ratio of 48:52, 67:33, 75:25, or 89:11, and a planetary mixer/deaerator (the MAZERUSTAR® KK-250S manufactured by Kurabo Industries Ltd.) was used for degassing and mixing for 4 min. The mixture was sonicated for a total of 15 min using an ultrasonic homogenizer (UH-600, SMT Corp.), followed by degassing and mixing for 4 min.

The acid capacity of the Nafion® used in the catalyst inks was 1.05 meq/g. The ionic strength of the catalyst inks was 0.058 mol/L. The Debye length ($1/\kappa$) was estimated using Equation (1):

$$1/\kappa = 1/\sqrt{\frac{2000e^2 N_A c z^2}{\varepsilon\varepsilon_0 kT}} \quad (1)$$

where e is the elementary charge (1.602×10^{-19} C), N_A is Avogadro's number (6.022×10^{23} mol^{-1}), ε_0 is the absolute permittivity of vacuum (8.854×10^{-12} F/m), k is the Boltzmann constant (1.381×10^{-23} J/K), c is the ionic strength (mol/L), z is the ion valency, ε is the relative permittivity of the dispersion medium, and T is the temperature (K). The $1/\kappa$ value of these catalyst inks, as determined using Equation (1), ranged from 1.0 to 1.2 nm at 25°C. Electrostatic repulsion due to the electrical double layer was eliminated by adding a high concentration of the Nafion ionomers, thereby making the Pt/C aggregates highly attractive.

Table 1. Sample specifications of catalyst inks

Sample series	Pt/C	Ionomer	Solvent
	Pt/C particles	Mass of Nafion (wt%)	Water:1-propanol ratio in the dispersion medium (w/w)
48% water ink	TEC10V30E	5.5	48:52
67% water ink	TEC10V30E	5.5	67:33
75% water ink	TEC10V30E	5.5	75:25
89% water ink	TEC10V30E	5.5	89:11
Pt/Vulcan ink	TEC10V30E	5.5	67:33
Pt/Ketjen ink	TEC10E40E	5.5	67:33
Vulcan ink	Vulcan XC72R®	5.5	67:33

7.2.2 Characterization of catalyst ink

7.2.2.1 Measurement of the adsorption ratio of ionomers on the surface of Pt/C

To evaluate the adsorption ratio of the ionomers on the Pt/C, a supernatant solution without Pt/C was separated from the catalyst ink by filtration and weighed. This experiment was carried out using a microelectronic balance (BM-20, A&D Co.) with 0.001 mg readability. The concentration of the ionomers in the supernatant (*Cp*) was measured by weighing the supernatant before and after vaporization of the dispersion medium at 80°C. Dividing the difference between the initial

concentration of the ionomers (Cp_0) in the catalyst inks and Cp by Cp_0 gives the adsorption ratio (Γ) of the ionomers on Pt/C (Equation (2)):

$$\Gamma = \frac{Cp_0 - Cp}{Cp_0} \quad (2)$$

The measurement was repeated twice, and measurement errors were recorded. In instances where the error bars are smaller than the symbol size, the error bars cannot be seen in Figure 3.

7.2.2.2 X-ray photoelectron spectroscopy (XPS)

The C and O elements of the Pt/C surface were characterized and the C 1*s* spectra were recorded by XPS (Quantera SXM, ULVAC-PHI) using Al Kα monochromatic radiation. The energy shift due to charging was corrected by setting the C 1*s* binding energy to 284.5 eV.

7.2.2.3 Rheological measurements

A rheometer (MCR301, Anton Paar GmbH) with a cone plate fixture (50 mm diameter, 1° angle, and 0.101 mm gap) was used. To ensure reproducible results, a pre-shear process was carried out to remove the shear history. A rheological measurement protocol was followed: (1) Catalyst inks were loaded onto a plate using a spoon. (2) The catalyst inks were sheared in one repetition at a shear rate from 0.01 s^{-1} to 1000 s^{-1} as the pre-shear process. (3) After the pre-shear process, the steady flow viscosity (η) was measured from 0.01 s^{-1} to 1000 s^{-1}. (4) After a quiescent rest for 3 min, (5) the amplitude of the oscillatory strain was changed from 0.01% to 1000% at a frequency of 1 Hz and the evolution of the storage modulus (G') and loss modulus (G'') vs strain was recorded. The experiments were performed at 25°C. The yield stress (σ_y), which is defined as the minimum shear stress required to initiate flow, was obtained by fitting the low-shear-rate regime to the Herschel–Bulkley model (Equation (3)):

$$\sigma = \sigma_y + k\dot{\gamma}^n \quad (3)$$

The plateau storage modulus (G'_0) was extrapolated from the data corresponding to 0.01–0.03% data. The limit strain of linearity (γ_0)) was determined by the point at which G' deviates by more than 10% from a constant value G'_0.

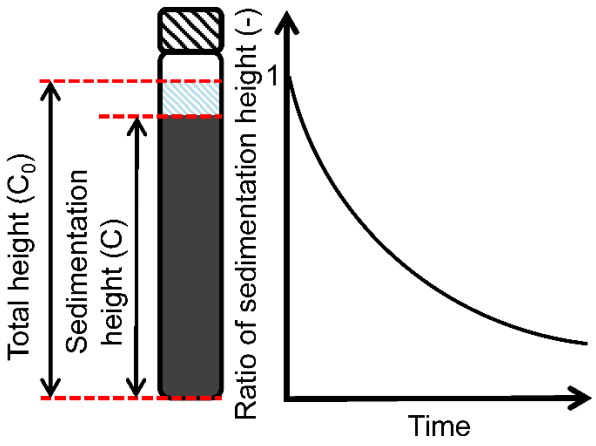

Figure 2. Sedimentation test

7.2.2.4 Sedimentation test

The catalyst inks were poured into glass tubes, where they separated into a clear supernatant and a sedimentation layer over time. The sedimentation height (C) over the total height (C_0) was measured as a function of the settling time (Figure 2).

7.2.2.5 Electronic conductivity measurement

Parallel plates (diameter = 25 mm, A = 491 mm^2) were connected to a rheometer (ARES-G2, TA Instruments) and a potentiostat (HA-151B, Hokuto Denko Corp.) as electrodes. The catalyst inks were placed between the electrodes, which were arranged with a gap (l) of 1 mm. When a voltage of E = 0.3 V was applied, the stabilized plateau current I was measured after approximately 2 min. The conductivity was calculated from Equation (4). All tests were performed at 25°C. During measurement, the solvent was filled near the parallel plates and a lid was used to minimize air exposure and protect the catalyst inks from evaporation.

$$\sigma = \frac{I}{E} \cdot \frac{l}{A} \tag{4}$$

7.3 Results and Discussion

7.3.1 Adsorption ratio of ionomers on the surface of Pt/C

Figure 3(a) shows the adsorption ratio of the ionomers on the Pt/C in the different dispersion media. The results show that the highest adsorption ratio was achieved for the ink containing 89% water and that the adsorption ratio decreased with increasing addition of 1-propanol. This trend implies that the hydrophobic fluorocarbon backbone of the ionomers adsorbed on the Pt/C surface in 89% water, that the ionomers had a sulfonic acid group that was readily ionized and negatively charged [6], and that the ionomers adsorbed on the Pt/C were dissolved as a result of the increasing 1-propanol content [31, 32].

Among the three Pt/C series, the highest adsorption ratio was achieved with Vulcan ink, followed by Pt/Vulcan ink and Pt/Ketjen ink (Figure 3(b)). Table 2 summarizes the results of the XPS surface chemical analysis of Pt/C. Both the element content and deconvoluted carbon spectra indicate that the Vulcan had a higher carbon content than the other inks. This result indicates that pristine Vulcan is more hydrophobic than Pt/Vulcan and Pt/Ketjen because Pt/Vulcan and Pt/Ketjen might be exposed to acid during the catalyst preparation process. Thus, Vulcan interacts more strongly with the ionomers via a hydrophobic–hydrophobic adsorption mechanism than Pt/Vulcan and Pt/Ketjen [33, 34].

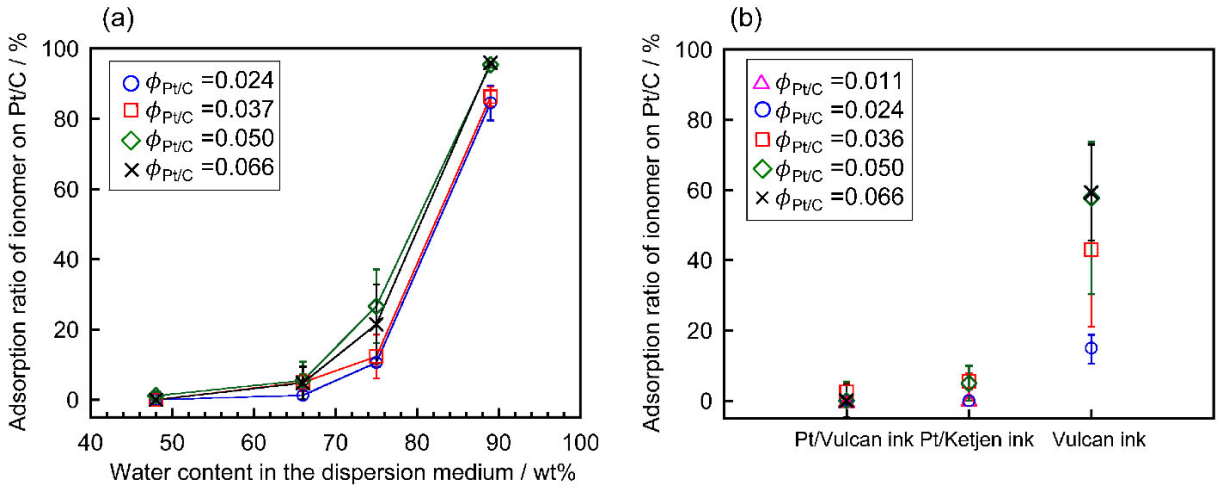

Figure 3. (a, b) The adsorption ratio of the ionomers on the surface of Pt/C in the catalyst inks. Effects of (a,c) the dispersion medium and (b,d) the type of Pt/C.

Table 2. Carbon and oxygen content and deconvolution of C 1*s* peaks by XPS

	Pt/Vulcan	Pt/Ketjen	Vulcan
Content (%)			
C (%)	96.2	96.3	99.3
O (%)	3.8	3.7	0.7
C 1*s* deconvolution			
C=C, C–C, C–H (284.50 eV)	95.9	96.3	98.8
C–O (286.50 eV)	2.1	1.9	0.7
C=O (288.00 eV)	0.5	0.5	0.0
O=C–O (289.00 eV)	1.6	1.3	0.4

7.3.2 Rheological properties

Figure 4 shows the rheological properties of the ink containing 48% water and $0.005 \leq \phi_{\mathrm{Pt/C}} \leq 0.067$ of Pt/C. Figure 4(a) shows the shear-rate dependence of the viscosity. Newtonian behavior was observed in the ionomer dispersion, whereas shear-thinning was observed in the catalyst inks. This result suggests that agglomerates formed in the catalyst inks under static conditions and were broken up by shear. The viscosity increased with increasing amount of Pt/C. Figure 4(b) shows the shear-rate dependence of the stress. The σ_y value increased with increasing amount of Pt/C. Figure 4(c) shows the strain dependence of G' and G''. At $\phi_{\mathrm{Pt/C}} = 0.005$, the storage modulus was lower than the loss modulus, suggesting that the Pt/C was randomly dispersed. At $\phi_{\mathrm{Pt/C}} > 0.024$, the storage modulus was sufficiently higher than the loss modulus in the low-strain regions, further implying that networked Pt/C agglomerates were formed. Agglomerates that displayed an elastic response in low-strain regions showed flow in high-strain regions. In the high-strain regions (>30%), remarkable strain-hardening, which is related to the phenomenon of shear-thickening, occurred as the volume fraction of Pt/C was increased. Figure 4(d) shows G'_0 and G''_0 as functions of the volume fraction of Pt/C. The intersection point of the two straight lines from G'_0 and G''_0 as functions of the volume fraction of Pt/C is defined as the critical volume fraction of the rheological percolation threshold ($\phi_{r,c}$). In the ink containing 48% water, G'_0 and G''_0

exhibited a power-law dependence on the volume fraction of Pt/C and $\phi_{r,c}$ was 0.005. The relationships between G'_0 and G''_0 suggest that the Pt/C agglomerates are randomly dispersed when $\phi_{Pt/C} \leqq 0.005$ and form well-developed network structures when $\phi_{Pt/C} > 0.005$ [35].

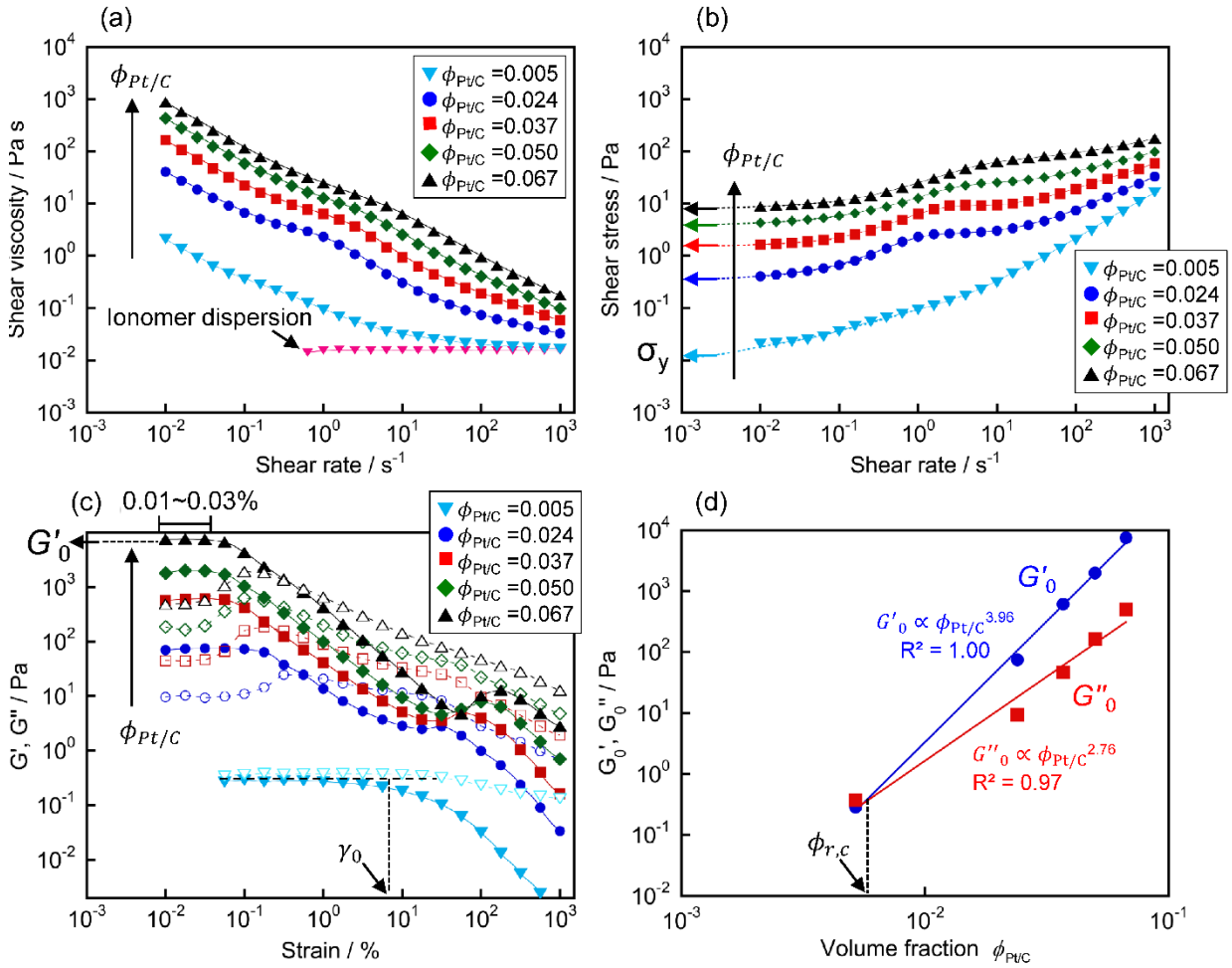

Figure 4. Rheological measurements of ink containing 48% water and $0.005 \leq \phi_{Pt/C} \leq 0.067$ of Pt/Vulcan in 5.5 wt% ionomer solution and a dispersion medium (water/1-propanol = 48/52): (a) steady shear viscosity (η) as a function of shear rate, (b) shear stress (σ) as a function of shear rate (the yield stress values (σ_y) were obtained by fitting to the Herschel–Bulkley model), (c) storage moduli (G') (●) and loss moduli (G'') (○) as functions of the strain amplitude at 1 Hz (the plateau modulus (G'_0) was extrapolated from 0.01–0.03% data), and (d) G_0' and G_0'' as functions of the volume fraction of Pt/C in the catalyst inks (the critical volume fraction ($\phi_{r,c}$) of the rheological percolation threshold was determined from the cross point between G'_0 and G_0'').

Figure 5(a–c) shows the rheological properties of catalyst inks containing $\phi_{Pt/C}$ = 0.050 of Pt/Vulcan with 48–89 wt% water contents in the dispersion medium. The η, σ_y, and G'_0 values decrease with increasing water content. This behavior was interpreted on the basis of the occupied volume fraction of the agglomerates such as carbon black. Loose agglomerates and the three-dimensional network structure of Pt/C with a low df have a higher occupied volume fraction than dense agglomerates of Pt/C with a high df at the same concentration. In addition, the dispersing medium becomes trapped in loose agglomerates of Pt/C as a pseudo-solid phase and the decrease in the volume of the free dispersing medium causes the η, σ_y, and G'_0 of the catalyst ink to increase [36]. Moreover, in the high-strain regions (>30%), the inks containing 48%, 67%, and 75% water exhibit greater strain-hardening with decreasing water content. The ink containing 89% water exhibits no strain-hardening (Figure 5(c)).

Figure 5(d–f) shows the rheological properties of catalyst inks containing $\phi_{Pt/C}$ = 0.037 of different types of Pt/C. In all shear rate regions, η, σ_y, and G'_0 were lowest for the Vulcan ink, followed by the Pt/Vulcan ink and Pt/Ketjen ink. As described by Khandavalli et al., the viscosity of porous carbon is higher than hard-sphere carbon and increases as the effective volume fraction increases [5]. The difference in η between Pt/Vulcan and Vulcan indicates a fractal structure of agglomerates and that the network of Pt/C develops. A comparison of the properties of the catalyst inks with the same $\phi_{Pt/C}$ reveals that, when fractal-like agglomerates are formed into three-dimensional continuous networks in the Pt/Vulcan ink, the η, σ_y, and G'_0 values are large. By contrast, when dense agglomerates and, thus, a sparsely continuous Pt/C network are formed in Vulcan ink, the η, σ_y, and G'_0 values are low. Typical behavior of G' and G'' as a function of strain was observed in the Pt/Vulcan ink and Pt/Ketjen ink in Figure 5(f). G' is constant and greater than G'' at low-strain regions and decreases at high-strain regions. Agglomerates with an elastic response of the gel network in the low-strain region showed breaking and flow of the gel network in high-strain regions, and the cross-point between G' and G'' was considered the gel point. Our evaluation of the fractal dimension and stability properties using G'_0 and σ_y values obtained from rheological data is discussed in section 3.3.

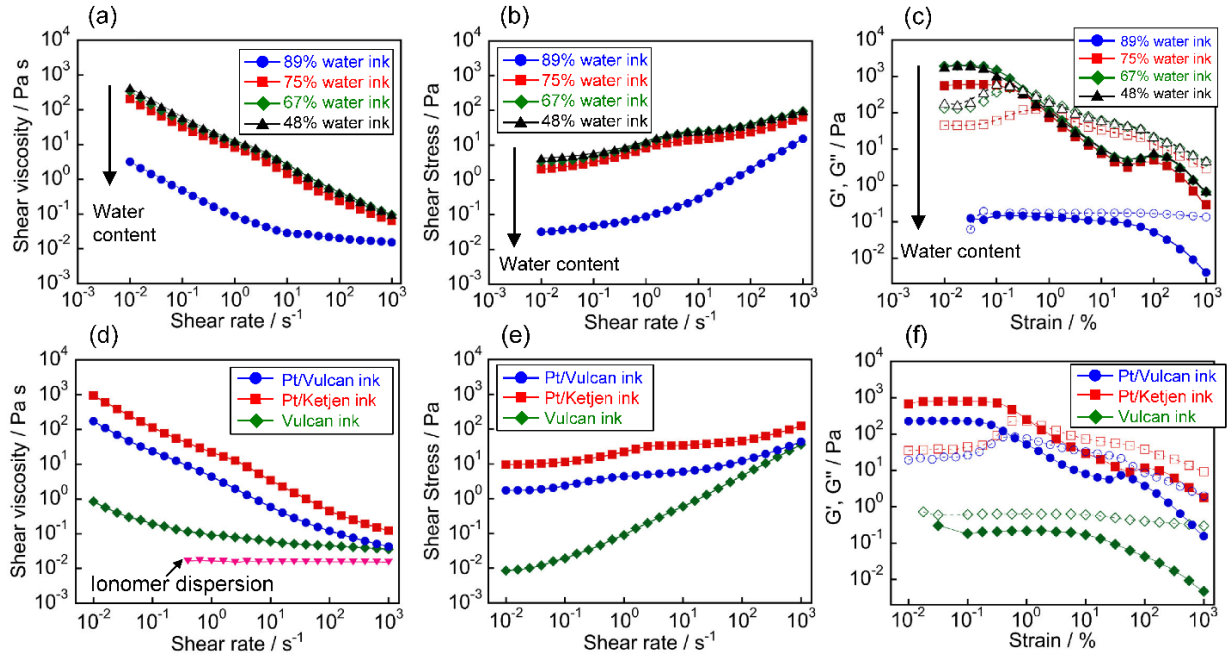

Figure 5. Rheological measurement of (a, b, c) catalyst inks containing $\phi_{\mathrm{Pt/C}}$ = 0.050 of Pt/Vulcan in dispersion media with 48–89 wt% water contents and (d, e, f) catalyst inks containing $\phi_{\mathrm{Pt/C}}$ = 0.037 of different types of Pt/C particles in a 5.5 wt% ionomer solution and a dispersion medium (water/1-propanol = 67/33). (a, d) η as a function of shear rate; (b, e) σ as a function of shear rate; (c, f) G' (●) and G'' (○) as functions of strain amplitude.

7.3.3 Evaluation of fractal dimension (df) from rheological data

Figure 6 shows how σ_y, G'_0, and γ_0 vary as functions of the volume fraction of Pt/C. In all of the catalyst ink series, the values of σ_y and G'_0 exhibit a power-law dependence on the Pt/C loading. Despite the variations, I obtained B from the slope by plotting $\log \gamma_0$ versus the Pt/C loading. From the measured values of G'_0 and γ_0 as a function of ϕ, A and B were calculated from Equations (5) and (6), and df was calculated from Equation (7). The scaling model reported in Ref. [22] that relates the structure of the agglomerates to the elastic properties was applied in the present work.

$$G'_0 \propto \phi^A \tag{5}$$

$$\gamma_0 \propto \phi^B \tag{6}$$

$$A = f(df) = \frac{(d-2)+(d+x)(1-\alpha)}{d-df} \tag{7}$$

The expression for $f(df)$ changes according to the interactions of the cluster constituting the

colloidal gel. Three different gel regimes were identified: strong-link gel (α = 0), weak-link gel (α = 1), and transition gel (0 < α <1) (Equation 7). Here, *d* is the Euclidean dimension 3 and the value of *x* is the fractal dimension of the cluster backbone, which was assumed to be between 1.0 and 1.3. Columns 2 and 3 of Table 3 show the scaling exponents *A* and *B* obtained from rheological measurements. The value of scaling exponent *A* decreases with increasing water content. Shih et al. classified boehmite alumina particle gels into a strong-link gel regime because the values of exponents *A* and *B* ere 4.1 and −2.1 (i.e., the *B* value was negative). Thus, inks containing 48% and 67% water were classified as strong-link gels because these inks have similar *A* and *B* values; df was subsequently calculated from α = 0 and *x* = 1.3 [23, 37, 38]. According to Ikeda et al., protein gels are classified as transition gels because the exponents *A* and *B* are 3.4 and −0.9 (i.e., the *B* value is negative) [38, 39]. Thus, the inks containing 75% water and Pt/Ketjen ink were classified as transition gels because these inks had similar *A* and *B* values; the df was calculated from α = 0.5 and *x* = 1.0. The inks containing 89% water and Vulcan ink were classified as weak-link gels (α = 1) because they exhibited positive *B* values and a much lower G' compared with the other inks at the same concentration.

Column 5 of Table 3 shows the calculated fractal dimensions. The values of df are ~1.7 for the inks containing 48% and 67% water, consistent with the DLCA results. The df values are 2.0 and 2.6 for the inks containing 75% and 89% water, respectively. These inks are assumed to form more compact agglomerates. The df value is 2.6 for the ink containing 89% water, which is quite high and consistent with the RLCA results. Among the different Pt/C series, the df values for the Pt/Vulcan ink, Pt/Ketjen ink, and Vulcan ink were 1.7, 2.1, and 2.6, respectively. I assumed that the inks would form increasingly compact agglomerates in the order Vulcan ink, Pt/Ketjen ink, Pt/Vulcan ink.

Our data were validated against the results of a previous study involving spherical polystyrene particles. Buscall et al. investigated the rheology of strongly flocculated dispersions of polystyrene particles at high concentrations, where a continuous network was formed [40]. They found that $\sigma_y \propto \phi^m$ with $2.5 \leq m \leq 3$ and $G_0' \propto \phi^A$ with $A = 4.3$. The obtained values for *m* and *A* for the polystyrene particles are similar to the corresponding values for the Pt/C agglomerates in a strong-link gel regime.

In addition, Rooij et al. obtained the fractal dimension of weakly aggregating polystyrene latex

dispersions from rheological data [41]. They reported *A* and *B* exponent values of 4.6 ± 0.3 and −2.5 ± 0.3 and a *df* value of 2.0 ± 0.2 calculated from Equation (8):

$$\mathrm{A} + \mathrm{B} = \frac{2}{3-df} \tag{8}$$

In the case of our results, the *df* value calculated from Equation (8) was in the range 1.89–2.1. Thus, the *df* value based on our results is within the same range as that reported by Rooij et al.; however, our results reveal no relationship between the *df* value and the water content in the 48–89% water inks. This discrepancy is likely attributable to differences in *B*, which is sensitive to disruption of the weak-link network. However, the df values for Pt/Vulcan ink, Pt/Ketjen ink, and Vulcan ink obtained using Equation (8) were 2.0, 2.0, and 2.6, in good agreement with our results obtained using α and *x*.

Table 3. The calculated fractal dimension and critical volume fraction of the percolation threshold

	Rheological					Electrical	
	Scaling exponent (A)	Scaling exponent (B)	Regime	Fractal dimension (df)	Critical volume fraction ($\phi_{r,c}$)	Scaling exponent (t)	Critical volume fraction ($\phi_{e,c}$)
48% water ink	4.0	−1.7	Strong-link gel	1.7	0.005	1.9	0.0006>
67% water ink	4.0	−1.9	Strong-link gel	1.7	0.005	1.8	0.0005>
75% water ink	3.3	−1.5	Transition gel	2.1	0.005	1.8	0.014
89% water ink	2.2	0.04	Weak-link gel	2.6	0.048	0.6	0.035
Pt/Vulcan ink	4.0	−1.9	Strong-link gel	1.7	0.005	1.8	0.0005>
Pt/Ketjen ink	3.4	−1.3	Transition gel	2.1	0.003	2.6	0.0005>
Vulcan ink	2.8	2.5	Weak-link gel	2.6	0.065	0.7	0.020

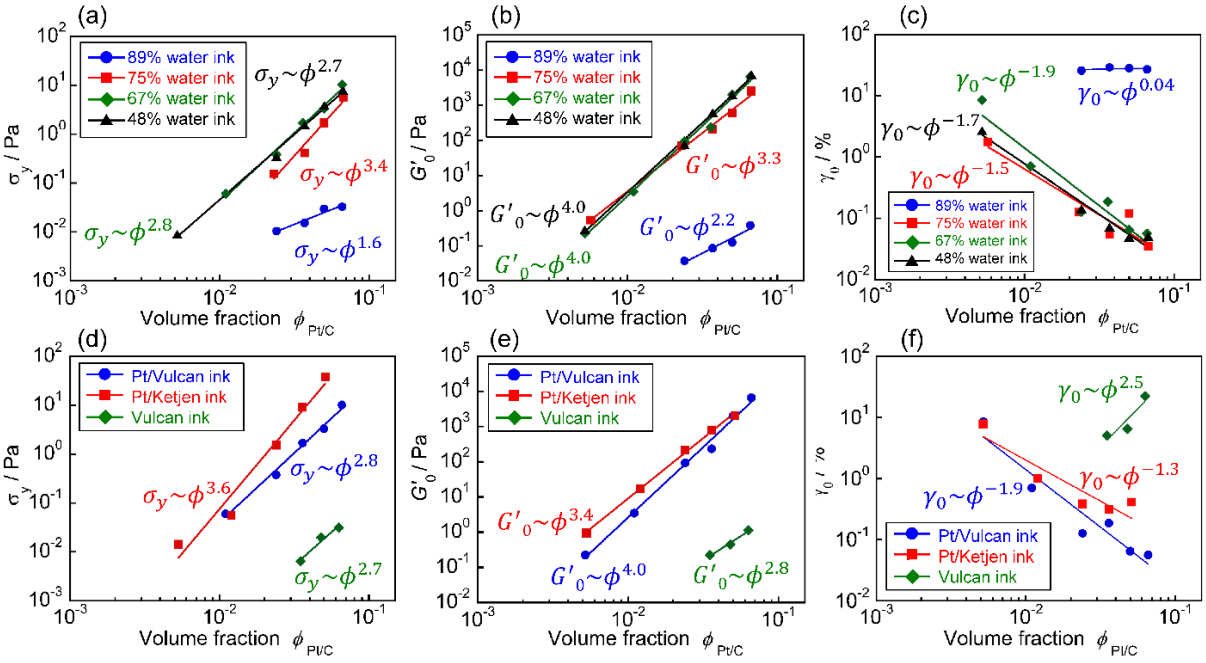

Figure 6. Variation of (a, d) the yield stress (σ_y), (b, e) the plateau storage modulus (G'_0), (c, f) and the limit of linearity (γ_0) with the volume fraction ($\phi_{Pt/C}$) of Pt/Vulcan in 5.5 wt% ionomer solution with different water contents (a, b, c) and different Pt/C particles in 5.5 wt% ionomer solution and a dispersion medium (water/1-propanol = 67/33) (d, e, f).

7.3.4 Stability properties

Figure 7 shows the sedimentation test results. With the inks containing 48%, 67%, and 75% water, $\phi_{Pt/C}$ = 0.011, 0.024, and 0.037 sedimentation occurred 1–5 days after separation between the clear supernatant and sedimentation layer initiated, whereas no sedimentation was observed after at least 30 days at $\phi_{Pt/C}$ = 0.050, 0.066. These results can be interpreted using yield stress σ_y as a representative parameter for the stability properties. Mayer et al. proposed Equation (9) as a method to obtain a stable suspension from the simple force balance between gravity and buoyancy for particles in suspension [42]:

$$\sigma_y \geq \frac{2}{3} a(\rho_p - \rho_l)g \tag{9}$$

where a is the mean diameter of the sediment particles, ρ_l is the density of the dispersing medium, and ρ_p is the density of the particles. Dividing the difference between the gravity force f_g

(= $\pi a^3 \rho_p g/6$) and buoyancy force f_b (= $\pi a^3 \rho_l g/6$) by the cross-sectional area of the particles $\pi a^2/4$ gives the theoretical minimum yield value based on the physical characteristics of the particles involved. If the theoretical yield value exceeds the experimentally determined yield value, sedimentation will occur in the suspension.

In the inks containing 48%, 67%, and 75% water, no sedimentation was observed when $\sigma_y \geq 1.7$ Pa because a continuous network of Pt/C agglomerates was formed, resulting in high yield stress in these inks. When $\sigma_y < 1.7$ Pa, the sediment/liquid interface is clearly separated because the continuous network of Pt/C agglomerates was not sufficiently strong, resulting in gradual sedimentation due to gravity [43]. In Equation (9), when the density of Pt/C (ρ_p = 2.7 g/cm^3) and the density of the dispersion medium (water, ρ_p = 1.0 g/cm^3) are considered, the lowest value of $\sigma_{y,c}$ to start sedimentation is expressed as $44a$. The $\sigma_{y,c}$ value was 1.7 Pa, and the evaluated average diameter of Pt/C agglomerates was a = 75 μm. These values ($\sigma_{y,c}$ = 1.7 Pa, a = 75 μm) agree with the values ($\sigma_{y,c}$ = 1 Pa, a = 100 μm) previously reported for carbon black suspensions [21].

By contrast, no sedimentation was observed after at least 30 days for the ink containing 89% water and the Vulcan ink, even though σ_y was lower by at least one order or more. This result indicates that the Pt/C agglomerates were likely stabilized by the steric and electrostatic repulsion effect of the ionomers [5, 32], inhibiting sedimentation [44].

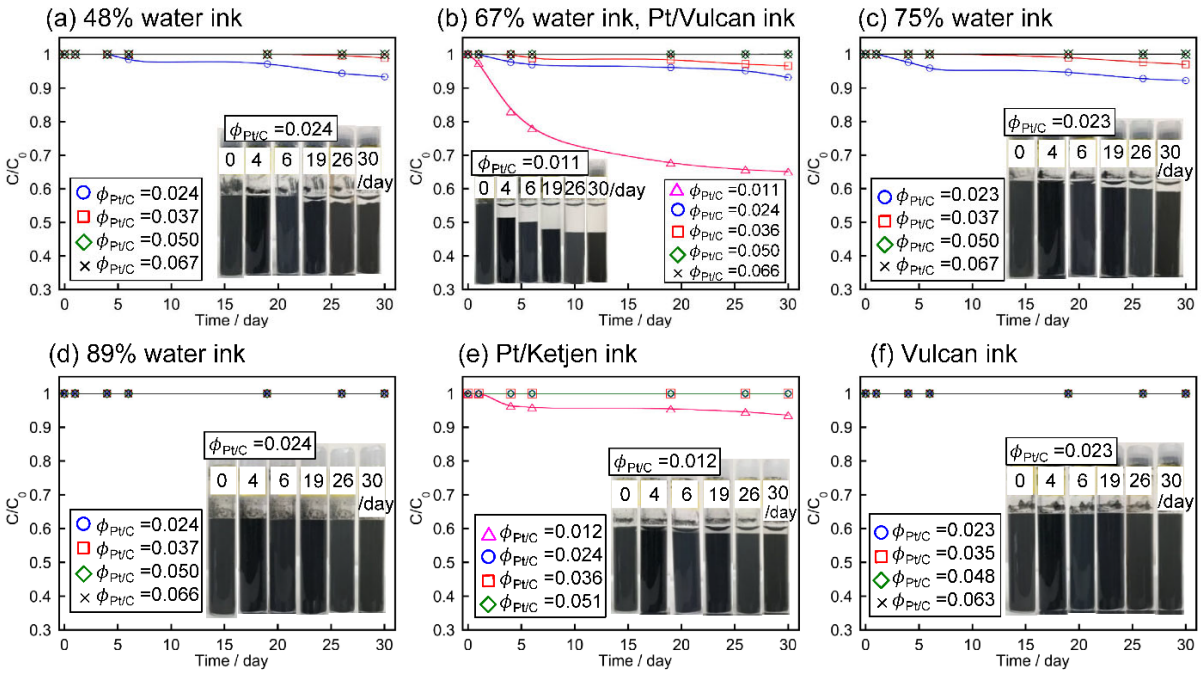

Figure 7. Sedimentation curves for different volume fractions of Pt/C in catalyst inks.

7.3.5 Electrical conductivity of catalyst inks

Measurements of the electrical conductivity of the catalyst inks enable their degree of agglomeration and extent of network structure formation to be evaluated. A comparison of the catalyst inks with the same $\phi_{Pt/C}$ reveals that, when fractal-like agglomerates are formed into three-dimensional continuous networks, the electronic conductivity should be high. By contrast, when dense agglomerates and, thus, sparingly continuous Pt/C networks are formed, the electronic conductivity should be low. The ionomers also prevent the Pt/C nanoparticles from seriously aggregating to form three-dimensional continuous networks, which could affect the electrical conductivity. When network pathways are formed, so-called percolation occurs, which is responsible for a sudden increase in conductivity. This transition occurs at the critical volume fraction of conductivity ($\phi_{e,c}$). The $\phi_{e,c}$ and t values were calculated from the measured electrical conductivity Σ by a least-squares curve fitting according to Equation (10), as listed in columns 7 and 8 in Table 3:

$$\Sigma \propto (\phi - \phi_{e,c})^t \tag{10}$$

Figure 8 shows the relationship between electronic conductivity and the volume fraction of Pt/C.

The inks containing 48% and 67% water show a sharp increase in electrical conductivity when a small amount of Pt/C is added, and a gradual increase when $0.005 \leq \phi_{\mathrm{Pt/C}} \leq 0.067$ is added. The inks containing 75% and 89% water show a gradual increase with increasing amount of Pt/C. Comparing the catalyst inks with the same $\phi_{\mathrm{Pt/C}}$ shows that electrical conductivity increases with decreasing water content (Figure 8(a)). Above the percolation concentration, the electronic conductivity rises continuously, exhibiting a power-law relationship that was fitted using Equation (10) (Figure 8(c)). The $\phi_{e,c}$ value increases with increasing water content, which implies that fractal agglomerates induce a lower percolation threshold (column 8 of Table 3). In terms of *t*, the authors of a previous study reported that *t* is in the range 1.65–2.2, which they theoretically calculated for three-dimensional networks [18]. Thus, a *t* value greater than 1.8 also supports the hypothesis that rigid network structures of Pt/C agglomerates are formed in inks containing 48%, 67%, and 75% water and that a weak-link or partially networked structure of Pt/C agglomerates is formed in ink containing 89% water. Among the different Pt/C series, the electrical conductivity was lowest for the Vulcan ink, followed by those for the Pt/Vulcan ink and the Pt/Ketjen ink (Figure 8(b)). The $\phi_{e,c}$ value was the highest for the Vulcan ink, followed by those for the Pt/Vulcan ink and the Pt/Ketjen ink. The Pt/Ketjen ink may exhibit the highest electrical conductivity because of both the effect of the agglomerate structures and the effect of its lower density per weight.

The electrical conductivity of the carbon black suspensions can be described by two different mechanisms: electrical conduction and electron hopping. Electrical conduction occurs throughout the network when agglomerates are in direct contact with each other [45]. Electron hopping occurs because of the tunneling effect when agglomerates are separated from each other [46]. Richards et al. revealed that electron hopping is the dominant charge transport mechanism for Vulcan and Ketjen suspensions [47]. Our results similarly demonstrate that an electrical percolation threshold smaller than rheological percolation implies that the agglomerates of carbon black are not formed by mechanical contact between the conducting phase when the electrical percolation threshold is reached. Thus, electron hopping occurs in low-concentration catalyst inks.

Moreover, the authors of another previous study reported that carbon black dispersions that form fractal-like agglomerates via DLCA display higher electrical conductivity than carbon black dispersions that form rather dense and spherical agglomerates via RLCA. Carbon black dispersions

that use RLCA for electrical percolation require approximately 2–5 times the amount of carbon black than carbon black dispersions that use DLCA for electrical percolation [21]. These results also demonstrate that a catalyst ink with a lower fractal dimension exhibits greater electrical conductivity than a catalyst ink with a higher fractal dimension because agglomerates formed via DLCA are closer together than agglomerates formed via RLCA. On the basis of a comparison of electrical conductivity, I found that the agglomerates differ in accordance with the dispersion medium and type of Pt/C.

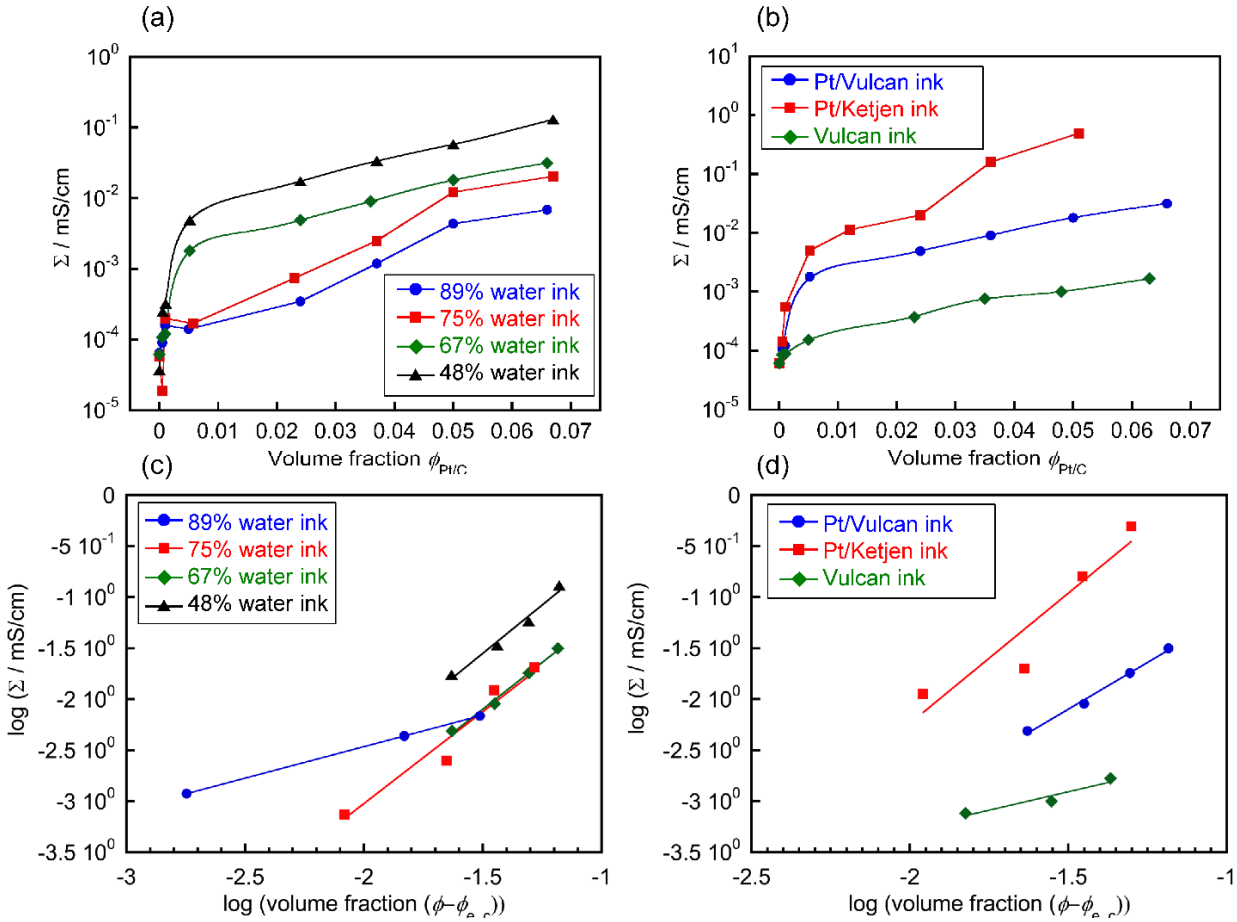

Figure 8. Relationship between electronic conductivity (Σ) and the volume fraction of Pt/C content. (a,c) Effect of the dispersion medium and (b,d) effect of the type of Pt/C, where (c,d) are log–log plots of the electronic conductivity as a function of the Pt/C content.

7.3.6 Catalyst ink formation

In catalyst inks containing 48–75% water, Pt/Vulcan ink, and Pt/Ketjen ink, the amount of adsorbed ionomers was lower; the shear viscosity (η), storage modulus (G'), and Σ thereby increased. The *df* also decreased from 2.1 to 1.7 with decreasing water content. These results demonstrate that the ionomers were not adsorbed on the Pt/C, resulting in the formation of a network of agglomerates by van der Waals attraction force via DLCA (Figure 9(a)). The sedimentation test results also demonstrate that forming a strong network with high σ_y enhanced sedimentation stability.

By contrast, in catalyst inks containing 89% water and Vulcan ink, the amount of adsorbed ionomers was higher, leading to the lowest values for η, G', and Σ and the highest *df* value of 2.6. These results demonstrate that the adsorbed ionomers, through steric and electrostatic repulsion, inhibit the formation of a rigid network (Figure 9(b)). In this case, more compact agglomerates are formed via RLCA because agglomerates are formed only when the repulsive force created by the adsorbed ionomers is overcome. The sedimentation test results also demonstrated that ionomer adsorption produces a highly stable dispersion state, despite the low σ_y.

In conclusion, this research demonstrates that the dispersion medium and type of Pt/C affect the agglomerate structures. The following rheological control method for the coating process can be proposed on the basis of these results. During coating with an HS catalyst ink, a high viscosity can lead to difficulty in the coating and liquid-transfer processes. Catalyst inks with the desired viscosity in the stable coating window can be obtained by changing the water content in the dispersion medium, rather than changing the concentration. Moreover, strain-hardening, which is related to the phenomenon of shear-thickening, can be restricted in the RLCA aggregation process. Shear-thickening adversely affects the quality of coating films with ribbing instability in slot-die coating in the roll-to-roll process [48]. Thus, these methods should be useful for improving the quality of coating films.

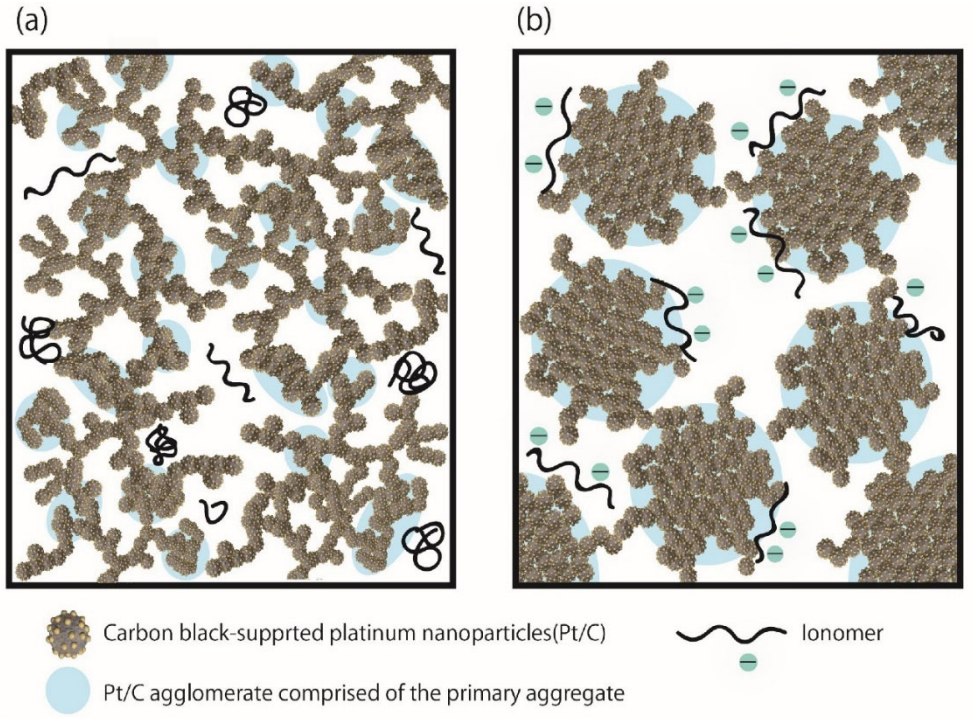

Figure 9. (a) Schematic of diffusion-limited cluster aggregation (DLCA) leading to aggregates with a low fractal dimension (loose aggregates) and that are bound to form a rigid network structure in inks containing 48%, 67%, and 75% water and Pt/Vulcan ink, Pt/Ketjen ink. (b) Schematic of reaction-limited cluster aggregation (RLCA) leading to aggregates with a higher fractal dimension (denser aggregates), which form a weak-link network in ink containing 89% water and Vulcan ink.

7.4 Conclusion

The aim of this study was to investigate the effects of ionomer adsorption on the formation of Pt/C agglomerates in HS catalyst inks. The agglomeration structures of different types of Pt/C in different dispersion media were examined on the basis of the rheological behavior, fractal dimension, stability, and electrical behavior of the dispersed samples.

When 1-propanol was added to the dispersion medium, the amount of ionomers adsorbed on the Pt/C decreased in accordance with the decreasing water content, thereby increasing the η, σ_y, G'_0, and electrical conductivity. The df value also decreased from 2.1 to 1.7 with decreasing water content. These results suggest that low fractal agglomerates and a percolating network with low fractal agglomerates were formed via DLCA in catalyst inks with a low water content.

The amount of ionomers adsorbed on the Pt/C increased when the water content was high, leading to the lowest values for η, σ_y, G'_0, and electrical conductivity. In this case, df reached the highest value of ~2.6, suggesting that more compact agglomerates formed via RLCA, where agglomerates formed a weak-link network as a result of steric and electrostatic stabilization by the ionomers. Similar ionomer adsorption results were obtained with the three Pt/C series.

Consequently, agglomeration can be controlled by ionomer adsorption onto Pt/C in HS catalyst inks, leading to changes in their rheological behavior, stability, and electrical behavior. Furthermore, this research demonstrates that the fractal dimension can be used to understand Pt/C aggregation in catalyst inks. As a future work, I will extend this analysis to include numerical simulations to provide a clear understanding of and method of controlling the coating process of HS catalyst inks.

References

[1] S. Holdcroft, *Chemistry of Materials*, **2014**, 26, 381-393.

[2] S. S. Kocha, Hand book of Fuel Cells -Fundementals, Technology and Applications-, vol. Volume 3 Fuel Cell Technology and Applications, **2003**.

[3] R. Sharma and S. M. Andersen, *ACS Applied Materials & Interfaces*, **2018**, 10, 38125-38133.

[4] H. Kuroki, K. Onishi, K. Asami, and T. Yamaguchi, *Industrial & Engineering Chemistry Research*, **2019**, 58, 19545-19550.

[5] S. Khandavalli, J. H. Park, N. N. Kariuki, D. J. Myers, J. J. Stickel, K. Hurst, et al., *ACS Applied Materials & Interfaces*, **2018**, 10, 43610-43622.

[6] M. Thoma, W. Lin, E. Hoffmann, M. M. Sattes, D. Segets, C. Damm, et al., *Langmuir*, **2018** 34, 12324-12334.

[7] S. Takahashi, T. Mashio, N. Horibe, K. Akizuki, and A. Ohma, *ChemElectroChem*, **2015**, 2, 1560-1567.

[8] T. T. Ngo, T. L. Yu, and H.-L. Lin, *Journal of Power Sources*, **2013**, 225, 293-303.

[9] T. Van Cleve, S. Khandavalli, A. Chowdhury, S. Medina, S. Pylypenko, M. Wang, et al., *ACS Applied Materials & Interfaces*, **2019**, 11, 46953-46964.

[10] S. A. Berlinger, B. D. McCloskey, and A. Z. Weber, *Journal of Physical Chemistry B*, **2018**, 122, 7790-7796.

[11] M. Shibayama, T. Matsunaga, T. Kusano, K. Amemiya, N. Kobayashi, and T. Yoshida,

Journal of Applied Polymer Science, **2014**, 131.

[12] R. Balu, N. R. Choudhury, J. P. Mata, L. de Campo, C. Rehm, A. J. Hill, et al., *ACS Applied Materials & Interfaces*, **2019**, 11, 9934-9946.

[13] F. Yang, L. Xin, A. Uzunoglu, Y. Qiu, L. Stanciu, J. Ilavsky, et al., *ACS Applied Materials & Interfaces*, **2017**, 9, 6530-6538.

[14] S. Takahashi, J. Shimanuki, T. Mashio, A. Ohma, H. Tohma, A. Ishihara, et al., *Electrochimica Acta*, **2017**, 224, 178-185.

[15] S. Shukla, S. Bhattacharjee, A. Z. Weber, and M. Secanell, *Journal of The Electrochemical Society*, **2017**, 164, F600-F609.

[16] M. B. Dixit, B. A. Harkey, F. Shen, and K. B. Hatzell, *Journal of The Electrochemical Society*, **2018**, 165, F264-F271.

[17] M. Takeno, T. Fukutsuka, K. Miyazaki, and T. Abe, *Chemistry Letters*, **2017**, 46, 892-894.

[18] M. Youssry, L. Madec, P. Soudan, M. Cerbelaud, D. Guyomard, and B. Lestriez, *Physical Chemistry Chemical Physics*, **2013**, 15, 14476-14486.

[19] M. Youssry, L. Madec, P. Soudan, M. Cerbelaud, D. Guyomard, and B. Lestriez, *Journal of Power Sources*, **2015**, 274, 424-431.

[20] L. Madec, M. Youssry, M. Cerbelaud, P. Soudan, D. Guyomard, and B. Lestriez, *ChemPlusChem*, **2015**, 80, 396-401.

[21] H. Parant, G. Muller, T. Le Mercier, J. M. Tarascon, P. Poulin, and A. Colin, *Carbon*, **2017**, 119, 10-20.

[22] S. Lazzari, L. Nicoud, B. Jaquet, M. Lattuada, and M. Morbidelli, *Advances in Colloid and Interface Science*, **2016**, 235, 1-13.

[23] W. H. Shih, W. Y. Shih, S. I. Kim, J. Liu, and I. A. Aksay, *Physical Review A*, **1990**, 42, 4772-4779.

[24] M. Y. Lin, H. M. Lindsay, D. A. Weitz, R. C. Ball, R. Klein, and P. Meakin, *Nature*, **1989**, 339, 360-362.

[25] F. D. Ma, Y. B. Fu, V. Battaglia, and R. Prasher, *Journal of Power Sources*, **2019**, 438, 226994.

[26] T. T. Ngo, T. L. Yu, and H. L. Lin, *Journal of Power Sources*, **2013**, 225, 293-303.

[27] M. Kishi, M. Tanaka, and T. Mori, *Journal of the Ceramic Society of Japan*, **2019**, 127,

942-951.

[28] J. C. Meier, C. Galeano, I. Katsounaros, J. Witte, H. J. Bongard, A. A. Topalov, et al., *Beilstein journal of nanotechnology*, **2014**, 5, 44-67.

[29] T. Suzuki, R. Hashizume, and M. Hayase, in Polymer Electrolyte Fuel Cells 14. H. A. Gasteiger, H. Uchida, F. N. Buchi, K. SwiderLyons, D. Jones, V. Ramani, et al., Eds., ed Pennington: Electrochemical Soc Inc, **2014**, 64, 313-319.

[30] Y. Kameya, N. Iriguchi, M. Ohki, K. Yokoyama, S. Sugawara, H. Sugimori, et al., in Polymer Electrolyte Fuel Cells 17. D. J. Jones, F. Buechi, K. E. SwiderLyons, P. N. Pintauro, H. Uchida, T. J. Schmidt, et al., Eds., ed, **2017**, 80, 819-827.

[31] J. H. Lee, U. Paik, J. Y. Choi, K. K. Kim, S. M. Yoon, J. Lee, et al., *Journal of Physical Chemistry C*, **2007**, 111, 2477-2483.

[32] N. Kumano, K. Kudo, A. Suda, Y. Akimoto, M. Ishii, and H. Nakamura, *Journal of Power Sources*, **2019**, 419, 219-228.

[33] S. M. Andersen, M. Borghei, R. Dhiman, V. Ruiz, E. Kauppinen, and E. Skou, *The Journal of Physical Chemistry C*, **2014**, 118, 10814-10823.

[34] W. Yoshimune and M. Harada, *Chemistry Letters*, **2019**, 48, 487-490.

[35] Y. Aoki, A. Hatano, and H. Watanabe, *Rheologica Acta*, **2003**, 42, 209-216.

[36] Mustafa, H. Usui, I. Shige, H. Suzuki, T. Kobayashi, Y. Miyazaki, et al., *Journal of Chemical Engineering of Japan*, **2004**, 37, 31-39.

[37] T. Hagiwara, H. Kumagai, and T. Matsunaga, *Journal of Agricultural and Food Chemistry*, **1997**, 45, 3807-3812.

[38] H. Wu and M. Morbidelli, *Langmuir*, **2001**, 17, 1030-1036.

[39] S. Ikeda, E. A. Foegeding, and T. Hagiwara, *Langmuir*, **1999**, 15, 8584-8589.

[40] R. Buscall, I. J. McGowan, P. D. A. Mills, R. F. Stewart, D. Sutton, L. R. White, et al., *Journal of Non-Newtonian Fluid Mechanics*, **1987**, 24, 183-202.

[41] R. Derooij, D. Vandenende, M. H. G. Duits, and J. Mellema, *Physical Review E*, **1994**, 49, 3038-3049.

[42] L. C. R.J.Meyer, *J Soc Cosmet Chem,* **1958**.

[43] M. P. Godfrin, A. Tiwari, A. Bose, and A. Tripathi, *Langmuir*, **2014**, 30, 15400-15407.

[44] H. Mizukawa and M. Kawaguchi, *Langmuir*, **2009**, 25, 11984-11987.

[45] A. Helal, T. Divoux, and G. H. McKinley, *Physical Review Applied*, **2016**, 6, 064004.

[46] A. Narayanan, F. Mugele, and M. H. G. Duits, *Langmuir*, **2017**, 33, 1629-1638.

[47] J. J. Richards, J. B. Hipp, J. K. Riley, N. J. Wagner, and P. D. Butler, *Langmuir*, **2017**, 33, 12260-12266.

[48] S. Khandavalli and J. P. Rothstein, *AICHE Journal*, **2016**, 62, 4536-4547.

Chapter 8

Controlling Cracking Formation in Fuel Cell Catalyst Layers

8.1 Introduction

Polymer electrolyte fuel cells (PEFCs) are power generators that produce electrical energy from the reaction between oxygen and hydrogen. PEFCs have the potential to become more efficient and produce higher power density than conventional internal combustion engines and are therefore regarded as one of the most promising future automotive power sources. Furthermore, hydrogen can also be produced from a variety of primary energy sources and are not reliant on fossil fuels. However, there are several hurdles preventing the spread of PEFCs as an automotive power source, including reducing cost through low platinum catalyst loading and improving durability. Key measures to help resolve these issues include improving material properties and controlling the structure of the electrode catalyst layers [1].

Catalyst layers are porous layers prepared from catalyst inks consisting of ionomer solutions, carbon black-supported platinum (Pt) nanoparticles (Pt/C) and dispersing solvents. There are two coating processing methods for catalyst layers: direct coating onto the membrane or gas diffusion layer, and decal transferring to the membrane. The decal transfer method is used to prevent solvents from swelling off the membrane in the manufacturing process [2]. The catalyst ink is coated on a Teflon® sheet and dried to form a catalyst layer that is transferred onto an electrolyte membrane, thereby creating a membrane electrode assembly (MEA). However, the drying of a thin catalyst ink film on a substrate often causes the formation of cracks. Several studies have reported changes in crack patterns depending on the type of catalyst ink solvent [3,4], the catalyst ink mixing time [5], and differences in the amount of ionomer and the microporous layer used as a substrate [6]. Cracks in catalyst layers are microstructures and have diverse effects on performance and durability.

Cracks in catalyst layers may have a positive effect on cell performance [7, 8]. The performance of catalyst layers with guided cracks was measured by stretching an MEA and altering the crack patterns of the catalyst layers. MEAs with guided cracks exhibited better performance than conventional MEAs, mainly because of improved water transportation efficiency [8]. The contribution of cracks that occurred in the manufacturing process to performance is not perfectly clear, but if a catalyst layer with controlled crack patterns could be prepared, it would be possible to further examine how cracks affect performance.

However, it has also been reported that catalyst layer cracks have an adverse effect on durability [9-14]. A previous study pointed out that flooding occurs at cracked parts of catalyst layers during

operation, which may cause cracks and pinholes in electrolyte membranes [9]. The crack density of catalyst layers and electrolyte membranes was examined by X-ray computed tomography during accelerated stress testing. It was found that catalyst layer cracks were related to electrolyte membrane crack occurrence [10-13]. In addition, the results of an investigation using FE-SEM at leakage points identified via a bubble point test showed that cracks in the membrane initiate within larger cracks of catalyst layers [14]. Cracking in membranes causes gas leaks, resulting in chemical reactions between oxygen and hydrogen. This induces MEA degradation, leading to immense damage to durability [15].

Hence, it is important to obtain an understanding of crack behavior because cracks in catalyst layers affect performance and durability. However, few previous reports have discussed the presence, density, and patterns of cracks in the catalyst layer due to a lack of understanding of the importance of the catalyst layer, as well as a lack of useful evaluation methods.

According to previous studies, cracks are formed due to stress caused by differences in the drying rate between the surface and interior [9, 16]. In addition, the nucleation of cracks correlates with the interaction of Pt/C and solvents in catalyst inks [7] and the interaction of ionomers with Pt/C [17]. The structural evolution of a catalyst ink during the drying process was investigated by the contrast-variation small-angle neutron scattering (CV-SANS) method. The results suggested that a catalyst layer contains many cracks, which could be explained by low interaction between ionomers and Pt/C [17]. There are various opinions on the factors affecting crack behavior in catalyst layers, and the mechanism is poorly understood.

Cracking in model colloidal suspensions has also been investigated, and a parameter called a critical crack thickness (CCT), below which films do not crack during drying, and which depends on the fracture resistance of the films was utilized [18,19]. The main cause of cracks is stress concentration at defects such as clumps and bubbles. If no defect exists, cracks are assumed to mainly occur due to tensile stress caused by capillary force propagating through ensembles of particles that are in contact each other during solvent evaporation. If this stress exceeds the strength of the porous film, the stress is released in the form of cracks [20]. The CCT is an index based on Griffith's conditions [21], and is calculated by Equation (1) [22].

$$h_c = \frac{2G_c E^*}{Z\sigma^2} \quad (1)$$

in which, $E^* = E/(1-\nu^2)$, where E is Young's modulus, ν is Poisson's ratio, and σ is the biaxial tensile

stress. Z is a constant expressing the geometry of the crack tip. G*c* is referred to as the fracture toughness or critical strain-energy release rate. The CCT has not previously been applied to catalyst layers, this study investigates whether it is applicable and whether it is useful as an index value to indicate the fracture resistance of these layers.

In addition, it has been reported that the CCT is dependent upon the state of particle flocculation. The CCT of films formed from flocculated (pH 9) and dispersed (pH 1.75) alumina suspensions with a PVA binder was observed by Carreras et al. These results showed that the CCT is three times greater for films obtained from dispersed suspensions than for films obtained from flocculated suspensions [23]. Therefore, this study will focus on the relationship between the dispersion state of Pt/C and the CCT in catalyst ink.

It was found that the addition of Nafion (the most typical ionomer) helped to increase ink stability and to reduce aggregate particle size [24]. This is because the hydrophobic backbone of Nafion becomes strongly anchored to the hydrophobic carbon surface, while hydrophilic portions become ionized to impart a sufficient ionic charge to the carbon surfaces. Therefore, ionomers can improve the dispersion stability of Pt/C by surface wrapping in a dispersion medium. However, when a highly hydrophobic solvent is added to the dispersion medium, contact between the hydrophobic Nafion and the solvent are promoted, which leads to a decrease in the amount of adsorbed Nafion on the Pt/C surface [25]. In this case, rheological methods provide information on the structures of the Pt/C [26, 31].

This research investigated the factors affecting crack behavior with the objective of controlling the cracking of catalyst layers. To change the dispersion state of Pt/C, hydrophobic solvents were added to the catalyst ink. The CCT was examined as a parameter for cracking characteristics. This paper discusses the cracking mechanism by focusing on the nano/microstructure between catalyst layers with different cracking characteristics.

8.2 Materials and Methods

8.2.1 Materials and catalyst ink preparation

Two types of catalyst ink were prepared with an ionomer/carbon weight ratio (I/C) of 0.75 and a solid content of 10 wt% by adding ethanol or 1-propanol. The catalyst ink prior to adding alcohol is referred to as "Pre-ink," catalyst ink with added ethanol as "E-ink," and catalyst ink with added 1-propanol as "P-ink." Ethanol and 1-propanol, which are alcohols commonly used for catalyst inks and differ in hydrophobicity (1-propanol is more hydrophobic than ethanol) were selected. Figure 1 and Table 1 summarize the preparation step and composition. In a typical experiment, a 20 ml sample tube was loaded with 6.46 g of hyperpure water and 0.80 g of Pt/C (Tanaka Kikinzoku Kogyo, TEC10V30E), and a planetary mixer/deaerator (KURABO INDUSTRIES LTD, MAZERUSTAR KK-50S) was used to perform degassing and mixing for 1 minute in the case of each ink. 1.89 g of Nafion liquid dispersion (The Chemours Company, DE2020) was added to the mixture. The mixture was sonicated for 9 minutes using an ultrasonic homogenizer (SMT Corporation, MODEL UH-600) to break up agglomerates in the Pre-ink. 2.70 g of 1-propanol or ethanol was added to the Pre-ink to fabricate the E-ink and P-ink, respectively. Furthermore, 10 mL of each catalyst ink was loaded into a thin-film spin system high-speed mixer (PRIMIX Corporation, FILMIX® Model 30-L). The wheel was rotated at a circumferential speed of 20 m/s, followed by dispersion processing for 3 minutes.

Table 1. Sample specifications of catalyst inks

	Pre-ink	E-ink	P-ink
Solids concentrations(wt%)	12.9	10	10
I/C (Ionomer/Carbon ratio(w/w))	0.75	0.75	0.75
Pt/Carbon (wt%)	8.4	6.6	6.6
Nafion (wt%)	4.5	3.4	3.4
H_2O(wt%)	78.2	60.3	60.3
1-propanol(wt%)	8.9	6.9	29.7
ethanol(wt%)	0	22.8	0
Total	100	100	100

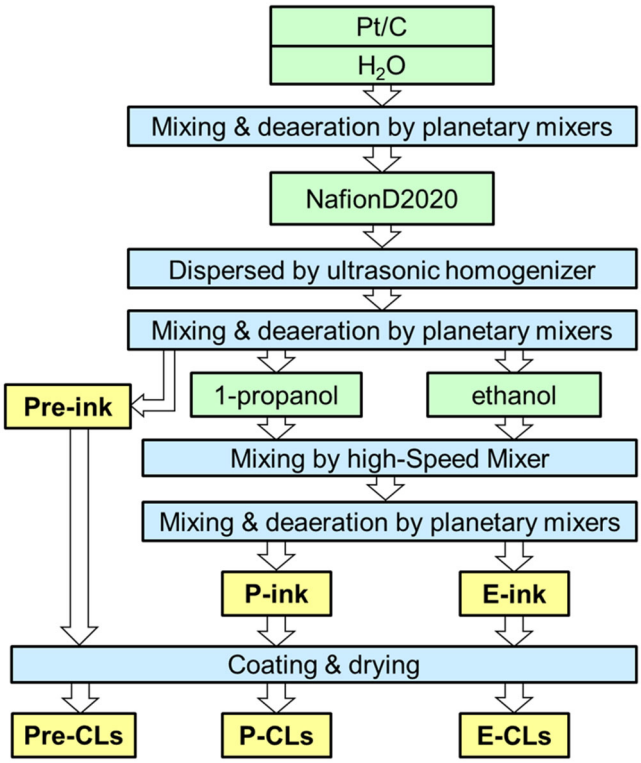

Figure 1. Procedure of catalyst inks and catalyst layers preparation

8.2.2 Catalyst ink characterization

8.2.2.1 Measurement of adsorption rate of ionomer into Pt/C

To quantitatively determine the adsorption rate of the ionomer into Pt/C, a supernatant solution including the free ionomer without Pt/C was separated from 2 ml of catalyst ink by a syringe filter and transferred to a weighing bottle (3 ml) that was weighed in advance. The concentration of the ionomer in the supernatant (Cp) was determined by weighing the bottle before and after heating the solvent for 1 hour at 80°C. The adsorption rate (Γ) of the ionomer into the Pt/C was calculated from Equation (2) by substituting the initial concentration of ionomer (Cp_0) in catalyst inks.

$$\Gamma = \frac{Cp_0 - Cp}{Cp_0} \tag{2}$$

A microelectronic balance (A&D Company, BM-20) with a readability of 0.001 mg was used.

8.2.2.2 Rheological measurements

Rheological experiments were carried out using a rheometer (Anton Paar GmbH, MCR301) with a cone plate fixture (50-mm diameter, 1° angle, and 0.101-mm gap). To obtain reproducible results, a

rheological measurement protocol was followed. The samples were left standing at 25°C for 10 minutes before the rheological experiments. The steady flow viscosity (η) shear-rate dependence was used to raise the shear rate from 0.01 s^{-1} to 1000 s^{-1} after two repetitions as pre-shear. In addition, the strain dependency of the storage modulus (G') and loss modulus (G'') was used to change the strain from 0.01% to 1000% at a frequency of 1 Hz after measurements of steady flow viscosity as pre-shear. The experiments were conducted at 25°C.

8.2.2.3 Dynamic light scattering (DLS) of dilute catalyst inks

The size of the Pt/C aggregates in the catalyst inks was measured by DLS (Microtrac BEL Corp., UPA-250EX). For the DLS measurements, 0.01 ml of the catalyst inks were diluted by 10 ml of a solution with the same liquid composition as originally prepared for each catalyst ink. The samples after dilution were sonicated in an ultrasonic bath for 3 minutes to obtain a homogeneous mixture before the DLS measurements.

8.2.3 Catalyst layer preparation

The coating experiments were carried out using an automatic film coater (BYK Gardner, byko-drive), and a gap-controlled film applicator (YOSHIMITSU SEIKI, YBA-1). Cleaned glass plates (ASAHI TECHNIGLASS, 70×150 mm) and Teflon sheets were examined as substrates. Two substrates were coated with the catalyst inks at a coating speed of 10 mm/s using the gap-controlled film applicator with a coating gap from 25 to 175 μm by changing the coating gap at 25 μm intervals. Pre-ink used an automatic film coater, a spacer with dimensions of 50 and 75 μm (Nitto Denko Corporation, Polyester-based adhesive tape No.31B), and a gap-controlled film applicator (Sheen instruments, SH1117/100) because its viscosity was too low to obtain a thick Pre-ink coating film in same way as the E-ink and P-ink. The Pre-ink was spread by the gap-controlled film applicator at a coating speed of 10 mm/s to remove the excess ink from the spacer. Drying experiments were performed for 1 h at 24°C at a humidity range of 70 to 75RH% to form catalyst layers of differing film thicknesses from 2 to 18 μm. In this study, the catalyst layers prepared by coating and drying the Pre-ink, E-ink, and P-ink were referred to as “Pre-CLs,” “E-CLs,” and “P-CLs,” respectively.

8.2.4 Catalyst layer characterization

8.2.4.1 Surface observations and measurement of critical crack thickness

Optical photographs of surface of catalyst layers were taken using a confocal microscope (Lasertec Corporation, PTELICS H1200). The film thicknesses of the catalyst layers were 2 μm, 8 μm, 12 μm, and 18 μm. Three types of cracks were defined: primary cracks (PCs), secondary cracks (SCs), and cracks caused by the presence of critical defects (DCs). Cracks with no defect that could be observed by a confocal microscope (×20) were defined as PCs, which is a failure mode applicable to the CCT. SCs were assumed to be further expansions of cracks from a PC or connected to existing cracks in the next stage of a PC [32]. Cracks with a defect that could be observed by a confocal microscope (×20) were defined as DCs. The film thickness was measured as the height difference between the substrate and catalyst layer at a height resolution of approximately 60 nm. The presence of cracks was examined from the thinnest to thickest films, and the largest film thickness in which a PC did not occur was defined as the CCT. DCs were often observed when clumps were included by inadequate dispersion, making it impossible to measure the CCT correctly. Thus, the CCT was measured using catalyst inks passed through a syringe filter (mesh opening, 20 μm).

8.2.4.2 Pore structure measurements

To estimate the internal nano/microstructure of the catalyst layers, the pore size distribution of E-CL and P-CL was measured by mercury porosimetry using a Quantachrome Pore Master GT60-1. Pores with a diameter ranging from 0.005 to 189 μm were measured.

8.2.4.3 Physical analysis of catalyst layers

The microstructure of the catalyst layers was investigated using a field emission-type scanning electron microscope (FE-SEM (Hitachi High-Technologies Corporation, S-5500)) operated at 0.7 kV. The samples were coated with a 3 nm Os layer using plasma CVD. Furthermore, the samples were polished by Broad Ion Beam (BIB) milling. Cross-sections were observed using a FE-SEM (Hitachi High-Technologies Corporation, S-4800) operated at 3.0 kV. The size of voids was measured by the open source image processing program ImageJ.

8.3 Results and Discussion

8.3.1 Catalyst ink properties

8.3.1.1 Adsorption rate of ionomer and average particle size

Table 2 shows the adsorption rate of the ionomer into Pt/C. The highest adsorption rate was achieved by the Pre-ink, followed in order by the E-ink and P-ink. The results show that adsorption rate decreased with the addition of solvent. This implies that the ionomer adsorbed into Pt/C was dissolved by the increasing hydrophobicity of the dispersion medium. Table 2 and Figure 2 show the results of DLS measurements. The Pre-ink has the smallest average particle size, followed by the E-ink and P-ink. This result indicates that Pt/C was adequately dispersed due to ionomer adsorption in the Pre-ink, and that the ionomer was eliminated from the Pt/C by adding solvents in the E-ink and P-ink, leading to the average aggregate size becoming larger. This interpretation in terms of hydrophobicity of the dispersion medium is in agreement with the effect of Nafion and its resulting interaction with single-walled carbon nanotubes (SWCNTs) on the solubility and dispersion properties of SWCNTs in bisolvents as reported in [25]. It is also possible that by changing the solvent environment, the pH [27] and dielectric permittivity [28] may also have changed, resulting in changes aggregation behavior. However, it was found that the pH and dielectric permittivity remained virtually unchanged by the addition of a solvent in our study (Table 3). Moreover, previous study reported that average aggregate size increases with increasing water content [27]. This result appears to be opposite to our results, but the discrepancy may be due to differences in mixing condition for preparation [5, 29], aging time [6] and the effect of dilution on DLS measurements [30]. Our results on DLS measurements demonstrate that the adsorption of ionomer on Pt/C is likely inhibiting agglomeration by steric and electrostatic repulsion effect of ionomer [31].

Table 2. Effect of different catalyst ink compositions on characteristics:

(a) Adsorption rate of ionomer on Pt/carbon; (b) average particle size based on DLS

	Pre-ink	E-ink	P-ink
Adsorption rate of ionomer on Pt/carbon(%)	97	23	0
average particle size (nm)	550	780	1030

Table 3. pH values and dielectric permittivity in catalyst ink solutions without Pt/C

	Pre-ink	E-ink	P-ink
pH	2.0	2.0	2.0
Dielectric permittivity	74.4	60.6	56.4

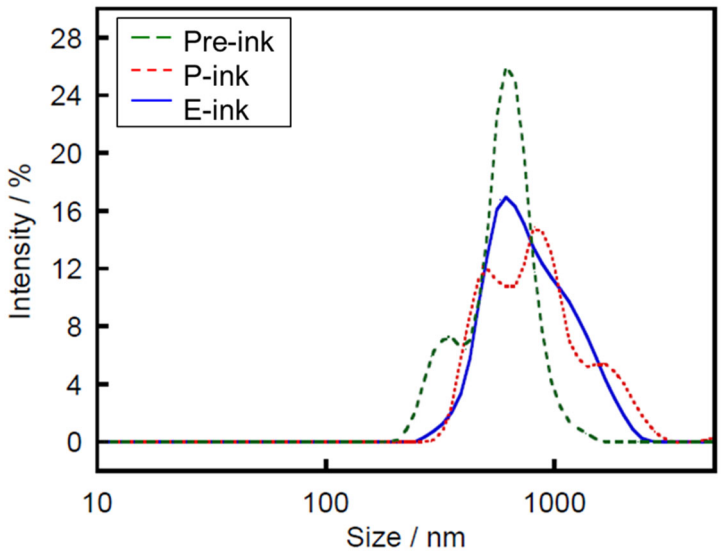

Figure 2. Particle size distribution of catalyst inks

8.3.1.2 Rheological properties

Figure 3(a) shows the shear-rate dependence of the viscosity. Shear-thinning behavior occurred in all the catalyst inks when the viscosity decreased in accordance with the shear rate. This implies that agglomerates were formed in the catalyst inks, and that shear-thinning was produced by the breakup of agglomerates due to shear. In all shear rate regions, viscosity was lowest for the Pre-ink, followed by the E-ink and P-ink as the hydrophobicity of the dispersion medium increased. This increase in viscosity is related to the adsorption rate of the ionomer into Pt/C. It was assumed that adding solvents generated agglomerates by eliminating the ionomer from the Pt/C and increasing the amount of free ionomer.

In addition, a shoulder was observed in the P-ink curve at a shear rate between 0.1 and 1 s^{-1}. This behavior was observed in Pt/C with no ionomer adsorbed into the surface [26]. This also suggests that the ionomer was eliminated from the Pt/C in the P-ink.

Figure 3(b) shows the strain dependency of G' and G''. The Pre-ink had the lowest in G' in all strain regions, followed by the E-ink and P-ink. In all catalyst inks, agglomerates that have an elastic response in low-strain regions showed breakage and flow in high-strain regions. The low-strain region storage modulus reflected the strength of the agglomerate structures, and the P-ink formed the strongest network structures. The storage modulus was distinctly higher than the loss modulus in the low-strain regions, also suggesting that network structures of Pt/C were formed in the P-ink.

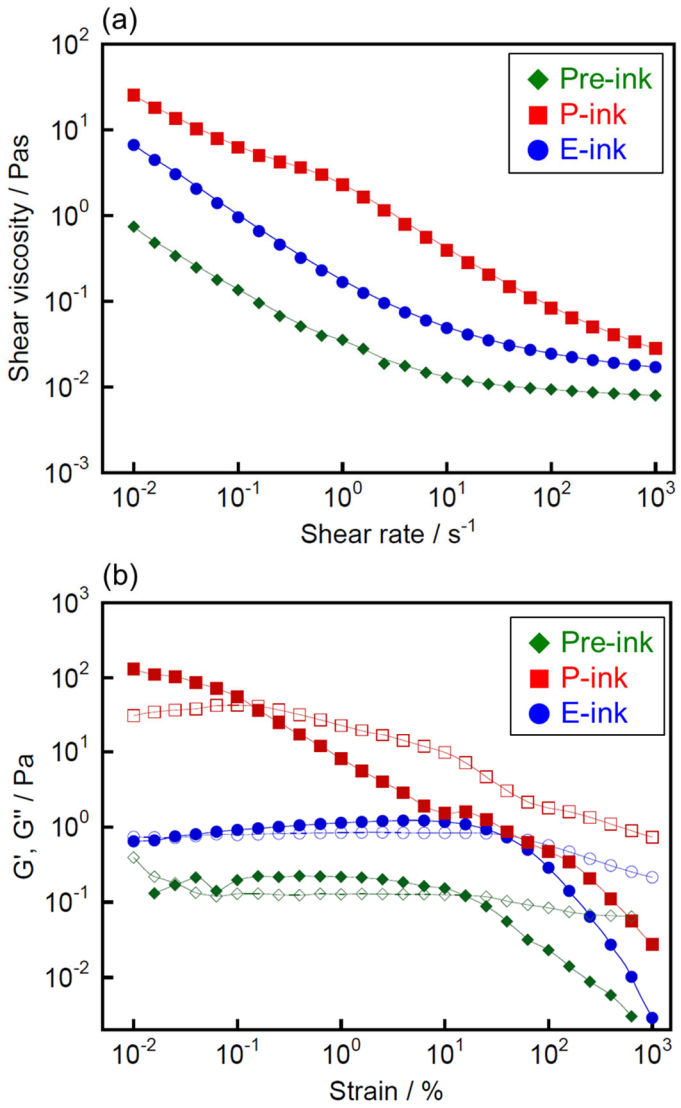

Figure 3. Rheological measurement of catalyst inks
(a) Shear rate dependent viscosity
(b) Strain dependent Storage moduli (G') (■●◆) and Loss moduli (G'') (□○◇) at 1 Hz

8.3.2 Physical properties of catalyst layers

8.3.2.1 Relationship between thickness and crack patterns

Cleaned glass plates and Teflon sheets were examined as substrates. There was no significant difference in the crack pattern (Figure 4 and 5). However, because of the difficulty of handling a catalyst layer coated on a PTFE substrate, accurate CCT measurement was impossible. As a PTFE substrate is easily bent or deformed by even gentle handling, such deformation inevitably affects the crack conditions. To avoid these concerns, this study used the CCT measurement results with a specimen coated on a rigid glass substrate.

Table 4 shows the results for the CCT, Figure 4 shows the confocal microscope images, and Figure 5 shows the typical crack pattern contained in each catalyst layer. No cracks were observed at 2 μm and 8 μm in the Pre-CLs (Figure 4(a)), and U-shaped cracks thought to be PC were observed at 12 μm. Moreover, cracks formed mesh patterns at 18 μm. The Pre-ink contained few clumps. Therefore, the CCT was unchanged before and after filtering of the Pre-ink.

In the E-CLs (Figure 4(c)), no cracks were observed at 2 μm, and V-shaped DCs with clumps were observed at 8 μm (Figure 6(a)). From EDX measurements of clumps that formed the origin of DCs and the surrounding areas, the clumps were formed by either the Pt/C or ionomer (Figure 7 and Table 5). After removing the clumps from the E-ink, the CCT was 12.0 μm.

In the P-CLs (Figure 4(b)), no cracks were observed at 2 μm, and multiple I- and V-shaped cracks were observed at 8 μm (Figures 6 (b, c)). Multiple T- and Y-shaped cracks were observed at 8 μm and 12 μm in Figure 6 (d, e). Fine mesh patterns were formed at 18 μm. In spite of the presence of clumps in the P-ink, the DC ratio was low. Thus, the CCT hardly changed before and after the P-ink was filtered.

During drying, catalyst ink films often crack to release growing tensile stresses. Although crack nucleation is not yet fully understood [32], the cause of crack nucleation may be small voids, clumps of Pt/C or ionomers, pinholes, or uneven density that cannot be seen by a confocal microscope. Crack nucleation starts to propagate in different directions due to the development of stress. Possible mechanisms for shape factors are as follows. I-shape cracks propagate perpendicular to the direction of major principal stresses under isotropic stress. When the major principal stress direction at the tip of cracks changes due to fracture resistance, I-shape cracks extend into a U-shape. Under anisotropic stress due to inhomogeneous microstructures like small

defects, I-shape cracks change to V-shape cracks. T-shape and Y-shape cracks are secondary crack nucleates from existing I- and V-shape cracks to release tensile stress in another direction.

Therefore, multiple I-shape cracks suggest that P-CLs exhibit brittle failure and U-shape cracks suggest that E-CLs and Pre-CLs have high fracture toughness. V- and Y-shape cracks in P-CLs suggest that P-CLs include small defects that cannot be seen by a confocal microscope.

Based on a comparison of the CCT of catalyst inks after filtering, the CCT was found to be four times greater for Pre-CLs and E-CLs than for P-CLs. To examine the difference in the CCT from catalyst inks with the same solid concentration and water content, the microstructure of the P-CLs and E-CLs was observed in more detail (see the following section).

Table 4. Critical crack thickness of catalyst layers

	Pre-CLs	E-CLs	P-CLs
As-prepared (μm)	11.0	-	2.3
After removing aggregations by filtration (μm)	11.9	12.0	2.8

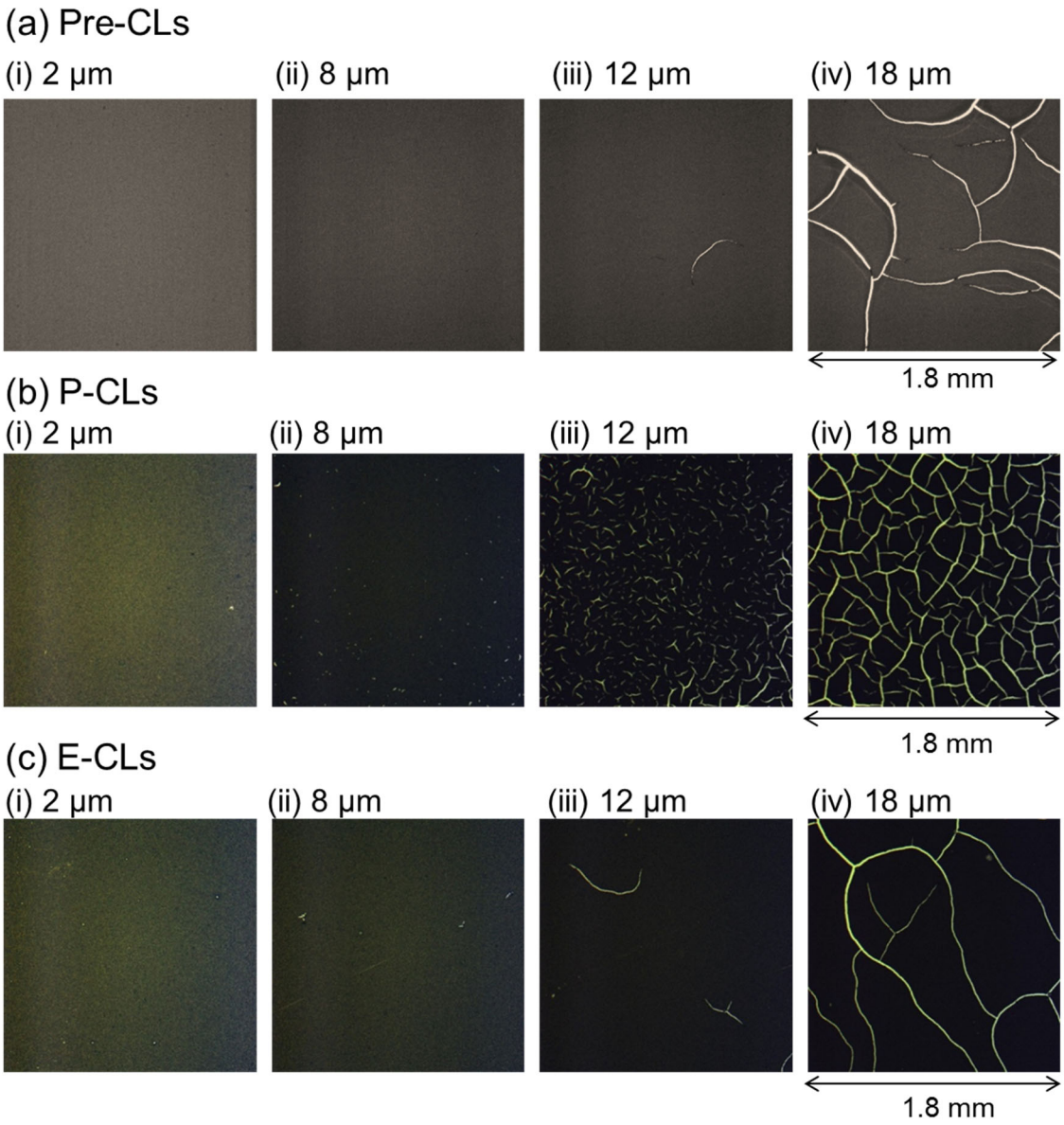

Figure 4. Pictures of catalyst layers in each film thickness

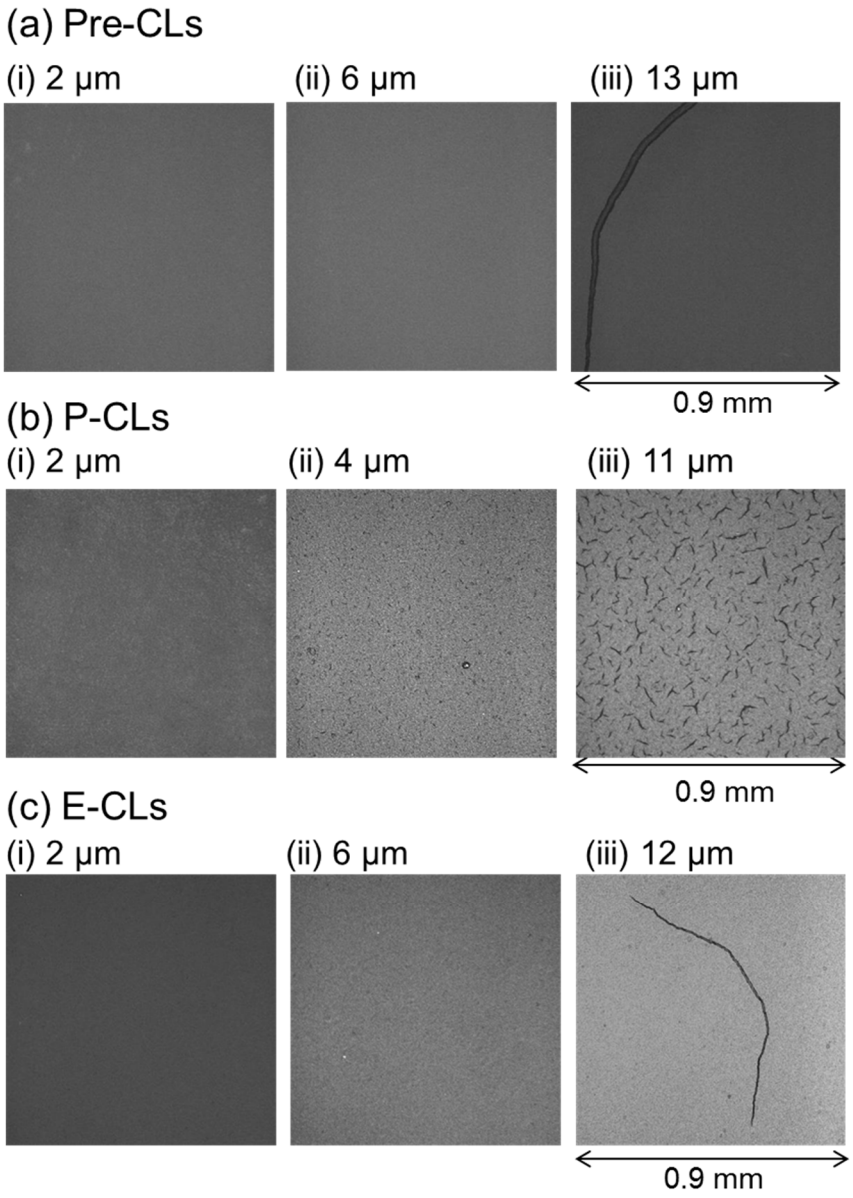

Figure 5. Pictures of catalyst layers in each film thickness on PTFE

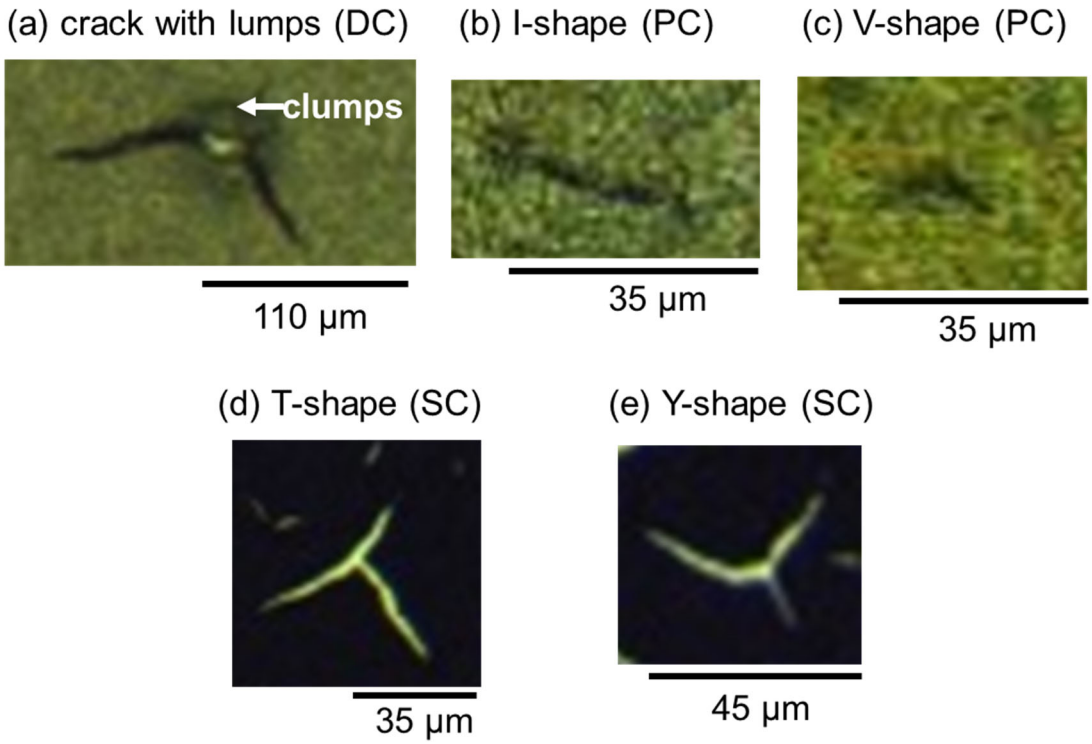

Figure 6. Pictures of cracks(a) E-CLs (8 μm), (b) P-CLs (8 μm), (c) P-CLs(8 μm), (d) P-CLs (12 μm), (e) P-CLs (12 μm)

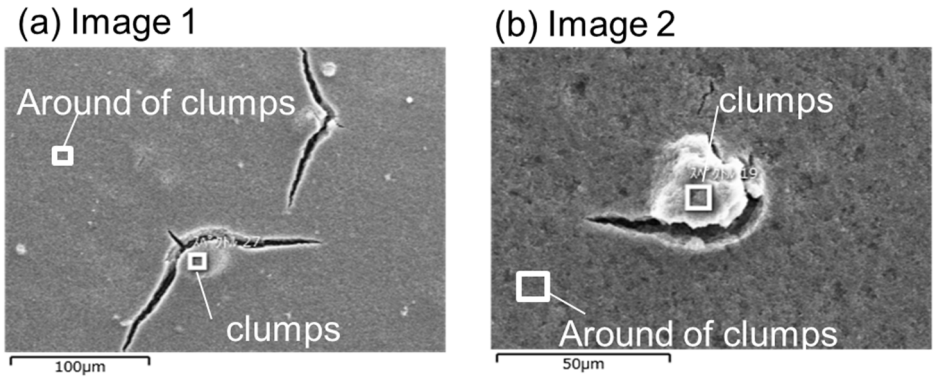

Figure 7. Typical SEM of clumps on E-CLs

Table 5. EDX analysis showing constituent elements of clumps on E-CLs

	Image 1		Image 2	
	clumps	Around of clumps	clumps	Around of clumps
Element	wt %	wt %	wt %	wt %
C	62.8	61.5	64.0	62.4
O	3.2	3.6	2.8	2.6
F	15.3	16.4	16.4	15.4
S	1.0	1.0	0.6	0.8
Pt	17.7	17.6	16.2	18.8
total	100	100	100	100
Pt/F (w/w)	1.2	1.1	1.0	1.2

8.3.2.2 Internal nano/microstructure of catalyst layers

The pore size distribution of catalyst layers was measured using mercury porosimetry, and the measurement results are shown in Figure 8(a). Three different types of pores were found in both E-CLs and P-CLs: primary pores with a pore diameter from 5 to 100 nm, secondary pores with a pore diameter from 1 to 5 μm, and macro pores with a pore diameter over 50 μm. It is considered that the primary pores correspond to the spaces within aggregates of Pt/C, secondary pores correspond to spaces between such individual aggregates [33] or voids, and macro pores correspond to cracks and the surface unevenness of the catalyst layers, respectively.

The volume of each type of pore was calculated for E-CLs and P-CLs (Figure 8(b)). The volume of the P-CL macro pores was larger than that of the E-CLs because the P-CLs contained more cracks and unevenness than the E-CLs, as shown in Figure 9.While the volume of the secondary pores of P-CLs and E-CLs was similar, the primary pore volume of the P-CLs was higher than that of the E-CLs. The most remarkable difference between the P-CLs and E-CLs is the size range of the primary pores. Although the primary P-CL pores are biased under the 20 nm range, the E-CL pores are evenly and moderately distributed in the range from 5 to 100 nm. This result shows that the ionomer might cover the pores in the carbon agglomerates in E-CLs.

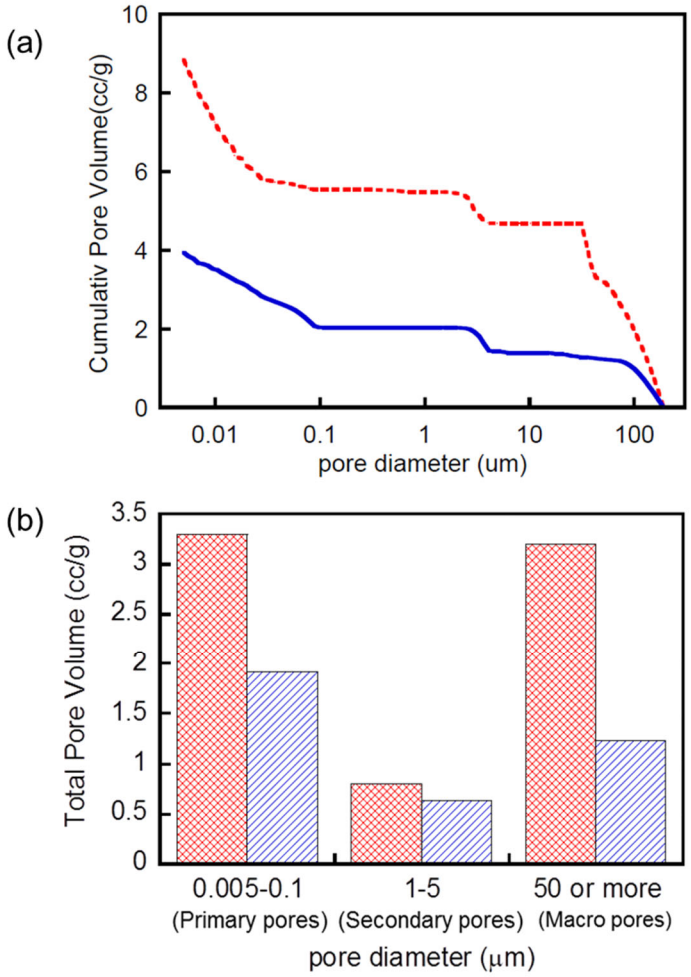

Figure 8. Pore size distribution of the catalyst layers.
(a) Cumulative pore volume distribution.
(b) Pore size distribution of primary pores, secondary pores and macro pores

8.3.2.3 Inhomogeneous microstructure of catalyst layers

Agglomerates were observed in the E-CLs. Agglomerates, as well as amoeba- (1:5,000, 1:30,000) and thread-shaped (1:100,000) ionomers between the agglomerates, which are self-organizing free ionomers, were observed in the P-CLs (Figure 9, arrows). More self-organizing free ionomers were observed in the P-CLs than the E-CLs.

Figure 9(a',b') shows cross-sectional SEM images of catalyst layers. The top of the E-CLs was relatively smooth, while the top of the P-CLs was uneven. Although there was a relative lack of uniformity in pore size on the E-CLs, the P-CLs included void over 500 nm.

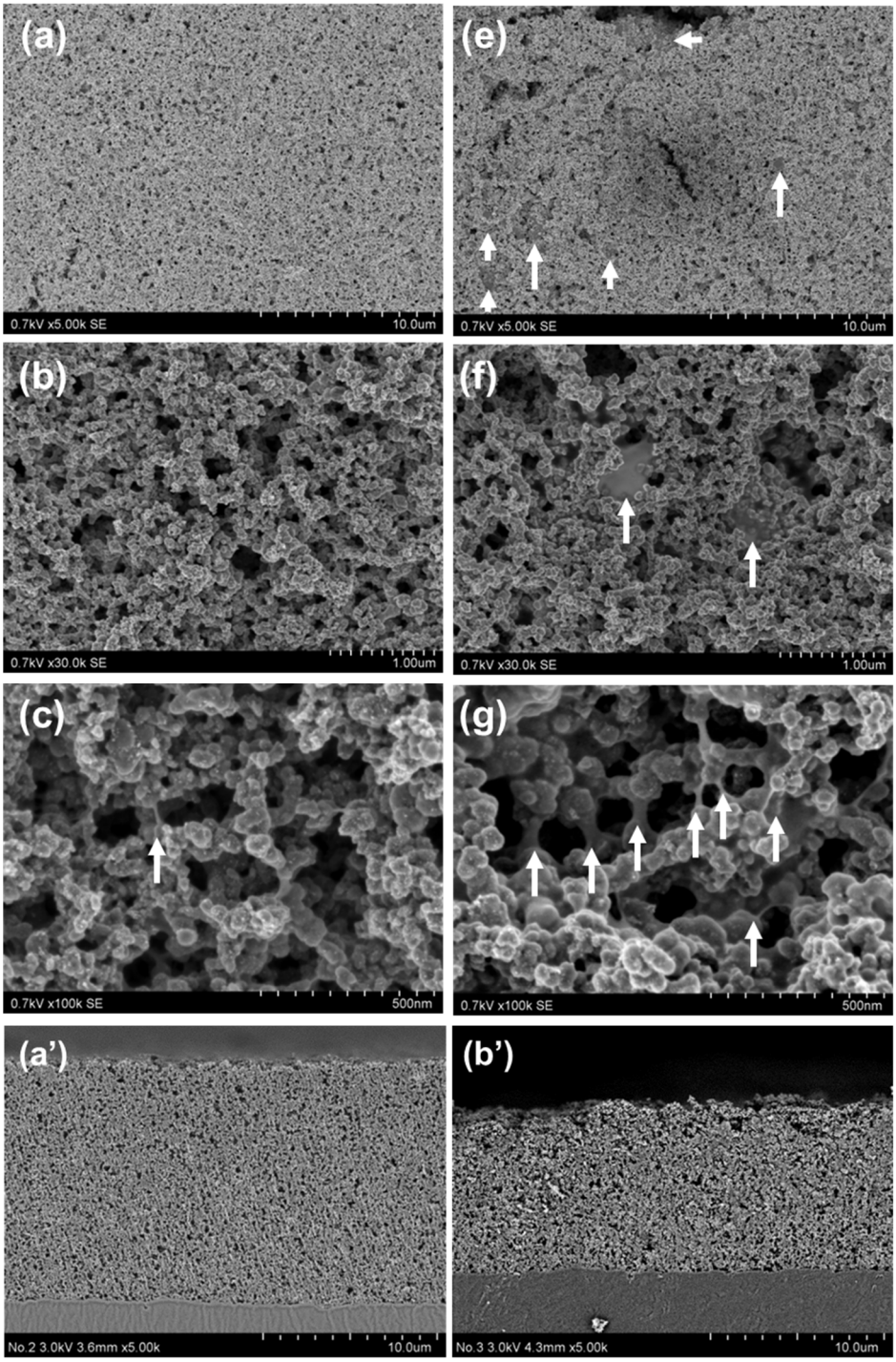

Figure 9. Surface SEM image of catalyst layers
(a)(b)(c) E-CLs, (d)(e)(f) P-CLs
(a) (d)×5,000, (b) (e)×30,000, (c) (f)×100,000
Cross section SEM image of catalyst layers
(a') E-CLs, (b') P-CLs (×5,000)

8.3.3 Cracking formation mechanism

This section discusses the mechanism leading to cracks focusing on the liquid structure of the catalyst inks and the structure of the catalyst layers. From Eq. (1), the critical crack thickness will depend on the tensile stress during drying and the fracture resistance of catalyst layers [18]. Figure 10 schematically depicts the mechanism of cracking.

Possible mechanisms for the tensile stress are as follows. The Pt/C is well-dispersed and stable in the E-ink, and steric and electrostatic stabilization by the ionomer ensured a better leveling effect during drying, allowing the pores to form a gradual densification. As a result, a hierarchic structure with little fluctuation is formed. Conversely, in the P-ink, network structures of Pt/C are formed immediately after application. During drying, the pore sizes decrease to maintain dense aggregates of Pt/C particles because of the absence of the ionomer on the Pt/C particles. The catalyst layers after drying maintained small primary pores, and a hierarchic structure with large fluctuation is formed.

The remarkable difference in size and number of primary pores is strongly related to the risk of cracking in terms of stress. During the drying process, capillary pressure develops on the structured agglomerated network, which is expressed by Eq. (3)

$$P_{cap} = \frac{2\gamma \cos\theta}{r_p} \tag{3}$$

Where γ is the liquid/vapor surface tension, θ is the liquid/solid contact angle, and r_p is the pore radius [20]. The stress σ in Eq. (1) is caused mainly by the capillary pressure in the pore liquid. The solvent seems to evaporate at the early stage of drying and water mainly remains at the end of drying. Therefore, the surface tension of the E-ink and P-ink at the end of drying may be supposed as similar. Therefore, the smaller porous structure in the P-CLs as observed by mercury porosimetry suggests higher capillary pressure and stress caused by large strain that caused the observed macro cracks.

Possible mechanisms for the fracture resistance of catalyst layers are explained as follows. Catalyst inks that are well dispersed by ionomer adsorption produce a homogeneous Pt/C and ionomer distribution in catalyst layers with high fracture toughness. The ionomer absorbed into the Pt/C might promote increases in adhesion strength between particle pairs with the ionomer acting as a binder. Thus, it is assumed that E-CLs have higher fracture resistance than P-CLs due to the

amount of ionomer in the Pt/C.

Moreover, the inhomogeneous microstructure of catalyst layers is also related to the risk of cracking in terms of stress concentration. The E-ink has low viscosity, indicating that it has a better leveling flow during drying. This minimizes the relative lack of voids and the surface unevenness of the catalyst layer after drying and restricts cracking. In the P-ink, the ionomers were eliminated from the Pt/C, and a network structure formed without a leveling flow in the wet film. Therefore, film shrinkage due to the network structure and evaporation of the dispersed medium leads to surface unevenness, and relatively large voids. Self-organizing free ionomers also existed in the P-CLs because of the absence of the ionomer on Pt/C. Cracks are likely to occur due to stress concentration in these defects, such as voids and clumps.

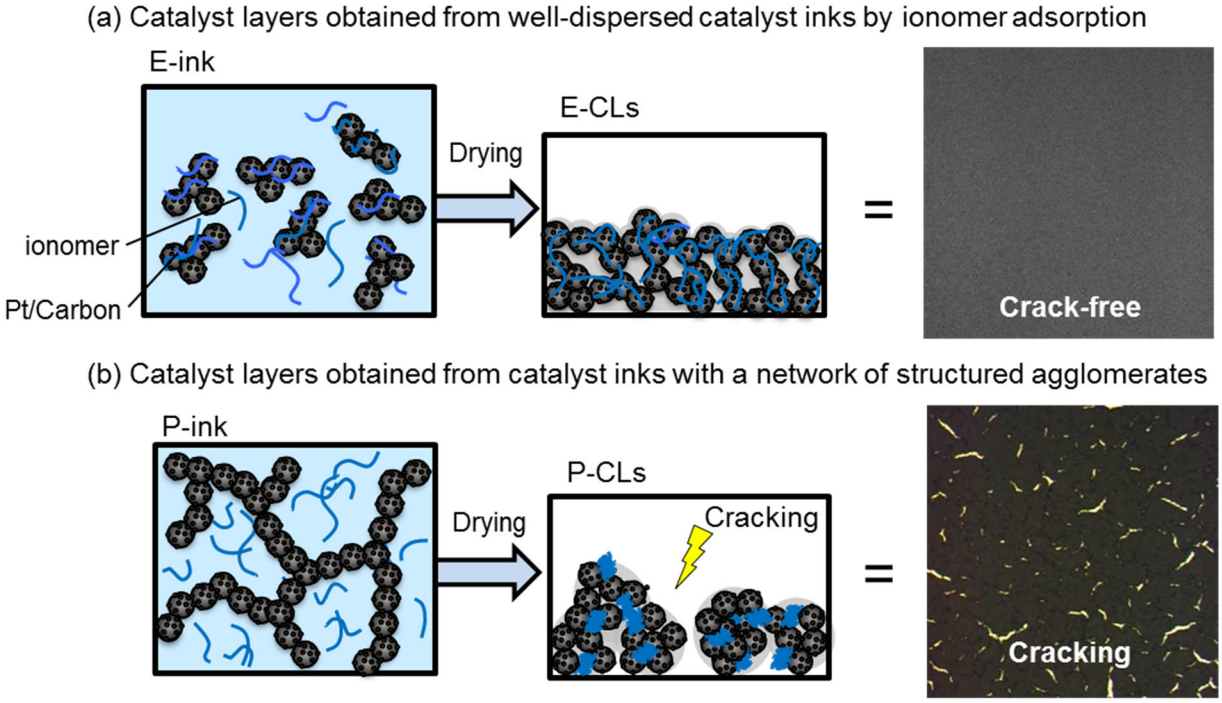

Figure 10. Schematic representation of the difference of critical crack thickness

(a)Catalyst inks(E-ink) that are well dispersed by ionomer adsorption contain a homogeneous Pt/carbon and ionomer distribution in E-CLs, while (b) catalyst inks(P-ink) with a network of structured agglomerates produce dense aggregates with small primary pores of bare Pt/carbon and a self-organizing free ionomer in P-CLs.

8.4 Conclusion

This study aimed to identify the factors affecting crack behavior in terms of the liquid structure in catalyst ink with the objective of controlling cracks in catalyst layers.

By adding two types of solvents with different hydrophobicity to the Pre-ink, the adsorption rate of the ionomer into the Pt/C decreased and the average particle size increased. The viscosity and storage modulus increased in accordance with the higher hydrophobicity in the dispersion medium. This result demonstrated that the ionomer was eliminated from the Pt/C, and agglomerates were formed by the addition of a hydrophobic solvent.

The CCT was found to be four times greater for the E-CLs and Pre-CLs than for the P-CLs. This suggests that the CCT decreases due to the poor affinity between the ionomer and Pt/C.

The following mechanisms for the difference of CCT were proposed. The Pt/C is well-dispersed and stable in the E-ink, and steric and electrostatic stabilization by the ionomer ensures a better leveling flow during drying, allowing the formation of a hierarchic structure with little fluctuation in the catalyst layer. Conversely, in the P-ink, network structures of Pt/C are formed immediately after application. Catalyst layers from the P-ink maintained small primary pores within aggregates of Pt/C and a hierarchic structure with large fluctuation is formed.

(1) Catalyst layers with a high number of primary pores generate high drying stress, suggesting that the risk of cracking increases. (2) The ionomer absorbed into the Pt/C might promote increases in the adhesion strength between particle pairs by acting as a binder, suggesting that the toughness and homogeneousness of the catalyst layer increases. In addition, (3) the presence of voids and the self-organizing free ionomer suggests stress concentration that results in the formation of cracks.

Consequently, crack behavior can be controlled by ionomer adsorption into the Pt/C in catalyst ink and the resulting dispersion state. Hence, possible measures to prevent catalyst layer cracking include increasing the affinity between the Pt/C and ionomer and creating better leveling flow for the catalyst ink.

Furthermore, this research also demonstrated that the CCT is a useful index for understanding the cracking behavior of catalyst layers. As a future work, the analysis will be extended to examine the effects of cracks on performance and durability in detail.

References

[1] Holdcroft, S., *Chemistry of Materials*, **2014**, 26, 1, 381-393.

[2] Suzuki, T., Tanaka, H., Hayase, M., Tsushima, S. and Hirai, S., *International Journal of Hydrogen Energy*, **2016**, 41, 44, 20326-20335.

[3] Huang, D. C., Yu, P. J., Liu, F. J., Huang, S. L., Hsueh, K. L., Chen, Y. C., Wu, C. H., Chang, W. C. and Tsau, F. H., *International Journal of Electrochemical Science*, **2011**, 6, 7, 2551-2565.

[4] Therdthianwong, A., Ekdharmasuit, P. and Therdthianwong, S., *Energy & Fuels*, **2010**, 24, 2, 1191-1196.

[5] Komoda, Y., Okabayashi, K., Nishimura, H., Hiromitsu, M., Oboshi, T. and Usui, H., *Journal of Power Sources*, **2009**, 193, 2, 488-494.

[6] Dixit, M. B., Harkey, B. A., Shen, F. Y. and Hatzell, K. B., *Journal of the Electrochemical Society*, **2018**, 165, 5, F264-F271.

[7] Kim, S. M., Ahn, C. Y., Cho, Y. H., Kim, S., Hwang, W., Jang, S., Shin, S., Lee, G., Sung, Y. E. and Choi, M., *Scientific Reports*, **2016**, 6.

[8] Ahn, C. Y., Jang, S., Cho, Y. H., Choi, J., Kim, S., Kim, S. M., Sung, Y. E. and Choi, M., *Scientific Reports*, **2018**, 8.

[9] Kundu, S., Fowler, M. W., Simon, L. C. and Grot, S., *Journal of Power Sources*, **2006**, 157, 2, 650-656.

[10] Ramani, D., Singh, Y., Orfino, F. P., Dutta, M. and Kjeang, E., *Journal of the Electrochemical Society*, **2018**, 165, 6, F3200-F3208.

[11] Singh, Y., Orfino, F. P., Dutta, M. and Kjeang, E., *Journal of the Electrochemical Society*, **2017**, 164, 13, F1331-F1341.

[12] White, R. T., Wu, A., Najm, M., Orfino, F. P., Dutta, M. and Kjeang, E., *Journal of Power Sources*, **2017**, 350, 94-102.

[13] Singh, Y., Orfino, F. P., Dutta, M. and Kjeang, E., *Journal of Power Sources*, **2017**, 345, 1-11.

[14] Pestrak, M., Li, Y. Q., Case, S. W., Dillard, D. A., Ellis, M. W., Lai, Y. H. and Gittleman, C. S., *J. Fuel Cell Sci. Technol.*, **2010**, 7, 4, 041009-1-041009-110.

[15] Wolf, V., Arnold Lamm., Hubert A. Gasteiger., Handbook of Fuel Cells: Fundamentals, Technology, Applications Volume 3, **2003**, John Wiley & Sons, Inc.

[16] Wang, W. T., Chen, S. Q., Li, J. J. and Wang, W., *International Journal of Hydrogen Energy*,

2015, 40, 13, 4649-4658.

[17] Kusano, T., Hiroi, T., Amemiya, K., Ando, M., Takahashi, T. and Shibayama, M., *Polymer Journal*, **2015**, 47, 8, 546-555.

[18] Chiu, R. C., Garino, T. J. and Cima, M. J., *Journal of the American Ceramic Society*, **1993**, 76, 9, 2257-2264.

[19] Chiu, R. C. and Cima, M. J., *Journal of the American Ceramic Society*, **1993**, 76, 11, 2769-2777.

[20] Kiennemann, J., Chartier, T., Pagnoux, C., Baumard, J. F., Huger, M. and Lamerant, J. M., *Journal of the European Ceramic Society*, **2005**, 25, 9, 1551-1564.

[21] Griffith, A. A., *Phil. Trans. R. Soc. Lond.*, **1921**, A 221, 163-198.

[22] Lange, F. F., *Science*, **1996**, 273, 5277, 903-909.

[23] Carreras, E. S., Chabert, F., Dunstan, D. E. and Franks, G. V., *Journal of Colloid and Interface Science*, **2007**, 313, 1, 160-168.

[24] Shukla, S., Bhattacharjee, S., Weber, A. Z. and Secanell, M., *Journal of The Electrochemical Society*, **2017**, 164, 6, F600-F609.

[25] Lee, J. H., Paik, U., Choi, J. Y., Kim, K. K., Yoon, S. M., Lee, J., Kim, B. K., Kim, J. M., Park, M. H., Yang, C. W., An, K. H. and Lee, Y. H., *Journal of Physical Chemistry C*, **2007**, 111, 6, 2477-2483.

[26] Mizukawa, H. and Kawaguchi, M., *Langmuir*, **2009**, 25, 20, 11984-11987.

[27] Berlinger, S. A., McCloskey, B. D. and Weber, A. Z., *J. Phys. Chem. B*, **2018**, 122, 31, 7790-7796.

[28] Hatzell, K. B., Dixit, M. B., Berlinger, S. A. and Weber, A. Z., *Journal of Materials Chemistry A*, **2017**, 5, 39, 20527-20533.

[29] Pollet, B. G. and Goh, J. T. E., *Electrochimica Acta*, **2014**, 128, 292-303.

[30] Shukla, S., Bhattacharjee, S., Weber, A. Z. and Secanell, M. *Journal of the Electrochemical Society*, **2017**, 164, 6, F600-F609.

[31] Khandavalli, S., Park, J. H., Kariuki, N. N., Myers, D. J., Stickel, J. J., Hurst, K., Neyerlin, K. C., Ulsh, M. and Mauger, S. A., *ACS Applied Materials & Interfaces*, **2018**, 10, 50, 43610-43622.

[32] Yamamura, M., Ono, H., Uchinomiya, T., Mawatari, Y. and Kage, H., *Colloids and Surfaces A: Physicochemical and Engineering Aspects*, **2009**, 342, 1-3, 65-69.

[33] M. Watanabe, M. Tomikawa, S. Motoo., *J. Electroanal. Chem.,* **1985**, 195, 81-93.

Chapter 9

Conclusions and Outlook

9.1 Conclusions

This thesis has described the development of particle-based functional materials for automotive applications. The studies on three major issues related to coatings and fuel cell electrodes have revealed the following:

First, automotive manufacturing industries must produce automobiles that are attractive to and functionally useful for their customers. Consumer desire for attractive colors necessitates the development of novel pigments that are ecofriendly and durable. To address this issue, this thesis proposed three types of new colored materials that contain no heavy metals, which can be toxic, and are less prone to fading under extended exposure to UV light. Some of these materials feature colors that can be tuned via changes in temperature.

Chapter 2 described the development of a thermosensitive colored system that lacks dyes or pigments yet undergoes color changes that cover the whole visible wavelength region in response to temperature. This system, which is composed of a porous gel network and a solvent such as toluene or mixed solvents, displays bright coloration as a result of the Christiansen effect because the wavelength dispersion of the refractive indices of the porous gel network and solvent intersects in the visible region. The coloration of the porous gels containing solvents can be tuned by changing the composition and temperature of the solvent; this change in color arises from the coincidence at one wavelength of the dispersion curves of the porous gels and solvent and depends on the refractive indices.

Chapter 3 reported a multicolor polymer-dispersed liquid crystal (LC) system that operates on the basis of the system described in Chapter 2. I demonstrated that particle gel networks filled with mixed nematic LCs exhibit changes in color covering the whole visible region and an opaque milky color in response to variations in temperature. The thermally tunable coloration of the colored materials arose from the coincidence at one wavelength of the dispersion curves of the particle gels and the isotropic phase of mixed nematic LCs, and an opaque milky color arose from the scattering of light as a result of the difference in the dispersion curves of the particle gels and the nematic phase. The transition point and its color could be controlled via manipulation of the composition and temperature of the mixed nematic LCs. This material displayed low-angle-dependent color and could function as a multicolor polymer-dispersed LC.

In Chapter 4, I reported that the prepared pigments exhibit enhanced colors caused by thin-film interference through absorption of scattered light by black materials. The graphite nanosheet (GNS) pigments contain no heavy metals and are nonfading pigments composed of exfoliated graphite and TiO_2. I demonstrated for the first time that GNSs that exhibit good dispersibility in water and maintain a sheet structure with few defects can be prepared via a simple procedure. The GNS pigments were obtained by sol–gel deposition of a TiO_2 layer and its various colors were displayed by adjusting the thickness of the TiO_2 film by varying the reaction time. Because of the light-absorbing properties originating from the black GNSs and the diffuse reflection derived from the random orientation of the GNS pigment in the coating, the coating film exhibited enhanced colors with angle independence.

Second, because consumers generally desire longer-lasting scratch-free coatings, scratch resistance has become one of the most important properties of automotive coatings. Scratches in these coatings are classified into two types: fracture-type scratches and deformation-type scratches that do not break and can recover over time, eventually even becoming invisible to the human eye. This feature, which arises from elastic–plastic behavior and is called “self-recovery,” is strongly demanded by customers. Hence, this thesis mainly focused on the recovery of scratch deformations.

To evaluate coating service life of scratch characteristics, I first investigated the relationship between chemical changes and scratch resistance using outdoor weathering tests in Chapter 5. The scratch properties and chemical changes were examined using Fourier transform infrared (FT-IR) spectroscopy. For all coatings containing acrylic polyols, the critical fracture force decreased after 1 month of outdoor exposure. The FT-IR spectra showed that crosslink scission occurred in the coating surface layer because of oxidation and hydrolysis during exposure. Degradation of the scratch resistance was found to be caused by chemical changes in the surface layer within a short time. Therefore, in Chapter 6, I explored the remarkable improvement of the scratch recovery characteristics and durability that resulted from using a base resin with a siloxane main chain instead of acrylic polyols.

As described in Chapter 6, crosslinked polyorganosilsesquioxane coatings (Si-films) achieved both hardness suitable for automobile coatings and improved scratch recovery characteristics superior to those of conventional coatings (C-films). The Si-films demonstrated a 20% better elastic

recovery index than the C-films, and the Si-films recovered approximately twice as fast as the C-films. Scratch deformations on the Si-films almost disappeared after 15 min, even at room temperature, whereas the disappearance of scratch deformations on the C-films required more than 24 days. Thus, coatings based on a siloxane main chain may offer dramatically improved self-recovery performance.

Third, to facilitate the widespread use of PEFCs, the stable production of high-quality catalyst layers is required. Catalyst ink formation influences the manufacturing productivity of PEFCs and also affects the catalyst layer structure, consequently determining the electrode performance. Therefore, an evaluation of the agglomerate structure of carbon-black-supported Pt (Pt/C) nanoparticles, which controls the dispersion state and stability, is necessary.

In Chapter 7 of this thesis, agglomeration behavior is demonstrated to be controlled by water content, leading to changes in the ionomer adsorption on Pt/C, which in turn leads to changes in the rheological behavior and stability of catalyst inks. Depending on the water content, Pt/C agglomerates have low-density network structures that form via a diffusion-limited cluster aggregation process because of weak repulsion force, which is a consequence of the lack of ionomer; alternatively, more compact agglomerates may form via a reaction-limited cluster aggregation process due to steric and electrostatic stabilization induced by the adsorbed ionomer. The proposed methods should be useful for improving the quality of coating films.

In addition, although the stable production of high-quality catalyst layers is required for the mass production of PEFCs, a catalyst ink film on a substrate often cracks during drying. Because cracks in the catalyst layers of a fuel cell affect performance and durability, elucidating the factors that control crack formation is important. In Chapter 8, crack behavior is shown to be controlled by ionomer adsorption into the Pt/C in catalyst ink. A well-dispersed catalyst ink produces a homogeneous Pt/C and ionomer distribution in catalyst layers with high fracture toughness, whereas catalyst inks with a network of structured agglomerates produce dense aggregates with small primary pores that generate high drying stress; catalyst inks with a self-organizing free ionomer cause stress concentration in catalyst layers, making them prone to cracking. This research provides useful information for controlling cracking during the manufacture of catalyst layers.

9.2 Outlook

The particle-based functional materials developed in this thesis research are promising; nevertheless, further effort is needed to achieve functional materials suitable for use in next-generation vehicles. I believe that at least the following work would be desirable:

The colored materials developed in this thesis have potential applications in coating materials, optical materials, and automotive devices, as demonstrated in Chapters 2 through 4. As discussed in Chapter 2, room exists for improving the solidification and increasing the saturation of the colored materials. Thus far, a few systems that exploit the Christiansen filter effect based on various dispersions of two different media have been reported. However, because most of these previously reported systems are composed of crushed insoluble inorganic powders immersed in organic solvents or prepared as colloidal suspensions, using them to create devices with a desired shape has been difficult. By contrast, our colored material generated using a porous gel network and solvent can be cast into desired shapes and exhibits brilliant colors. However, solvents are not appropriate for practical use. A solid–solid system such as a film is more convenient than a solid–liquid system. For example, a film composed of porous gel networks filled with a polymer or resin that satisfies the requirements for the Christiansen filter effect would be more practical.

In addition, greater saturation color is preferred by consumers. Achieving greater saturation color requires the selection of materials that generate a sharp reflectance peak. The large difference in the wavelength dispersion of the refractive indices between a porous gel network and the dispersion medium results in a sharp reflectance peak, which leads to bright color. However, the combination of a polymer porous gel and solvent is close to the limit. By contrast, the combination of inorganic porous materials and organic materials or the combination of hybrid porous materials and organic materials is attracting efforts to develop brighter-colored materials. Furthermore, the optimal scattering properties of diffuse reflective materials are not yet fully understood, impeding the development of brighter-colored materials. Only by understanding the pore-size dependence of the reflection intensity of diffuse reflection and the thickness of porous gels can I expect to achieve optimal designs of colored materials for practical applications.

Room also exists for further improving the stimuli-sensitive materials mentioned in Chapter 3.

Because the newly prepared colored materials are composed a particle gels filled with stimuli-sensitive materials, and because they can be incorporated into other stimuli-sensitive polymer systems, they have potential applications as chromic (thermochromic, electrochromic, and photochromic) materials. For example, the system that comprises particle gel networks filled with LCs might be controllable by an electric field because of the sensitivity of the LCs to electric fields. The electrically tunable coloration of colored materials arises from the coincidence at one wavelength of the dispersion curves of the particle gels and the alimented LCs by an electric field, and an opaque milky color arises from the scattering of light due to the difference in the dispersion curves of the particle gels and randomly orientated LCs when the electric field is removed. This system is easy to prepare as a large-sized display because of its facile one-pot preparation method and its mechanism of coloration. This colored material represents a promising new material for the manufacture of reflective full-color displays with angle independent and which are controllable by an electric field; it is also an energy-saving, nonfading color material. For photochromic materials, the system composed of particle gels filled with photochromic molecules might be controllable by irradiation with light. The photochromic-tunable coloration of colored materials arises from the coincidence at one wavelength of the dispersion curves of the particle gels and photochromic molecules by photoisomerization, and an opaque milky color arises from the scattering of light due to the difference in the dispersion curves of the particle gels and isomers when the light source is turned off. This system may be promising new dimmable glass that is expected to apply as antiglare mirror or smart windows. Therefore, these systems based on stimuli-sensitive materials exhibit optical properties that change in response to various stimuli such as light, electric fields, temperature, and magnetic fields can be used to prepare new color-changing materials for automotive applications.

In Chapter 4, GNSs were shown to enhance the color contrast and a randomly oriented GNS pigment was shown to exhibit angle-independent color in a coating film by diffuse reflection. However, the obtained colors are still dark, and the reflection is weak. Although I believe that GNS pigments can potentially be used with minimal improvement as dark-colored pigments in, for example, the cosmetics or ink industry, their brightness and saturation should be improved to enable their use in the automotive industry. To control the brightness and saturation, the relationship between the orientation and size of the pigments and the coloration should be explored. In principle,

several options are available to enhance the reflection. Large pigment particles exhibit greater brilliance than small pigment particles because their reflection area is larger. In general, interference pigments are visually most appealing when there is good parallel orientation to the surface. Using a low-refractive-index polymer for the matrix is also effective. However, several hurdles remain to achieving these objectives and angle independence has yet to be achieved.

As discussed in Chapter 6, automotive coatings based on a siloxane main chain may offer dramatically improved self-recovery. However, the potential differences in the chemical and morphological structures of the siloxane main chain and the acrylic polyol main chain remain unclear. To address this issue, I additionally examined the structures of Si-films by TEM and small-angle X-ray scattering (SAXS). However, no structures were observed in the TEM images, and no peak was observed in the SAXS pattern, even when the density fluctuation was less than 10 nm; these results imply that Si-film is uniform at the molecular level. Further explorations using other methods are needed to clarify the reason for the dramatically improved self-recovery. Moreover, from the viewpoint of practical appreciation, I need to further explore whether the materials, when used as automotive coatings, exhibit good total balance between appearance, durability, water resistance, and environmentally compatibility.

The influence of various ionomer dispersion solvents on catalyst ink formation was discussed in Chapters 7 and 8. The materials used in catalyst inks and the processing method of the inks are decided on the basis of various parameters. However, because the structure of catalyst inks changes with time, a comprehensive understanding of their structure is required. As a future work, I will extend this study to include numerical simulations to provide a clear understanding of and method for controlling the coating process of catalyst inks. In addition, the analysis of cracking will be extended to examine the effects of cracks on the performance and durability of PEFCs in detail. Furthermore, the factors that impede the high-speed production of fuel cells must be overcome to enable their widespread use. Currently, some parts that cannot be mass produced are carefully hand-made by craftsmen. However, the evolution of production methods is expected to enable the continuous mass production of fuel cells, and 1 million fuel-cell-powered cars are expected to be produced annually in 2030. I hope that the findings of this thesis will provide insights into the

high-speed production of fuel cells.

Finally, although the coating materials have been improved, dramatic advancements are required and cannot be achieved through the extension of conventional ideas. In addition, the materials and processing for fuel cell vehicles will be further improved through the development of next-generation vehicles in the technological competition called the “Global Challenge.” I hope that the findings of this study will provide insights into the development of particle-based functional materials for the automotive industry.

List of Publications

This thesis is based on the following papers which were already published.

1. Original papers corresponding to this thesis

-Chapter 2-

[1] Kumano, N., Seki, T., Ishii, M., Nakamura, H. and Takeoka, Y. “Tunable Angle-Independent Structural Color from a Phase-Separated Porous Gel.”*Angewandte Chemie International Edition*, 50, 17 (2011), 4012-4015.

-Chapter 3-

[2] Kumano, N., Seki, T., Ishii, M., Nakamura, H., Umemura, T. and Takeoka, Y. “Multicolor Polymer-Dispersed Liquid Crystals.” *Advanced Materials*, 23, 7 (2011), 884-888.

-Chapter 4-

[3] Kumano, N., Tanaka, H., Akimoto, Y. and Nakamura, H., “Preparation of Interference Pigment Using Black Graphite Nanosheet.” *Journal of Materials Chemistry C*, 8 (2020)16749-16756.

-Chapter 5-

[4] Kumano, N., Mori, K., Kato, M. and Ishii, M., “Degradation of scratch resistance of clear coatings by outdoor weathering.” *Progress in Organic Coatings*, 135 (2019), 574-581.

-Chapter 6-

[5] Kumano, N., Mori, K. and Kato, M. “Recovery of scratch deformation formed on crosslinked polyorganosiloxane films.” *Progress in Organic Coatings*, 127 (2019), 124-130.

-Chapter 7-

[6] Kumano, N., Kudo, K., Akimoto, Y., Ishii, M. and Nakamura, H. “Influence of Ionomer Adsorption on Agglomerate Structures in High-Solid Catalyst Inks.” *Carbon*, 169 (2020), 429-439.

-Chapter 8-

[7] Kumano, N., Kudo, K., Suda, A., Akimoto, Y., Ishii, M. and Nakamura, H. “Controlling cracking formation in fuel cell catalyst layers.” *Journal of Power Sources*, 419 (2019), 219-228.

2. International Conferences

(1) “Preparation and Optical Properties of self-organizingly microphase-separated gel.”
Kumano, N., Seki, T., Ishii, M., Nakamura, H. and Takeoka, Y.
Conference: The 1st Federation of Asian Polymer Society Polymer Congress
Location: Nagoya, Japan, Date: October 20-23, 2009

(2) “Recovery mechanism of scratch deformation formed on automotive clearcoats.”
Kumano, N., Mori, K. and Kato, M.
Conference: 85th JSCM Anniversary Conference (The Japan Society of Colour Materials)
Location: Tokyo, Japan, Date: October 24-25, 2013

(3) “Colloid chemical approach to cracking formation in fuel cell catalyst layers.”
Kumano, N., Kudo, K., Akimoto, Y., Ishii, M. and Nakamura, H.
Conference: 255th National Meeting and Exposition of the American-Chemical-Society
Location: New Orleans, LA, Date: March 18-22, 2018

(4) “Investigation of Cracking Formation of Catalyst Layers for Polymer Electrolyte Fuel Cells.”
Kumano, N., Kudo, K., Suda, A., Akimoto, Y., Ishii, M. and Nakamura, H.
Conference: 18th Asian Pacific Confederation of Chemical Engineering Congress
Location: Sapporo, Japan, Date: September 23, 2019

3. Awards

(1) The Young Scientist Poster Award
Conference: the 1st Federation of Asian Polymer Societies Polymer Congress
Location: Nagoya, Japan, Date: October 20-23, 2009

(2) 名古屋大学材料バックキャストテクノロジー研究センター若手研究奨励賞
Date: November 1, 2009

(3) The Excellent Lecture Award
Conference: 85th JSCM Anniversary Conference (The Japan Society of Colour Materials)
Location: Tokyo, Japan, Date: October 24-25, 2013

(4) The Excellent Lecture Award
Conference: 2014 Annual Conference (The Japan Society of Colour Materials)
Location: Nagoya, Japan, Date: October 24, 2014